First measurement of the associated production of a photon and a bottom quark in proton–proton collisions

Sébastien Prince

Doctor of Philosophy

Department of Physics

McGill University

Montréal, Québec

2018-08-24

A thesis submitted to McGill University in partial fulfillment of the requirements of the degree of Doctor of Philosophy

ABSTRACT

The first measurement of the differential cross section of the associated production of a photon and a bottom quark in proton–proton collisions is presented. Protons are accelerated and brought into collision at a center-of-mass energy of 8 TeV by the Large Hadron Collider. The collisions are recorded with the ATLAS detector and correspond to an integrated luminosity of up to 20.2 fb^{-1}. The measurement is performed in two regions of the absolute value of the photon pseudorapidity: from 0 to 1.37 and from 1.56 to 2.37. The measurement is performed as a function of the photon transverse energy, from 25 to 400 GeV in the former pseudorapidity region and from 25 to 350 GeV in the latter region. The relative uncertainty in the measurement varies between 13% and 54% and is dominated by the uncertainty in the efficiency of identifying jets containing bottom quarks. The ratio of the cross section in the two pseudorapidity regions is also measured to reduce the positively correlated systematic uncertainties in the measurement between the two regions. The measurement is compared to predictions of perturbative quantum chromodynamics at the leading order and at the next-to-leading order. At low transverse energy, a good agreement is observed between the measured and the predicted values. At high transverse energy, however, the measured values are observed to be up to a factor of two larger than the most precise predicted values. This measurement can help improve the modelling of bottom quarks in perturbative quantum chromodynamics.

ABRÉGÉ

La première mesure de la section efficace différentielle de la production associée d'un photon et d'un quark bottom dans des collisions proton–proton est présentée. Des protons sont accélérés et amenés à entrer en collision à une énergie de 8 TeV au centre de masse par le Grand collisionneur de hadrons. Les collisions sont enregistrées par le détecteur ATLAS et correspondent à une luminosité intégrée allant jusqu'à 20.2 fb^{-1}. La mesure est effectuée dans deux régions de la valeur absolue de la pseudorapidité du photon : de 0 à 1.37 et de 1.56 à 2.37. La mesure est effectuée en fonction de l'énergie transverse du photon, de 25 à 400 GeV dans la première région de pseudorapidité et de 25 à 350 GeV dans la seconde région. L'incertitude relative de la mesure varie entre 13% et 54% et est dominée par l'incertitude sur l'efficacité de l'identification des jets contenant un quark bottom. Le ratio de la section efficace dans les deux régions de pseudorapidité est aussi mesuré afin de réduire les incertitudes systématiques sur la mesure qui sont positivement corrélées entre les deux régions. La mesure est comparée à des prédictions de chromodynamique quantique perturbative d'ordre le plus bas et d'ordre supérieur. À basse énergie transverse, les valeurs mesurées sont en accord avec les valeurs prédites. Cependant, à haute énergie transverse, les valeurs mesurées sont jusqu'à deux fois plus grandes que les valeurs prédites les plus précises. Cette mesure peut permettre de parfaire la modélisation du quark bottom dans la chromodynamique quantique perturbative.

AUTHOR'S CONTRIBUTION

This doctoral thesis presents the measurement of the cross section of the associated production of a photon and a bottom quark in proton–proton collisions. It is the first time that the measurement of this physical process is performed. Consequently, the results presented in this thesis are an original and distinct contribution to knowledge.

The measurement is published in Phys. Lett. B **776** (2018) 295, along with the similar measurement of the cross section of the associated production of a photon and a charm quark. This publication is signed by a collaboration of about three thousand authors who all contributed to the overall experiment and made this measurement possible, but not necessarily to this specific measurement. A group of eight of the authors of the publication contributed directly to that particular publication. The author of this thesis led the group for the measurement presented in this thesis. The author also contributed significantly to the measurement that is part of the publication but that is not presented in this thesis.

Specifically, the author of this thesis designed, coded, carried out and optimized the complete data analysis through which the cross section is measured; identified and evaluated the uncertainty sources that affect the measurement; contacted and discussed with theoretical physicists what state-of-the-art theoretical predictions are available to compare to the measurement; and interpreted the results in terms of the underlying physics. The author also wrote the majority of the above publication on behalf of the collaboration, including the production of all the published plots.

Furthermore, the author made publicly available on the Web the measured values of the cross section and of the correlations of their individual uncertainties. Finally, the author wrote and made publicly available on the Web software that implements the definition of the fiducial phase-space region in which the cross section is measured, which simplifies the comparison of the measurement with future theoretical predictions.

A summary of the contributions of the author of this thesis and of the co-authors of the publication follows for each chapter.

In Chapter 1, the author motivates the measurement of the physical process presented in this thesis from the context of measurements of other physical processes performed prior to it.

In Chapter 2, the author synthesizes the theoretical description of the physical process that is measured and provides a literature review of the possible theory predictions of that process. The particular predictions that are compared to the measurement are chosen by the author but are technically produced by the co-authors of the publication.

In Chapter 3, the author presents the experimental apparatus that is used to perform the measurement and which has been built by the co-authors of the publication. The author contributed partially to the operation of the trigger system of the apparatus.

In Chapter 4, the author summarizes the reconstruction of physical objects from the signals measured by the apparatus. This reconstruction has been developed by the co-authors of the publication.

In Chapters 5, 6, 7, 8 and 9, the original contribution to knowledge of the author is presented. In these chapters, the author presents the data analysis that is originally developed, making use of what has been presented in the previous chapters, and of the ensuing results. Every figure presented in these chapters is produced by the author. The co-authors of the publication provided supervision to the author, such as to perform the most accurate and the most precise measurement possible.

In Chapter 10, the author summarizes the data analysis and the results and provides ideas on how to improve upon them in a possible future iteration of the measurement.

In Appendices A, B and C, the author defines observables, physical objects and techniques that are used throughout the thesis.

In Appendices D and E, the author provides the measured values of the cross section and of the correlations of their uncertainties, which have been made publicly available on the Web.

ACKNOWLEDGEMENTS

Above all, I want to acknowledge the work of my supervisor, Prof. Brigitte Vachon, and thank her for her constant support. She has believed in me throughout my studies and worked hard on making me thrived as a researcher. I am grateful for her unrelenting devotion.

I want to express my gratitude to Dr. Mark Stockton for serving as a mentor during my time at CERN. He helped me in the physical, technical and social aspects of my research. I asked for a lot of his time and he was always willing to give it. I want to thank him for all of this.

I would like to thank the Madrid group, Prof. Claudia Glasman, Prof. Juan Terrón and Dr. Josu Cantero, for their help in the data analysis concerning the subtleties of the physics and of the technical aspects. Similarly, I would like to thank Dr. Matthias Saimpert for his inexorable determination to make the measurement the best it can be and for allowing the timely publication of the measurement.

An important actor in the publication is Dr. Robert Keyes, a fellow student who worked on a similar measurement and with whom I shared the writing of the publication. He was the person with whom I worked the closest and thus with whom I had uncountable discussions and arguments. I have learned much from his efficient way of working and I thank him for this.

I would also like to mention and thank Dr. Ricardo Gonçalo and Prof. David Miller,

who have appreciated my work in the trigger system of the detector and who have granted me authorship regarding the publications of the collaboration.

The fellow students in the research group at McGill provided me with an opportunity to crystallize my new-found physical and technical knowledge. I thank them for trusting me to answer their questions.

Finally, thanks to my family and friends for their support during this long endeavour that I undertook. In particular, I want to thank Anabel, Benoit and Robert, with whom I have started my doctoral studies and with whom I have shared moral support during both the successes and the hardships that we individually or commonly experienced.

TABLE OF CONTENTS

CHAPTER 1
Introduction

The bottom quark was discovered at Fermilab in 1977 by the experiment E288 [1]. A resonance at 9.5 GeV was observed in the production of oppositely charged muons produced in the collisions of protons with fixed targets made of copper and platinum. This resonance was due to the presence of the Υ composite particle, a bound state of a pair of bottom quark and antiquark. The existence of the bottom quark, alongside that of the top quark, had been predicted in 1973 by Makoto Kobayashi and Toshihide Maskawa to explain violation of the charge–parity (CP) symmetry in kaons [2]. However, this prediction published in Japan had not reached North America at the time of the discovery, such that the resonance came as a surprise [3]. The bottom quark was at the time the first particle to be accepted as part of a new third generation of elementary fermions, even though evidence for the existence of the τ lepton existed since 1975 [4].

Composite particles containing bottom quarks can possess uniquely interesting properties. They can have relatively heavy masses and long lifetimes, making them compelling objects to study both theoretically and experimentally.

Electron–positron colliders have been built to produce abundantly bottom quarks. These colliders enable experiments such as BaBar [5], Belle [6] and the upcoming Belle II [7] to search for new physical phenomena and to study precisely CP violation,

a phenomenon related to the matter–antimatter asymmetry of the universe. Bottom quarks have also been used in the CDF [8] and D0 experiments [9] at the Tevatron [10] to discover the top quark in 1995 in proton–antiproton collisions [11, 12]. Bottom quarks can also help establish the nature of the Higgs boson since it is expected to decay predominantly into a pair of bottom quark and antiquark. Using proton–proton collisions provided by the Large Hadron Collider (LHC) [13], the ATLAS [14] and CMS [15] experiments recently found evidence for that decay channel [16, 17]. Furthermore, several theories predict new particles that would decay into bottom quarks, such as compositeness models [18], in which the quarks are not elementary particles and could be excited; supersymmetric models [19], in which known elementary particles are associated to heavier unknown particles; or models with new heavy gauge bosons [20].

In searches for new physics, the production of bottom quarks from known mechanisms in quantum chromodynamics (QCD) constitutes an important background that needs to be well modelled. A measurement of the production cross section of particle jets containing composite particles made up of bottom quarks, referred to as b-jets, in proton–proton collisions provides a quantity that can be compared to theory predictions. This comparison can help improve the modelling of the production of bottom quarks.

The production of b-jets in QCD processes at the LHC has been measured by the ATLAS [21, 22] and CMS [23] experiments. An experimentally more precise way of measuring the production of b-jets is through the associated production of electroweak gauge bosons, since these can be measured more precisely than jets. The associated

production of a Z boson with a b-jet has been measured recently by ATLAS [24] and CMS [25, 26]. In addition, the LHCb experiment [27] has measured that process [28]. The associated production of a W boson with a b-jet has also recently been measured by ATLAS [29], CMS [30, 31] and LHCb [32, 33]. The associated production of a photon with a b-jet has not been measured in proton–proton collisions.

The production of prompt photons is theoretically and experimentally interesting in its own right, where prompt photons refer to photons not produced by the decays of composite particles. Photons are among the most abundantly produced particles in proton–proton collisions. They are also directly observable, in contrast to most other types of particles that are produced in the collisions. The photons that are detected are the same ones that are produced in the scattering of the protons. The detected photons directly probe the QCD dynamics of the proton–proton collisions. In addition, photons are measured by calorimeters through the electromagnetic shower that they produce. These showers can be measured precisely and thus the energy of the photons can also be measured precisely.

The inclusive prompt photon production in proton–proton collisions, where inclusive refers to the possible production of any other particles, has been measured by ATLAS [34–36] and CMS [37]. These measurements provide a test of the predictions of perturbative QCD (pQCD). The less inclusive measurement of a prompt photon produced in association with a jet allows to test pQCD through additional observables, in addition to being an important background to Higgs bosons decaying into two photons. This process has also been measured by ATLAS [38–40] and CMS [41–43]. Beyond testing the predictions of pQCD, the ubiquitous production of a prompt

photon in association with a jet makes it an interesting channel in which to search for new physics, such as excited quarks and quantum black holes. These searches have recently been performed by ATLAS [44] and CMS [45].

In proton–proton collisions, the even more exclusive production of a prompt photon with a b-jet has been used to search for new physics by CMS [45] but has yet to be measured. Measurements of this process, however, have been performed in proton–antiproton collisions by CDF [46, 47] and D0 [48, 49]. The production was measured as a function of the component of the photon momentum that is transverse to the momenta of the colliding particles, the transverse momentum.[1] These measurements did not agree with the most precise theoretical predictions of this process available in pQCD, the next-to-leading order (NLO) calculations. This disagreement can be seen in the most recent D0 measurement, reproduced in Figure 1–1. This measurement has the largest kinematic acceptance for the prompt photon and the b-jet out of the Tevatron measurements. The ratio of the data to the NLO prediction is shown, as well as that of other predictions that are less precise but which test different aspects of the calculations.

In proton–proton or proton–antiproton collisions, Compton scattering is the largest contribution to the production of a photon and a b quark. The quark–antiquark annihilation is an additional contribution that is important in the collisions of protons

[1]The main observables describing the kinematics of this process, i.e. the transverse momentum, p_{T}, and the rapidity, y, are discussed in Appendix A.

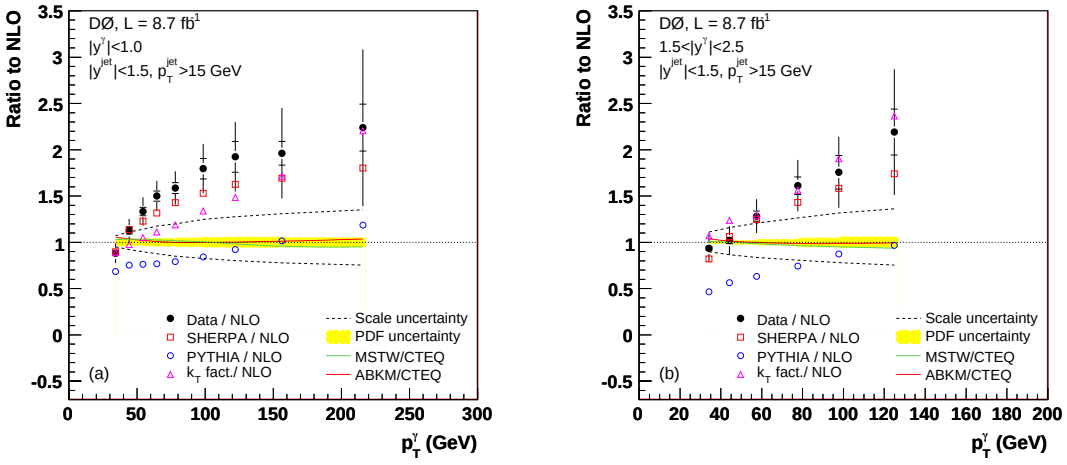

Figure 1–1 – Ratio of the D0 measurement to the NLO prediction of the associated production cross section of a prompt photon and a b-jet in proton–antiproton collisions as a function of the photon transverse momentum, for two mutually exclusive regions of photon rapidity. Reproduced with permission from Ref. [49].

and antiprotons due to the increased presence of antiquarks. This contribution is not as well predicted as the Compton scattering contribution and is believed to be the source of the disagreement between the Tevatron measurements and the NLO calculations. As such, the production of a photon and a bottom quark in proton–proton collisions is expected to be better described by NLO predictions than in proton–antiproton collisions. A measurement at the LHC would provide a stringent test of pQCD, especially for the aspects related to the bottom quark. Furthermore, the Compton scattering contribution is sensitive to the presence of bottom quarks in the proton, while the quark–antiquark annihilation contribution is not. A measurement of this type of production at the LHC would thus also provide increased sensitivity to the bottom-quark content of the proton compared to the Tevatron measurements.

Motivated by these reasons, this thesis presents the first measurement of the cross section of the inclusive production of a prompt photon in association with a b-jet in proton–proton collisions. Collisions are provided by the LHC at a center-of-mass energy of 8 TeV and are measured with the ATLAS detector. The measured cross section is fiducial in the four-momenta of the particles, i.e. boundaries are placed on the measured photon and b-jet four-momenta. The measured cross section is differential as a function of the photon transverse momentum. The cross section is measured statistically from an ensemble of collisions; no single collision is explicitly determined to have produced a prompt photon and a b-jet. The measurement is performed in two mutually exclusive regions of photon rapidity. The ratio of the cross section in these two regions is also measured to reduce theoretical and experimental uncertainties that are positively correlated between the two regions.

This thesis is divided into the following chapters.[2] Chapter 2 discusses the theoretical background of the concepts introduced in this chapter and of the predictions of the measured process. Chapter 3 covers the experimental setup that allows for two protons to collide and for the detection of the particles that are produced in the collisions. Chapter 4 gives details about how the physical objects of interest are reconstructed from the measured signals. Chapter 5 describes the selection criteria that are applied on the reconstructed objects to measure the desired particles. Chapter 6 explains how background contributions are subtracted from the selection. Chapter 7 discusses how

[2]Natural units are used throughout the thesis, for which the speed of light and the reduced Plank constant are equal to unity: $c = 1$ and $\hbar = 1$.

the measurement is corrected to allow comparisons to theory predictions. Chapter 8 goes into details about the uncertainties that are considered in the measurement and theory predictions. Chapter 9 presents the measured and predicted values of the cross section and cross-section ratio and provides an interpretation of the results. Chapter 10 summarizes the results and offers some ideas on how to improve the measurement.

CHAPTER 2
Theoretical Background

This chapter covers the theoretical background necessary to interpret the results presented in this thesis. The first section presents the Standard Model of particle physics in terms of its particle content and associated interactions. The second section describes how this theory is actually used to predict the outcome of collisions between protons, such that the theory can be compared to experimental results. The details specific to the predictions of the cross section of the associated production of a photon and a bottom quark are discussed in the third section.

2.1 Standard Model

The theoretical description of nature at the smallest distance scales that have been measured is given by the Standard Model [50–53]. The Standard Model describes mathematically the dynamics of nature's fundamental components, the elementary particles, which are believed to be point-like. To satisfy the requirements of a theory describing multiple objects at small scales and with possible high velocities, the Standard Model is a quantum field theory, which is based on concepts of field theory, quantum mechanics and special relativity. As such, it is a probabilistic description of nature. Although the theory can make predictions, several of its parameters are free and must be measured prior to making quantitative predictions about nature.

The Standard Model describes the interactions of the elementary particles listed in Table 2–1. The measured particle masses, which are free parameters in the theory, and some of the quantum properties of the particles in the model are also listed. Particles are divided into fermions and bosons. The spin, J, of these kinds of particles respectively takes half-integer and integer values. Due to the conservation of angular momentum, fermions only interact in pairs with bosons. If a boson has $J = 1$, it is called a gauge boson and it mediates a force between two fermions. Gauge bosons can also interact among themselves. The Higgs boson is the only scalar boson, i.e. a boson with $J = 0$. Its interactions are related to the origin of particle masses, which would be zero otherwise. It only interacts with massive particles.[1]

The rules of the interactions between the particles are governed by two theories that make up the Standard Model: the electroweak theory and quantum chromodynamics (QCD). The electroweak theory describes the interactions of particles under a combined U(1) and SU(2) gauge symmetry. This electroweak symmetry is spontaneously broken via the Brout–Englert–Higgs mechanism [55, 56]. The symmetry breaking results in the electromagnetic force, described by a U(1) symmetry, and the weak force. The electromagnetic force is mediated by the photon. Fermions that interact under that force carry an electric charge, q_e, and the sum of the electric charges is conserved in an electromagnetic interaction. The weak force is mediated by the W and Z

[1] Although neutrinos are measured to be massive, they do not interact with the Higgs boson, and thus are formally massless, in the Standard Model. They acquire non-vanishing masses via a currently unknown mechanism.

Table 2–1 – Particle content of the Standard Model. The values for the mass m, the spin J, the electric charge q_e, and the z-component of the weak isospin T_z of the particles are given. If a particle carries a color charge, it is indicated as such by a checkmark and, otherwise, by a cross. The mass values come from measurements [54]. They are reported here with three significant figures, if the precision allows, and with two significant figures otherwise; their uncertainties are omitted. The upper limit at 95% confidence level on the sum of the neutrino masses is reported for each neutrino flavour. The electric charge is given as a multiple of the fundamental electric charge.

	Name	Symbol	Generation	m	J	q_e	T_z	Colored
Leptons	Electron neutrino	ν_e	I	< 0.12 eV	$\frac{1}{2}$	0	$\frac{1}{2}$	×
	Muon neutrino	ν_μ	II	< 0.12 eV	$\frac{1}{2}$	0	$\frac{1}{2}$	×
	Tau neutrino	ν_τ	III	< 0.12 eV	$\frac{1}{2}$	0	$\frac{1}{2}$	×
	Electron	e	I	511 keV	$\frac{1}{2}$	-1	$-\frac{1}{2}$	×
	Muon	μ	II	106 MeV	$\frac{1}{2}$	-1	$-\frac{1}{2}$	×
	Tau	τ	III	1.78 GeV	$\frac{1}{2}$	-1	$-\frac{1}{2}$	×
Quarks	Up	u	I	2.2 MeV	$\frac{1}{2}$	$\frac{2}{3}$	$\frac{1}{2}$	✓
	Charm	c	II	1.28 GeV	$\frac{1}{2}$	$\frac{2}{3}$	$\frac{1}{2}$	✓
	Top	t	III	173 GeV	$\frac{1}{2}$	$\frac{2}{3}$	$\frac{1}{2}$	✓
	Down	d	I	4.7 MeV	$\frac{1}{2}$	$-\frac{1}{3}$	$-\frac{1}{2}$	✓
	Strange	s	II	96 MeV	$\frac{1}{2}$	$-\frac{1}{3}$	$-\frac{1}{2}$	✓
	Bottom	b	III	4.18 GeV	$\frac{1}{2}$	$-\frac{1}{3}$	$-\frac{1}{2}$	✓
Gauge Bosons	Gluon	g		0	1	0	0	✓
	Photon	γ		0	1	0	0	×
	W	W		80.4 GeV	1	1	1	×
	Z	Z		91.2 GeV	1	0	0	×
	Higgs boson	H		125 GeV	0	0	$-\frac{1}{2}$	×

bosons. The mathematical structure of the weak force is more complex than the electromagnetic force, but it can be approximately understood as the conservation of the z-component of the weak isospin, T_z.[2] All fermions interact through the weak force. Quantum chromodynamics describes the interactions of particles coupling via a strong force, described by an SU(3) symmetry. Particles interacting this way carry a color charge, such as quarks and gluons, of which the latter mediate the force. Quarks are defined as fermions carrying a color charge, the colored fermions, while leptons are the fermions that do not. The flavour of a quark or lepton refers to a specific type of quark or lepton. Quarks and leptons can be further separated into three generations of corresponding particles. Corresponding particles across generations interact in the same way but have different masses. The first generation refers to the least massive particles and the third generation refers to the most massive ones.[3] In addition to the particles of Table 2–1, distinct antiparticles exist for the fermions and the W boson.[4] The values of q_e and T_z for these antiparticles are opposite to those of the particles.

The symmetries of the Standard Model define the interactions between a gauge boson mediating a force and other particles up to a dimensionless proportionality constant.

[2]For completeness, all interactions conserve this quantity, except those involving the Higgs boson.

[3]As the neutrinos are massless in the Standard Model, their generations instead refer to that of the electrically charged leptons. It is currently unknown if the ordering of the non-vanishing masses of the neutrinos coincides with their generation ordering.

[4]It is possible that the neutrinos do not have distinct antiparticles. It is yet undetermined if this is the case.

The constants are called α_{S}, α and α_{W} respectively for the strong, electromagnetic and weak forces. Being dimensionless, these coupling constants define the intrinsic strength of the force. Their values are free in the theory and have to be measured. The values of these constants change with the energy of the interaction, Q. This energy dependence is called the running of the constants. The values of the coupling constants at an energy scale corresponding to the mass of the Z boson are given in Table 2–2. The strength of the weak force is in practice weaker at energy scales below $Q \approx m_Z$ since, in contrast to the other forces, the gauge bosons mediating that force are massive. At those low energy scales, the coupling constant α_{W} is accompanied by a factor of about $1/m_Z^2$ [57]. Thus, the effective value of the weak coupling constant is $\alpha_{\mathrm{W}}/m_Z^2 \approx 0.000004\ \mathrm{GeV}^{-2}$, much weaker than the other two forces at interaction energies of about 1 GeV. In addition, for interactions involving the W boson and quarks, an additional coupling parameter is involved specific to the pair of quarks interacting. The W boson has a value $T_z = 1$, such that quarks must be of different flavours, giving rise to nine possible quark-pair interactions. The collection of these nine additional coupling parameters form the unitary Cabibbo–Kobayashi–Maskawa (CKM) matrix [2, 58]. The values of the parameters are measured to be ordered such that interactions of quarks within the same generation are stronger than between generations, with interactions between the first and the third generations being the weakest.

The values of the coupling constants of the electromagnetic and weak forces slowly increase with increasing energy. In contrast, the coupling constant of the strong force decreases with increasing energy, a phenomenon known as asymptotic freedom [59, 60].

Table 2–2 – Forces described by the Standard Model and their mediating gauge bosons. The measured values of their coupling constants are given at an energy scale, Q, equal to the mass of the Z boson. The values presented in the table are derived from the values of the physical constants given in Ref. [54]. The values are given with two significant figures and their uncertainties are omitted.

Name	Gauge boson	Coupling constant at $Q = m_Z$
Strong	Gluon	$\alpha_{\mathrm{S}} = 0.12$
Electromagnetic	Photon	$\alpha = 0.0078$
Weak	W and Z	$\alpha_{\mathrm{W}} = 0.034$

As a comparison point to the value in Table 2–2, the strong coupling is about 0.33 at the energy scale corresponding to the mass of the tau lepton [61]. An additional phenomenon occurs in QCD: color confinement, i.e. colored particles cannot be observed. A consequence of this phenomenon is that quarks are bound together to form composite particles known as hadrons. A quark and an antiquark can bind together to form a meson and three quarks can bind together to form a baryon. The proton, p, is a baryon made up of two up quarks and one down quark. These three quarks that define the content of the proton are called valence quarks.

The running of a coupling constant can be calculated by its renormalization group equation. In the case of the strong coupling constant, that equation [59, 60] is

$$\frac{d\,\alpha_{\mathrm{S}}(\mu_{\mathrm{R}})}{d\ln\mu_{\mathrm{R}}^2} = \beta(\alpha_{\mathrm{S}}(\mu_{\mathrm{R}})) = -(b_0\alpha_{\mathrm{S}}^2(\mu_{\mathrm{R}}) + b_1\alpha_{\mathrm{S}}^3(\mu_{\mathrm{R}}) + b_2\alpha_{\mathrm{S}}^4(\mu_{\mathrm{R}}) + \cdots), \tag{2.1}$$

where μ_{R} and $\beta(\alpha_{\mathrm{S}}(\mu_{\mathrm{R}}))$ are respectively an energy scale called the renormalization scale and the beta function. The latter can be expanded and calculated perturbatively

in α_{S}, as is done on the right-hand side. The b_i coefficients depend on the number of active quark flavours, that is the number of quark flavours with a mass smaller than μ_{R}. They have been computed up to b_4 [62] and are positive for up to five active quark flavours. Therefore, the beta function is negative, which explains the asymptotic freedom.

In the Standard Model, physical processes are difficult to calculate exactly. A solution to this challenge is the use of perturbation techniques, in which the equation describing a physical process is essentially expanded as a Taylor series in terms of a small parameter. The coupling constant is taken as the small parameter, given its presence in every interaction and its value usually less than unity. The terms in the expansion of a perturbative series are proportional to an increasing number of powers of the coupling constant. Each power of the coupling constant can be interpreted as corresponding to one interaction between a gauge boson and other particles. Therefore, each term in a perturbative series expansion describing a physical process can be interpreted as describing an increasing number of interactions. The perturbative term with the smallest number of interactions, and thus the simplest to compute, is known as the leading-order (LO) term, while the next smallest is known as the next-to-leading-order (NLO) term. Although the mathematical description of a single interaction is known, the calculation of combinations of several different interactions, corresponding to higher-order terms, remains complicated. The mathematical description of physical processes are typically known only up to a few orders in the series.

Predictions of the Standard Model have been experimentally tested many times. Numerous measurements and their associated Standard Model predictions are, aside

from one exception, in agreement, showing the validity of the theory as a description of nature. The one exception is the non-zero mass of neutrinos. In the Standard Model, neutrinos are massless, while experiments have shown that they are massive [63, 64]. This shortcoming of the Standard Model is however not the only one. Although this theory describes three forces of nature, a fourth one is known: the gravitational force. Attempts have been made to reconcile quantum mechanics and general relativity, a necessary step to include the gravitational force in the Standard Model, but these have not yet been successful [65]. Still, neglecting the effects of the gravitational force does not compromise the predictions of most elementary physical processes, since the gravitational force is relatively much weaker than the electromagnetic, weak and strong forces. The impact of gravitational effects on measured processes is usually within experimental uncertainties. However, the lack of predictive power regarding the gravitational force is an additional shortcoming of the Standard Model. Despite providing robust predictions for processes related to the strong, electromagnetic and weak forces, the Standard Model is incomplete.

2.2 Event Generation

Theory predictions for the scattering of particles, such as the associated production of a photon and a bottom quark ($\gamma + b$) in the collision of two protons, are given in terms of a cross section, σ. As in classical mechanics, cross sections have a dimension of area. However, the notion of the geometric size of the colliding objects is replaced by the intrinsic probability of the dynamical process, which is given by the interactions described by the Standard Model.

In the case of proton–proton collisions, an important force at play is the strong force, since protons are composite particles made up of colored particles. Perturbative techniques can be used to describe physical processes involving the strong force at high energies or, equivalently, at small distances. The scattering of particles in this regime is referred to as a hard scattering. The perturbative approach breaks down if the coupling constant is not small compared to unity, which happens in QCD at distances larger than about one femtometer. These distances correspond to energies smaller than $\Lambda_{\mathrm{QCD}} \sim 200$ MeV. In this case, non-perturbative models have to be used to make predictions. These models are built on the phenomenology of QCD. As these models are not based on first principles, they are not unique. Predictions of the outcome of collisions between protons that can be compared to experimental results therefore relies on both the rigorous calculations of the process in the perturbative regime of QCD (pQCD) and on non-perturbative QCD models.

Computer programs have automated the LO, and even NLO, calculations in pQCD of any process in the Standard Model and also include the use of non-perturbative QCD models, thereby providing a complete description of the outcome of collisions between protons. Due to the complexity of the Standard Model, these programs make use of the probabilistic Monte Carlo integration technique to compute the kinematic integrals that appear in predictions of cross-section values. Given the probabilistic nature of the theory, these techniques are well suited to this task and are further used to determine probabilistically the four-momenta of the produced particles. This approach to determine the four-momenta of particles is referred to as event generation. The programs performing these calculations are thus called Monte

Carlo event generators. These programs provide a fully exclusive final state of a collision, that is the four-momenta of all particles are specified.

The generation of a particular outcome of a proton-proton collision can be broken down into different components: the parton distribution functions, which describe the proton in terms of elementary particles; the matrix elements, which describe the dynamics of the hard scattering of a given process; the parton shower, which describes additional particle emissions before and after the hard scattering; the hadronization, which describes via a non-perturbative QCD model how the colored elementary particles form composite particles; and the particle decays, which describe how unstable particles decay to stable particles that can be observed. In addition, the parts of the proton that did not participate in the hard scattering can still influence the event and must thus be taken into account in what is known as the underlying event. These different components of the event generation are all illustrated in Figure 2–1. They are the topic of the forthcoming sections.

2.2.1 Parton Distribution Functions

When a proton collides at high energy, it is its constituent particles that collide. Although a proton is made up of three valence quarks, two up quarks and one down quark, the gluons keeping them bound together can also collide. The gluons in the proton can in turn split into quark–antiquark pairs, $g \to q\bar{q}$, and one of these quarks can collide. Other particles than quarks and gluons, such as photons can also be created by the interactions between the valence quarks and can thus collide. However, since these interactions are not mediated by the strong force, their

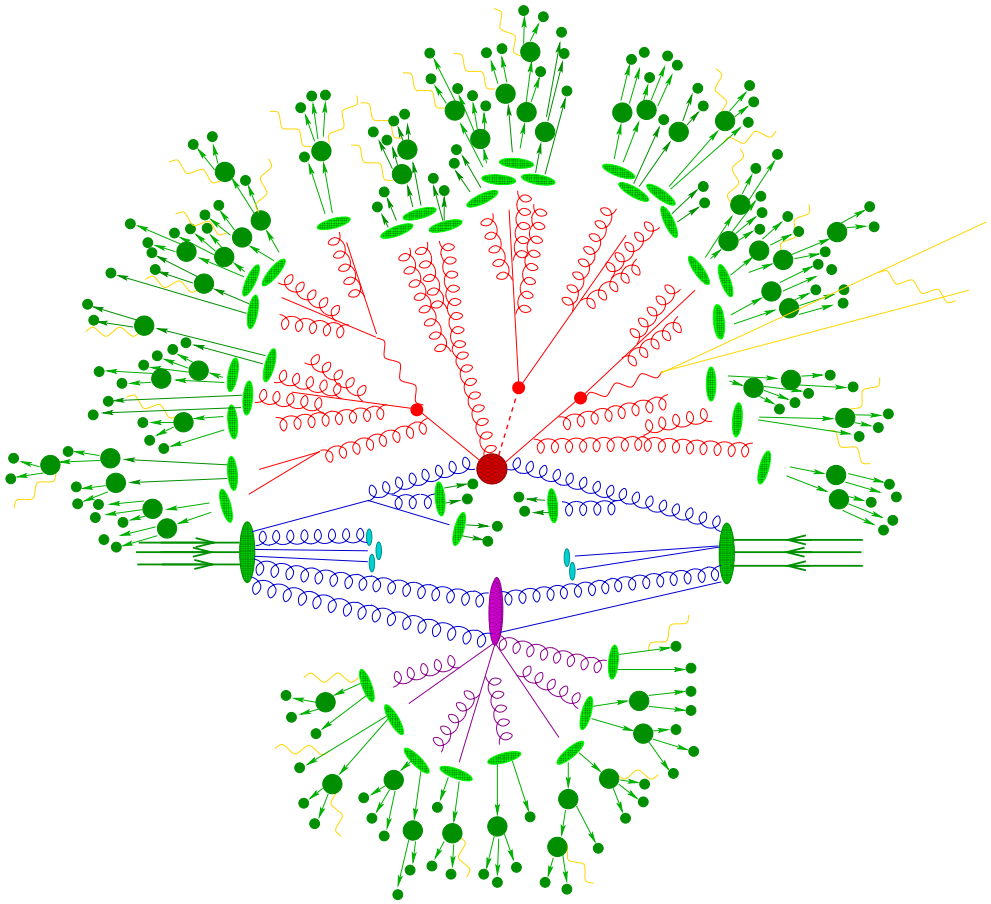

Figure 2–1 – Schematic illustration of a hard scattering process in a proton–proton collision [66]. The three green lines coming from both the left and right of the diagram represent the valence quarks of the protons and the green ellipses represent the parton distribution functions of the proton. Initial-state particles are represented in blue, along possible initial-state particle emissions. The large red circle represents the hard scattering, producing two top quarks and one Higgs boson. These particles decay, as indicated by the small red circles, and also emit other gluons and quarks, in red. The light green ellipses represent the hadronization of the colored particles. Hadrons decay until stable particles are formed, represented by the dark green circles. Particles interacting electromagnetically, in yellow, are produced throughout the process. An additional parton interaction, represented by the purple ellipse, occurs as part of the underlying event. The softer particles produced, in purple, evolve in a similar way as those in the hard interaction. The remaining particles of the incoming protons make up the beam remnants, in cyan, also part of the underlying event.

interaction probability is smaller and they are often neglected as constituents of the protons.

The constituents of the proton are called partons. The content of the proton in terms of partons is described by parton distribution functions (PDFs) as a function of x, the fraction of the proton momentum carried by the parton. As the interactions inside the proton involve low energies, where the strong coupling constant is large, the PDFs cannot be calculated from pQCD and therefore must be inferred from measurements. However, as quarks can emit gluons, $q \to qg$, and gluons themselves can split into additional gluons, $g \to gg$, there is an interplay between the PDFs of the quarks and gluon. At higher energies, there is a higher probability of such gluon and quark splittings compared to lower energies due to the available larger phase space. The PDFs thus have a dependence on the energy scale Q of the interaction, of which the square usually corresponds to the square of the four momentum of the exchanged particle in the interaction. The energy at which PDFs are evaluated is called the factorization scale, μ_{F}.

The dependence of the PDFs on μ_{F} can be described in pQCD via the Dokshitzer–Gribov–Lipatov–Altarelli–Parisi (DGLAP) evolution equations [67–69]:

$$\frac{d\, f_i(x, \mu_{\text{F}})}{d \ln \mu_{\text{F}}^2} = \int_x^1 \frac{dz}{z} \sum_j P_{i \leftarrow j}(z, \alpha_{\text{S}}(\mu_{\text{F}})) f_j \left(\frac{x}{z}, \mu_{\text{F}} \right), \tag{2.2}$$

shown here for the PDF of parton i, $f_i(x, \mu_{\text{F}})$. The sum is over all partons, such that the equations for the PDFs of the different partons are coupled. The splitting function $P_{i \leftarrow j}(z, \alpha_{\text{S}})$ represents the probability of a parton j to split into a parton i

with a momentum fraction z. The splitting functions can be calculated perturbatively in α_S, in a way similar to the right-hand side of Equation 2.1, and the expansion coefficients are known up to the next-to-next-to-leading order (NNLO) [70, 71].

The PDFs represent the number density of a given parton inside the proton in an interval between x and $x + dx$ at an energy μ_F. As such, they must respect the following equations:

$$\int_0^1 dx \, (f_i(x, \mu_F) - \bar{f}_i(x, \mu_F)) = n_i, \tag{2.3}$$

$$\sum_i \int_0^1 dx \, x f_i(x, \mu_F) = 1. \tag{2.4}$$

In Equation 2.3, i is one of the quark flavours and $n_u = 2$, $n_d = 1$, $n_s = n_c = n_b = n_t = 0$. In Equation 2.4, i runs over all quark flavours and also the gluon. These equations respectively have the meaning that the proton has the quantum properties of its valence quarks and that the sum of the momentum of every parton must be equal to the proton momentum.

Parton distribution functions have been shown to be independent of the ensuing hard parton scattering by the factorization theorem [72]. In proton–proton collisions, this theorem has only been proven for Drell–Yan processes [73], i.e. quark–antiquark annihilation leading to the pair production of oppositely charged leptons, and inclusive processes [74], i.e. processes for which the final state is not specified. It is however believed to hold for processes that are more exclusive, i.e. processes for which the four-momenta of some final-state particles are specified.

Since different types of partons can collide when two protons collide, the description of a process with a given final state is obtained by convoluting the PDFs with the cross section for a specific partonic initial state, summed over all possible partons:

$$\sigma_{pp\to X}(\mu_{\mathrm{R}}, \mu_{\mathrm{F}}) = \int_0^1 dx_1 \int_0^1 dx_2 \sum_{i,j} f_i(x_1, \mu_{\mathrm{F}}) f_j(x_2, \mu_{\mathrm{F}}) \hat{\sigma}_{ij\to X}(x_1, x_2, \mu_{\mathrm{R}}, \mu_{\mathrm{F}}, \alpha_{\mathrm{S}}(\mu_{\mathrm{R}})). \tag{2.5}$$

In this equation, the left hand-side is the cross section of the production of the final state X in proton–proton collisions and $\hat{\sigma}_{ij\to X}$ is the parton-level cross section for producing X when the partons i and j collide. The dependence of the cross section on μ_{R} and μ_{F} is not physical and only appears due to the use of perturbation theory at a finite order. The dependence on the renormalization scale is associated to divergences at higher energies than μ_{R}. Similarly, the dependence on the factorization scale is associated to divergences at lower energies than μ_{F}. Divergences at high and low energies are known respectively as ultraviolet and infrared divergences. Usually, for the purpose of calculating the outcome of collisions, the values of the scales are taken to be $\mu_{\mathrm{R}} = \mu_{\mathrm{F}} = Q$.

Several collaborations provide quantitative values for the PDFs, such as those provided in NNPDF3.0 [75] and CT14 [76]. The PDFs are extracted from data by parameterizing the PDFs at a low starting scale Q_0, evolving the PDFs to the higher values of μ_{F} that correspond to the measurements and using calculations of $\hat{\sigma}_{ij\to X}$ and Equation 2.5 to obtain predictions for $\sigma_{pp\to X}$. The predicted values of the cross sections are compared to all relevant measurements and the procedure is repeated by

varying the values of the PDF parameters until the predictions best agree with the measurements. This procedure is known as a global PDF fit.

A common PDF parameterization at the starting scale Q_0, used in both the NNPDF3.0 and CT14 PDF sets for example, is $xf_i(x, Q_0) = A_i x^{a_i}(1-x)^{b_i} P_i(x)$, where A_i, a_i and b_i are parameters to be fitted and $P_i(x)$ is a function that varies slowly and that can contain additional parameters. The dependence of the PDF on the exact choice of the parameterization at Q_0 is lost at higher energies through the DGLAP evolution. The value for Q_0 is thus usually taken to be about 1 GeV as this value is high enough to be in the perturbative region of QCD and low enough that the PDFs at high energy are not too sensitive on the parameterization. As this energy is smaller than the mass of either the c or the b quark, the PDFs for these two types of quarks are set to zero. When the evolution energy scale becomes greater than their masses, the c- and b-quark PDFs start to become non-zero due to the DGLAP evolution. Therefore, the contributions of the c and b quarks to the content of the proton originate solely from gluons splitting into those types of quarks. These contributions are referred to as the extrinsic quark contributions. The possibility of non-perturbative contributions, referred to as the intrinsic quark contributions, has recently been explored for the charm quark in NNPDF3.1 [77] and CT14 [78] by choosing $Q_0 \approx m_c$ and by parameterizing and fitting the charm quark PDF. A small contribution of intrinsic charm, around 1%, has been found to be compatible with the measurements used as input to this global PDF fit.

The available PDF sets mainly differ in the choice of $P_i(x)$ in the PDF parameterization and in the choice of which measurements to include in the PDF fit. For example,

CT14 uses polynomial functions while NNPDF3.0 uses the output of a neural network. In general, global PDF fits make use of measurements from a variety of experiments such as to extend the coverage in the x–Q phase space. Measurements from fixed-target experiments, such as BCDMS [79] and NuTeV [80], are used to provide input data at high x and low Q, i.e. $x > 0.01$ and $Q < 10$ GeV. Measurements from deep-inelastic scattering experiments at HERA [81], which measured the results of collisions between a proton and either an electron or a positron, provide constraints at low x and moderate Q, i.e. $x > 0.0001$ and $Q < 100$ GeV. Measurements from hadron colliders, such as the Tevatron and the LHC, are used to cover the region at low x and high Q, i.e. $x > 0.0001$ and $Q < 1$ TeV. Cross-section measurements at the LHC particularly sensitive to PDFs typically involve the production of photons, W bosons, Z bosons, top–antitop quark pairs and jets [82].[5]

Parton distribution functions are available at LO, NLO and NNLO in pQCD. The order of a PDF is determined by the order of the expansion of the splitting functions in Equation 2.2. Parton distribution functions at different orders can be qualitatively different. For example, some singularities in the splitting functions used in the DGLAP equations only start appearing at NLO, changing the behaviour of the b-quark PDF at small x compared to LO [83]. In order to achieve a consistent theoretical precision, the parton-level cross sections and the beta function of the strong coupling constant need to be calculated at the same relative order in pQCD as the PDFs in the global

[5]Jets are defined in Appendix B.

PDF fit.[6] Similarly, the order of the input PDFs is usually chosen to agree with the order of the pQCD calculations when predicting cross sections in proton–proton collisions.

Figure 2–2 shows the NNPDF3.0 PDF set at NLO for two different energy scales: 3.16 GeV and 100 GeV. At the lower energy scale, the b-quark PDF is zero since the energy scale is below the value of the b-quark mass. In contrast, at the higher energy scale, which is above the value of the b-quark mass, the PDF of the b quark is non-zero. For about $x > 0.2$, the up- and down-quark PDFs are the largest, while for about $x < 0.2$ the gluon PDF is the largest. As the energy scale increases, the valence quarks can radiate an increasing number of gluons, which can split into quarks. This distributes some of the proton momentum associated to the up and down quarks to the rest of the partons. Consequently, as the energy scale increases, the gluon and the quark PDFs increase at low x, while the up- and down-quark PDFs decrease at high x. Furthermore, since the b-quark has a relatively heavy mass, its PDF is relatively small. This is because its PDF has not received contributions from the gluon splittings at the energy scales that are below the value of its mass, while the PDFs of the lighter quarks did receive the contributions at those energy scales.

[6]It can be argued that this is not always necessary, for example due to the lack of precision of the input data [76] or to improve the fit quality [84].

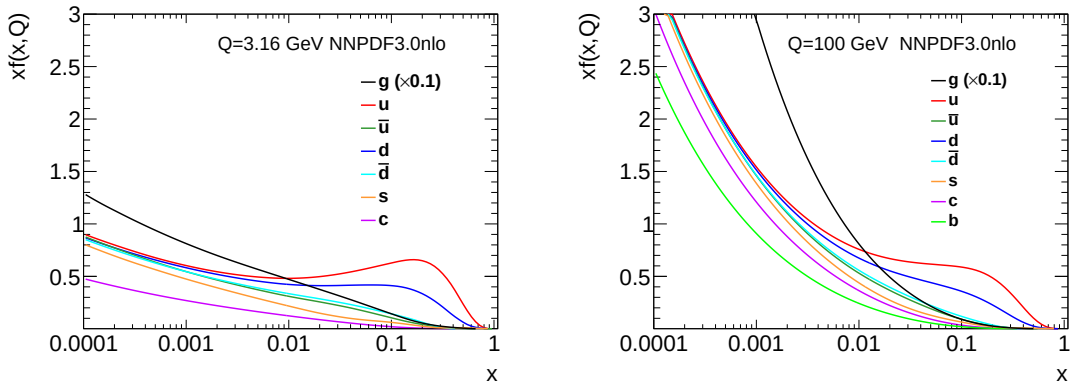

(a) (b)

Figure 2–2 – Parton distribution functions of the proton from NNPDF3.0 at NLO in pQCD as a function of the fraction of the proton momentum at two energy scales: (a) $Q = 3.16$ GeV and (b) $Q = 100$ GeV. For display purposes, the gluon PDF is divided by 10 and the PDFs are weighted by the momentum fraction. Due to this weight, the graphs represent the momentum density associated to a parton type instead of its number density. No uncertainties are shown.

2.2.2 Matrix Elements

The parton-level cross section in Equation 2.5, describing the large momentum exchange in proton–proton collisions, can be obtained by computing the matrix elements (MEs) relevant to a given process. The MEs are complex numbers that depend on the particle kinematics and dynamics, of which the latter correspond to a specific arrangement of individual particle interactions. The LO MEs in pQCD are those with the fewest interactions, while the NLO MEs contain additional interactions with a gluon. For inclusive processes, NLO MEs can have an additional particle in the final state. The MEs of the complete process can be categorized into subprocesses according to the particles in the initial and final states that are involved. To obtain the cross section associated to a subprocess, all the MEs associated to that subprocess

are first summed and then multiplied by their complex conjugate, such as to give a real number. Within a subprocess, interferences between matrix elements thus happen. The cross section of the complete process is given by the sum of the cross sections of the different subprocesses, as per the factorization theorem.

For the case of the inclusive production of a photon in association with a bottom quark in proton–proton collisions, where the bottom quark is not distinguished from its antiparticle, i.e. both $pp \to \gamma bX$ and $pp \to \gamma \bar{b} X$, with X representing possibly any other particles, the leading order in pQCD correspond to a cross section of order $O(\alpha\alpha_{\mathrm{S}})$. At this order, if the b-quark PDF is non-zero, only the Compton scattering subprocess, $gb \to \gamma b$, can occur. At NLO in pQCD, i.e. $O(\alpha\alpha_{\mathrm{S}}^2)$, the additional gluon interaction increases the number of subprocesses that can occur. The LO and NLO subprocesses are given in Table 2–3. The NLO MEs that have an additional final-state particle compared to the LO MEs are referred to as real contributions. The NLO MEs that contribute to the LO subprocess are referred to as virtual contributions.

Matrix elements can be represented schematically via Feynman diagrams. In those diagrams, the horizontal axis represents time, from left to right, while the vertical axis represents space. Fermions are denoted by lines pointing in the forward time direction, antifermions by lines pointing in the backward time direction, gluons by curly lines and photons by wavy lines. Figure 2–3 shows the only two MEs possible at LO for $\gamma + b$ production: Compton scattering in the s-channel and t-channel. The s-channel refers to a diagram in which the incoming particles directly interact to produce a particle that momentarily carries all the incoming four-momentum, while

Table 2–3 – Subprocesses for the inclusive production of a photon and a bottom quark, or antibottom quark, in pp collisions at leading and next-to-leading orders in pQCD. The leading-order subprocess can include virtual contributions. The quark q represents a specific quark flavour different from b. Additional subprocesses obtained from the ones listed by exchanging particles to their antiparticles are implied.

LO	NLO
$gb \to \gamma b$	$gg \to \gamma b\bar{b}$
	$gb \to \gamma gb$
	$qb \to \gamma qb$
	$\bar{q}b \to \gamma \bar{q}b$
	$q\bar{q} \to \gamma b\bar{b}$
	$b\bar{b} \to \gamma b\bar{b}$
	$bb \to \gamma bb$

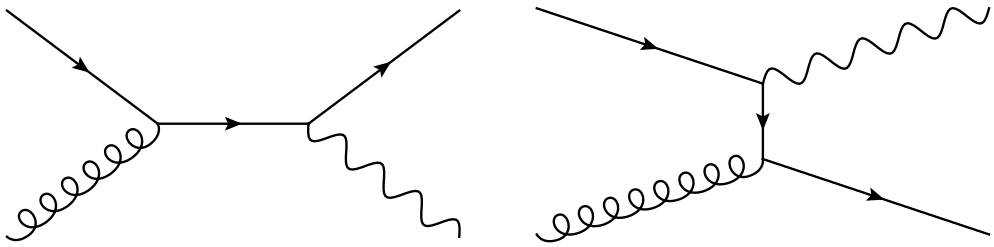

(a) (b)

Figure 2–3 – Compton scattering in the (a) s-channel and (b) t-channel. The fermion lines represent a b quark.

the t-channel refers to a diagram in which the incoming particles interact indirectly via an exchanged particle.

At NLO, there are about one hundred diagrams that exist for the $\gamma + b$ production process. Figure 2–4 shows examples of NLO diagrams. In all these diagrams, and those at LO, the fermion lines could be replaced by antifermion lines, to account for the production of $\gamma + \bar{b}$, which is implied.

Figures 2–4(a) and 2–4(b) show examples of virtual contributions at NLO to the LO Compton scattering. These diagrams have two additional gluon interactions compared to the LO diagrams. Thus, they are $O(\alpha\alpha_{\mathrm{S}}^3)$ contributions to the cross section, a higher order than NLO. However, since they have the same initial-state and final-state particles as the LO subprocess, these matrix elements interfere with the LO ones. The interference terms are $O(\alpha\alpha_{\mathrm{S}}^2)$ contributions and must be included for a complete NLO calculation in pQCD. Also, since they correspond to interference terms, the virtual contributions can be negative. The loops in the diagrams of the virtual contributions can carry an arbitrarily large amount of four-momentum and are the source of the ultraviolet divergences. If the bottom quark is considered to be massless, as the gluon is also massless, infrared divergences also occur since the four-momentum can reach zero. The ultraviolet divergences are regularized by redefining the value of the strong coupling constant such as to include those divergences. The value of the strong coupling constant can then be obtained through a measurement, circumventing the limitations of perturbative theory. This step, known as renormalization, however comes at the cost of introducing an unphysical scale, the renormalization scale μ_{R}, in

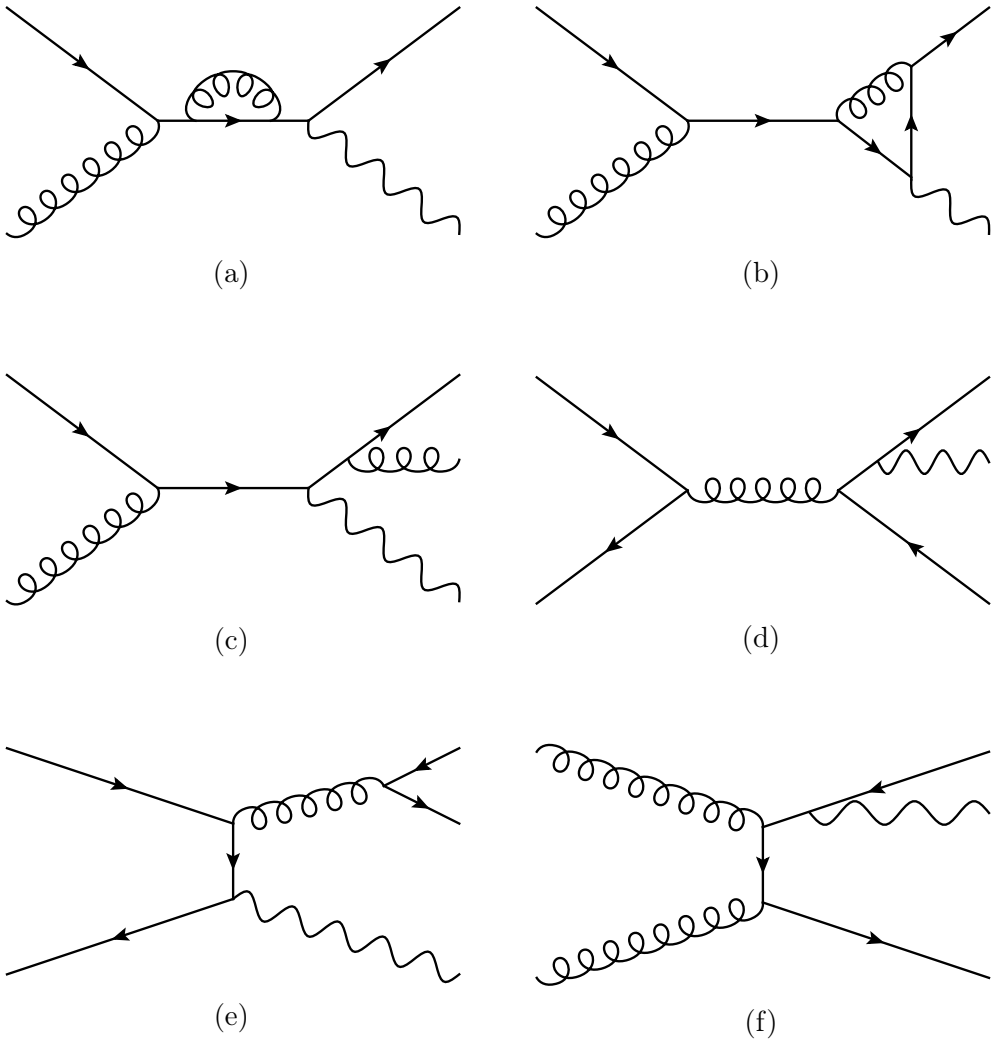

Figure 2–4 – Examples of next-to-leading-order contributions. Specifically, the diagrams show examples of (a) and (b) virtual contributions to Compton scattering, (c) final-state radiation of a gluon, (d) final-state radiation of a photon, (e) gluon-splitting creation of b quarks and (f) t-channel creation of b quarks. The fermion lines represent a b quark in (a), (b), (c) and (f). In (d) and (e), the incoming fermion lines represent a quark–antiquark pair of any flavour and the outgoing fermion lines represent a bottom–antibottom quark pair.

the calculation of the cross section. This step also creates the running of the strong coupling constant, as its value now depends on μ_{R}.

Examples of real contributions at NLO to the $\gamma+b$ cross section are given in Figures 2–4(c) and 2–4(d), showing different subprocesses. These diagrams represent the emission of a photon or a gluon from the final-state particles, known as final-state radiation. Radiation of a photon or a gluon from initial-state particles can also happen and is known as initial-state radiation. Since the photon and the gluon are massless, infrared divergences arise when quarks are considered as massless partons and the energy of the emitted particle goes to zero or when it is perfectly collinear to the particle that emitted it. In the case of the diagram with a radiated gluon, the infrared divergences cancel those appearing in the virtual contributions and the sum of the real and virtual contributions gives a finite contribution to the cross section. This is assured by the Kinoshita–Lee–Nauenberg theorem [85, 86] for inclusive observables in pQCD, which states that these divergences cancel between real and virtual contributions to give finite cross sections at each order of the perturbative expansion. Inclusive observables could be jets for example, for which both the real and virtual contributions give rise to the same final state. The Bloch–Nordsieck theorem [87] assures a similar cancellation of infrared divergences for radiated photons. The same idea of inclusiveness also applies for photons since photons with arbitrarily low energy cannot be distinguished from no photon emission at all, thus giving rise to the same final state between real and virtual contributions. However, in the case of the diagram describing the real contribution of a radiated photon, since the process without the radiated photon, $q\bar{q} \to b\bar{b}$ is of no relevance to the $\gamma + b$ production and therefore not considered, there

is no virtual contribution to cancel the divergences. The infrared divergences remain and must be regularized in a different way, as discussed in Section 2.3.1.

Figures 2–4(e) and 2–4(f) give other examples of real contributions at NLO. In particular, these show examples of the dynamic creation of bottom quarks, that is the b quark in the final state is not present in the initial state. In addition to the quark–antiquark annihilation leading to gluon splitting and to the gluon-fusion t-channel flavour excitation, the quark–antiquark annihilation s-channel flavour creation subprocess shown in Figure 2–4(d) also creates bottom quarks dynamically. The case of the gluon-splitting diagram is unique as a collinear divergence associated to the splitting of the gluon can occur. If the bottom quarks are considered to be massive, no divergence happens as the non-zero mass restricts the four-momentum from going to zero. However, if the calculation of the ME is done in the approximation that the b quark is massless, a collinear divergence does occur. This divergence is not compensated by virtual contributions since the subprocess without gluon splitting, $q\bar{q} \to \gamma g$, is not considered in the $\gamma + b$ production. Ways to regularize this divergence are discussed in Section 2.3.2.

As can be seen from the diagrams, the b quark produced in Compton scattering is directly related to the b quark in the initial state. In other words, it is sensitive to the b-quark PDF. On the other hand, the subprocesses related to the dynamical creation of b quarks are not directly sensitive to the b-quark PDF.

2.2.3 Parton Shower

The convolution of the PDFs with the parton-level cross sections as in Equation 2.5 provides a prediction for the $\gamma + b$ production cross section in proton–proton collisions. However, as the energy scale goes down from the high-momentum exchange of the collision, Q, to a perturbative energy scale close to the non-perturbative transition of quarks into hadrons, $Q_{\text{had}} \approx 1$ GeV, the value of the strong coupling constant increases. This increase is of particular importance in the collinear and low-energy regimes associated with parton splittings, where divergences appear. Each parton splitting in these regimes give rise to logarithms of the different energy scales, thus to terms proportional to $\alpha_{\text{S}}(Q)\ln(Q/Q_{\text{had}})$. These terms are $O(1)$ since $\alpha_{\text{S}}(Q) = (b_0 \ln(Q/Q_{\text{had}}))^{-1}$, as can be obtained by integrating Equation 2.1 when considering only the b_0 term, and since b_0 is itself $O(1)$. These additional collinear and low-energy contributions, compared to what is predicted by LO and NLO pQCD calculations, cannot be ignored to obtain an accurate calculation of the cross section. They can be accounted for by considering the change in the matrix elements, and thus in the cross section, that is caused by parton emissions in these regimes. As multiple such emissions can happen between the energy scales Q and Q_{had}, not only from the original parton but also from the partons that were themselves produced in previous splittings, this technique is referred to as a parton shower. Parton emissions are assumed to be independent of one another. Each emission gives rise to a factor of α_{S} multiplied by a logarithm. This type of correction thus takes into account, at all orders in α_{S}, a subset of the complete higher-order pQCD correction, referred to as the leading logarithm terms.

Considering the parton splitting $i \to jk$, with four-momentum conservation rule $P_i = P_j + P_k$, and defining $t = P_i^2$, the small angle approximation gives for massless partons:

$$t = 2E_jE_k(1 - \cos\theta) \approx E_jE_k\theta^2, \tag{2.6}$$

where θ is the separation angle between partons j and k. The relation between the cross section before the splitting, σ_N, and after, σ_{N+1}, is

$$\sigma_{N+1} = \sigma_N \int \frac{dt}{t} \frac{\alpha_S(t)}{2\pi} \int dz\, P'_{j\leftarrow i}(z). \tag{2.7}$$

The logarithmic nature of the divergence in the collinear regime, i.e. $\theta \to 0$, in particular can be seen from that equation. The splitting functions $P'_{j\leftarrow i}(z)$, where z is the energy fraction carried by the parton j relative to parton i, are related to the possible divergences at low energy. The splitting functions are similar to those in the DGLAP equations 2.2, but with the exception that some of them are singular at $z = 0$ and $z = 1$. These singularities are associated with the emission of a low-energy gluon and can occur even if the quark from which the gluon is emitted is not considered to be massless. In practice, the singularities do not come as an issue, since the energy only goes down to Q_{had} and not 0. The splitting functions are usually considered at LO, but parton showers at NLO have recently started to be considered [88].

The collinear divergences affect the emissions of either quarks or gluons, while the low-energy divergences only happens for gluon emissions. Considering the more generally applicable case of collinear divergences, the probability that a parton i does not split in the final state of the hard scattering when it evolves down from the energy

scale t_2 to t_1 is given by the QCD Sudakov form factor [89, 90]:

$$S_i(t_1, t_2) = \exp\left(- \int_{t_1}^{t_2} \frac{dt}{t} \frac{\alpha_S(t)}{2\pi} \int dz \sum_j P'_{j \leftarrow i}(z) \right), \tag{2.8}$$

where the limits of the integral with respect to z depend on t. Given a starting scale t_2, the scale t_1 at which a splitting occurs can be obtained via a Monte Carlo (MC) method by generating the uniform random number $S_i(t_1, t_2)$ between 0 and 1 and solving the previous equation for t_1 [91]. For each of those splittings, the value of the energy fraction z is generated in a similar way: generating a uniform random number between 0 and 1 and solving for z the normalized cumulative distribution of the splitting functions that corresponds to that random number. This procedure is iteratively repeated, from the starting scale Q until t_1 is smaller than the value of t corresponding to Q_{had}, at which point the shower stops.

Equation 2.8 describes the evolution of partons from the high energies of the scattering calculated by the matrix elements down to the non-perturbative energies. Such a description is natural for final-state partons and a similar description can also be used for initial-state partons, which can split before they enter the matrix element. To ensure the kinematics of the matrix element are correct, the parton evolution is still done from high to low energies, although this is backwards in time. In contrast to the final-state showers, the low-energy regime of the initial-state showers is described by the PDFs. The effect on the cross section of a parton splitting, $i \to j$, in the initial state is thus

$$\sigma_{N+1}(x) = \sigma_N(x) \int \frac{dt}{t} \frac{\alpha_S(t)}{2\pi} \int dz \, P'_{j \leftarrow i}(z) \frac{f_i\left(\frac{x}{z}, t\right)}{f_j(x, t)}. \tag{2.9}$$

The PDF multiplying the cross section in the factorization theorem changes upon the presence of the splitting. If no splitting occurred, the parton j participating in the matrix element with a fraction x of the proton momentum is described directly by the PDF. If the splitting occurred, the PDF must instead describe parton i with a momentum fraction increased to x/z such as to recover, after the splitting, the value x that enters into the calculation of the cross section. The ratio of the PDFs enforces the change of PDFs in the factorization theorem. The corresponding Sudakov form factor for initial-state showers [92] is

$$S_j(x, t_1, t_2) = \exp\left(- \int_{t_1}^{t_2} \frac{dt}{t} \frac{\alpha_S(t)}{2\pi} \int_x^1 \frac{dz}{z} \sum_i P'_{j\leftarrow i}(z) \frac{f_i\left(\frac{x}{z}, t\right)}{f_j(x,t)} \right). \tag{2.10}$$

The MC method can also be applied here with the modification that the energy fraction z is to be generated following the cumulative distribution of the product of the splitting function and the numerator of the PDF ratio.

PDFs are thus not only used in the calculation of the cross section via the factorization theorem but also in initial-state showers. Parton showers are not used in global PDF fits as the convolution between the PDFs and the parton-level cross sections cannot be easily implemented. Also, the previous discussion implies that PDFs can be interpreted as having already resummed the contributions of collinear parton splittings up to the scale μ_F at which they are evaluated. In other words, the PDFs regularize the initial-state infrared divergences. This is possible since the PDFs are obtained from measurements, which are not affected by divergences. However, this regularization comes at the cost of introducing a dependence on the unphysical scale μ_F in the calculation of the cross section.

The large masses of heavy quarks such as the bottom quark have various effects on the parton shower. For example, as $m_b > Q_{\text{had}}$, where m_b is the mass of the bottom quark, the natural cutoff for the evolution towards low energy becomes the mass of the bottom quark instead of Q_{had}, thus ending sooner. In comparison to massless quarks, the heavy quarks produced in the matrix element will carry a larger fraction of their momenta until the end of the shower. On the other hand, fewer heavy quarks will be produced in the shower. Other effects in the parton shower related to non-zero masses can be assessed either by correcting the parton shower based on the calculations of matrix elements [93] or by modifying the splitting functions [94].

In the discussion up to now, the parton showers have been evolved with the square of the parton four-momentum in the small angle approximation. Other approaches make use of different evolution variables, such as the separation angle, θ, or the transverse momentum relative to the splitting parton, and of different splitting functions making different approximations. The separation angle is a particularly interesting evolution variable as it provides a good description of the divergences specific to low-energy gluon emissions, which can happen even at large separation angles. A low-energy gluon emitted at a large angle could have originated from different partons in the scattering, it is not strictly associated to a single parton as is the case in collinear emissions. An interference between the emissions from the different partons occur. The evolution variable θ allows to properly consider this interference. An alternative to using θ as the evolution variable that still produces coherent low-energy emissions is considering parton splittings from dipoles instead of individual partons. This is essentially considering splittings as $2 \to 3$ processes instead of as $1 \to 2$. For example,

the Catani-Seymour dipole splitting functions [95] describe such kind of splittings. These allow to correlate the parton undergoing a splitting with the parton that does not and thus provide a different approximation of the splitting process.

2.2.4 Hadronization

After the parton shower, all quarks and gluons are free particles at the energy scale Q_{had}. As the energy decreases towards Λ_{QCD}, the strong coupling constant becomes large enough to spoil the convergence of the perturbative expansion in QCD. At these energies, the phenomenon of color confinement happens [96]. The colored particles stop evolving freely and instead become bound into baryons and mesons, i.e. particles with no color. This transition from partons to hadrons is known as hadronization. As hadronization is in the realm of non-perturbative QCD, it cannot be calculated from first principles. Instead, models based on the properties of QCD and the phenomenology of hadrons are developed. They take as input the colored particles produced in the parton showers, create quark pairs as necessary and output hadrons and their kinematics.

Several hadronization models have been used in the past [97, 98], but modern MC event generators mainly use two models, which can have their variants: the cluster model [99] and the string model [100]. These non-perturbative QCD models have differences that can be significant, or not, in the produced hadrons. It is this inherent uncertainty in the hadronization that makes the photon an interesting probe to study QCD. As the photon is not colored, it does not hadronize and is not affected by the modelling of the hadronization and of other QCD effects.

The descriptions of the cluster and string models follow.

Cluster model The cluster model, illustrated in Figure 2–5(a), is based on color preconfinement [101]. It is the phenomenological observation that colored particles produced in the parton shower are organized in groups in such a way that the groups, called clusters, are not colored. As gluons are not valence constituents of hadrons, they are manually split into quarks with the quarks going into different clusters, thus separating the clusters. The shape of the mass distribution of these clusters does not depend on the collision energy, only on Q_{had}. This universality of the mass distribution makes clusters a robust way to describe hadrons. The mass distribution of clusters peaks at around Q_{had} and steeply falls down at higher masses, with clusters having a typical mass of about $3Q_{\text{had}}$. Clusters with large masses are broken into two clusters along an axis defined by the original quarks until the masses of the clusters are below some cutoff value. The clusters then decay isotropically into two hadrons. Alternatively, low-mass clusters can transition readily to a single hadron. The specific hadrons produced follow a probability distribution based on the available kinematic phase-space, the quark flavours and the spins of the hadrons.

String model The string model, illustrated in Figure 2–5(b), is based on the description of color confinement as a linear potential between two quarks with a proportionality constant of about 1 GeV/fm [103]. As the distance between the quarks from the parton shower increases, the field lines of the strong force form a tube, i.e. a string, between the quarks. The energy increases linearly

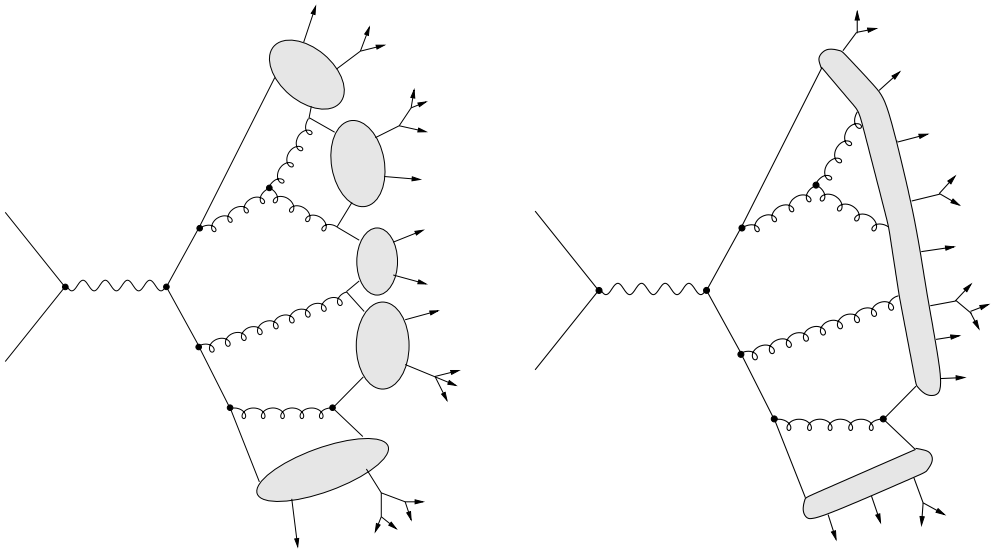

Figure 2–5 – Illustrations of hadronization models for a generic scattering process: (a) the cluster model and (b) the string model [102]. The grey regions in (a) represent the clusters and in (b) the strings.

until it becomes energetically favorable to create a pair of massless quarks. A gluon produced in the parton shower in-between quarks will stretch the string perpendicularly. The creation of quark–antiquark pairs will happen at an angle compared to the original direction of the string, thus creating transverse momentum in the otherwise one-dimensional string. This procedure is repeated until the energy of the string cannot create additional quark–antiquark pairs. The pairs then form mesons. To form baryons, the creation of a pair of diquarks, two loosely bound quarks, can happen instead of a quark–antiquark pair. The types of hadrons produced are based on the quark flavours and the spins of the hadrons. The kinematics of the hadrons follow a given functional form.

2.2.5 Particle Decays

The hadrons produced in the hadronization are not necessarily stable relative to the time scale relevant for their detection. Unstable hadrons can decay via the strong, electromagnetic and weak forces. These decays must be taken into account by the MC event generators to have a realistic description of proton–proton collisions. Most particles that can be detected are produced in this step.

Unstable hadrons are made to decay into all possible combinations of stable particles, which are $O(1000)$. The branching fractions of each decay channel follow the measured values [54]. However, some decay channels have not been measured or have inconsistencies. In particular, this is the case for hadrons containing heavy quarks. Approximations have to be made to ensure that the lifetimes of the hadrons are consistent with the sums of the branching fractions of each decay channel. These approximations can change the production of some hadrons. As changing the parameterization of the hadronization can also change the production of these hadrons, the modelling of these two aspects must be coherent to ensure the measured hadron abundances are correctly reproduced.

The four-momenta of the particles produced in the decays follow the available phase-space. They can however be corrected by matrix elements to take into account correlations among the produced particles. The decays of hadrons containing heavy quarks are especially complex due to their large masses and successive decays of their decay products. The complete decay chain can be considered at once to keep all correlations among the produced particles.

2.2.6 Underlying Event

The theoretical description of the large-momentum scattering in proton–proton collisions, from PDFs to stable particles that can be detected, is not sufficient to fully describe proton–proton collisions. While some constituents of the proton entered the hard scattering described by the matrix elements, the remaining constituents of the protons can also interact between the two protons. This additional activity in the event is called the underlying event of the hard collision.

To understand its contribution, the total scattering cross section of the collision of two protons can be divided into three categories, where the fractional contributions are derived from the predicted cross sections [104]:

- **Elastic scattering**, in which the two protons remain intact after the scattering. No exchange of color happens and no new particles are created. It amounts to approximately 25% of the total cross section.
- **Inelastic diffractive scattering**, in which one proton, or both, dissociate and do not remain intact after the scattering. No color exchange happens but new particles are created by the dissociation. This category corresponds to about 20% of the total cross section.
- **Inelastic non-diffractive scattering**, in which a color exchange between the protons and the creation of new particles happens. Parton–parton scatterings that can be described by pQCD fall in this category. It represents around 55% of the total cross section.

Therefore, the underlying event is defined in inelastic non-diffractive proton–proton scattering and is believed to come from additional parton interactions. Multiple parton interactions (MPI) can thus occur in addition to the hard parton interaction. From the PDFs of Figure 2–2, it can be expected that MPI is the result of the scattering of soft gluons, due to their prevalence. This low-momentum region borders the realm of non-perturbative QCD and as such models describing MPI have been conceived [105]. The average number of parton interactions in a given inelastic proton–proton collision can be larger than one [106]. The exact number can be expected to follow a Poisson distribution as the interactions should be approximately independent. This approximation is however subjected to the constraint that momentum must be conserved, reducing the number of events with a large number of parton interactions.

The underlying event contains on average more parton interactions than the average inelastic collision, a phenomenon known as the pedestal effect [107]. This can be understood as a selection bias. The underlying event is defined for events containing a large-momentum exchange. A given collision is more likely to have such a large-momentum exchange if it contains more than one parton interaction.

The new particles that are created in the underlying event can shower and hadronize. The inclusion of the effects of the underlying event is thus an essential part of the MC event generators. Beyond the production of new particles, the effects can also include the MPI affecting the particles produced in the hard parton interaction through parton rescattering and interleaved showers [108]. Furthermore, the partons in the protons that did not scatter, the beam remnants, are still correlated to the rest of

the event. Although they do not produce measurable particles, they can still affect the event. Models of these effects of the underlying event have been devised [109].

2.2.7 Generator Tuning

The non-perturbative models of the previous sections make use of a multitude of parameters that are a priori unknown and which can be adjusted, or tuned, to provide a better description of the data. Some observables are more sensitive to certain parameters of the event generation than others. Measurements of these observables can be used to constrain specific subsets of parameters. Also, as models mainly describe non-perturbative QCD, that is phenomena at low energy, parameter tunes are determined separately for the underlying event and for the average inelastic collision, since they correspond to different amounts of low-momentum scattering activity.

2.3 Signal Cross-section Predictions

Predictions of the inclusive $\gamma + b$ production cross section can be obtained at LO in pQCD with the PYTHIA [110] and SHERPA [66] event generators. Both of these generators include the various steps discussed in the previous section and thus generate stable particles for a given physical process. The two generators differ in their predictions due to the use of different modelling options at the various steps of the event generation. Their main differences are now discussed.

In PYTHIA, matrix elements are calculated for $2 \to 2$ processes, i.e. processes with two initial-state particles and two final-state particles. The parton shower is evolved as a function of the transverse momentum of the partons. Usual $1 \to 2$ parton

splitting is used instead of dipoles, but the parton kinematics follow that of dipoles. The combination of transverse momentum and dipole kinematics ensures coherent low-energy gluon emissions [111]. Furthermore, the initial-state parton shower is interleaved with multiple parton interactions. Partons that have already participated in the hard scattering can also rescatter. The string model is used for hadronization.

In SHERPA, matrix elements can be calculated not only for $2 \to 2$ processes but also for real contributions up to $2 \to N$, where N is arbitrarily large and only limited by computing power. Virtual contributions are not included such that the calculations are still formally at LO in pQCD, although NLO and higher-order effects are partly included, i.e. up to $O(\alpha\alpha_{\mathrm{S}}^{N-1})$ for $\gamma + b$. The transverse momentum is used to evolve the parton shower to low energies and the splitting procedure is based on Catani-Seymour dipoles. The hadronization model is based on a modification of the cluster model that improves some aspects of the cluster formation and decay [112]. The use of matrix elements of different multiplicities with a parton shower is referred to as a calculation in the ME+PS scheme. In this scheme, parton showers following a $2 \to 2$ process can generate jets with similar kinematics as the real contributions of the higher multiplicity processes, thus duplicating the contributions of these jets. The double counting of these contributions can be avoided by enforcing that a jet must come from a real contribution to the matrix element if it is above a given combined energy scale and angular separation, known as the merging scale Q_{cut}, and from the parton shower if not. This procedure of merging real contributions of different jet multiplicities with the parton shower is implemented in SHERPA with a theoretically

motivated jet algorithm [113].[7] This approach makes use of the better modelling properties at collinear angles and low energies of the parton shower and that of the high-multiplicity matrix element in the rest of the phase-space.

In addition to the LO pQCD predictions of Pythia and Sherpa, predictions for NLO matrix elements are obtained with MadGraph5_aMC@NLO [115]. This software can calculate LO and NLO matrix elements for a large variety of processes, but it does not implement non-perturbative QCD models. However, MC event generators can be interfaced to those calculations to obtain a complete exclusive description of the event in terms of stable particles, i.e. matching the matrix elements to the parton shower. In that case, the NLO+PS calculation scheme is used, where PS refers to the parton shower and to the other aspects of the event generation. In this scheme, similarly to the ME+PS scheme, a double counting of the real contributions and of the parton emissions from the parton shower must be avoided. However, the presence of virtual contributions complicates things as cancellations of infrared divergences must be maintained between the virtual and the real contributions. Two prescriptions can be used: MC@NLO [116], which uses the parton shower as a counter term in the calculation of the cross section to cancel the double counting, and POWHEG [117], which scales the cross section from LO to NLO and modifies the Sudakov factor of the parton shower to avoid the double counting. Differences in predictions between the two prescriptions can occur in regions of the kinematic phase space that are sensitive

[7] The second major version of Sherpa, Sherpa 2, also allows this procedure to be done at NLO in pQCD, in the MEPS@NLO scheme [114].

to higher order effects. MadGraph5_aMC@NLO uses the MC@NLO prescription to provide NLO+PS predictions. MadGraph5_aMC@NLO also allows a merging of matrix elements of different jet multiplicities at NLO, similarly to Sherpa, using the FxFx scheme [118]. However, this approach cannot be used for processes that contain a bottom quark or a jet in their final state at LO, such as $\gamma + b$ production.

The Jetphox [119] and Diphox [120] computer programs are also often used to provide dedicated NLO calculations of cross sections for the production of prompt photons, as is done for example in Refs. [36, 121]. Although they cannot currently provide predictions for the production of $\gamma + b$, they could be modified to allow for such predictions [122].

The difficulties in the modelling of prompt photons and b quarks that arise in the predictions of the $\gamma + b$ cross section are discussed in the following sections. A discussion of the exact theoretical predictions that are compared to the measurement presented in this thesis ends this chapter.

2.3.1 Prompt Photon Divergences

As mentioned in Section 2.2.2, the production of photons is affected by infrared divergences. The divergence at low energy is avoided by simply requiring the photon to be above some finite value of transverse momentum. Although the divergence is avoided, this cut reduces the total phase space to a fiducial phase space. This fiducial cut is motivated by the impossibility of measuring arbitrarily small photon energies. The collinear divergence can be regulated in two ways: by using parton-to-photon fragmentation functions or by requiring the photon to be isolated from other particles.

The fragmentation functions (FFs) are essentially the opposite of the PDFs. Whereas PDFs describe the probability that a given parton inside a hadron initiates a high-energy collision, FFs describe the probability of producing a hadron, or a photon, from a given final-state parton. They depend on the momentum fraction of the parton and on a new unphysical energy scale at which the fragmentation occurs, the fragmentation scale μ_{f}. The scale evolution can be described in terms of analogous equations to the DGLAP equations and with the additional splitting $q \to q\gamma$ for photon FFs. As for the PDFs, the FFs are convoluted with the parton-level cross section, giving predictions in terms of specific final-state hadrons, or photons, instead of partons. While the PDFs absorb collinear divergences in the initial state, the FFs absorb collinear divergences in the final state. Due to being sensitive to this non-perturbative regime, their exact values are extracted from measurements, similarly to the PDFs.

The Bourhis–Fontannaz–Guillet gluon-to-photon and quark-to-photon FFs [123] are the most modern photon FFs. Figure 2–6 shows their representation in Feynman diagrams. Without the fragmentation part, these diagrams are formally $O(\alpha_{\mathrm{S}}^2)$. However, the fragmentation functions are $O(\alpha/\alpha_{\mathrm{S}})$ [123]. They bring the diagrams to the same order as the LO diagrams, $O(\alpha\alpha_{\mathrm{S}})$. The production cross section of photons from fragmentation is thus commensurate to that of photons from the hard scatter, referred to as direct photons. These two contributions make up the production of prompt photons. The production of fragmentation photons is taken into account in the calculations of JETPHOX and DIPHOX up to NLO, thus requiring calculations of diagrams with only quarks and gluons in the final state, formally at order α_{S}^3.

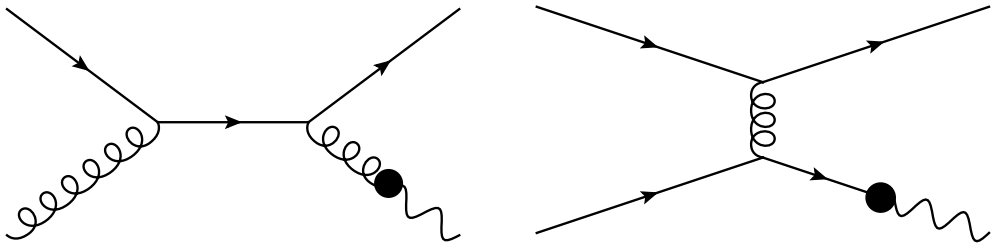

(a) (b)

Figure 2–6 – Production of photons through fragmentation from a (a) gluon and (b) quark. The filled circles represent the gluon-to-photon and quark-to-photon fragmentation respectively. In (a), the fermion lines represent a b quark, while in (b) the fermion lines at the top represent a b quark and the fermion lines at the bottom represent a quark of any flavour.

This fragmentation contribution is shown to be important at small values of photon transverse energy [124]. Additionally, some observables can distinguish between the contributions of fragmentation and direct photons due to the unique t-channel gluon exchange diagram of Figure 2–6(b), which occurs at $O(\alpha\alpha_{\mathrm{S}})$ for the former contribution but not for the latter [40].

Sherpa and MadGraph5_aMC@NLO do not include the contribution of fragmentation photons in the cross sections of prompt photons. Instead, as the collinear divergences are associated to the production of photons close, in the angular phase-space, to other partons, an isolation requirement is imposed. The isolation requirement restricts the energy sum of the particles that are angularly close to the photon to be below some given value. This cuts away a significant fraction of the contribution of fragmentation photons, while keeping the contribution of direct photons mostly intact. Thus, this approach avoids altogether the calculation of the fragmentation contribution, at the cost of adding the fiducial isolation cut. However, a similar

fiducial isolation cut is required in any case, even with the fragmentation function approach, for experimental reasons that will be discussed in Section 4.2.3. Thus, for a well-chosen isolation cut, this approach has effectively no more drawbacks than the fragmentation function approach.

The photon isolation requirement can be implemented in different ways. An appropriate isolation definition is given by the Frixione isolation criterion [125]:

$$\sum_i E_{\mathrm{T},i}\,\theta(\delta - \Delta R_{i\gamma}) \leq \epsilon_\gamma E_{\mathrm{T},\gamma} \left(\frac{1-\cos\delta}{1-\cos\delta_0}\right)^n, \quad \forall\delta \leq \delta_0, \tag{2.11}$$

where the sum runs over all partons, $\theta(x)$ is the Heaviside step function, $\Delta R_{i\gamma}$ is the angular distance between parton i and the photon, i.e. $\Delta R_{i\gamma} = \sqrt{(y_i - y_\gamma)^2 + (\phi_i - \phi_\gamma)^2}$ and δ_0, ϵ_γ and n are parameters. In words, this isolation requires that, for all angular distances below a given value δ_0, the sum of transverse energies of all particles within that angular distance is below a certain value, which smoothly decreases as the angular distance decreases. Such a requirement removes the possibility of having partons collinear to photons, as desired, while not restricting the production of low-energy gluons. This last point is important as the low-energy gluons must be produced inclusively, since they are associated to the parton-splitting infrared divergences. The Frixione isolation criterion is therefore infrared safe, i.e. infrared divergences from real and virtual contributions properly cancel. This type of isolation is used in MadGraph5_aMC@NLO. Sherpa uses instead a simpler isolation cut that only requires that all partons are not within a cone around the photon: $\Delta R_{i\gamma} > \delta_0$ for every parton i and some value δ_0. This is not infrared safe, since it rejects events

in which low-energy gluons lie in that cone, but it does not cause problems in this specific case as SHERPA does not compute virtual contributions.

PYTHIA is a particular case as it only calculates $2 \to 2$ processes such that no photons are radiated from quarks in the matrix element. No collinear divergences are encountered. However, to approximate the effects of these radiative photons, photons are emitted in the parton shower through the splitting $q \to q\gamma$. The production of these bremsstrahlung photons requires the additional calculation of all $2 \to 2$ LO matrix elements with two partons in the final state, which are $O(\alpha_S^2)$.

2.3.2 Bottom Quark Divergences

After jet formation and cancellation of the infrared divergences between the real and virtual contributions, two infrared divergences remain related to the parton splittings. One of them is a divergence related to jets at low energy. Low-energy gluons emitted at large angles could be considered as separate jets, implying that the infrared divergences would not cancel between real and virtual contributions since they would have different final states. This divergence can be regularized by imposing a minimum value on the transverse momentum of the jet, similarly to the photon. The second remaining divergence, which is more problematic, is the collinear divergence from the gluon-splitting process of Figure 2–4(e), as already discussed in Section 2.2.2.

In general, infrared divergences related to parton splittings are due to terms proportional to $\ln(Q/m_q)$, where m_q is the mass of the quark. For the up, down and strange quarks, the values of their masses are smaller than the energy scale below

which pQCD calculations are possible, i.e. $m_q \ll \Lambda_{\mathrm{QCD}}$. As such, their masses cannot be included in pQCD calculations and the quarks are taken to be massless, which creates the divergences. On the other hand, the value of the mass of the bottom quark is much higher than the perturbative scale of QCD, that is $m_b \gg \Lambda_{\mathrm{QCD}}$. This implies that the logarithmic terms can be included explicitly in pQCD calculations, in contrast to the case of the lighter quarks. The ways the collinear divergence associated to the gluon splitting into bottom quarks can be regularized depend on whether terms proportional to $\ln(Q/m_b)$ are included explicitly in the pQCD calculations or not.

If the logarithmic terms are included explicitly in the matrix element, the calculation is said to be in the four-flavour (4F) scheme and the bottom quark is considered to be massive, while if they are not included explicitly, the b quark is treated as any other parton and the calculation is said to be in the five-flavour (5F) scheme. Other calculation schemes have also been devised [83]. The numbers in the names of these two schemes are a reference to the number of quarks considered to be massless. In all cases, the parton shower is performed with massive quarks as otherwise b quarks would be overproduced and would also end up being too soft due to a larger number of gluon emissions [126]. Predictions in these two schemes can differ. For example, the evolution in energy of the strong coupling constant is different, as it depends on the number of massless quarks. Also, the splitting functions can be different if the mass effects are taken into account, leading to different showers and jet kinematics. It is important however to note that any prediction differences between two schemes are due to the finite expansion of pQCD. An all-order calculation in a given scheme would

agree with an all-order calculation in the other. In other words, the two schemes simply represent different ways of rearranging terms in the perturbative expansion.

In the 4F scheme, the terms proportional to $\ln(Q/m_b)$ are kept in the calculation of the matrix element as well as other terms dependent on m_b, which are power suppressed. As long as $Q \approx m_b$, the logarithm will be small and will not spoil the convergence of the pQCD series. This suggests that the 4F scheme is better suited at energies closer to the mass of the bottom quark. As the logarithm is considered to be small, no infrared divergences related to the bottom quarks occur. The large value of their mass serves as an infrared cutoff. In particular, no jets need to be formed from the b quarks and no minimum transverse momentum needs to be required. Having no infrared divergences in the final state implies that no special consideration need to be made concerning the produced b quarks from the gluon splitting in particular. Similarly, having no divergences in the initial state implies that a PDF is not needed to describe the effects of b quarks prior to the hard scattering, as the splittings are included explicitly in the matrix element. Consequently, no b quarks can be in the initial state of the matrix elements. All b quarks are created in pairs from gluon splittings in the matrix element.[8] This means that the $2 \to 2$ Compton scattering diagrams do not represent a valid process in the 4F scheme. The lowest order at which a photon and a b quark can be produced in proton–proton collisions is $O(\alpha\alpha_{\mathrm{S}}^2)$. The production of $\gamma + b$ is really the production of $\gamma + b + \bar{b}$ in that scheme. The

[8]Bottom quarks can also be produced individually via an interaction with a W boson.

Table 2–4 – Subprocesses for the inclusive $\gamma + b$ production in pp collisions in the four-flavour scheme at leading and next-to-leading orders in pQCD. The leading-order subprocesses can include virtual contributions. The quark q represents a specific quark flavour different from b. Additional subprocesses obtained from the ones listed by exchanging particles to their antiparticles are implied.

LO	NLO
$gg \to \gamma b\bar{b}$	$gg \to \gamma b\bar{b}g$
$q\bar{q} \to \gamma b\bar{b}$	$q\bar{q} \to \gamma b\bar{b}g$
	$gq \to \gamma b\bar{b}q$

LO diagrams become those of Figures 2–4(d), 2–4(e) and 2–4(f), among others. The NLO diagrams have additional gluon interactions, with the real contributions representing $2 \to 4$ processes at $O(\alpha\alpha_S^3)$. A list of the LO and NLO subprocesses for $\gamma + b$ production in the 4F scheme is given in Table 2–4. Although the number of subprocesses is smaller than when considering a non-zero b-quark PDF, the matrix elements they represent are more complex. About a thousand diagrams need to be calculated at NLO. Jet formation still needs to be done with the partons, excluding the bottom quarks, such as to have infrared safe observables. Then, the bottom quarks can be showered and hadronized similarly to the other partons if passed to an MC event generator.

In the 5F scheme, the terms proportional to $\ln(Q/m_b)$ are considered to be divergent and cannot be included in the matrix element. Initial- and final-state infrared divergences must be regularized. As the logarithms do not appear explicitly in the calculations, this scheme is better suited for interaction energies that are large

compared to the mass of the b quark. The regularization of the initial-state divergences is done by using a b-quark PDF, since PDFs resum the large logarithms associated to collinear splittings at all orders in pQCD. Matrix elements with initial-state b quarks are thus allowed and the diagrams discussed in Section 2.2.2 are relevant to the 5F scheme. Since the matrix elements are different between the 4F and 5F schemes, along with the aforementioned differences in the evolution of α_{S} and the splitting functions, a given scheme might be better suited than the other to predict certain observables or certain processes.

The final-state splitting of the gluon into collinear b quarks creates a divergence in the 5F scheme, in contrast to the 4F scheme. The divergence can be regularized in three ways: by introducing an infrared cutoff, by using parton-to-hadron FFs or by forming flavour-k_t b-jets. These approaches aim to solve the issue of the divergence at the parton level. They are now described.

Cutoff approach The cutoff approach simply regularizes directly the collinear divergence by constraining the gluon to have an invariant mass of at least twice the mass of the bottom quark. In other words, the b quark is considered to be massive for that particular subprocess. Therefore, the logarithm is cut off by the mass of the b quark, as in the 4F scheme and does not diverge. With the gluon-splitting divergence regularized, jet formation can follow for the other partons. As this approach needs the mass of the b quark to be different for different subprocesses, it requires a dedicated parton-level calculation, which is not available for $\gamma + b$ production.

FF approach The FF approach uses parton-to-hadron FFs to regularize collinear divergences. It follows the same idea as for the photon FFs, discussed in the previous section: the FFs resum final-state collinear divergences at all perturbative orders. The transition from partons in the matrix element to hadrons containing at least one bottom or antibottom quark, referred to as a b hadron, is then performed with FFs obtained from measurements [127]. Similarly to the photon case, the use of FFs requires the introduction of the new unphysical fragmentation scale μ_{f}. Not all relevant FFs have been measured however, such that predictions using this approach have an inherent uncertainty related to the choice of modelling of the missing information. A similar approach is the use of FFs transitioning partons to a b quark, instead of b hadrons. This approach has been pursued for the charm quark in Ref. [128]. No current calculations of $\gamma + b$ production make use of FFs, but DIPHOX could be modified to follow this approach.

Flavour-k_t approach The flavour-k_t approach relies on forming jets that can distinguish b quarks against the other partons. The flavour-k_t algorithm [129] is such an appropriate algorithm since it is infrared safe in forming b-jets, i.e. jets initiated by bottom or antibottom quarks.[9] By requiring that the partonic final state contains such a b-jet instead of a b quark, the gluon-splitting diagram is not considered to be part of the relevant process since its jet is initiated

[9]The flavour-k_t algorithm is defined in Appendix B.

by a gluon and not by a b quark. Thus, this procedure avoids its divergence altogether. JETPHOX could be modified to make use of this approach. However, b-jets defined that way are experimentally hard to measure and this approach is not followed further to make predictions.

Considering that the three previous parton-level approaches are not adequate in their current state to provide predictions, the alternative of particle-level predictions is considered. At this level, the flavour-k_t approach can be modified by using an experimentally accessible definition of b-jets. In this approach, b-jets are defined as jets containing at least one b hadron. This jet definition is not infrared safe, but the infrared effects have already been taken into account, as the jet formation is done at the particle level, such that this is not an issue. Since jets are identified as b-jets only at the particle level, all matrix elements producing a photon and a parton must be considered. These are necessary as a gluon splitting into b quarks, thus creating a b-jet, can originate from any parton. In this case, several hundred diagrams need to be calculated. By considering all such matrix elements, the infrared divergences are then cancelled between the real and virtual contributions, after jet formation. This is the case in particular for the collinear divergence associated to the gluon splitting into b quarks, since the corresponding virtual contribution, $q\bar{q} \to \gamma g$, becomes relevant to $\gamma + b$ production. This is the approach used to produce predictions with PYTHIA, SHERPA and MADGRAPH5_aMC@NLO.

An inconvenience of the predictions in the previous approach in comparison to those in the parton-level approaches is that they cannot be used to perform global PDF fits, since they need to generate fully-exclusive events. Furthermore, the definition of

b-jets at the particle level implies that the cross section of the production of b quarks at high energy is dominated by b-jets in which the b quark is produced through gluon splitting. This reduces the sensitivity of the $\gamma + b$ process to the b quark PDF in that phase-space region. On the other hand, an advantage of that approach compared to the flavour-k_t one is that measurements that can be compared to theory predictions are easier to perform. Also, an advantage compared to the FF approach is that jets are more inclusive observables to study b quarks than hadrons. Thus, the predictions are less sensitive to the details of the non-perturbative effects. For example, they are not affected by the lack of knowledge of every FF [130].

The particle-level jet approach can supplement the cutoff and FF approaches in the 5F scheme and it can also be implemented in the 4F scheme. For the FF approach, this can be done such as to allow comparisons of the b-hadron predictions to measurements of b-jets. In that case, the fragmentation scale is chosen to be $\mu_{\mathrm{f}} = Rp_{\mathrm{T}}$, where R and p_{T} are respectively the radius and transverse momentum of the jet [131]. In the cutoff approach and in the 4F scheme, particle-level b-jets can be formed to be compared to b-jet measurements. However, matrix elements with a photon and a parton in the final-state are not taken into account in these cases, thus missing contributions to the production of b-jets. An underestimation of the cross section of the production of a photon in association with a b-jet is expected. The underlying reason is that b-jets defined this way are not infrared safe. This approach is used to produce predictions with MadGraph5_aMC@NLO in the 4F scheme, such that the predictions in the 4F and 5F schemes are with respect to the same observables.

Table 2–5 – Summary of the theoretical predictions. The details are given in terms of the perturbative order in QCD of the matrix element, the parton distribution function, the treatment of the b quark mass in the matrix element and in the parton shower and the treatment of the collinear divergences associated to the photon and to the b quark in the matrix element. For the treatment of the b quark mass, a checkmark and a cross indicate respectively that the b quark is considered to be either massive or massless. The treatment of the photon divergence relates to the type of photon isolation used.

			Massive b		Collinear divergence	
Generator	ME pQCD order	PDF	ME	PS	γ	b
Pythia 8.160	LO ($2 \to 2$)	CTEQ6L1	×	✓	–	–
Sherpa 1.4.5	LO ($2 \to 2, 3, 4, 5$)	CT10	✓	✓	Cone	Jet+PS
MadGraph5_aMC@NLO 2.3.3	NLO ($2 \to 2, 3$)	NNPDF3.0nlo 5F	×	✓	Frixione	Jet+PS
MadGraph5_aMC@NLO 2.3.3	NLO ($2 \to 3, 4$)	NNPDF3.0nlo 4F	✓	✓	Frixione	–

2.3.3 Measurement Predictions

Details of the specific theoretical predictions that are compared to the measurement of the $\gamma + b$ production cross section in proton–proton collisions, in which the b quark is observed as a particle-level b-jet, are now given. The information is also summarized in Table 2–5.

Pythia 8.160 is used to generate events based on $2 \to 2$ LO matrix elements with a photon and a parton in the final state. The parton is recognized directly as a jet since no other partons are present. The low-energy divergences of the photon and the jet are regularized by the single requirement $p_{\mathrm{T}} > 15$ GeV, where the transverse momentum refers to both the jet and the photon by virtue of the conservation of the transverse momentum. As only $2 \to 2$ matrix elements are considered, no collinear divergences regarding either the photon or the bottom quark occur. All partons are

generated and bottom quarks are only selected via b-jets at the particle level. The generator is tuned with the AU2 set of parameters [132], optimized for the presence of an underlying event, i.e. for events with a hard scattering. The five-flavour CTEQ6L1 LO PDF set [133] is used in conjunction with massless quarks in the matrix elements, such that the calculations are in the 5F scheme. The quarks are taken to be massive in the shower.

SHERPA 1.4.5 is used to generate events in the ME+PS scheme based on $2 \to 2$, $2 \to 3$, $2 \to 4$ and $2 \to 5$ LO matrix elements with one photon and one parton in the final state, supplemented by up to three partons. The photon is required to satisfy $p_{\mathrm{T}} > 15$ GeV and a separation of $\Delta R > 0.3$ from every other parton. The soft jet divergence is regularized by the merging procedure of matrix elements of different jet multiplicities with the parton shower, for which a merging scale around $Q_{\mathrm{cut}} = 30$ GeV is used and is allowed to vary based on $Q = E_{\mathrm{T}}^{\gamma}$ [134]. All partons are generated and b-jets are only selected at the particle level. Due to a software limitation, the mass of the quarks must be treated in the same way in both the matrix elements and the parton shower.[10] The bottom quark is thus taken to be massive in both the matrix elements and the parton shower and it is not considered as a parton. Still, the five-flavour CT10 NLO PDF set [135] is used. The calculations are thus in a crude massive 5F scheme [136]. The default tuning of parameters based on CT10 is used.

[10] This limitation has been lifted in SHERPA 2.

MadGraph5_aMC@NLO 2.3.3 is used to compute NLO matrix elements in the NLO+PS scheme using the MC@NLO prescription. The calculations are done separately in the 4F and 5F schemes. In the 4F scheme, the process of interest is $pp \to \gamma b\bar{b}$ and thus the calculated matrix elements are $2 \to 3$ for the LO and virtual contributions and $2 \to 4$ for the real contributions. The b quark is taken to be massive and thus does not need any regularization. The four-flavour NNPDF3.0 NLO PDF set is used. In the 5F scheme, the $2 \to 2$ LO and virtual contributions of $pp \to \gamma b$ are calculated in addition to the $2 \to 3$ real contributions. The b quark is treated as a massless parton and the five-flavour NNPDF3.0 NLO PDF set is used. In both schemes, jets using the k_t algorithm with parameter $R = 1$ are built from the massless partons and are required to satisfy $p_{\mathrm{T}} > 10$ GeV. Photons must satisfy $p_{\mathrm{T}} > 20$ GeV and also the Frixione isolation requirement given by Equation 2.11 with $\delta_0 = 0.4$, $\epsilon_\gamma = 1$ and $n = 1$. In the matrix elements, the strong coupling constant value is set to $\alpha_{\mathrm{S}}(M_Z) = 0.118$ at the energy scale corresponding to the mass of the Z boson and its running is considered at two loops, i.e. up to coefficient b_1 in Equation 2.1, that is at NLO. The running of the electromagnetic coupling constant is not considered and the value is set to $\alpha = 1/137$, as is appropriate for photon emissions [137]. The renormalization and factorization scales are set to half of the sum of the transverse masses of the final-state particles in the matrix element. This corresponds approximately to the transverse energy of the photon. The matrix elements are then interfaced to Pythia 8.212 [138] with the A14 set of tuned parameters [139] to obtain events at the particle level. In either calculation scheme, quarks are taken to be massive in the shower.

The theory predictions compared to the D0 $p\bar{p} \to \gamma b$ measurement in Figure 1–1 are now addressed. The way that the PYTHIA and SHERPA predictions are obtained is similar to the ones presented above but with some differences. For PYTHIA, the predictions compared to the D0 measurements only take into account Compton scattering, $gb \to \gamma b$, and quark–antiquark annihilation, $q\bar{q} \to \gamma g$, where the gluon splits into bottom quarks in the parton shower. For SHERPA, the predictions are obtained with only up to $2 \to 4$ matrix elements and by requiring one of the jets to be a b-jet. The k_T factorization [140] refers to an approach in which both the PDFs and matrix elements retain a dependence on the transverse momentum of the partons, which is only integrated in the factorization theorem. This approach allows to resum at all orders terms containing logarithms of the form $\ln(1/x)$, where x is the usual fraction of the proton momentum, which can be large when $Q \ll \sqrt{s}$ since $x \approx Q/\sqrt{s}$. The specific parton-level predictions in this approach that are compared to the D0 measurements only take into account a subset of the possible $\gamma + b$ subprocesses at $O(\alpha\alpha_S^2)$ [141]. The NLO predictions are based on the cutoff approach and the jet formation is done at the parton level only [142].[11] A correction factor that accounts for the non-perturbative effects of the hadronization and of the underlying event, which differs from unity by at most 10%, is applied to the NLO predictions. The SHERPA, NLO and k_T-factorization predictions all require the photon to be isolated such that no fragmentation functions are used. The k_T-factorization predictions describe the data appropriately in some regions of phase-space but not in others. Both the NLO

[11] The software implementing these NLO calculations is not available anymore.

and PYTHIA predictions do not take into account the possibility of gluons splitting into b quarks in jets that would otherwise not be b-jets, apart from the $q\bar{q} \rightarrow \gamma g$ process. As such, they underestimate the data since the b-jet definition that is used is not infrared safe. On the other hand, the SHERPA predictions include higher-order matrix elements in which additional jets can contain these gluon splittings and thus be identified as b-jets. These predictions describe better the D0 data.

CHAPTER 3
Experimental Setup

This chapter explains how protons are made to collide at high energy and how the results of the collisions are measured. The first section gives details about the Large Hadron Collider and how it operates. The second section discusses the ATLAS detector and details of its sub-detectors. The chapter ends with a section presenting the sample of events recorded in 2012 and details pertaining to the simulation of event samples.

3.1 Large Hadron Collider

Collisions between two protons are achieved by the Large Hadron Collider (LHC) [13], currently the highest-energy particle accelerator ever built. The LHC, with a circumference of 26.7 km, is a synchrotron located at the CERN laboratory site, near Geneva in Switzerland. The LHC is the last accelerator in the accelerator complex illustrated in Figure 3–1. The accelerator chain starts with a hydrogen bottle. Hydrogen atoms are stripped of their electrons and the resulting protons are sent to the LINAC 2 linear accelerator, which accelerates them up to a kinetic energy of 50 MeV. They are then accelerated by the subsequent Proton Synchrotron Booster (PSB), up to 1.4 GeV, and by the Proton Synchrotron (PS), up to 25 GeV, which also groups them into bunches. The proton bunches are then sent to the Super Proton Synchrotron (SPS), which accelerates them up to 450 GeV. The SPS provides the LHC with both

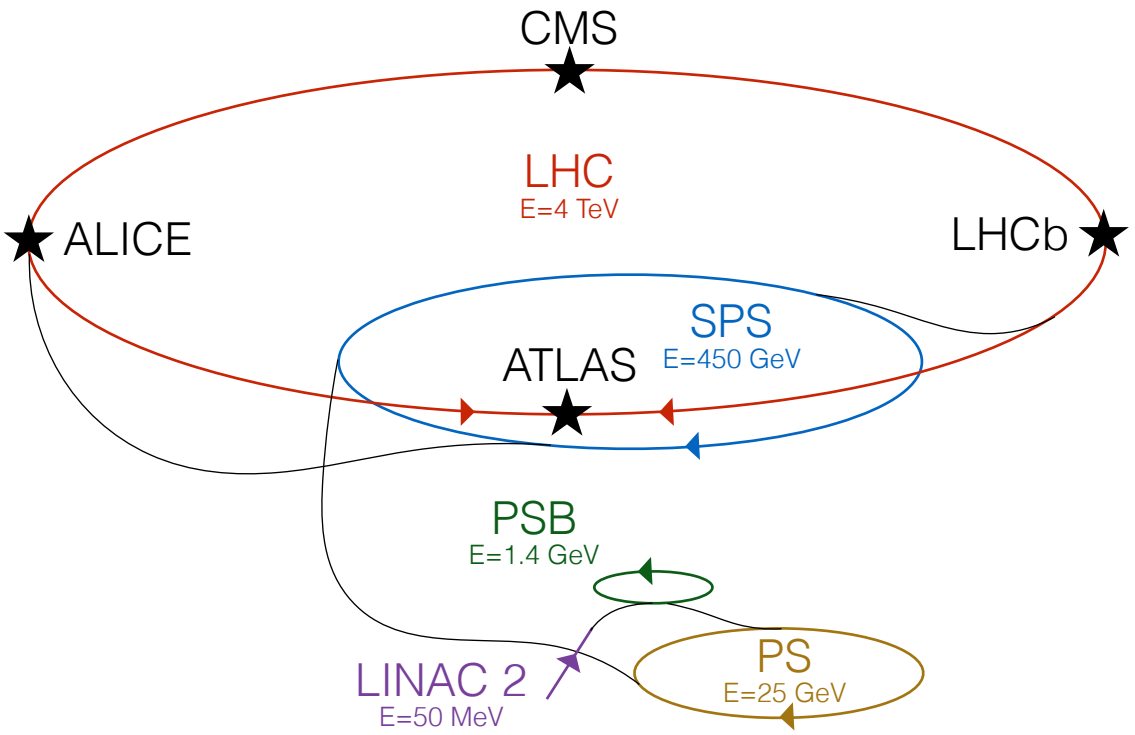

Figure 3–1 – The CERN accelerator complex providing protons to the LHC. The stars indicate interaction points at which the LHC collides protons.

clockwise- and anticlockwise-circulating bunches. This proton accelerating procedure is repeated multiple times until the proton bunches fill up the LHC rings. The LHC then accelerates the protons up to an energy of several teraelectronvolts, depending on the year of operation, and brings the beams into collision at four different interaction points where particle detectors are located: ALICE [143], ATLAS [14], CMS [15] and LHCb [27].

The LHC itself is mainly composed of radiofrequency cavities, in which an electromagnetic field accelerates the protons, and of dipole magnets, which bend the trajectory of the protons such that they move in a circular trajectory. This circular trajectory

allows the protons to travel through the same radiofrequency cavities multiple times, repeatedly increasing their energy. The energy that the protons acquire has an upper bound determined by the strength of the magnetic field that the dipole magnets can produce. Indeed, keeping the same orbit around the LHC for protons of increasing energy requires an increasingly stronger magnetic field. To this end, superconducting dipole magnets, producing a magnetic field strength up to 8.33 T, are used. To prevent protons from colliding with particles outside of the designated interaction points, the beam pipes, in which protons circulate, is in a vacuum state. Quadrupole magnets are used to focus the proton beams such that they do not hit the beam pipe and also to reduce the transverse size of the beams at the interaction points. Higher multipole magnets are used to correct further the trajectories of the protons.

The luminosity, $\mathcal{L}$, of a particle collider is related to the production rate, R, of a particular final state via $R = \mathcal{L}\sigma$, where σ is the cross section to produce that final state in proton–proton collisions. The luminosity has the same dimensionality as a flux. Integrated over a specific period of time, the relation is

$$N = \mathcal{L}_{\text{int}}\sigma, \tag{3.1}$$

where N is the number of events produced and $\mathcal{L}_{\text{int}}$ is the integrated luminosity. The luminosity is an experimental quantity entirely determined by parameters of the collider. It factorizes the experimental parameters from the intrinsic physical processes. A higher luminosity results in a higher number of events produced for a particular physical process. Thus to investigate rare processes and to reduce

statistical uncertainties caused by the finite sample size of events, a higher luminosity is desirable.

The luminosity of a collider represents the number of interactions per unit time and per unit area. It is calculated in the following way [13]:

$$\mathcal{L} = \frac{f_{\text{rev}} n_b N_1 N_2}{A}, \tag{3.2}$$

where f_{rev} is the revolution frequency of the proton bunches, n_b is the number of bunches that are paired between the two beams and that can collide at an interaction point and N_1 and N_2 are the numbers of particles in each bunch of the pair, since each particle in one bunch can interact with any particle in the other bunch. The geometrical area factor A is related to the transverse area of the beam at an interaction point, which is determined by the focusing of the beams and their crossing angle. Out of the four LHC interaction points, those associated to ATLAS and CMS have been designed to have a high luminosity, with a nominal value of $\mathcal{L} = 10^{34}$ cm^{-2}s^{-1} [13]. During LHC operation, the luminosity degrades with time, as the number of protons per bunch decreases due mainly to collisions. Beams are dumped and the filling process starts anew when doing so would result in a larger integrated luminosity. It is common for beams to collide continuously for more than ten hours.

In contrast to the Tevatron, which collided protons with antiprotons, the LHC collides protons with protons. This is motivated both by physical and technical reasons. Although the production cross sections of several physical processes are higher for collisions of quarks with antiquarks than for collisions of two quarks, and thus respectively for $p\bar{p}$ and pp collisions, the difference between the latter two becomes

less significant as the collision energy increases, such as from that of the Tevatron, $O(1\text{ TeV})$, to that of the LHC. This is due to the larger momentum density fraction of the proton carried by antiquarks and gluons at higher energy, as can be seen from Figure 2–2, which compensates for the lower cross section between two valence quarks. The increasingly smaller difference between the cross sections of proton–antiproton and proton–proton collisions as a function of the center-of-mass energy happens for example for the production cross section of a pair of W bosons [144], a pair of Z bosons [145] and a pair of top quarks [146]. In parallel, since it is technically easier to accelerate protons than antiprotons, as they are naturally occurring and thus there is no need to produce and collect them, a higher luminosity can be achieved. This higher luminosity can compensate a smaller cross section to ultimately produce more physically interesting events.

The LHC started producing proton–proton collisions with commissioning beams in late 2009. Beams producing collisions intended for physics analysis started in 2010, with essentially all of the integrated luminosity produced at a center-of-mass energy of 7 TeV. In 2011, the integrated luminosity continued to ramp up for collisions at 7 TeV. In 2012, the center-of-mass energy increased to 8 TeV and the integrated luminosity increased further. After 2012, the LHC went into a two-year long shutdown for various consolidations and upgrades, ending Run 1 of the LHC. It is the collisions provided by the LHC in 2012 at 8 TeV, i.e. protons accelerated up to 4 TeV, that are used for the measurement presented in this thesis.

In 2012, the LHC was filled with up to 1380 colliding paired bunches with a time interval between consecutive bunches as short as 50 ns [147]. The peak luminosity

attained was 7.7×10^{33} cm^{-2}s^{-1} with a number of protons per bunch of about 1.7×10^{11} [147]. These values imply the presence of multiple inelastic proton–proton interactions in a given crossing of paired bunches, known as pileup interactions. The number of pileup interactions, μ, can be obtained from the ratio of the inelastic event rate to the bunch crossing rate:

$$\mu = \frac{\mathcal{L}\sigma_{inel}}{f_{\text{rev}} n_b}, \tag{3.3}$$

with $\sigma_{\text{inel}} = 75.6$ mb at $\sqrt{s} = 8$ TeV [104] and with the revolution frequency of the proton bunches around the LHC being approximately given by the speed of light divided by the circumference of the LHC, i.e. $f_{\text{rev}} = 11.2$ kHz. In 2012, the maximum number of pileup interactions was about 38, while the average over the data-taking period was about 21 [147]. In the nominal LHC design, there are 2808 colliding bunches, giving a maximum number of pileup interactions of about 24. The larger number of maximum interactions per bunch crossing in 2012 compared to the nominal design can be mainly attributed to the smaller number of proton bunches per beam. A larger number of bunches is allowed in the nominal design as a narrower bunch spacing of 25 ns is assumed.

3.2 ATLAS Detector

The ATLAS detector, shown in Figure 3–2 is one of two general-purpose detectors, the other being CMS, that measure the momenta and energies of particles produced in the collisions provided by the LHC. It is a hermetic detector with a cylindrical geometry. The system of coordinates describing the detector has its origin placed in the geometrical center of the detector, with the x-axis pointing towards the center of

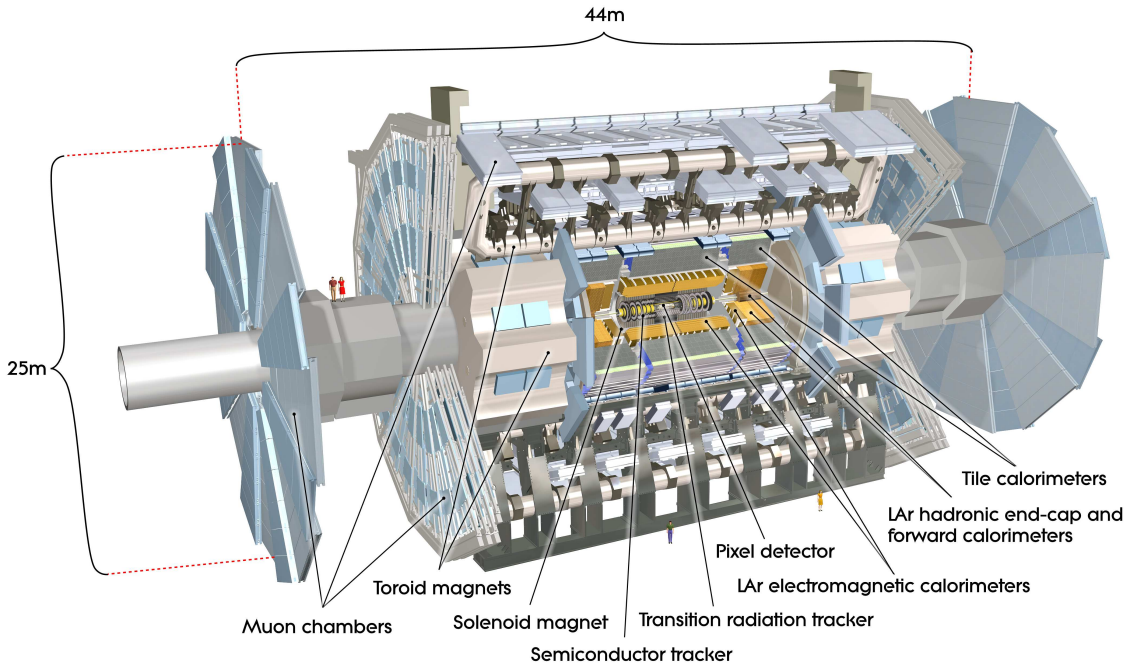

Figure 3–2 – Representation of the ATLAS detector with an opening in ϕ allowing for the labelling of the different sub-detectors [14].

the LHC ring, the y-axis pointing upwards and the z-axis pointing in the anticlockwise direction of the LHC ring when viewed from above, thus forming a right-handed coordinate system. Cylindrical coordinates are defined by the azimuthal angle around the z-axis, ϕ, equal to zero in the direction of the x-axis, and the radius, R, defined as the distance from the z-axis. Additionally, the pseudorapidity, η, is used and is given in terms of the polar angle, θ, by $\eta = -\ln \tan \frac{\theta}{2}$, where θ is zero in the direction of the z-axis. The pseudorapidity is zero in the transverse plane defined by $z = 0$, increases towards infinity towards the direction of the z-axis and decreases towards minus infinity in the direction opposite to the z-axis. The pseudorapidity is used over the polar angle since, for massless particles, it corresponds to the rapidity, whose measure is invariant under Lorentz boosts along the z-axis.

The ATLAS detector is composed of several sub-detectors differing in technology and purpose that are placed in concentric cylindrical layers around the nominal interaction point. Tracking detectors occupy the innermost region of the ATLAS detector, closest to the beam pipe. They are inside a magnetic field created by a solenoidal magnet that surrounds them. Outside of the solenoidal magnet lie the electromagnetic and hadronic calorimeters. A muon spectrometer acts as the external layer of the detector. Toroidal magnets provide a magnetic field for the spectrometer. Following the cylindrical geometry of the detector, the sub-detectors are further separated into barrel and end-cap sections. The barrel section is referred to as being central and the end-caps as being forward. A trigger system making use of the information from the sub-detectors selects in real time which events to record to long-term storage.

3.2.1 Inner Detector and Solenoidal Magnet

The Inner Detector [14] is composed of three tracking detector technologies: pixel, silicon microstrip and transition radiation trackers. Their purpose is to provide a measurement of the positions of charged particles while not disturbing their trajectories. By combining measurements of the position of a particle at different locations in space, its trajectory can be reconstructed. Furthermore, when a charged particle moves inside a magnetic field, its trajectory curves with a radius of curvature proportional to its momentum and inversely proportional to its electric charge. A measurement of the momentum and of the charge becomes possible in addition to the trajectory of the particle. The tracking detectors are located inside a superconducting solenoidal magnet that produces an axial field of 2 T along, and pointing towards, the z-axis direction. This specific magnetic field configuration allows to measure the momentum component transverse to the z-axis of a charge particle. The transverse momentum is a physically relevant quantity at a hadron collider since it is boost invariant along the z-axis.

The pixel detectors and the silicon microstrip trackers, of which the latter are also called the semiconductor tracker (SCT), are silicon-based solid-state detectors with an operating principle based on a p–n junction diode. When charged particles pass through the depletion region of the detector, they ionize the material. Due to a bias voltage applied to the electrodes on either side of the depletion region, the electron-hole pairs drift towards the electrodes, producing an electric current that is measured. In the case of the pixel trackers, the electrodes are segmented in two dimensions, while the microstrip trackers are only segmented in one direction. The pixels provide

the highest granularity, most of them having a size of 50 μm $\times$ 400 μm, and thus the highest resolution of the position of the particles: 10 μm and 115 μm [14] along the respective granularity directions. As such, they are located closest to the center of ATLAS. Regarding the microstrips, to provide a measurement of the coordinate along their non-segmented direction, pairs of microstrip trackers are layered together with an angle of about 2° between the directions of the strips. The combined measurement of the position of a particle in the two layers allows to reconstruct the component of the position along the non-segmented direction, albeit with a reduced resolution compared to the pixels: 17 μm and 580 μm [14], for a respective strip pitch of 80 μm and a strip length of 12 cm.

The transition radiation tracker (TRT) is a collection of drift tubes located outside of the SCT. These cylindrical tubes, with an inner radius of 2 mm, are filled with a gas mixture mainly composed of xenon and with a wire located in the middle of the tube along the axis. A high voltage is applied between the surface of the tube and the wire. Charged particles going through the tube ionize the gas and the ionization electrons drift to the wire, generating an electric current. The time it takes for the electrons to reach the wire, with respect to the reference time associated to the bunch crossings, given by the LHC, is used to infer at what distance to the wire a charged particle travelled. This distance restricts the position of the particle in the transverse section of the tube to a circle around the wire, with a resolution of 130 μm [14]. The tubes do not measure the position of charged particles along their axes. The TRT has a worse resolution than the silicon-based trackers, but the performance is compensated by the larger number of independent position measurements it produces.

Additionally, the TRT can distinguish electrons from pions, which are light mesons. When charged particles cross interfaces of differing dielectric constants, they emit transition radiation photons [148]. The space between the tubes is filled with fibres and foils of polypropylene, for the barrel and the end-caps respectively. When charged particles cross the polypropylene, they radiate X-ray photons. Through the photoelectric effect, these photons are absorbed by the gas in the tube and produce additional ionization electrons. Impinging pions radiate fewer photons than electrons, such that the TRT can distinguish between these two types of particles.

Figure 3–3 shows the disposition of the tracking detectors in both the barrel and the end-caps. The pixel modules are disposed into three cylindrical layers in the barrel and into three disks perpendicular to the beam pipe in either end-cap. They are aligned such that the direction with the better resolution is in the R–ϕ plane. In the barrel, the direction with the worse resolution is aligned along z, while it is aligned along R in the end-caps. Double-layered microstrip modules are assembled into four cylindrical layers in the barrel and in nine disks on either side of the barrel. They are aligned along the same directions as the pixel modules. The TRT in the barrel is composed of up to 73 layers of tubes, while the end-caps each contain up to 160 layers. The TRT tubes are positioned along z in the barrel and along R in the end-caps. A charged particle traverses typically 36 tubes. In terms of the pseudorapidity, the coverage of the pixels and microstrips extends up to $|\eta| = 2.5$, while that of the TRT extends up to $|\eta| = 2.0$. Thus, ATLAS has tracking capabilities up to $|\eta| = 2.5$.

In the context of the measurement of $\gamma + b$ production, the Inner Detector is used to distinguish photons from electrons, as the former do not leave tracks while the latter

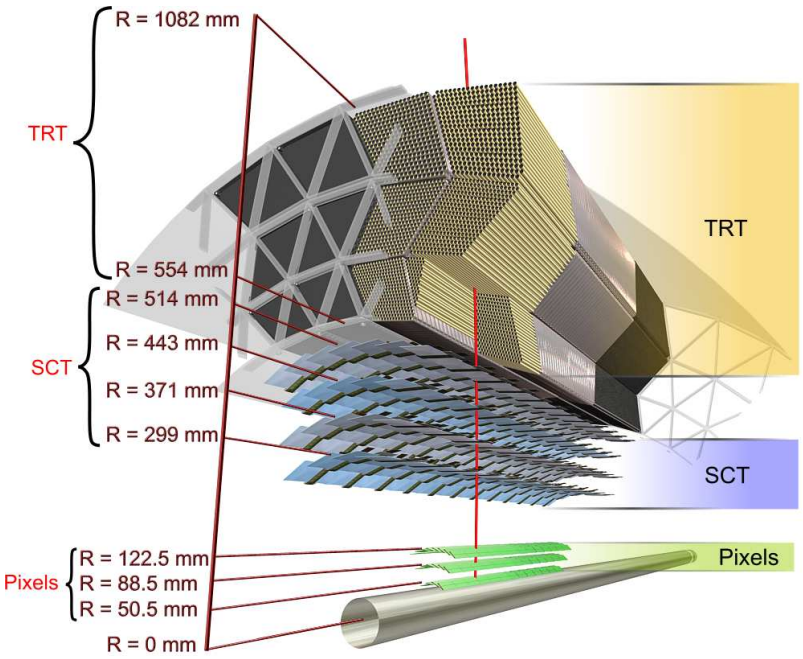

(a)

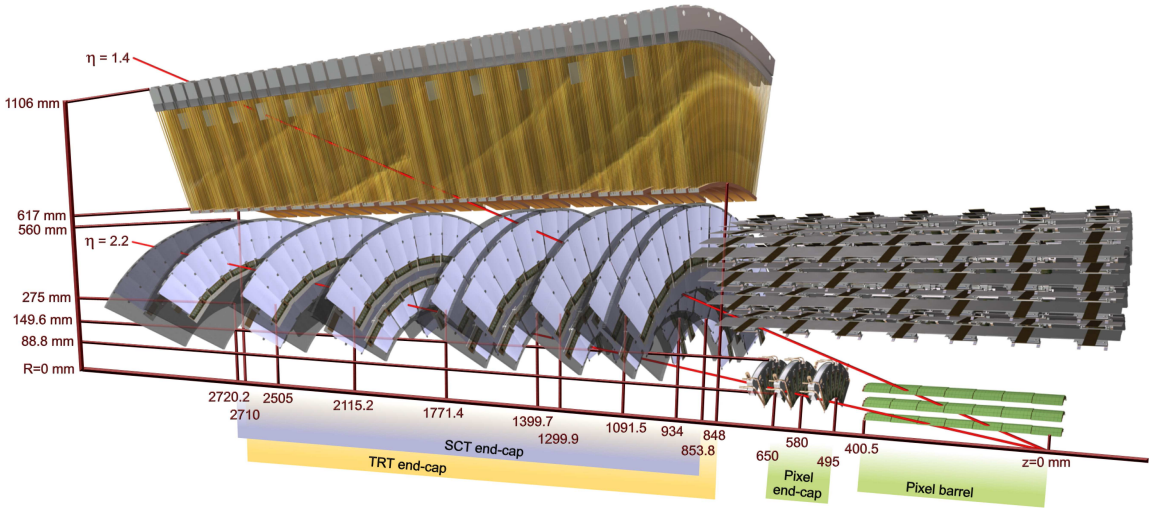

(b)

Figure 3–3 – Section in ϕ of the Inner Detector in (a) the barrel and (b) one of the end-caps [14].

do. Also, the Inner Detector is used to tag jets that contain b hadrons from those that do not. Therefore, the measurement presented in this thesis is restricted to the pseudorapidity coverage of the Inner Detector.

3.2.2 Calorimeter System

The calorimeter system of ATLAS, shown in Figure 3–4, is located outside of the solenoidal magnet. It is divided into the electromagnetic calorimeter and the hadronic calorimeters, of which the latter is composed of different detector technologies. The purpose of the calorimeters is to measure the energy of particles. This is done through the destructive process of absorbing the energy of the particles and converting it into an electric current, which is then calibrated to the corresponding energy of the incoming particle. The electromagnetic calorimeter measures the energy of photons and electrons, while the hadronic calorimeters are designed to measure the energy of hadrons.

All ATLAS calorimeters are sampling calorimeters, which means that they contain successive layers of both active material that is instrumented and absorber material that is not. The role of the absorber material, usually dense, is to increase the number of interactions the impinging particles will have with the calorimeter. An incoming photon or electron impinging on the electromagnetic calorimeter will produce a cascade of secondary particles, called a shower, primarily via bremsstrahlung and pair-production processes. The typical distance over which an electron emits a photon, or a photon converts into an electron pair, is given by the radiation length, X_0, of the material. In the case of an incoming hadron, since hadrons are made up of colored

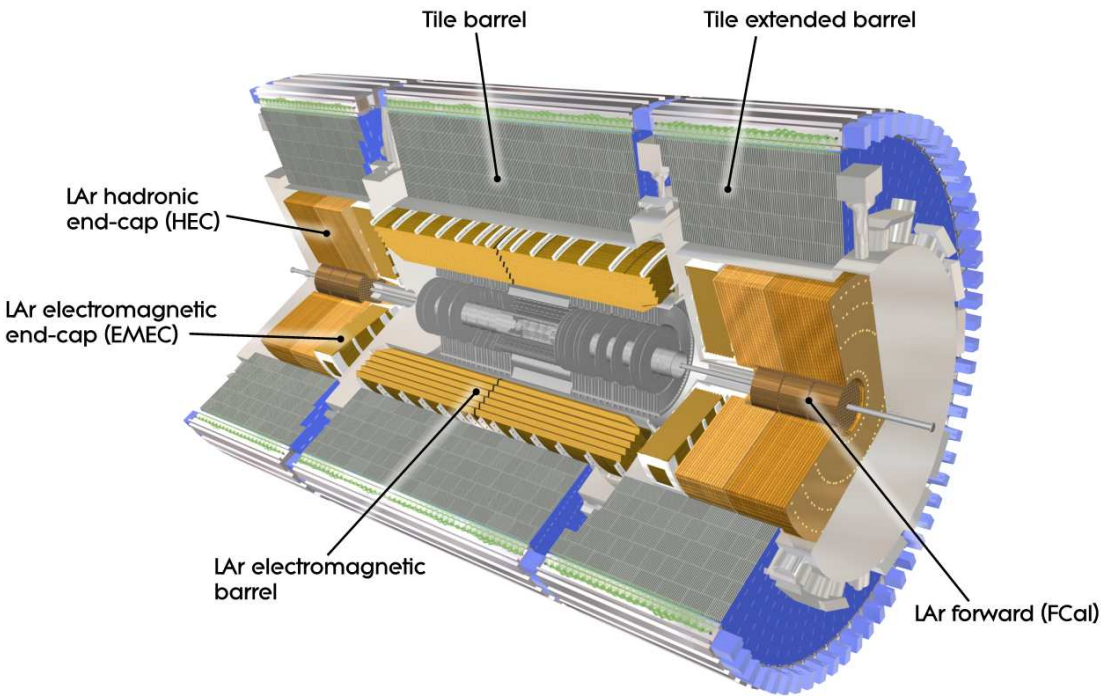

Figure 3–4 – The calorimeter system of ATLAS with an opening in ϕ allowing for the labelling of the different calorimeter components [14].

particles, they interact via the strong force. They can interact with the nuclei of the calorimeters, producing a more complex hadronic shower. This shower, characterized by the interaction length λ in analogy to the radiation length, is usually longer and larger, i.e. $\lambda > X_0$. The electromagnetic calorimeter is designed to optimize the measurement of electromagnetic showers while the hadronic calorimeters, which enclose the electromagnetic calorimeter, are designed to measure and contain the larger hadronic showers.

The ATLAS electromagnetic calorimeter [14] uses lead as the absorber and liquid argon (LAr) as the active material. The passage of electrons within an electromagnetic shower in the LAr ionizes argon atoms. Ionization electrons drift to an electrode located in the middle of the LAr gap under the influence of an electric field, thereby creating an electric current that is measured. To alternate the absorber and active materials while ensuring that no gaps are present in ϕ, the calorimeter has an accordion shape in the longitudinal direction of the shower. The layout of the electromagnetic calorimeter is illustrated in Figure 3–5. It is divided into three longitudinal layers, themselves segmented in cells along η and ϕ. The first layer is the most finely segmented in η, but is the coarsest in ϕ. The size in η of these cells is the smallest in the barrel and increases with the pseudorapidity in the end-caps. The cells have a $\Delta\eta \times \Delta\phi$ granularity of about 0.003×0.1 in the barrel. Due to the fine granularity of the cells, they are referred to as strip cells. The second layer collects most of the shower energy and has a granularity of about 0.025×0.025 in $\Delta\eta \times \Delta\phi$. The third layer is mainly used to capture the tail of the electromagnetic shower and is the coarsest in η with a granularity of about 0.05×0.025 in $\Delta\eta \times \Delta\phi$. The size of

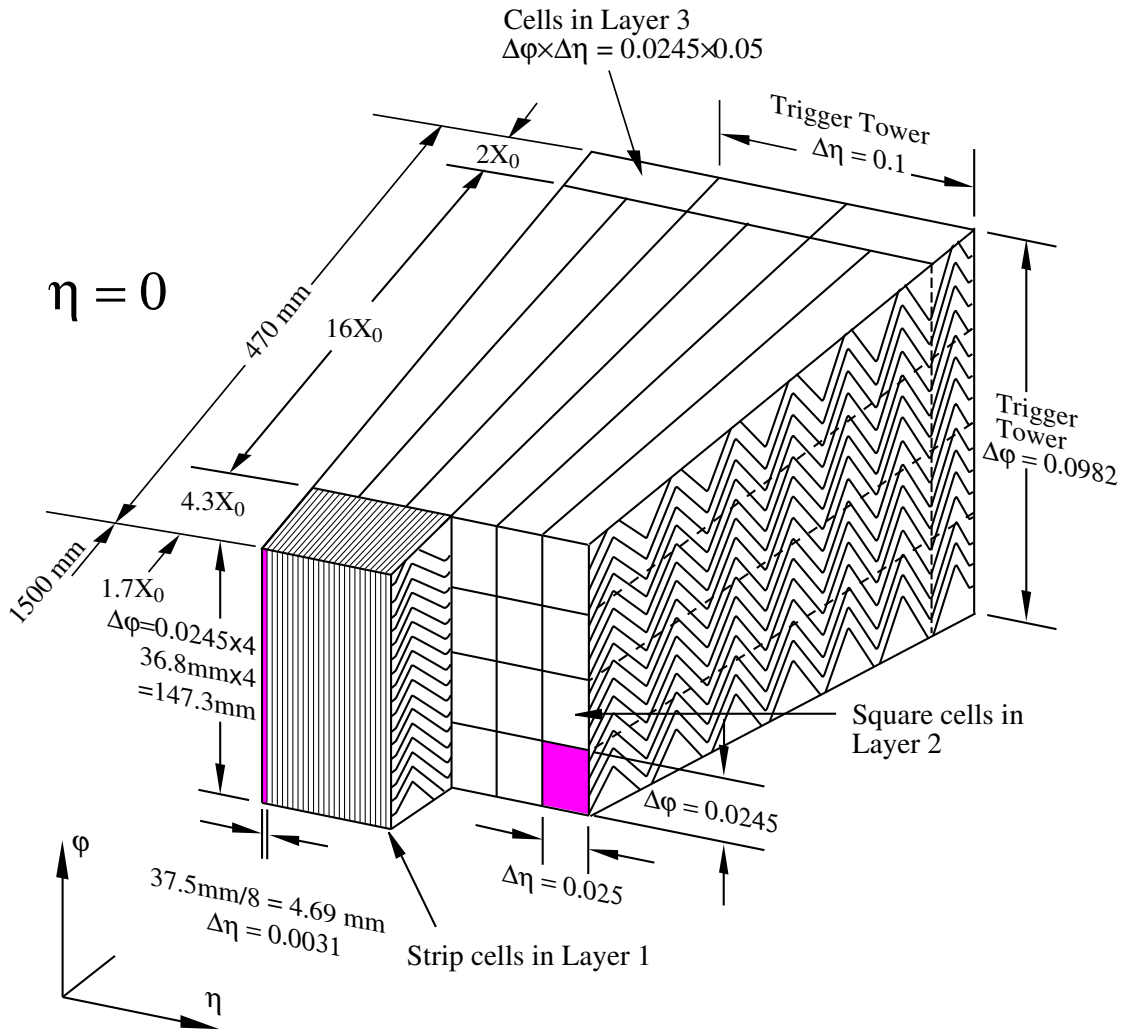

Figure 3–5 – Geometry of cells in the barrel electromagnetic calorimeter [14]. The accordion shape of the calorimeter is also displayed.

the cells in the first and third layers are integer multiples or fractions of those in the second layer. The fine segmentation of the first layer allows to distinguish an electromagnetic shower initiated by one photon from that initiated by two photons, produced for example by the decay of a π^0 meson into two photons close to the calorimeter. Its coarser segmentation in ϕ is motivated by photons converting into electron pairs inside the Inner Detector, which can happen since the amount of material upstream of the first layer corresponds to about $3X_0$, varying as a function of the pseudorapidity. Due to the solenoidal field, the trajectories of electrons and positrons become separated in ϕ, however, with a coarser cell in ϕ, the energy can still be collected by one cell as if the conversion had not happened. Furthermore, to help in correcting for electromagnetic showers that start before the calorimeter, an additional layer, the presampler, is located closer to the solenoidal magnet, while still being outside of it. The granularity of this layer is about 0.025×0.1 in $\Delta\eta \times \Delta\phi$. In total, the electromagnetic calorimeter has a thickness of at least $22X_0$, varying with pseudorapidity.

The ATLAS hadronic calorimeters [14] make use of different technologies. In the barrel, the calorimeter uses steel as the absorber and scintillating plastic, composed mainly of polystyrene, as the active material. The scintillator is shaped into thin tiles that are inserted into the steel support structure. When charged particles from the hadronic shower pass through the scintillating tiles, ultraviolet photons are emitted. These scintillation photons travel through wavelength-shifting fibres to photomultiplier tubes, which convert the light into an electric current. This tile hadronic calorimeter is separated into three longitudinal layers, with $\Delta\eta \times \Delta\phi$

granularities of 0.1×0.1 for the first two layers and of 0.2×0.1 for the third layer. The tile calorimeter is separated into two parts: the barrel and the extended barrel. The former lies behind the barrel of the electromagnetic calorimeter while the latter extends the pseudorapidity coverage to complete the cylindrical layer. The end-cap hadronic calorimeters use LAr as the active material, similarly to the electromagnetic calorimeter, but uses copper as the absorber instead. It has four layers of cells, whose granularities range from 0.1×0.1 to 0.2×0.2 in $\Delta\eta \times \Delta\phi$. The amount of material traversed by the particles originating from the interaction point and travelling to the end of the hadronic calorimeters corresponds to about 10λ.

The coverage of the electromagnetic and hadronic calorimeters extends up to $|\eta| = 3.2$. To extend further the coverage, up to $|\eta| = 4.9$, forward calorimeters [14] are located close to the beam pipe in the inner regions of the end-caps. They have three layers: the first one serving as the electromagnetic calorimeter and the other two serving as the hadronic calorimeter. All layers use LAr as the active material. The first layer uses copper as the absorber while the other two use tungsten.

The transition from the electromagnetic barrel to the electromagnetic end-cap occurs in the region around $|\eta| = 1.5$. In this region, the amount of material upstream of the calorimeter, due to the tracking detectors and other non-active service material, is large relative to the rest of the pseudorapidity region. Figure 3–6 shows the amount of material as a function of η in that region. The amount of material in front of the calorimeter accordion is more than double of that outside the transition region. Scintillating tiles are placed in the transition gap in front of the end-cap electromagnetic calorimeter to improve the energy resolution in this region. However,

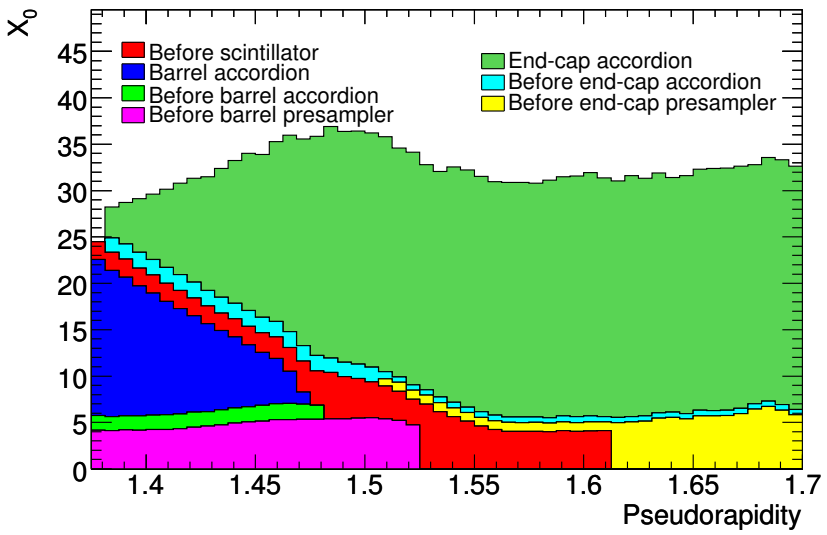

Figure 3–6 – Amount of material in front of the electromagnetic calorimeter and inside of it, expressed in units of radiation lengths, as a function of the pseudorapidity [14].

even with those tile cells, the energy resolution is poor compared to that outside the transition region. As a consequence, the region $1.37 < |\eta| < 1.56$ is not used for the physics measurement of photons. Additionally, the first layer is not finely segmented in this region. It is only finely segmented in the regions $|\eta| < 1.4$ and $1.5 < |\eta| < 2.4$, roughly matching the coverage of the Inner Detector.

In general, the relative resolution at which a calorimeter can measure the energy of an incoming particle can be parameterized as [149]

$$\frac{\sigma(E)}{E} = \sqrt{\left(\frac{a}{\sqrt{E}}\right)^2 + \left(\frac{b}{E}\right)^2 + c^2}, \tag{3.4}$$

where a, b and c are parameters and E is the energy of the particle. The first term represents the contribution to the resolution coming from the stochastic process of the

shower and of the sampling of its energy. The second term represents the contribution due to the signal noise, coming from either the electronics used to process the signal or from particles produced in other proton–proton collisions than that of interest, i.e. from pileup. The third term is the constant contribution that does not depend on the energy of the incoming particle, such as a non-uniform response across the calorimeter due to detector imperfections. The relative resolution improves with higher energy and in particular the noise term becomes negligible.

For the electromagnetic calorimeter, the resolution is described by $a = 10\%\sqrt{\text{GeV}}$ and $c = 0.2\%$ [14]. For the tile calorimeter, the parameters are $a = 56\%\sqrt{\text{GeV}}$ and $c = 6\%$ for an impinging pion [14]. The hadronic end-cap calorimeter is described by $a = 71\%\sqrt{\text{GeV}}$ and $c = 6\%$ for an incoming pion [14], while the forward calorimeter is described by $a = 29\%\sqrt{\text{GeV}}$ and $c = 4\%$ for an electron [14] and by $a = 70\%\sqrt{\text{GeV}}$ and $c = 3\%$ for a pion [14]. The expected noise contribution for the different calorimeters under the pileup conditions of 2012 is given in Figure 3–7. It is below 100 MeV for most of the electromagnetic and tile calorimeters, below 1 GeV for the hadronic end-cap calorimeter and below 10 GeV for the forward calorimeter.

In the context of $\gamma + b$ production, calorimeters are used to measure the energy of the photon and of the b-jet. Additionally, the cell segmentation of the electromagnetic calorimeter allows to distinguish electromagnetic showers from hadronic ones. This is used to distinguish photons from jets.

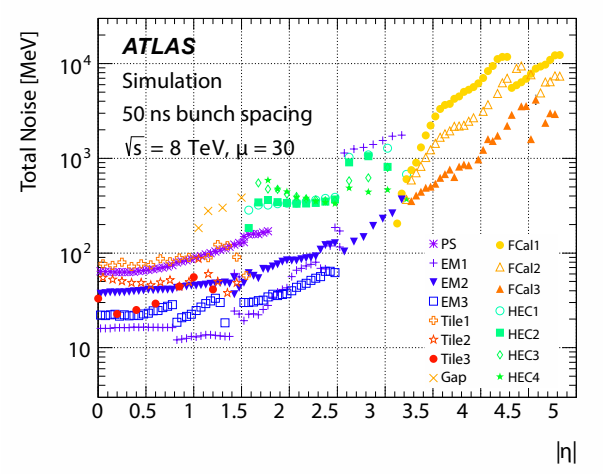

Figure 3–7 – Total noise expected in the calorimeter cells as a function of the pseudorapidity. The total noise is defined as the sum in quadrature of the electronic noise and of the pileup noise and is representative of the pileup conditions in 2012 [150]. PS refers to the presampler, EM to the layers of the electromagnetic calorimeter, Gap to the tile scintillator in the transition region between the barrel and the end-caps, FCal to the forward calorimeters and HEC to the hadronic end-cap calorimeters.

3.2.3 Muon Spectrometer and Toroidal Magnets

The muon spectrometer [14] is the outermost sub-detector in ATLAS. Its purpose is to provide an independent measurement of the momentum of muons. Muons pass through the calorimeters since, at the energy scale at which they are likely to be produced, i.e. $O(100\ \text{GeV})$, they interact with the detector material mostly via ionization rather than by emitting bremsstrahlung photons. Muons do not create showers in the calorimeters. This is in contrast to electrons and is due to the higher mass of muons. Consequently, muons are easily identified by tracking detectors placed after the calorimeters.

The ATLAS muon spectrometer is a collection of four tracking detector technologies: monitored drift tubes (MDTs), cathode strip chambers (CSCs), resistive plate chambers (RPCs) and thin gap chambers (TGCs). To provide a measurement of the momentum, the trackers are located inside a toroidal magnetic field provided by three superconducting toroidal magnets, one for the barrel and one in either end-cap. These magnets provide an azimuthal magnetic field up to $|\eta| = 2.7$. The field bends the trajectories of the muons in the R–z plane, perpendicular to the curvature plane of the solenoid magnet. The trackers, which are located up to $|\eta| = 2.7$, thus offer an independent measurement of the muon momentum. Figure 3–8 shows the location of the components of the muon spectrometer in ATLAS.

In the context of the $\gamma + b$ measurement, only the MDTs are used. They provide a correction to the jet energy resolution that accounts for showers punching through the calorimeters into the muon spectrometer.

3.2.4 Luminometers

The luminosity of the LHC beams at the ATLAS interaction point is measured by luminometers. In 2012, the primary ATLAS luminometer was the BCM detector [151], composed of diamond-ionization sensors that are nominally used to detect abnormal beam conditions. Additionally, the LUCID detector [152], a Cherenkov-light detector measuring inelastic pp scattering, and the ATLAS detector, via the counting of tracks in the Inner Detector, were used to provide complementary measurements of the luminosity [147]. These detectors provide a measurement of the relative luminosity of the LHC beams.

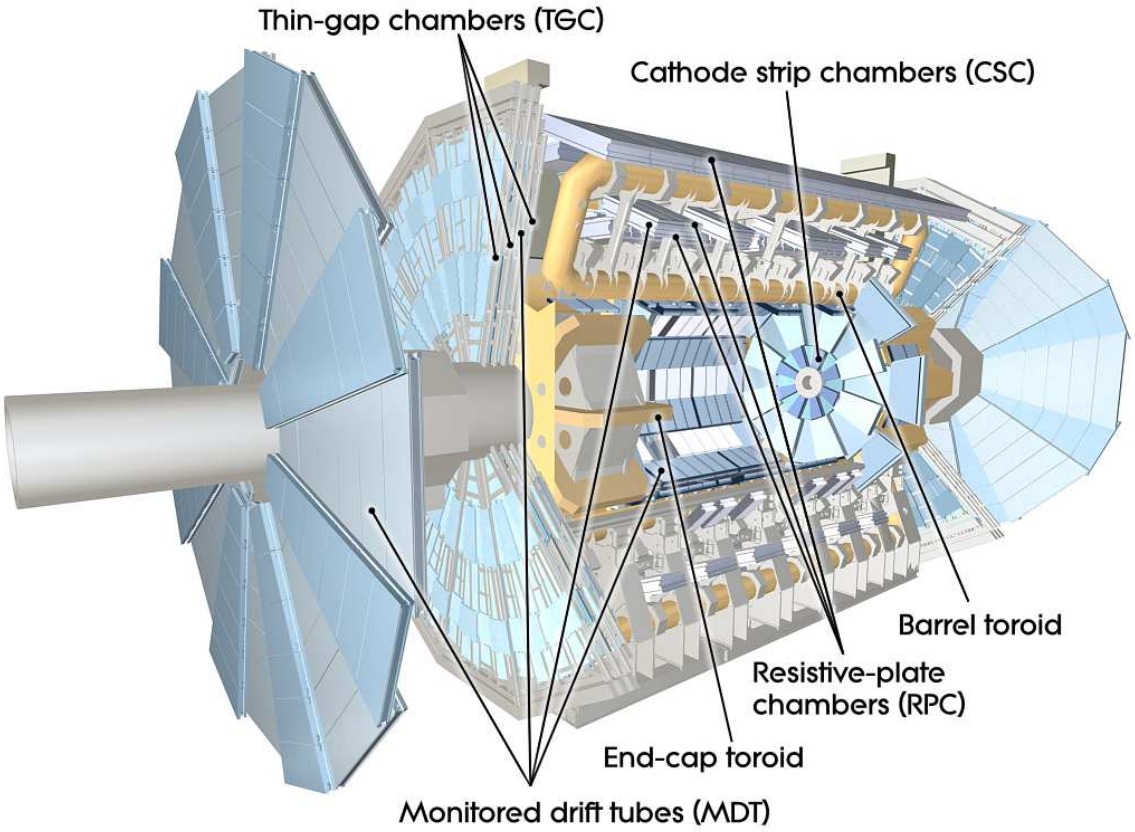

Figure 3–8 – Layout of the muon trackers and of the toroidal magnets in ATLAS [14].

The relative luminosity is a measurement of the absolute LHC luminosity up to a calibration factor [147]. It is given by

$$\mathcal{L} = \frac{\mu_{\text{vis}} f_{\text{rev}}}{\sigma_{\text{vis}}}, \tag{3.5}$$

where f_{rev} is the revolution frequency of the proton bunches and μ_{vis} is the number of inelastic interactions per bunch crossing, for a given bunch pair, that is visible to a particular measurement procedure. It is obtained by counting in a given time interval the number of bunch crossings for which a signal was detected, by assuming that number follows a Poisson distribution and by comparing it to the total number of bunch crossings in that time interval. The last quantity, σ_{vis}, is the cross section of the production of that visible signal and its value is smaller than that of the pp inelastic cross section. It is a priori unknown and can be considered as a calibration constant.

To measure σ_{vis}, a simultaneous measurement of $\mathcal{L}$ and μ_{vis} is required. The measurement of $\mathcal{L}$ can be performed through van der Meer beam scans [153]. These scans, during which the beams successively cross one another in the horizontal and the vertical directions, allow for a direct measurement of the beam transverse area, making possible the use of Equation 3.2 to measure the luminosity. As μ_{vis} can be simultaneously measured during the scans, σ_{vis} can be obtained. Therefore, the relative luminosity that is measured by the luminometers can be calibrated to the absolute LHC luminosity.

3.2.5 Trigger System

The event rate of 20 MHz provided by the LHC in 2012 was too high to permit the recording of every event to permanent storage. To reduce the number of events, a list of physically interesting features in events of interest was designed. A trigger system compares in real time this list to the features of the current event and records the event if it satisfies at least one of them. The 2012 ATLAS trigger system [14] was a succession of three levels of trigger decisions, each reducing the event rate towards the recording rate of 400 Hz. By partially reducing the event rate, each level allows more time for the subsequent level to reach a decision and thus allows for more complex features to be investigated.

The first level, the Level-1 trigger, is implemented in hardware for the fastest decision time, with a latency of 2.5 μs. It reduces the event rate to 75 kHz by using simple algorithms that are run on a subset of detector systems and making use of a coarser detector granularity. It can select events based on information from the calorimeters or from the muon spectrometer. Several selection criteria have been conceived to cover all physically interesting possibilities. An event is accepted if it satisfies at least one of them. Additionally, the Level 1 identifies regions of interest.

The second level of the trigger, the Level-2 trigger, is implemented in software and has a latency of 40 ms. It reduces the event rate to 3.5 kHz. It has access to the full detector granularity but only in the regions of interest that are passed to it by the Level 1. To avoid trigger inefficiencies, the software algorithms that are investigating the features of the event are usually similar in nature to the ones used in physics

analyses of recorded events. An event satisfying any of the predefined criteria on the extracted features of the event is accepted to be studied by the third level of the trigger system.

The third level is called the Event Filter and is also implemented in software. It has a latency of 4 s and reduces the event rate to the recording rate of 400 Hz. The full detector information is available at this level. The algorithms are essentially the same as those used in the physics analyses. Events satisfying the criteria of the Event Filter are committed to permanent storage, allowing for thorough physics analyses.

At any of the trigger levels, a prescale factor p can be applied to any of the trigger criteria. In those cases, only $1/p$ events, randomly chosen, that would have been analyzed for the associated feature are actually investigated. The other events are automatically made to fail to satisfy the criterion. This functionality is used for criteria that are satisfied by a large number of events but which are still of physical interest. An example is a low energy threshold on a group of calorimeter cells. Having the prescale functionality allows to record a fraction of events while maintaining a low latency and event rate. Features that are to be investigated, algorithms, criteria and prescale factors are all chosen to optimize the trigger rates at every trigger level while still selecting a physically diversified sample of events.

3.3 Event Samples

With the goal of measuring the cross section of the production of $\gamma + b$, the recorded events need to be analyzed. However, these events do not contain the information on a per-particle basis but only the signals that were measured by the detector. To

understand the relation between the particles and the signals that they produce in the detector, simulations of the interactions of the particles with the detector are necessary. These allow to assess the performance of the detector, to estimate the efficiency of various algorithms and to calibrate the measured signals such that they describe accurately the properties of the particles that produced them. Details of the recorded events and of the simulated events are now discussed.

3.3.1 Recorded Events

The data analyzed for the measurement of the cross section production of $\gamma + b$ were recorded from the collisions of two protons by the LHC at $\sqrt{s} = 8$ TeV in 2012. The evolution of the integrated luminosity throughout the year, from April to December, is shown in Figure 3–9. The LHC delivered an integrated luminosity of 22.7 fb^{-1} at the ATLAS interaction point [147]. The delivered integrated luminosity is not fully recorded by ATLAS. This recording inefficiency occurs to allow for safe operations of the detector and to avoid overloading its readout system. Furthermore, events are only considered suitable for physics analysis if all the sub-detectors are fully operational. The overall ATLAS physics data-taking efficiency in 2012 was 95.5% [154]. Taking these inefficiencies into account, the integrated luminosity of the sample of events recorded by ATLAS in 2012 and suitable for physics analysis is 20.2 fb^{-1}.

3.3.2 Simulated Events

Monte Carlo event generators produce exclusive events by generating particles of definite properties such as their four-momenta. As such, they can be made to interact with a simulated detector. Detector simulation software, such as GEANT4 [156],

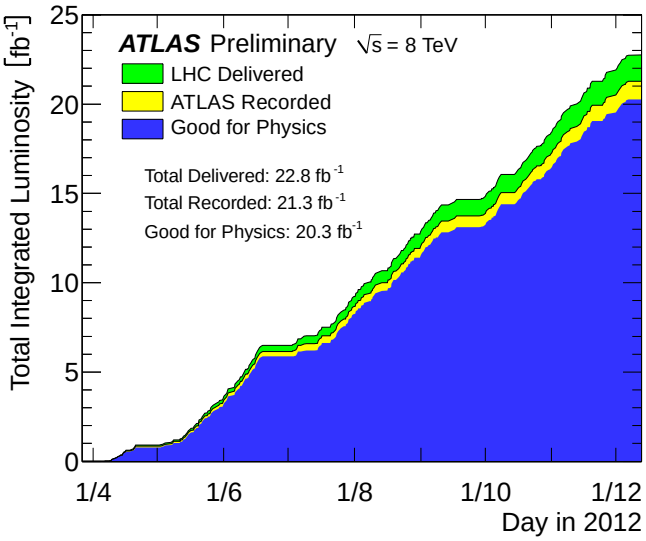

Figure 3–9 – Time evolution of the integrated luminosity in 2012 at the ATLAS interaction point [155]. The preliminary value of the total delivered integrated luminosity shown in the plot has been updated to a value of 22.7 fb^{-1} [147]. This results in an updated good-for-physics integrated luminosity of 20.2 fb^{-1}.

takes as input a detector geometry and its material composition to simulate the interactions of particles with that detector. Such a simulation of the ATLAS detector has been developed [157]. The physical interactions that are simulated include multiple Coulomb scattering, the photoelectric effect, bremsstrahlung, ionization among others. The energy deposited in the detector via these interactions is recorded as hits. The hits can then be interfaced to a simulation of the electronics system specific to each sub-detector, taking into account effects such as electronic noise and crosstalk. This step is referred to as the digitization of the hits since the output are the same kinds of digital information that would be obtained from real detected signals. The output of the digitization step is similar to the recorded information

of real data events. Therefore, the simulated events, called MC events due to their origin, can be analyzed in the same way as the real recorded events.

During the digitization step, the effect of pileup is taken into account. Since a detector signal takes in general more time to process than the time between two bunches, the recorded signals are not only affected by multiple interactions happening during the same bunch crossing but are also affected by interactions happening before and after that bunch crossing. These interactions are referred to as out-of-time pileup. Each sub-detector has a different time window during which it is sensitive to out-of-time pileup, depending on the speed of its signal processing. Therefore, the simulation must take into account not only the in-time pileup but also this out-of-time pileup. This is achieved by generating soft inelastic pp scatterings with PYTHIA 8.186, using the A2 set of tuned parameters [132], optimized for events with no hard scattering, and the MSTW2008LO PDF set [158]. These soft collisions are representative of the average inelastic pp collision. They are interfaced through the ATLAS detector simulation to produce hits, independently of other MC samples. It is at the digitization step that the hits of these soft collisions are combined to the simulated samples of interest. The overlay of the hits follows the proper timing structure of the bunch crossings as they are in the LHC, i.e. some bunches are separated by more than 50 ns. The results of the digitization are then simulated samples with the effect of pileup included in a way similar to how it affects recorded data.

CHAPTER 4
Physical Object Reconstruction

This chapter treats the topic of the association of signals measured by the ATLAS detector to physical objects, such as photons and jets, and the determination of their kinematics. This reconstruction procedure includes the calibration of the kinematic quantities, which ensures that they are not biased and that the simulated samples describe appropriately the recorded data. The reconstruction algorithms are adjusted to account for the larger amount of pileup in 2012 compared to the LHC nominal value, which amounts to a larger amount of activity in the detector and higher noise levels. The first section presents the reconstruction of objects that are themselves used as input to other reconstruction algorithms. The second section presents the reconstruction of photons. The third and last section explains how jets are reconstructed and how b quarks are identified.

4.1 Intermediate Objects

The reconstruction of the photon and jet objects that are to be analyzed for the measurement of the $\gamma + b$ production cross section is in most cases not directly performed on the detector signals, such as the position measurements from the trackers and the energies in the calorimeter cells. Rather, they are performed on intermediate objects, which are themselves reconstructed out of the detector signals.

Such intermediate objects are reconstructed in both the tracking system, that is tracks and primary vertices, and in the calorimeters, the topological cell clusters.

4.1.1 Tracks

The reconstructed trajectories of charged particles, based on the combination of position measurements, are called tracks. In the Inner Detector, due to the solenoidal magnetic field, the trajectories of charged particles describe a circular motion in the plane transverse to the z-axis. The z-component of the trajectories is not affected since it is parallel to the magnetic field and thus has no Lorentz force acting on it. The overall motion of the charged particles is that of a helix. A parameterization of this motion can be given as a function of five parameters: d_0, z_0, ϕ, θ and q/p. These parameters are evaluated at the perigee, which is the point of the trajectory that is closest in the transverse plane to a reference point, for example the origin. The first and second parameters are the values of the distance between the perigee and the reference point projected respectively onto the transverse plane and the z-direction, i.e. the impact parameters. The next two parameters are the angles of the vector momentum. The last parameter is the ratio of the electric charge of the particle to the magnitude of its momentum, which is related to the curvature of the trajectory.

A typical charged particle in the Inner Detector will hit three pixel layers, eight microstrip layers and about 36 drift tubes. As hundreds of particles are produced in an event, considering pileup conditions, hundreds of tracks can be reconstructed. In practice, because of the high number of hits, the number of possible tracks that can be reconstructed is considerably larger, due to the misassignment of hits to tracks. To add

to the complexity, the trajectories of charged particles can be deflected due to multiple Coulomb scatterings with the detector material. Two procedures are employed to tackle the difficult task of reconstructing tracks that provide a precise description of the trajectories of the charged particles while avoiding tracks reconstructed by the wrong combinations of hits: inside-out and outside-in tracking [159].

Inside-out tracking The first procedure starts the track reconstruction from all possible track seeds of three hits in the silicon layers that satisfy some cuts on the transverse momentum and on the transverse impact parameter. The tracks are then built in the rest of the silicon detectors with a Kalman filter [160], an iterative algorithm that predicts what the parameters of the track will be at the next tracker layer, taking into account the effects of particle interactions with the detector material. The filter combines that prediction with the measured hit on that layer via a weighted mean to produce a statistically optimal estimate of the track parameters and of their covariance. The filter then iterates towards the next tracker layer. This filter is equivalent to a global least-square fit, but is computationally more efficient. Among all the silicon-only tracks produced, some will share hits. To remove tracks with incorrectly assigned hits, tracks are scored according to their precision and whether they cross layers without hits when hits are expected. Shared hits are associated to the higher-score tracks and tracks with a score below a given threshold are removed. The surviving tracks are then simply extrapolated to the TRT where compatible hits are added to the tracks. Finally, the tracks are refitted with the TRT hits.

Outside-in tracking The second procedure starts with TRT hits, removing hits associated to tracks from the first procedure. A Hough transform [161] is performed on the remaining TRT hits. This transform scans the possible values for the track parameters and counts the number of tracker hits that are compatible with those values. Maxima in the parameter distributions are used to identify TRT tracks. The tracks are then extrapolated to the silicon layers, where compatible hits are added to the tracks, and refitted.

The first procedure is the main one for reconstructing tracks. However, some particles will travel a short distance in the Inner Detector, such that they might interact with too few silicon layers and thus not create seeds for the first procedure. The second procedure, which is not based on silicon seeds, is used to recover their reconstruction.

The presence of pileup produces additional hits in the Inner Detector. Tracks from a combination of hits not associated to the passage of a charged particle are more likely to be reconstructed. To reduce this possibility tracks can be required to have at least nine hits in the silicon layers and to have no missing hits in the pixel layers when hits are expected. The track reconstruction efficiency with these selection criteria is approximately 80% in the central region and 70% in the forward region [162].

Given a track describing a circle of radius R in the transverse plane under a uniform magnetic field B, the transverse momentum associated to the track can be found, via the description of the circular motion due to the Lorentz force, to be

$$p_{\mathrm{T}} = qBR. \tag{4.1}$$

In the case of particles whose electric charge is the fundamental electric charge, $q_e = \sqrt{4\pi\alpha} \approx 0.3$, and assuming a value $B = 2$ T ≈ 2 GeV/m, this equation becomes

$$p_{\mathrm{T}} \approx R \times 0.6 \frac{\mathrm{GeV}}{m}. \tag{4.2}$$

Therefore, the trajectory of a charged particle produced on the z-axis with $p_{\mathrm{T}} < 0.4$ GeV will significantly bend and never exit the Inner Detector, since the solenoidal magnet is located at a distance of about 1.2 m.

The relative transverse momentum resolution depends on the number of measured track hits, N, and it is given by [163], for a particle with an electric charge equal to the fundamental electric charge,

$$\frac{\sigma(p_{\mathrm{T}})}{p_{\mathrm{T}}} \approx \sqrt{\left(\frac{A_N p_{\mathrm{T}} \sigma_{R\phi}}{0.3BL^2}\right)^2 + \left(\frac{0.045 \text{ GeV}}{B\sqrt{LX_0}}\right)^2}, \tag{4.3}$$

where A_N is a statistical factor depending on N, with $A_N = \sqrt{720/(N+4)}$ for $N \to \infty$, $\sigma_{R\phi}$ is the hit position uncertainty in the transverse plane and L is the length of the track. The first term is the contribution of the uncertainty related to the measurement of the track. The second term is the contribution related to the deflection due to multiple Coulomb scatterings. The first term dominates at high transverse momentum. In contrast to the relative energy resolution, which improves at higher energy, the relative resolution of the transverse momentum worsens with larger values of transverse momentum.

4.1.2 Primary Vertices

A primary vertex is the reconstructed object corresponding to the position of an inelastic proton–proton collision. Although the LHC beams are colliding at a nominal interaction point, due to the finite transverse area of the beams and to the finite length of the proton bunches, the proton–proton collisions occur in a region of space. This region is called the beam spot and has a size of about 15 μm in the transverse plane and about 50 μm in the z-direction [164]. Primary vertices are to be distinguished from secondary vertices, which represent the decays of particles and the interactions of particles with the detector material that produce new particles. Secondary vertices are separated from a primary vertex by a measurable distance in the transverse plane. Both types of vertices are reconstructed based on the information of reconstructed tracks.

The primary vertices are reconstructed in two steps [164]. The first step consists in a vertex reconstruction without any constraints on the coordinates of the vertices to be reconstructed. The goal of this step is to determine the position of the beam spot. Only a small subset of events are used. A second step of the vertex reconstruction is performed using the position of the beam spot to constrain the coordinates of the vertices.

The vertex reconstruction begins by the identification of a vertex seed. This seed is determined by the transverse position of the beam spot and, for the z-coordinate, by the most frequent value of the z-coordinates of the tracks, evaluated at the perigee with respect to the center of the beam spot. An adaptive iterative least-square fitting

procedure [165] is then performed. In each iteration, tracks are weighted. The weights are defined as a continuous monotonic function of the distance between a track and the vertex. The vertex position is calculated using the weighted tracks and a new iteration of the fitting procedure begins anew. The smoothness of the weight function is reduced in each iteration to approach ultimately a step function. This procedure makes it possible to remove outlying tracks from the fit. After a given number of iterations, tracks still compatible with the vertex are associated to it and are removed from the pool of tracks. The whole procedure is repeated with the remaining tracks. This occurs until all tracks are associated to vertices or no additional vertex can be produced. Vertices with at least two associated tracks are taken to be the primary vertices. The track selection criteria based on the number of silicon hits, discussed in the previous section, eliminates the reconstruction of primary vertices that do not correspond to an actual pp collision.

Tracks associated to a primary vertex are refitted taking as reference point the position of their reconstructed vertex. Among all reconstructed primary vertices in an event, the vertex chosen to correspond to the hard scattering process is the one with the largest value of $\sum p_{\mathrm{T}}^2$, where the sum runs over the associated tracks and the transverse momentum refers to that of the tracks. This selected vertex is referred to as the hard vertex of the event. The combined efficiency of the reconstruction of primary vertices and of the selection of the hard scattering among them is stable with respect to the level of pileup and is above 99% within typical detector acceptance used in physics analyses [164].

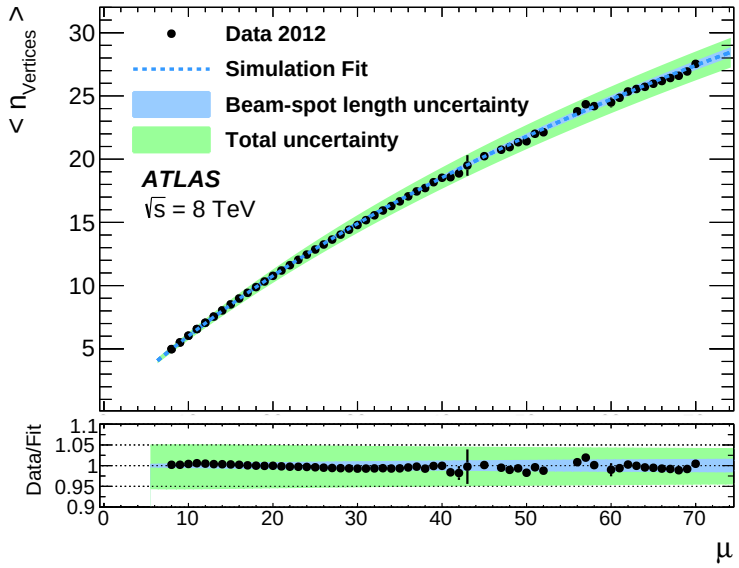

Figure 4–1 – Dependence of the average number of reconstructed primary vertices on the level of pileup [164]. The simulation fit refers to a fit to the MC distribution with values of μ scaled by 1.11.

A larger number of pp collisions in an event reduces the average distance between them. Collisions that are too close to each other to be resolved are reconstructed as a single, merged primary vertex. For this reason, the number of reconstructed primary vertices is smaller than the number of pileup interactions. Furthermore, the dependence of the average number of primary vertices as a function of the pileup is different between data and the detector simulation. This difference is due to the length of the beam spot along z being longer in the simulation, leading to fewer merged vertices. A multiplicative correction factor of 1.11 is applied to the value of μ in the simulated events of the MC samples to bring their distribution in agreement with that of the data [164]. Figure 4–1 shows the agreement between the data and the simulation after the correction.

4.1.3 Topological Cell Clusters

The topological cell clusters are collections of calorimeter cells assembled in three dimensions based on the energy measured in each individual cell of the calorimeters. [150]. These clusters are built in order to reduce the effect of the both electronic and pileup noise on the energy measurement of showers in the calorimeters. Furthermore, they allow for an energy calibration that depends on cluster properties.

Topological clusters are built from individual calorimeter cells according to the energy significance of the cells, i.e. the ratio of the cell signal, E_{cell}, to the expected cell noise, σ_{cell}. The expected noise per cell is given in Figure 3–7. The clusters are seeded by cells for which the significance satisfies $|E_{\text{cell}}|/\sigma_{\text{cell}} > 4$. All neighbouring cells to a seed are added to the cluster. The neighbouring cells are defined as those being adjacent in a given calorimeter layer or, if in different layers, as overlapping in (η, ϕ). Cells can be neighbours across different calorimeter subsystems. If a neighbouring cell to a seed satisfies $|E_{\text{cell}}|/\sigma_{\text{cell}} > 2$, all of its neighbouring cells are also added to the cluster. This process is repeated until no neighbouring cells satisfy that significance requirement. As a last step, all neighbouring cells to the cells in the cluster are added to the cluster, irrespective of their significance. If multiple cells corresponding to local energy maxima are found in a cluster, the cluster is split to ensure that each reconstructed cluster only contains one energy maximum.

The clustering criteria on the cell energy significance are defined in terms of the absolute value of the cell energy in order to take into account cells with a negative energy. Negative values are possible due to fluctuations of the cell noise, mostly

caused by pileup fluctuations. These negative-energy cells are added to the cluster in order to compensate on average for positive noise fluctuations in other cells.

The kinematics of a topological cluster are defined by its energy and its angular position, i.e. (η, ϕ). The topological cluster energy is defined as the energy sum of the individual cells making up the cluster. The angular position of the cluster is calculated as the energy-weighted mean of the position of each cell in the cluster, as defined with respect to the center of the detector. A mass of zero is associated to the topological cluster in order to build a momentum four-vector.

Next, the topological cluster energy is calibrated. This is achieved by individually calibrating the energy of each cell in a cluster via a weighting of its energy. This calibration is referred to as a local cell weighting. The calibration corrects for the lower response of the calorimeters to hadronic showers, compared to electromagnetic showers, i.e. it corrects for the calorimeter non-compensation. The calibration also corrects for energy deposits measured outside of the clusters and for energy deposits not measured by the calorimeters. These corrections depend on the energy and the position of the considered cell and of its associated cluster. The corrections are derived from the signal response of neutral and charged pions in MC event samples. The neutral pion decays to two photons and thus produces an electromagnetic shower while the charged pion produces a hadronic shower in the calorimeters. As a result of this calibration procedure, the cluster energy is typically increased by roughly 50%. The (η, ϕ) position of the cluster is also recalculated after this calibration procedure is applied.

An electromagnetic shower caused by a single neutral pion produces typically one topological cluster while a hadronic shower caused by a single charged pion produces typically three topological clusters. This difference comes from the nature of hadronic showers, which are made up of a significant fraction of undetected energy due to strong interactions.

Topological clusters are used to quantify the amount of activity around a reconstructed photon and are used as input to jet algorithms.

4.2 Photon Object

Prompt photons are abundantly produced in proton–proton collisions due to the relatively high value of the electromagnetic coupling constant. Particles that are most often mis-reconstructed as photons are hadronic particles, which are observed as jets. The distinctive features in the detector of prompt photons are the absence of tracks in the Inner Detector, since they do not carry an electric charge, and the production of an electromagnetic shower. However, a complication in the measurement of photons occurs due to the non-negligible probability that a photon interacts with the detector material upstream of the calorimeter, thereby producing an electron–positron pair. These photons are called converted photons. Their reconstruction differs from photons that did not convert into an electron–positron pair, the unconverted photons. The reconstruction of photons and their identification via their shower properties are now discussed. Also discussed is the photon isolation, an additional photon identification requirement.

4.2.1 Photon Reconstruction

The photon reconstruction in the calorimeter is based on a sliding window algorithm searching for clusters of electromagnetic towers, which are projections of cells across the different layers of the electromagnetic calorimeter [166]. Topological clusters are not used since clusters of fixed size, provided by the sliding window, allow for a straightforward calibration of the photon energy [167]. The window has an initial size in $\Delta\eta \times \Delta\phi$ of about 0.075×0.125, corresponding to 3×5 cells in the second layer of the electromagnetic calorimeter. The energy of the cluster is defined as the sum of the energy of the cells composing the cluster. Clusters with an energy above 2.5 GeV are used as seeds for the next steps of the reconstruction. Tracks from the Inner Detector are considered matched to a seed if their position extrapolated to the second layer of the electromagnetic calorimeter lies within a given distance around the cluster center in (η, ϕ).

Converted photons are reconstructed by first reconstructing the secondary vertex at which the photon produced the electron–positron pair. The reconstruction of this vertex uses tracks matched to the cluster seed. A vertex fit is done for tracks that approach each other with a constraint that the tracks be parallel at the vertex, since photons are massless. Although in a photon conversion the electron and positron are collimated, they have opposite electric charges. Their trajectories will bend in opposite directions in the transverse plane. If the conversion occurs in the outermost layers of the Inner Detector, the electron and positron tracks will not be significantly deflected and the two tracks will be reconstructed as a single track. Therefore, converted

photons are separated into two categories: two-track and one-track conversions. One-track conversions can also happen due to an asymmetric conversion, in which one particle has significantly less energy than the other and ends up not being properly reconstructed. The position of the conversion vertex in those cases is taken to be at the first track hit. Selection criteria are imposed on tracks associated to conversion vertices, based on for example the number of track hits in the various tracker layers and the likelihood of the particle to be an electron as determined via the measured amount of transition radiation in the TRT. The selection criteria applied to tracks associated to single-track conversion vertices are more stringent in order to compensate for the inability to perform a secondary vertex fit.

If no tracks are matched to a calorimeter cluster seed, the cluster is classified as an unconverted photon. If the tracks associated to the conversion vertices are matched to a cluster seed, the cluster is classified as a converted photon. A possible ambiguity exists between photons and electrons produced in the hard scattering of the event, since both are defined by the presence of tracks and electromagnetic clusters. If an electron track is associated to the conversion vertex matched to a cluster, the cluster is identified as a converted photon. If the electron track is matched to a cluster but is not associated to a conversion vertex matched to the cluster, the cluster is classified as a converted photon only if the transverse momentum of the electron track is smaller than that of the tracks associated to the conversion vertex. Additional criteria are also used to resolve further the identification ambiguity between electrons and converted photons. These criteria are based on the ratio of the cluster energy to

the track momentum, the transverse momentum of the track and whether the track has hits in the silicon layers.

After the classification of the photon cluster, a reclustering is done on the electromagnetic towers with a window size that depends on the classification of the cluster and also if it is located in the barrel or in the end-caps. In the barrel, the sizes of the window correspond to 3×5 and 3×7 second-layer cells, for unconverted and converted photons respectively. The larger window size in ϕ used for the converted photons accounts for the opening angle between the electron and the positron due to the solenoidal magnetic field. In the end-caps, the size of the sliding window corresponds to 5×5 second-layer cells for both unconverted and converted photons.

If the photon is a converted photon and the tracks associated to the conversion vertex have hits in the silicon layer, its pseudorapidity and its azimuthal angle are based on those of the tracks. Otherwise, the values of pseudorapidity and azimuthal angle of the photon are based on those of the calorimeter cluster.

The photon reconstruction efficiency is shown in Figure 4–2. While the reconstruction of unconverted photons is close to 100%, the more difficult case of converted photons, with an efficiency of about 94%, brings down the overall photon reconstruction efficiency to around 98% [168]. The efficiency decreases at larger values of pseudorapidity due to the larger amount of detector material. The reconstruction efficiency of converted photons decreases for $p_{\mathrm{T}} > 150$ GeV, due to the electron and positron tracks becoming more collimated. The criteria on the reconstruction of single-track

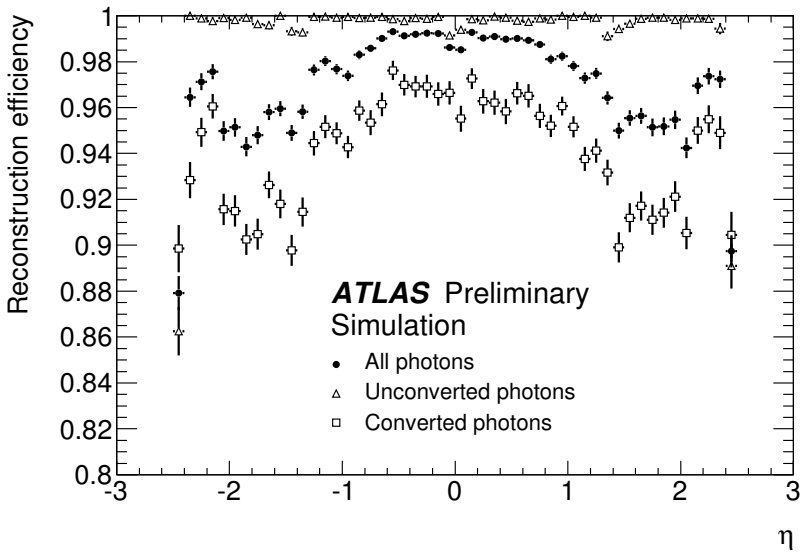

Figure 4–2 – Photon reconstruction efficiency as a function of the photon pseudorapidity [168].

conversion vertices become too stringent and the efficiency decreases. The overall photon reconstruction efficiency is about 90% for $p_{\mathrm{T}} = 1$ TeV [166].

Next, the energy of the photon cluster is calibrated. Without being calibrated, the energy of a photon cluster is shifted with respect to that of the corresponding particle prompt photon. The difference in the energy scales can be caused for example by energy lost in the material upstream of the calorimeter or by energy deposits in the calorimeter outside of the cluster. Additionally, the dispersion of the reconstructed energy with respect to the particle energy can be different between recorded and simulated photons. This difference in the energy resolutions can be caused for example by inhomogeneities in the response of the calorimeter cells. The calibration procedure is based on four steps and is applied to the photon energy in both recorded data

events and MC events [169]. The purpose of the steps differ between the two types of events. Their descriptions follow.

1. (a) For recorded events, to correct for different levels of energy response across the layers of the electromagnetic calorimeter, the responses of the layers are calibrated with respect to the simulation. An intercalibration of the responses of the first two layers of the electromagnetic calorimeter is performed using $Z \to \mu\mu$ decays, since muons are insensitive to the amount of material in front of the calorimeter. The response of the presampler is calibrated from electrons produced in W and Z decays, to understand the amount of material before the presampler and between the presampler and the first layer of the electromagnetic calorimeter. No calibration is performed for the third layer of the calorimeter as its contribution is negligible to the measured energies.

   (b) For MC events, a boosted decision tree (BDT) is trained based on cluster and track information to produce a calibration factor that brings the cluster energy to the particle photon energy. The training is done separately for converted and unconverted photons.

2. For recorded events, the BDT calibration is applied to the cluster energy. This is the main contribution to the photon energy calibration.

3. For recorded events, additional corrections for hardware effects that are not simulated are applied. The effects include high-voltage inhomogeneities in space and time, the widening of gaps between the different parts of the barrel

electromagnetic calorimeter due to gravity and the difference between the energy responses of medium- and high-gain amplifiers.

4. (a) For recorded events, the electron energy scale is shifted with respect to that in simulated events, as determined from $Z \to ee$ decays. A scaling correction is applied to the electron energy in data such that the electron energy scale matches that in the simulation. The same scaling correction is applied to the photon energy.

   (b) For MC events, the electron energy resolution is better than that in data, as determined from $Z \to ee$ decays. A Gaussian smearing correction is applied to the electron energy in the MC events in order for it to match the resolution in the recorded events. The same smearing correction is applied to the photon energy.

In the fourth step of the calibration procedure, the decays of Z bosons are used since the distribution of the invariant mass of the electron–positron pairs that they produce forms a well-described resonant peak. The position and the width of the peak allows for an absolute calibration of the energy scale and resolution between recorded and MC events. The calibration procedure is validated via the invariant mass distributions of $J/\psi \to ee$ decays for electrons and of radiative decays of the Z boson, $Z \to ee\gamma$ and $Z \to \mu\mu\gamma$, for photons.

The overall energy scale correction is typically within 5% of unity. The correction is independent of the amount of pileup since the energy response of the electromagnetic calorimeter is stable as a function of pileup at the 0.05% level [169]. Figure 4–3

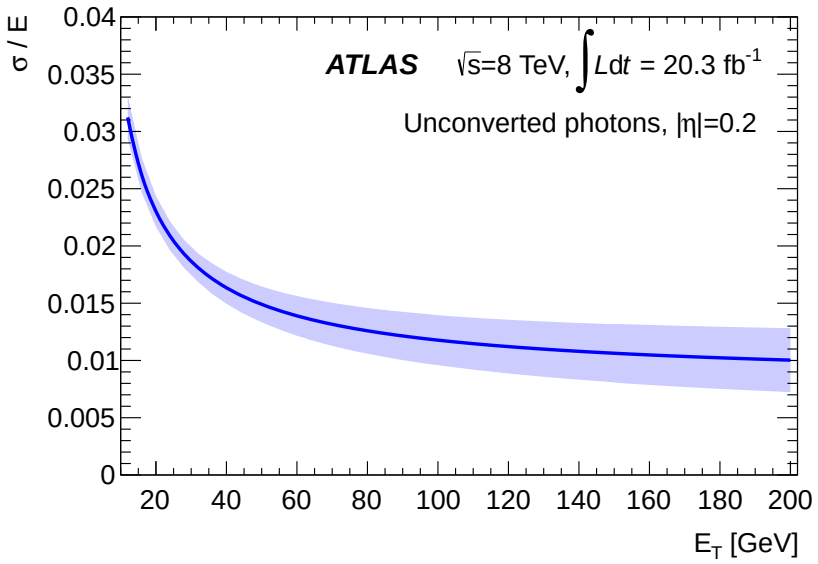

Figure 4–3 – Relative photon energy resolution as a function of the photon transverse energy for unconverted photons at $|\eta| = 0.2$ [169].

presents the energy resolution for unconverted photons, showing that it is smaller than 3% over the energy range investigated.

4.2.2 Photon Identification

The energy-calibrated photon cluster is required to be identified as a prompt photon. In comparison to the hadronic-shower background, created by hadrons, or jets, the electromagnetic shower of prompt photons is narrower and has a smaller portion of its energy in the hadronic calorimeter. Still, hadronic jets can be mis-reconstructed as photons in two ways. It can be that non-prompt photons, produced in hadron decays, inside jets carry a significant fraction of the jet energy, mimicking prompt photons as a result. Also, it can be that the distribution of the energy deposits in the calorimeters of the hadrons themselves is consistent with that of a prompt

photon. The former is the source of the majority of background photon clusters. An important subset of the non-prompt photon background comes from the π^0 mesons and other neutral mesons that decay into two photons. The energy they deposit exhibits two maxima in the first layer of the electromagnetic calorimeter due to the two photons, as long as the decay happens in the r–η plane, since the segmentation in ϕ is coarse. The fine segmentation along the pseudorapidity of the first layer enables this distinction between nearby maxima.

To distinguish prompt photons from the hadronic background, photon identification criteria based on the values of nine variables are used [166]. These variables describe the shape of an electromagnetic shower. Variables based on the information of strip cells of the first calorimeter layer mainly aim to reduce the background from neutral mesons. Variables based on the second layer, in which most of the electromagnetic energy is deposited, aim to test the compatibility of the width of the shower with the expected narrow width of electromagnetic showers, while an additional variable based on the hadronic calorimeter tests the length of the shower. The description of the variables follows.

- First electromagnetic calorimeter layer

  $\boldsymbol{F_{\text{side}}}$ Ratio of the energy contained in seven cells centered around the most energetic strip cell, $E(\pm 3)$, minus that in the central three cells, $E(\pm 1)$, to the energy in the central three:

$$F_{\text{side}} = \frac{E(\pm 3) - E(\pm 1)}{E(\pm 1)}. \tag{4.4}$$

$w_{s,3}$ Energy-weighted pseudorapidity width in units of strip cells, considering three cells along η centered around the most energetic strip cell:

$$w_{s,3} = \sqrt{\frac{\sum_i E_i (i - i_{max})^2}{\sum_i E_i}}, \tag{4.5}$$

where i is the identification number of the considered strip cell along η, i_{max} is the identification number of the most energetic strip cell and E_i is the energy of strip cell i.

$w_{s,tot}$ Energy-weighted pseudorapidity width in units of strip cells, similarly to $w_{s,3}$, but considering cells in a window of size about 0.06×0.2 in $\eta \times \phi$, corresponding to 20×2 strip cells in the barrel calorimeter, centered around the most energetic cell in the second layer.

E_{ratio} Ratio of the energy difference between the largest energy deposit in the strip cells, E_1^{max}, and the second largest energy deposit in the strip cells, E_2^{max}, to their energy sum:

$$E_{ratio} = \frac{E_1^{max} - E_2^{max}}{E_1^{max} + E_2^{max}}. \tag{4.6}$$

ΔE Difference in energy between the second largest energy deposit in the strip cells, E_2^{max}, and the smallest energy deposit that is located in-between the largest and second largest energy deposits in the strip cells, $E_{1,2}^{min}$:

$$\Delta E = E_2^{max} - E_{1,2}^{min}. \tag{4.7}$$

- Second electromagnetic calorimeter layer

  $\boldsymbol{R_\eta}$ Ratio of the energy contained in 3×7 cells of the second layer, $E_{3\times7}$, to the energy contained in 7×7 cells of the second layer, $E_{7\times7}$, in $\eta \times \phi$:

$$R_\eta = \frac{E_{3\times7}}{E_{7\times7}}. \tag{4.8}$$

  $\boldsymbol{R_\phi}$ Ratio of the energy contained in 3×3 cells of the second layer, $E_{3\times3}$, to the energy contained in 3×7 cells of the second layer, $E_{3\times7}$, in $\eta \times \phi$:

$$R_\eta = \frac{E_{3\times3}}{E_{3\times7}}. \tag{4.9}$$

  $\boldsymbol{w_{\eta 2}}$ Energy-weighted width in pseudorapidity, considering 3×5 cells of the second layer in $\eta \times \phi$:

$$w_{\eta_2} = \sqrt{\frac{\sum_i E_i \eta_i^2}{\sum_i E_i} - \left(\frac{\sum_i E_i \eta_i}{\sum_i E_i}\right)^2}, \tag{4.10}$$

  where i is an index that runs over all considered cells, η_i is the pseudorapidity coordinate of cell i and E_i is the energy of cell i.

- Hadronic calorimeter

  $\boldsymbol{R_{\mathrm{had}}}$ Ratio of the transverse energy deposited in the cells of the first layer of the hadronic calorimeter that are located in a region of 0.24×0.24 in $\Delta\eta \times \Delta\phi$ behind the photon cluster, $E_{\mathrm{T}}^{\mathrm{had,1}}$, to the transverse energy of the photon cluster, E_{T}:

$$R_{\mathrm{had}} = \frac{E_{\mathrm{T}}^{\mathrm{had,1}}}{E_{\mathrm{T}}}, \quad \text{for } |\eta| < 0.8 \text{ or } |\eta| > 1.37. \tag{4.11}$$

For photon clusters within the region $0.8 < |\eta| < 1.37$, the numerator of the ratio is taken to be the transverse energy deposited in the cells of the hadronic calorimeter that are located in a region of 0.24×0.24 in $\Delta\eta \times \Delta\phi$ behind the photon cluster, $E_{\mathrm{T}}^{\mathrm{had}}$:

$$R_{\mathrm{had}} = \frac{E_{\mathrm{T}}^{\mathrm{had}}}{E_{\mathrm{T}}}, \quad \text{for } 0.8 < |\eta| < 1.37. \tag{4.12}$$

Within the region $0.8 < |\eta| < 1.37$, this definition provides a better discrimination against hadronic showers compared to the former definition [168].

The distributions of these identification variables are given in Figure 4–4 for unconverted photons and in Figure 4–5 for converted photons. The distributions of these variables for jets, the main photon background, are also given. The distributions are similar between the unconverted and the converted photons, with the exception of R_ϕ. Converted photons have smaller values of R_ϕ than unconverted photons on average. The electron and the positron produced in a photon conversion get separated in ϕ by the magnetic field. This separation widens the shower shape along the ϕ-direction, decreasing the value of R_ϕ. Taken together, the distributions of these nine identification variables show the narrower and shallower nature of photon-initiated showers compared to jet showers.

Different sets of cuts on the values of the variables, with varying efficiencies and background rejection capabilities, have been devised. Cut values are optimized separately for unconverted and converted photons. Cut values also vary as a function of the photon cluster but are mostly independent of the transverse energy of the cluster.

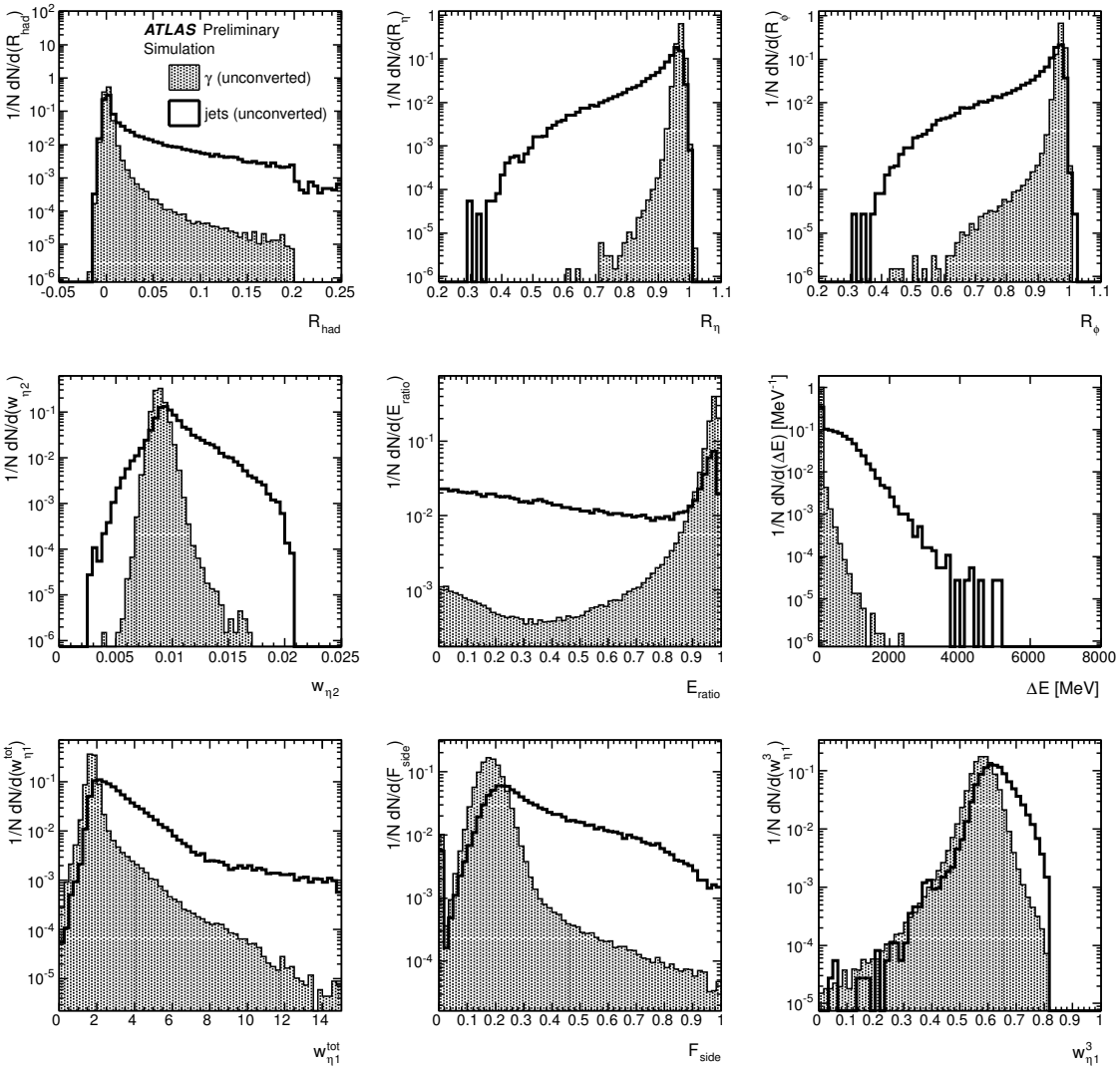

Figure 4–4 – Distributions of the photon identification variables for unconverted photons and jets [168]. The variables $w_{\eta 1}^{\mathrm{tot}}$ and $w_{\eta 1}^{3}$ in this figure correspond respectively to $w_{\mathrm{s,tot}}$ and $w_{\mathrm{s},3}$ in the text.

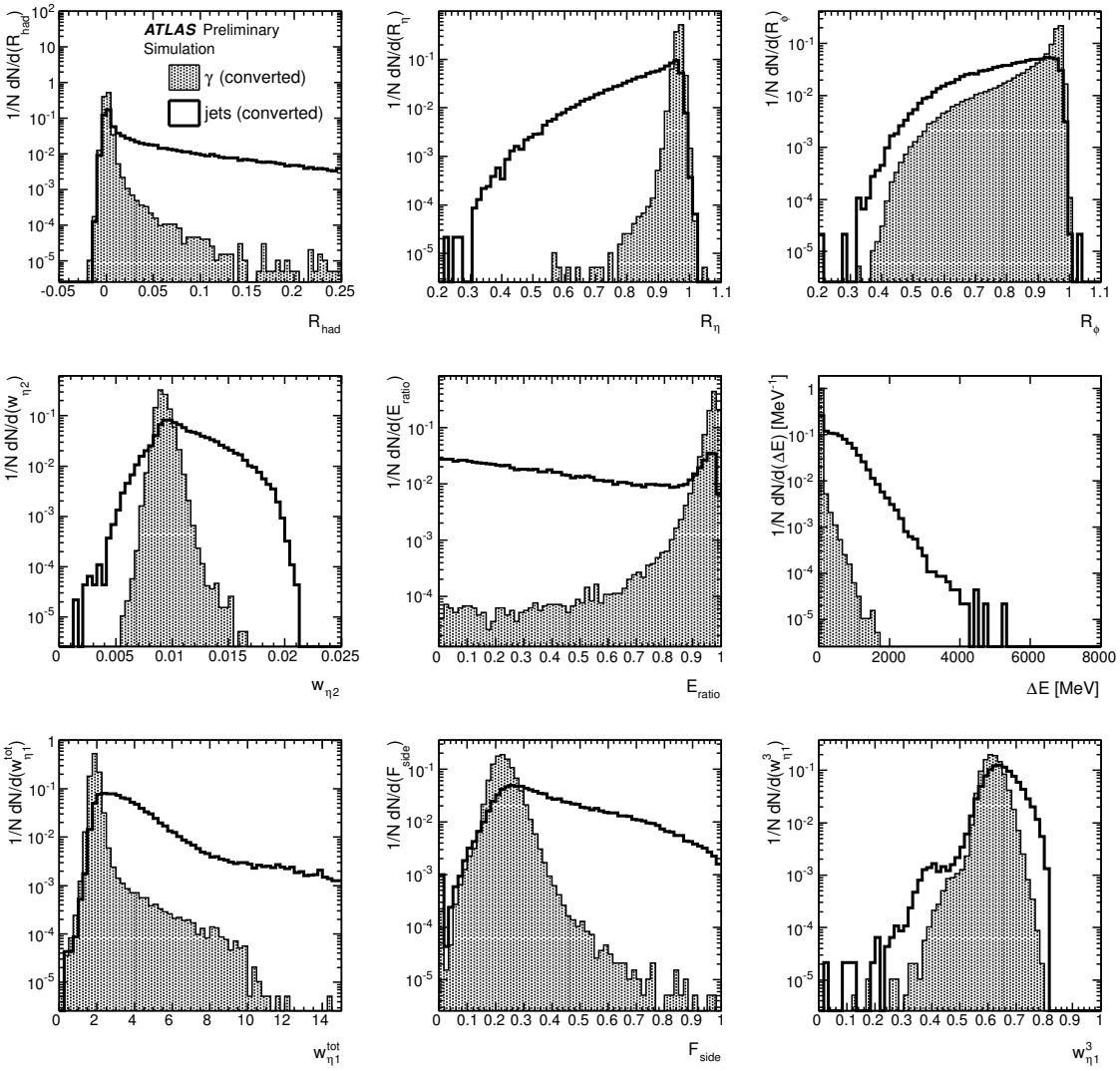

Figure 4–5 – Distributions of the photon identification variables for converted photons and jets [168]. The variables $w_{\eta 1}^{\mathrm{tot}}$ and $w_{\eta 1}^{3}$ in this figure correspond respectively to $w_{\mathrm{s,tot}}$ and $w_{\mathrm{s},3}$ in the text.

Two sets of cuts are primarily used, referred to as *tight* and *relaxed tight* [166]. Both of these have the same cut values. The tight definition cuts on all nine variables and corresponds to the strictest set of photon identification criteria. It has a jet background rejection factor of about 5×10^3 [168], i.e. only one out of about five thousand jets passes the cuts. An example of such a jet is one containing a neutral meson that is sufficiently boosted that the two photons produced in its decay become collimated and are reconstructed as a single photon. Similarly, the two photons can be reconstructed as a single one if the decay is along ϕ. The tight definition cannot distinguish these photons from prompt photons.

The relaxed tight set of cuts requires at least one failed cut on the four following variables: F_{side}, $w_{\text{s,3}}$, E_{ratio}, ΔE. Relaxed tight and tight are mutually exclusive due to the veto on at least one of these variables. The four variables on which a failed cut is required are chosen to be variables based on the information of the first calorimeter layer, in order to increase the probability that photons produced in the decay of neutral mesons satisfy the relaxed tight definition. As will be explained in Section 6.1, the relaxed tight set of photon identification criteria is used to further suppress the residual background of prompt photons. As the particular choice of these four variables is somewhat arbitrary, two variants of the relaxed tight definition are also used for the purpose of estimating the systematic uncertainty related to this choice. One variant is more stringent than the nominal relaxed tight definition and one variant is less stringent. Respectively, the two variants are defined by requiring that ΔE satisfies its cut value and by adding $w_{\text{s,tot}}$ to the list of possible variables on which a cut has failed. Table 4–1 summarizes all four identification definitions.

Table 4–1 – Description of the various photon identification definitions in terms of the discriminating variables defined in the text. A checkmark means that the variable must have passed its cut value. For a given photon identification definition, at least one of the asterisked variables must have failed its cut value.

Photon identification	F_{side}	$w_{\text{s,3}}$	$w_{\text{s,tot}}$	E_{ratio}	ΔE	R_η	R_ϕ	$w_{\eta 2}$	R_{had}
Tight	✓	✓	✓	✓	✓	✓	✓	✓	✓
Relaxed tight	*	*	✓	*	*	✓	✓	✓	✓
Relaxed tight (tighter)	*	*	✓	*	✓	✓	✓	✓	✓
Relaxed tight (looser)	*	*	*	*	*	✓	✓	✓	✓

Differences exist in the distributions of the discriminating variables between the data and the detector simulation. Corrective shifts are applied to the discriminating variables in the MC event samples to bring their distributions in closer agreement to the data distributions, that is the χ^2 between the two distributions is minimized. These shifts are binned as a function of transverse momentum and pseudorapidity and are different for unconverted and converted photons. The magnitudes of the shifts are typically 10% of the root mean squares of the distributions. After applying these shifts, differences remain in the tight photon identification efficiency between data and simulated events. Scale factors, defined as data-to-simulation efficiency ratios, $\epsilon^{\text{data}}/\epsilon^{\text{MC}}$, are measured in radiative decays of the Z boson. These scale factors are applied as event weights on the MC events such that the tight identification efficiency in the MC events agrees with that in the recorded events. They are binned in transverse energy and pseudorapidity and are different for unconverted and converted photons.

The effect of pileup on the tight identification efficiency and on the scale factors has been reduced by optimizing the cut values on the identification variables for the pileup conditions observed in 2012. For photons with $E_{\mathrm{T}} > 30$ GeV, the photon identification efficiency at $\mu = 25$ is approximately 5% lower than that at $\mu = 0$. However, the values of the scale factors are found not to strongly depend on the level of pileup, indicating that pileup effects are properly accounted for in simulation.

Figure 4–6 shows the tight photon identification efficiencies for photons produced in radiative decays of the Z boson. The efficiency increases as a function of the photon transverse energy since background contributions to the discriminating variables become less important relative to that of the photon. The scale factors are also shown. Their values are typically within 3% of unity. The photon identification efficiency shown in Figure 4–6 was measured after requiring that the isolation energy of the photon be less than 4 GeV. The definition of the isolation energy is the topic of the next section.

4.2.3 Photon Isolation

The photon transverse isolation energy, $E_{\mathrm{T}}^{\mathrm{iso}}$, referred to as the isolation energy, is the amount of energy deposited around the photon cluster. It is used in addition to the discriminating variables on the shower shape to reject further the background due to jets, as the wide physical dispersion of particles inside jets will increase this quantity. For example, jets in which photons carry most of the jet energy might pass the tight identification variables; however they will be accompanied by other particles. These

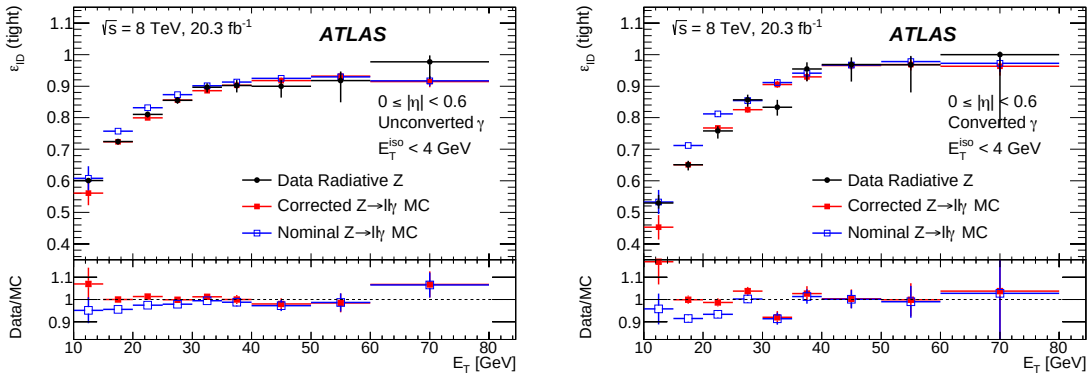

(a) (b)

Figure 4–6 – Tight photon identification efficiency measured in radiative decays of the Z boson as a function of the photon transverse energy in the region $0 < |\eta^{\gamma}| < 0.6$ for (a) unconverted and (b) converted photons [166]. The scale factors are given in the bottom panels. Efficiencies determined in MC $Z \to ee\gamma$ and $Z \to \mu\mu\gamma$ samples with and without the corrective shifts to the photon shower discriminating variables are also shown.

other particles will deposit energy in the calorimeter around the photons and increase the isolation energy.

The isolation energy is defined as the sum of the transverse energies of positive-energy topological clusters whose barycenters are located within an angular distance of $\Delta R = \sqrt{\Delta\eta^2 + \Delta\phi^2} = 0.4$ to the barycenter of the photon cluster. The energy falling within a window of size corresponding to 5×7 second-layer cells in $\eta \times \phi$ around the center of the photon cluster is subtracted from $E_{\mathrm{T}}^{\mathrm{iso}}$ to remove the contribution of the photon itself. Figure 4–7 illustrates the geometry of the definition.

The isolation energy is meant to be a measure of the activity around the photon cluster that comes from the hard scattering but that is not due to the photon. If the photon shower is wider than the 5×7 window, it contributes to the isolation energy.

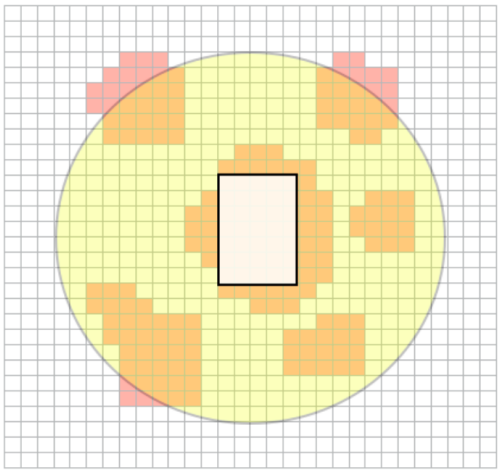

Figure 4–7 – Diagram of the definition of the photon transverse isolation energy. The grid corresponds to the granularity of the cells in the second layer of the electromagnetic calorimeter in the η–ϕ plane. The yellow circular region is the region in which the transverse energy is summed. The pink squares represent cells part of a topological cluster. The white rectangle represents the area in which the isolation energy is not summed.

Additionally, energy deposits from the pileup and the underlying event contribute to the isolation energy. Corrections to the isolation energy are used to subtract these contributions.

The correction for the leakage of the photon energy outside of the 5×7 window is derived by evaluating this effect in single-particle MC event samples. The value of this leakage correction increases with the photon transverse energy and is typically 5 GeV for photons with $E_{\mathrm{T}} = 400$ GeV.

Pileup and underlying-event contributions to the isolation energy are reduced via a correction based on the jet area subtraction method [170]. In short, the correction is derived by forming jets via the k_t algorithm [171, 172] with a parameter $R = 0.5$,

taking as input positive-energy topological clusters.[1] The median value among all the jets of the ratio of the jet transverse momentum to its angular area is taken to be the ambient transverse-momentum density. This procedure is performed in different pseudorapidity regions. The ambient transverse-momentum density is then multiplied by the area in which the isolation energy is measured, i.e. the circular area of radius $R = 0.4$ minus the central window, to obtain the correction. The typical size of this correction is 2 GeV.

Differences in the distribution of $E_{\mathrm{T}}^{\mathrm{iso}}$ between data and simulated events are observed. In the central region of the detector, the MC events have a shifted $E_{\mathrm{T}}^{\mathrm{iso}}$ distribution and, in the forward region, the distribution is additionally narrower. Shifts and smearing corrections are considered as a function of the photon transverse energy and pseudorapidity. Shifts are applied to the MC events in the central region, such that the χ^2 between the distributions in the recorded and MC events is minimized. For the forward events, shifts and Gaussian smearing corrections are applied in the same manner. The values of the shifts and of the standard deviations of the Gaussian smearing corrections are about 1 GeV.

4.3 Jet Object

The reconstruction of the b quark in the $\gamma + b$ event production can be done either by reconstructing the b hadron in which it hadronizes or the hadronic jet that it produces. The reconstruction of the b hadron is less efficient than the jet approach

[1]The k_t algorithm is defined in Appendix B.

since specific decay channels must be investigated. In turn, this low efficiency can potentially restrict the measurement in the regions where few events are produced. Additionally, the reconstruction and the theory predictions have to agree on the objects that are investigated. As only jet predictions are available at NLO in pQCD, the reconstruction of the b quark is done by reconstructing jets and identifying those that contain b hadrons. The details of these aspects are now treated.

4.3.1 Jet Reconstruction

Jets are reconstructed by using the anti-k_t algorithm [173] with a parameter $R = 0.4$ using as input positive-energy topological clusters.[2] Typically, about ten topological clusters are part of a jet [150]. The four-momentum recombination scheme is used, i.e. the four-momentum of the jet is the sum of the four-momenta of the topological clusters [174]. The anti-k_t algorithm is chosen to build jets since its performance is less dependent on the amount of pileup. This behaviour can be explained by the fact that the anti-k_t algorithm starts the jet formation with particles with large values of transverse momentum. The value for the parameter R is chosen to be large enough to encompass most of the jet energy deposited in the calorimeter, while still being small enough to reduce the sensitivity to the pileup contributions. Particle-level jets are built with the same algorithm as detector-level jets and with the same R parameter value. To build particle-level jets, the algorithm takes as input all long-lived particles,

[2]The anti-k_t algorithm is defined in Appendix B.

defined as particles with a lifetime longer than 10 ps, except muons and neutrinos since they do not deposit energy in the calorimeters.

Although the jet formation makes use of calibrated topological clusters, the energy scale of the jets is shifted with respect to that of particle jets. The difference can be caused for example by large pileup energy deposits that were included in the topological clusters and thus in the jets. A jet calibration is necessary to correct for this effect, among others, and to set the absolute jet energy scale. The jet calibration procedure has five steps [175], which are applied to both recorded and MC events, except for the last step which is only applied to recorded events. Each step of the jet calibration procedure is described below.

1. The direction of the reconstructed jet is defined with respect to the center of the detector since the directions of the topological clusters are also defined with respect to that position. The origin of the jet is changed to be the position of the hard vertex of the event. This is accomplished by redefining the pseudorapidities and azimuthal angles of the topological clusters such that their origin is the hard vertex. The jet direction is recomputed. Since the energies of the topological clusters are not modified, the jet energy is not modified either, but the jet transverse momentum does change.

2. The effect of the pileup is subtracted using the jet area method, similarly to the photon isolation, that is, by subtracting from the transverse momentum of the jet the product of the jet area and ambient p_{T} density. After this subtraction, a residual pileup dependence remains. An additional correction

is applied to mitigate this. It contains two terms, one proportional to the average number of interactions per bunch crossing and one proportional to the number of reconstructed primary vertices. The two proportionality constants are determined from MC samples. The correction is applied on the jet four-momentum.

3. The bulk of the jet calibration comes from an evaluation in MC samples of the jet energy response. The jet energy response is defined as the ratio of the energy of the detector-level jet to that of the geometrically matched particle-level jet. The response is measured as a function of the jet energy and pseudorapidity. The inverse of the response is applied to the reconstructed jet four-momentum as a calibration factor. Furthermore, an additive correction is applied to the jet pseudorapidity, which is obtained from the difference in pseudorapidities between detector-level jets and particle-level jets. This compensates for a possible bias due to differences in the calorimeter response in different regions of the calorimeters, such as the transition region between the barrel and the end-caps, which would make the jet direction point towards the region with the better response.

4. A global sequential calibration [176] is then applied to improve the jet energy resolution. The jet energy response is parameterised in terms of the jet energy, pseudorapidity and a global jet variable based on tracking information. A calibration factor proportional to the inverted response is then applied on the jet four-momentum. The proportionality constant is chosen such as not to change the average jet energy. This procedure is done sequentially for each

global jet variable. Those variables are, in order, the number of tracks associated to the jet, the p_{T}-weighted angular distance of a track from the jet axis for the tracks associated to the jet and the number of muon track segments in MDTs behind the jet.

5. For recorded events only, an absolute in situ calibration is applied [177, 178]. It is derived by measuring in data the ratio of the transverse momentum of the jet to the transverse momentum of a reference object: either another jet, a Z boson, a photon or multiple jets. In all cases, the average of the ratio measured in data is compared to that measured in the MC samples and their ratio is taken as the calibration factor on the jet four-momentum.

The overall energy scale correction is typically within 20% of unity. This value is larger than the correction of the photon energy scale, as is expected, since the response of the calorimeters to electromagnetic showers is higher than to hadronic showers.

The resolution of the jet energy is obtained in recorded events from in situ analyses. The jet energy resolution is related to the width of the distribution of the ratio of the transverse momentum of the jet to that of the reference object. In MC events, the resolution is taken to be the width of the distribution of the jet energy response. The resolution obtained in recorded events agree with that obtained in MC events. No further corrections are necessary.

Figure 4–8 shows the relative resolution of the jet transverse momentum in recorded events as a function of the jet transverse momentum. It can be seen that the relative resolution, which is at most 30% for $p_{\mathrm{T}} > 20$ GeV, is worse than the photon relative

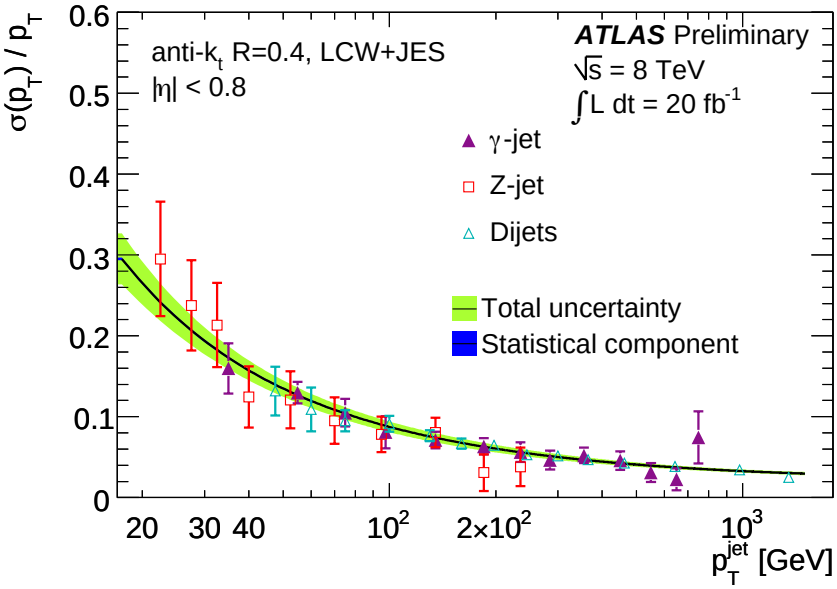

Figure 4–8 – Relative resolution of the jet transverse momentum as a function of the jet transverse momentum for jets in $|\eta| < 0.8$ that are built from topological clusters calibrated with local cell weighting (LCW) and that have a calibrated jet energy scale (JES) [175]. Equation 3.4 is fitted to the in situ measurements of the resolution.

energy resolution by about an order of magnitude. This is the reason why the $\gamma + b$ production cross section is measured as a function of the photon transverse energy and not as a function of the jet transverse momentum.

4.3.2 Jet Identification

Reconstructed jets can be produced in hard or pileup vertices. Most pileup jets have a small value of transverse momentum. To reduce the contribution of pileup jets in the low-p_{T} region, a quantity called the jet vertex fraction (JVF) [179] is used to distinguish the jets produced in the hard scattering from the pileup jets. The JVF takes as input two quantities, a jet and a vertex. It is defined as the ratio of the scalar sum of the transverse momenta of the tracks associated to the jet that comes

from the given vertex over the scalar sum of the transverse momenta of all tracks associated to the jet. As such, its value is between 0 and 1. The JVF value associated to the hard vertex will be small for pileup jets and large for jets produced in the hard scattering thus allowing to distinguish between them. If a jet has no tracks associated to it, its JVF value is -1.

4.3.3 *b*-tagging Identification

The b quarks hadronize into b hadrons within a timescale given by the perturbative QCD scale, Λ_{QCD}, corresponding to $O(10^{-24}$ s) or equivalently $O(1$ fm), which is too short to be measured by the detector. The b quarks are thus identified via the presence of b hadrons. The b hadrons decay via the strong or electromagnetic forces until a b hadron that decays via the weak force is produced.[3] These weakly decaying b hadrons decay via a W boson mostly to hadrons containing a c quark, due to the ordering of the values of the CKM matrix. In turn, these c hadrons decay strongly or electromagnetically until a c hadron that decays via the weak force is produced, which then decay weakly into hadrons containing s quarks, the hyperons, and similarly for them until stable hadrons with u and d quarks are produced.[4] The weak decays, due to the small effective coupling of the weak force, have a low probability of occurring. The lifetimes of the weakly decaying hadrons are longer than those of the hadrons

[3]The known weakly-decaying b hadrons are B^0, B^+, B_s^0, B_c^+, Λ_b^0, Ξ_b^0, Ξ_b^-, Ω_b^- and their antiparticles [54].

[4]The known weakly-decaying c hadrons are D^0, D^+, D_s^+, Λ_c^+, Ξ_c^0, Ξ_c^+, Ω_c^0 and their antiparticles [54].

that decay via the strong or electromagnetic forces. The weak b-hadron decays in particular are suppressed further due to the CKM matrix, since the b and c quarks are not in the same generation. The lifetime, τ, of weakly decaying b hadrons is $\tau \approx 10^{-12}$ s, to be compared to the weakly decaying c hadrons which have a lifetime of $\tau \approx 10^{-13}$ s and whose decays are not suppressed by the CKM matrix. The lifetime of these b hadrons is long enough that it allows them to travel a measurable distance away from the position of the hard scattering before decaying, which can be reconstructed as a secondary vertex. For example, a b hadron with an energy of 50 GeV will roughly have a Lorentz factor of $\gamma \approx 10$ in the reference frame of the detector and thus have a dilated lifetime of $\gamma\tau \approx 10^{-11}$ s, corresponding to a measurable distance of $\beta c\gamma\tau \approx 3$ mm between the primary vertex and the secondary vertex.

The b hadrons are identified by assigning a value to the reconstructed jets according to the likelihood that they contain a b hadron. This approach is called b-tagging. Jets can then be selected according to this value with an arbitrary efficiency.

The b-tagging identification relies on properties of the jet that emerge from the long lifetime and heavy mass of a weakly decaying b hadron to assign a b-jet likelihood weight to the jet. Figure 4–9 summarizes the different properties that are used. Some tracks associated to the jet will have large values for their impact parameter with respect to the primary vertex, since they will originate from the secondary vertex. The secondary vertex will have a large number of associated tracks and they will carry a significant fraction of the jet momentum, due to the mass of the b quark acting as a cutoff in the parton shower. For the same reason, the c hadron produced in the

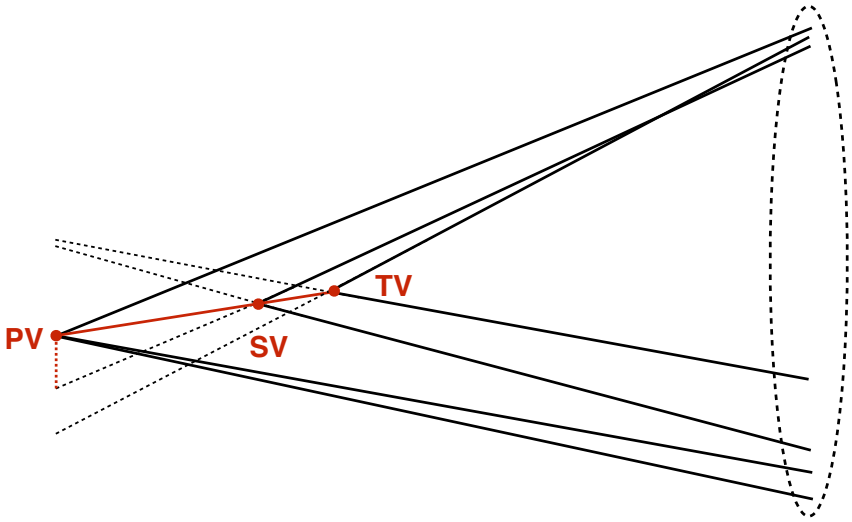

Figure 4–9 – Diagram of a b-jet and of the properties that can be used to perform b-tagging. The solid black lines represent the trajectories of charged particles and the red dots labelled PV, SV and TV represent respectively the primary, secondary and tertiary vertices. The dashed black lines represent the extrapolation of the trajectories to the primary vertex, with the red dashed line being an example of the impact parameter of one of the trajectories. The solid red line connecting the three vertices is the line of flight of the b and c hadrons.

decay of the b hadron will travel in the same direction as the b hadron. Therefore, a tertiary vertex, associated to the decay of the c hadron, will be present in a b-jet and will likely form a line with the primary and secondary vertices. This axis is referred to as the line of flight of the b hadron.

A b-tagging algorithm must assign a large weight to b-jets while assigning a low weight to other jets that form the background. Jets that do not contain b hadrons can contain c hadrons, the c-jets, or contain no b or c hadrons, the light jets. Another possible jet category are the τ-jets that can be reconstructed from the hadronic decays of τ leptons, however their contribution compared to the hadronic jets is in

general negligible. Although the light jets do not contain b or c hadrons, they can still contain secondary vertices due to particle interactions with the material or due to the presence of hyperons. The weakly decaying hyperons have lifetimes that can be longer than $\tau \approx 10^{-10}$ s and thus their decays also produce measurably displaced secondary vertices with respect to the primary vertex. However, they are less massive than b hadrons and do not have the same properties. Observable differences remain between the b-jets and the c- and light jets, such that the b-tagging is a viable approach.

In the MC samples at both the detector and the particle levels, the flavour of a jet is determined according to its associated hadron as follows. The jet is labelled as a b-jet if a b hadron with $p_{\mathrm{T}} > 5$ GeV is located within an angular distance of 0.3 of the jet axis. The jet is labelled as a c-jet if no such b hadron is found but a c hadron with $p_{\mathrm{T}} > 5$ GeV is located within an angular distance of 0.3 of the jet. The jet is called a τ-jet if no b or c hadrons are found but a τ lepton with $p_{\mathrm{T}} > 5$ GeV is located within an angular distance of 0.3 of the jet. If none of those particles are found, the jet is called a light jet. The requirement of 5 GeV on the transverse momentum of the particles reduces the infrared effects related to the presence of low-p_{T} b or c hadrons.

An algorithm that can be used for the b-tagging of jets is MV1 [180]. It is an artificial neural network based on the output of three simpler b-tagging algorithms: IP3D [180], SV1 [180] and JetFitter [180].[5] These are all algorithms making use of the properties of jets emerging from the long lifetimes and heavy masses of the weakly decaying b

[5]The details of the IP3D, SV1 and JetFitter algorithms are given in Appendix C.

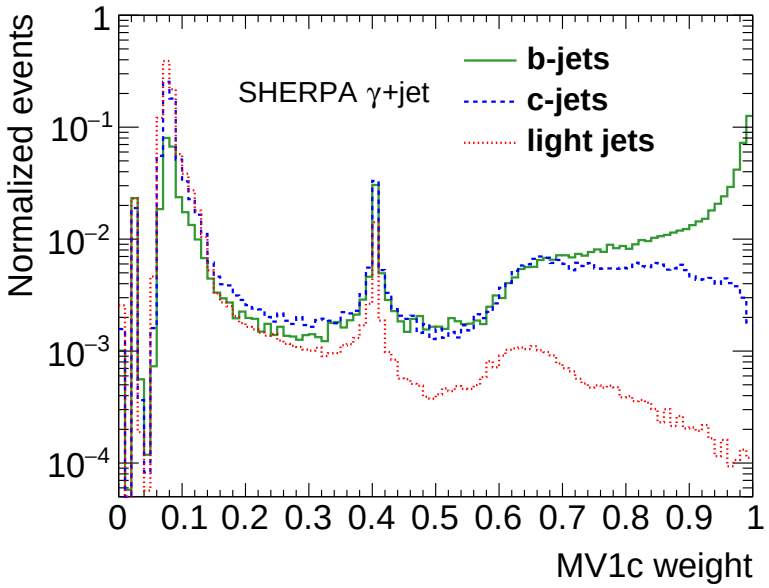

Figure 4–10 – Normalized distribution of the MV1c weight for b-, c- and light jets in γ + jet SHERPA events.

hadrons. The MV1 algorithm is trained on MC events to discriminate b-jets against light jets. A variation of this algorithm, called MV1c, is trained to discriminate b-jets against both c-jets and light jets. It is the MV1c algorithm that is used for b-tagging in the measurement of the $\gamma + b$ production.

The output of the MV1c algorithm is a tagging weight that is normalized to a unit integral and goes from 0 to 1. The distributions of the MV1c tagging weight for the three jet flavours are shown in Figure 4–10. Its b-jet identification power can be seen at large weight values. The peak around the value of 0.4 is associated to jets in which no secondary vertex could be reconstructed and the spikes close to the value of 0 correspond to jets which have no associated tracks satisfying the selection criteria of the algorithms.

Table 4–2 – MV1c weight values above which the integrated MV1c distribution corresponds to the working-point b-jet tagging efficiencies.

MV1c weight	Efficiency [%]
0	100
0.4051	80
0.7068	70
0.8349	60
0.9195	50
1	0

A b-jet b-tagging efficiency can be associated to an MV1c weight simply by integrating the b-jet MV1c distribution from that weight value up to 1, since the distribution is unit-normalized. The MV1c weight values corresponding to predetermined b-tagging efficiency values of approximately 80%, 70%, 60% and 50%, and the trivial 100% and 0% values, are listed in Table 4–2. These specific weight values are called working points and jets that have a weight value larger than that of a given working point are said to be tagged. The efficiency of a working point is only an approximation. The value of the actual efficiency depends on the event selection, with the pre-determined values corresponding to a simulated $t\bar{t}$ event sample. In such an event sample, the rejection factors for c- and light jets are respectively about 5 and 120 at the 70%-efficiency working point.

Although a b-tagging efficiency can easily be associated to the MV1c weight, differences are observed between the efficiencies obtained in MC events and those obtained in data events. A calibration is required for them to agree. For each jet flavour, data-to-simulation efficiency scale factors have been measured in an analysis of recorded and

simulated events. These scale factors are applied as event weights on the MC events to bring the b-tagging efficiency in the MC events to the level of that in the recorded events, similarly to the scale factors discussed in Section 4.2.2. These scale factors depend on the jet transverse momentum, and also on the jet pseudorapidity for the light-jet scale factors. They are measured for the working points listed in Table 4–2. The calibration analyses are described below.

***b*-jets** The b-jet calibration analysis uses a maximum likelihood fit to extract the b-jet b-tagging efficiency distribution in data [181]. It uses a $t\bar{t}$ selection in which most selected jets are b-jets. It performs the fit on those jets, using probability density functions of the MV1c weight taken from MC events for the c- and light jets. The b-jet probability density function of the MV1c weight is the quantity fitted. Once obtained, it can then be integrated from a given weight value up to 1 to obtain the corresponding b-tagging efficiency.

***c*-jets** The c-jet calibration analysis explicitly reconstructs D^{*+} mesons, or the antiparticles, in the jets of multijet events [182]. The c-jet b-tagging efficiency is extracted from the simultaneously fitted yields of D^{*+} mesons in jets that are tagged and in those that are not. Since b hadrons can also produce D^{*+} in their decays, a template fit to subtract the background due to b-jets is performed using the pseudo-proper time of the meson as the observable. The templates are built from physics arguments related to the decay times of the mesons. The c-jet b-tagging efficiency measured this way is restricted to c-jets containing D^{*+}. An extrapolation based on the experimental values and on the predictions of the EvtGen [183] MC event generator of the production and branching

fractions of the c hadrons is performed to obtain the efficiencies for inclusive c hadrons.

Light jets The light-jet calibration analysis employs the negative-tag method in multijet events [182]. Light jets are tagged as b-jets mainly due to the finite tracking resolution, which affects the sign of the impact parameter of the tracks and the sign of the decay length of the reconstructed vertices. This method reverses the sign of these two quantities in the algorithms. The weight distribution of this modified MV1c weight for all jet flavours is similar to that of the original MV1c weight for light jets. Consequently, the b-tagging efficiency of all jets in data using this modified MV1c weight is taken as the light-jet b-tagging efficiency. The MC samples are used to correct the measured efficiency in data for effects that are not related to the tracking resolution, for example the contamination of b and c hadrons, hyperons and material interactions.

The b-tagging efficiencies are measured for jets with transverse momenta up to $p_{\mathrm{T}} = 300$ GeV for the b- and c-jets and up to $p_{\mathrm{T}} = 750$ GeV for the light jets. A lack of events prevents the accurate measurement of efficiencies above these values. Furthermore, the light-jet efficiencies are measured in two different regions: $|\eta| < 1.2$ and $1.2 < |\eta| < 2.5$. This is motivated by the different amount of material in the Inner Detector in these two regions, which can cause a different amount of material interactions and thus change the light-jet efficiency. The values of the b-tagging efficiency scale factors for all three jet flavours are within 30% of unity.

For the measurement of the $\gamma + b$ production cross section, a special form of the b-tagging calibration is used, referred to as the continuous calibration. The difference with the standard working-point calibration is that no jets are tagged by requiring them to have a larger MV1c weight value than that of the working point. Instead, the complete MV1c weight distribution is used. In particular, the MV1c weight distribution can be separated into bins whose boundary values correspond to the working points.

The b-jet calibration analysis, which measures the efficiency via the integral of the b-jet probability density function, is easily adapted to the case of the continuous calibration. The boundaries of the integral are simply changed to match the various working points. The integral between the boundaries then gives the efficiency for a particular MV1c weight bin.

The continuous calibration for the c- and light-jet scale factors is done using a different approach. As the MV1c weight distribution is normalized to unity and bounded by 0 and 1, the scale factors are correlated across the MV1c bins. However, since working points are simply lower bounds on the MV1c weight, a simple relation can be used to derive scale factors in an MV1c bin delimited by the working points i and $i+1$, SF'_i, from scale factors measured at a working point i, SF_i:

$$\mathrm{SF}'_i = \frac{\epsilon_i^{\mathrm{MC}}\mathrm{SF}_i - \epsilon_{i+1}^{\mathrm{MC}}\mathrm{SF}_{i+1}}{\epsilon_i^{\mathrm{MC}} - \epsilon_{i+1}^{\mathrm{MC}}} = \frac{\epsilon_i^{\mathrm{data}} - \epsilon_{i+1}^{\mathrm{data}}}{\epsilon_i^{\mathrm{MC}} - \epsilon_{i+1}^{\mathrm{MC}}}. \tag{4.13}$$

In this relation, i goes from 1 to $N-1$ and represents the working points in decreasing order of efficiency, i.e. $\epsilon_1^{\mathrm{MC}} = 1$ and $\epsilon_N^{\mathrm{MC}} = 0$, with N being the number of working points and with $N = 6$ for MV1c. The second equality comes from the definition of

the scale factor at a working point, $\mathrm{SF}_i = \epsilon_i^{\mathrm{data}}/\epsilon_i^{\mathrm{MC}}$. Although the first equality is the one used technically, the second one shows that the definition of a scale factor in an MV1c bin is equivalent to the definition of a scale factor at a working point: it is the data-to-simulation ratio of tagging efficiencies for events in a range of the MV1c weight. This type of calibration is referred to as the pseudo-continuous calibration, since the efficiency has not been measured directly in a continuous manner, as in the case of the b-jets. Despite its look, it is not an iterative process as the information for any SF_i' is readily available. By construction, it ensures a similar correlation across the bins as for the continuous calibration and also ensures the boundaries at 0 and 1. The values of the scale factors for the continuous calibration are similar to that of the working points.

CHAPTER 5
Event Selection

This chapter explains how the reconstructed and calibrated physical objects are used to select events in which a photon and a jet are produced. The measurement of the number of $\gamma + \text{jet}$ events leads to the measurement of the $\gamma + b$ production cross section when used in conjunction with a measurement of the integrated luminosity. Furthermore, the measurement of the cross section requires a knowledge of how the detector-level event selection compares to the fiducial phase space of the cross section at particle level. To this end, simulated samples of the signal $\gamma + b$ process are necessary. The detector-level event selection is applied to simulated $\gamma + b$ events in conjunction with a particle-level selection that defines the fiducial phase space of the cross-section measurement. The first section of this chapter describes the simulated signal samples. The second section lists the different detector-level selection criteria. The third section does the same for the particle-level selection.

5.1 Simulated Signal Samples

Simulated samples of the production of prompt photons from Sherpa and Pythia are necessary to measure the $\gamma+b$ production cross section in proton–proton collisions. The specific simulated samples that are used for the measurement are generated in the way explained in Section 2.3.3 and are interfaced to a simulation of the ATLAS

detector as detailed in Section 3.3.2. Since these samples contain $\gamma + b$ events, they are signal MC samples.

Background MC samples consist of events containing mainly jets. However, due to the high rejection factor of the tight photon identification criteria, only one out of about five thousand jet events would pass these criteria and be suitable for an analysis of background events. This has the implication that most of the computer processing time necessary to generate, simulate, digitize and reconstruct events would not be useful from a physics point-of-view. For this technical reason and since they are not strictly necessary for the measurement of the cross section, the use of background MC samples is not considered further.

The SHERPA sample is taken as the nominal simulated sample. Most studies of the signal that require a knowledge of the particle-level information are performed with this sample. The choice of this sample over the PYTHIA sample stems from the observation that SHERPA provides an overall better description of the inclusive production cross section of prompt photons in pp collisions at $\sqrt{s} = 8$ TeV [35]. The PYTHIA sample is used to provide a comparison point to the studies performed with the SHERPA sample, allowing to test the differences in the non-perturbative QCD models. Additionally, the PYTHIA sample approximates the production of fragmentation photons via the emission of bremsstrahlung photons in the parton shower. The fragmentation and the direct photons are associated to different matrix elements. The events with fragmentation photons can be distinguished from those with direct photons. The possibility of this distinction enables the investigation of

the impact of the relative contribution to the $\gamma + b$ production of the fragmentation photons in comparison to that of the direct photons.

The production cross section of prompt photons steeply decreases as a function of the photon transverse momentum, spanning several orders of magnitude at the energy scales accessible with the LHC [35]. To generate efficiently events with large values of photon transverse momentum, p_{T}^{γ}, the SHERPA and PYTHIA samples are each divided into different individual samples. These individual samples each have a different requirement on the minimum p_{T}^{γ} value of the event. This requirement acts as a filter on the generation of events. A luminosity event weight, w_{lumi}, is applied to each sample to reconstruct a smooth physical p_{T}^{γ} spectrum representative of the recorded events. The weight is based on the integrated luminosity of the data and also on the cross section and the number of generated events associated to a filtered sample. A lower boundary on p_{T}^{γ} is applied at particle level after the generation to avoid any filter inefficiency. Furthermore, an upper boundary on p_{T}^{γ} is applied at particle level after the generation to avoid the double counting of events between the filtered samples. In addition to the p_{T}^{γ} filter, a filter based on the presence of b hadrons is used for the SHERPA samples to increase the number of events with b hadrons. The reconstruction of the smooth spectrum from the combination of the different filtered sample is referred to as the stitching of the samples.

Table 5–1 lists the requirements of the various p_{T}^{γ} filters used in the SHERPA and PYTHIA samples and the corresponding particle-level cuts on p_{T}^{γ} that ensure an efficient filter and no double counting of events. Figure 5–1 shows the weighted spectra of the SHERPA samples as a function of the particle-level p_{T}^{γ} before and after

Table 5–1 – Requirements on the photon transverse momentum imposed by the filters and the boundaries defining the p_{T}^{γ} ranges in which the associated filters are used at particle level. The two values for the lowest-threshold filter correspond to SHERPA and PYTHIA respectively.

Filter [GeV]	Particle-level boundaries [GeV]
$p_{\mathrm{T}}^{\gamma} > 15$ or 17	$25 < p_{\mathrm{T}}^{\gamma} < 55$
$p_{\mathrm{T}}^{\gamma} > 35$	$55 < p_{\mathrm{T}}^{\gamma} < 105$
$p_{\mathrm{T}}^{\gamma} > 70$	$105 < p_{\mathrm{T}}^{\gamma} < 200$
$p_{\mathrm{T}}^{\gamma} > 140$	$200 < p_{\mathrm{T}}^{\gamma} < 400$
$p_{\mathrm{T}}^{\gamma} > 280$	$400 < p_{\mathrm{T}}^{\gamma} < 650$
$p_{\mathrm{T}}^{\gamma} > 500$	$650 < p_{\mathrm{T}}^{\gamma} < 1100$
$p_{\mathrm{T}}^{\gamma} > 800$	$1100 < p_{\mathrm{T}}^{\gamma}$

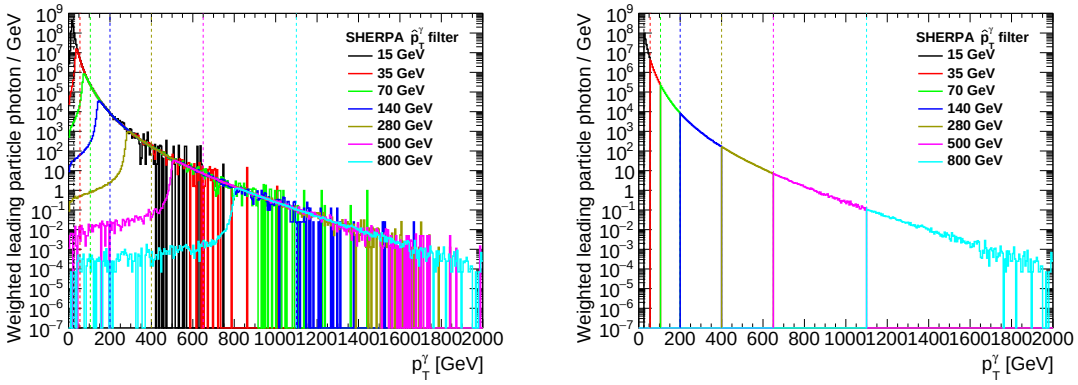

(a) (b)

Figure 5–1 – Weighted number of leading particle-level photons as a function of the particle-level photon transverse momentum in the generated SHERPA filtered samples (a) without particle-level cuts and (b) with particle-level cuts. The vertical dashed lines represent the values of the particle-level cuts. The symbol $\hat{p}_{\mathrm{T}}^{\gamma}$ in the legend indicates that the photon filter is applied at parton level.

stitching the different filtered samples together. A smooth spectrum is reconstructed after the stitching procedure. Similar weighted spectra are obtained with the PYTHIA samples. In the case that an event contains more than one photon, only the photon with the largest value of p_{T}^{γ}, i.e. the leading photon, is considered.

The properly normalized number of events in a given p_{T}^{γ} bin, N'_{bin}, of the smoothly falling p_{T}^{γ} distribution is related to the number of simulated events in that bin, N_{bin}, via

$$N'_{\mathrm{bin}} = \sum_{i=1}^{N_{\mathrm{bin}}} w^{i}_{\mathrm{lumi}} = w_{\mathrm{lumi}} N_{\mathrm{bin}}, \tag{5.1}$$

where the sum runs over all events contributing to that bin and where w^{i}_{lumi} is the luminosity weight of event i. With the application of particle-level cuts in the reconstruction of the expected smoothly falling spectrum of events, all events within a given p_{T}^{γ} bin come from the same filtered sample and thus have the same weight, w_{lumi}. The number of simulated events in a given bin is a random process that follows a Poisson distribution. Therefore, the statistical uncertainty in N'_{bin}, $\Delta N'_{\mathrm{bin}}$, is that of a sum of weighted independent Poisson distributions of mean one, which is

$$\Delta N'_{\mathrm{bin}} = \sqrt{\sum_{i=1}^{N_{\mathrm{bin}}} (w^{i}_{\mathrm{lumi}})^2} = \sqrt{w^{2}_{\mathrm{lumi}} N_{\mathrm{bin}}} = w_{\mathrm{lumi}} \sqrt{N_{\mathrm{bin}}}. \tag{5.2}$$

The statistical uncertainty, ΔN_{bin}, in the number of simulated events in a particular p_{T}^{γ} bin is the standard deviation of a Poisson distribution of mean N_{bin}, i.e. $\Delta N_{\mathrm{bin}} = \sqrt{N_{\mathrm{bin}}}$. As can be seen, the relative statistical uncertainties are not modified by the weights: $\Delta N'_{\mathrm{bin}}/N'_{\mathrm{bin}} = \Delta N_{\mathrm{bin}}/N_{\mathrm{bin}} = 1/\sqrt{N_{\mathrm{bin}}}$. As a result of the decreasing cross section as a function of p_{T}^{γ} within a given filtered sample, the relative statistical

uncertainty in the reconstructed smooth p_{T}^{γ} spectrum sharply decreases at each of the filter p_{T}^{γ} boundaries. Although the weighted spectrum is smooth as a function of p_{T}^{γ}, the relative statistical uncertainty is not smooth as a function of p_{T}^{γ}.

In addition to the luminosity weight, other weights are applied to the simulated events. The simulated samples are weighted such that the simulated conditions of proton-proton collisions agree with those provided by the LHC. Specifically, event weights are applied to simulated samples in order to correct the description of the pileup level and of the reconstructed position of the hard scattering vertex along the z-direction (PVz). As shown in Figure 4–1, there is a known correspondence between the average number of reconstructed primary vertices and the amount of pileup. Event weights are applied to simulated events in order to correct the number of reconstructed primary vertices (NPV), which can be determined on a per-event basis.[1] Event weights are applied sequentially to simulated events, first to correct the NPV simulated distribution and then to correct the PVz distribution.

Figure 5–2 shows the distributions of NPV and of the z-coordinate of the hard vertex in data and in the SHERPA simulated samples before and after the application of the NPV and PVz event weights. The ratios in the bottom panels of Figures 5–2(a) and 5–2(b) correspond to the weights that are applied. The SHERPA NPV distribution after the weighting differs from the data by at most 3%, since the subsequent PVz

[1]The NPV event weights are derived separately for events recorded with prescaled and unprescaled trigger selections.

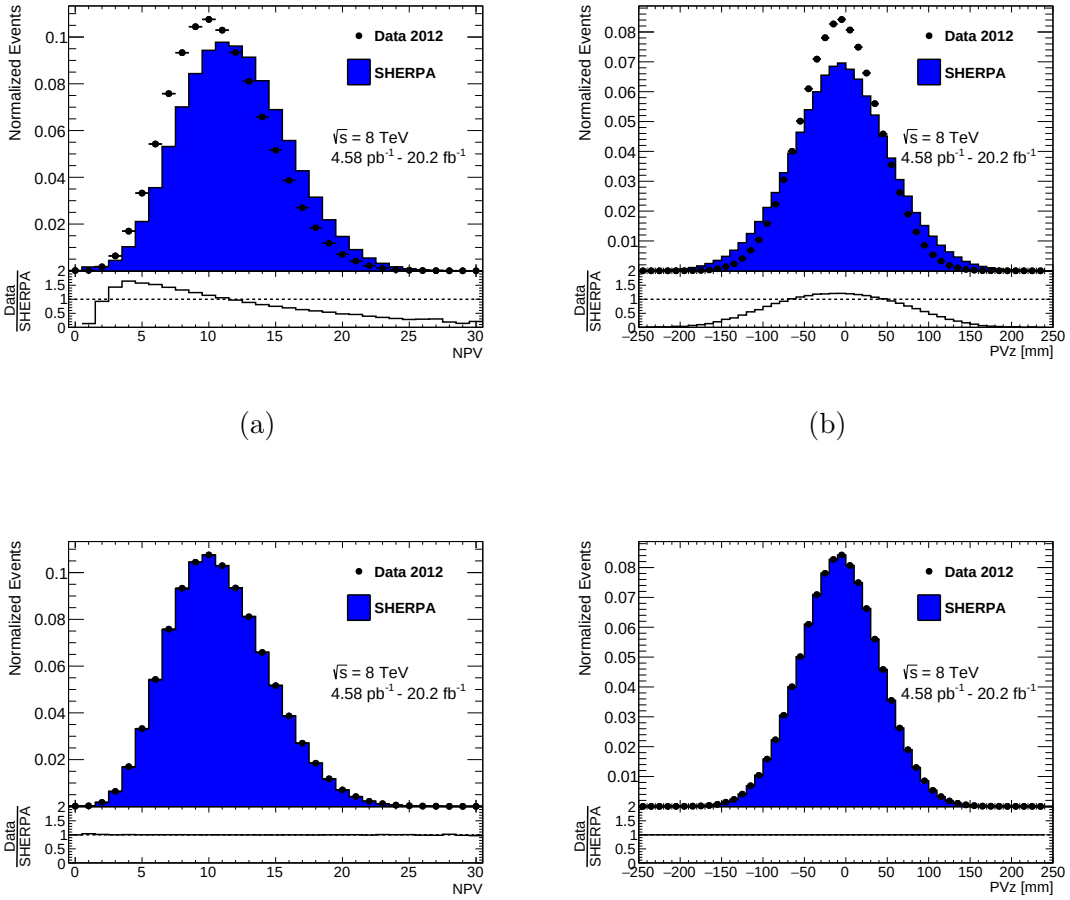

Figure 5–2 – Normalized data and SHERPA distributions of (a) the number of reconstructed primary vertices before the weighting, (b) the z-coordinate of the hard vertex before the weighting, (c) the number of reconstructed primary vertices after the weighting and (d) the z-coordinate of the hard vertex after the weighting. The ratio of the data distribution to that of SHERPA is given in the bottom panel. The vertical error bars in the data distribution correspond to the statistical uncertainty.

weighting modifies slightly the distribution. A perfect description of the data PVz distribution is reached by the weighted SHERPA samples. Similar distributions and levels of agreement with data are obtained after the weighting of the PYTHIA simulated samples.

5.2 Detector-level Selection

The measurement of the $\gamma+b$ production cross section relies on the use of Equation 3.1, solved for the cross section. Detector-level selection cuts are applied on the recorded events in order to select a subset of events compatible with at least one photon and one hadronic jet having been produced in a proton-proton collision. The determination of the jet flavour is done after the event selection cuts are applied.

The event selection consists in first selecting events suitable for physics analysis, next selecting events in which at least one photon has been reconstructed and, lastly, selecting events that additionally contain at least one reconstructed hadronic jet. In order to understand the impact of these detector-level selection criteria with respect to the particle level, the event selection is applied to both recorded and simulated events. The selection criteria used in this analysis are presented below in the order in which they are applied.

1. **Hard scattering vertex**

   Events are selected if the hard vertex of the event has at least two associated tracks, each with a transverse momentum satisfying $p_{\mathrm{T}} > 0.4$ GeV. This cut ensures that the hard vertex is a properly reconstructed primary vertex.

2. Trigger selection

Recorded events are selected if they satisfy one of the trigger criteria designed to select photons.

The Level-1 algorithm used to select photons aims to identify electromagnetic showers based on the distinctive feature that they are narrower than hadronic showers. Calorimeter cells used as input to the algorithm are grouped longitudinally within the electromagnetic calorimeter and within the hadronic calorimeters. The cells are also grouped transversely to reach a coarse granularity of approximately 0.1×0.1 in $\Delta\eta \times \Delta\phi$. These groups of cells are called trigger towers and are identified in Figure 3–5. The towers are scanned in groups of 4×4 to find a group of towers of size either 2×1 or 1×2 in the inner 2×2 towers that has a sum of transverse energies greater than some predefined threshold [184].

The Level-2 and the Event Filter trigger selections make use of a similar photon reconstruction as the one discussed in Section 4.2.1 [184]. At both of these trigger levels, photons must satisfy a photon identification based on variables discriminating the shapes of showers in the calorimeters, similarly to the approach discussed in Section 4.2.2. The cuts on the discriminating variables are not as stringent in the trigger selections as the tight set of cuts in order to avoid inefficiencies related to the trigger selection.

The photon trigger selection criteria in the Event Filter (EF) are called EF_gXX_loose, where XX is a placeholder for one of the many possible

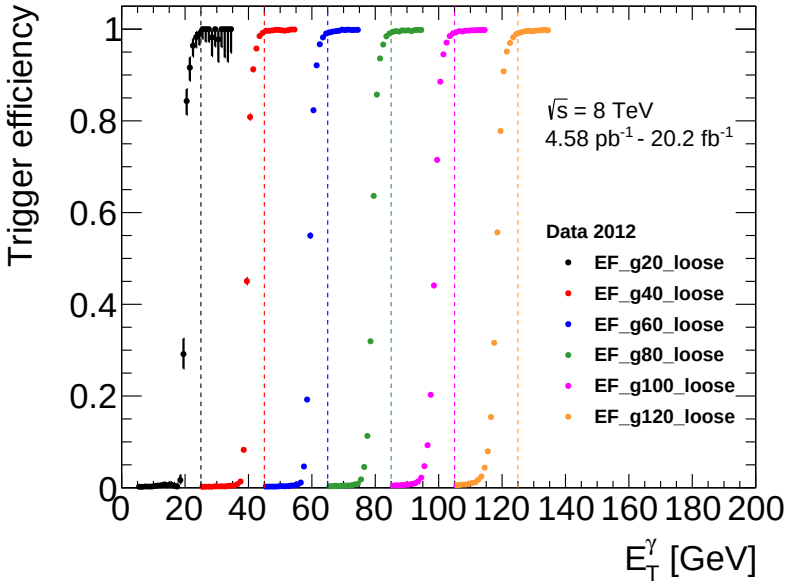

Figure 5–3 – Trigger efficiencies of the photon trigger selection criteria as a function of the photon transverse energy. The dashed lines indicate the lower boundaries beyond which each trigger criterion is used for the measurement presented in this thesis. The vertical error bars represent the statistical uncertainty in the efficiencies.

E_{T} thresholds that the photon cluster must exceed: 20, 40, 60, 80, 100 and 120 GeV. Figure 5–3 shows the efficiencies of these trigger criteria as a function of the photon transverse energy, E_{T}^{γ}, reconstructed after the recording of the events. The trigger efficiency is defined as the ratio of the number of events satisfying the photon trigger criterion and all detector-level selection cuts presented in this section to the number of events satisfying all detector-level selection cuts presented in this section. Trigger efficiencies are measured using event samples that were recorded by a different trigger selection than that for which the efficiency is being measured. The efficiency of the trigger selection with the lowest-E_{T} threshold criterion is measured with respect to inelastic

proton–proton collisions producing a minimum amount of activity in the detector. Efficiencies of the other, higher-E_{T} threshold criteria are measured with respect to the events that satisfy the lower-E_{T} threshold criteria thus building towards higher E_{T}^{γ} values. This so-called bootstrapping method provides a higher number of events with which to measure the trigger efficiency of the different trigger selection criteria. This approach at measuring the trigger efficiencies does not introduce biases because the reference trigger criteria used in the efficiency measurement are fully efficient at the energy scales of the higher trigger selection. The statistical uncertainty in the trigger efficiency of EF_g20_loose is larger than that of the other trigger selections since few inelastic pp collisions satisfy the detector-level selection cuts. The statistical uncertainty in the efficiencies is taken to be the Clopper–Pearson asymmetric binomial intervals at the 68% confidence level [185]. A given trigger criterion is used in the event selection when it is at least 99% efficient. This corresponds to using photon trigger criteria only for photons that have values of E_{T}^{γ} at least 5 GeV higher than the values of the trigger thresholds.

The rates of events satisfying the photon trigger criteria are too large to allow the recording of every event that satisfies them. The trigger criterion with a threshold of 120 GeV is unprescaled while the criteria with thresholds below 120 GeV have prescale factors with increasingly larger values as the value of the thresholds decreases. A prescale factor p reduces the recorded luminosity of the associated trigger criterion by $1/p$. The trigger criterion with a threshold of 20 GeV thus has the lowest recorded integrated luminosity. The trigger criteria

Table 5–2 – Efficiencies, average prescale factors, and integrated luminosities of the photon trigger criteria and the E_{T}^{γ} ranges in which they are used. The listed efficiency is the trigger efficiency at the lower boundary of the E_{T}^{γ} range. The average prescale factors are rounded to the nearest unit.

Trigger criterion	Range [GeV]	Efficiency [%]	Prescale factor	$\mathcal{L}_{\mathrm{int}}$ [pb^{-1}]
EF_g20_loose	$25 < E_{\mathrm{T}}^{\gamma} < 45$	100^{+0}_{-2}	4418	4.58
EF_g40_loose	$45 < E_{\mathrm{T}}^{\gamma} < 65$	$99.6^{+0.1}_{-0.2}$	349	58.0
EF_g60_loose	$65 < E_{\mathrm{T}}^{\gamma} < 85$	$99.3^{+0.1}_{-0.1}$	81	250
EF_g80_loose	$85 < E_{\mathrm{T}}^{\gamma} < 105$	$99.41^{+0.08}_{-0.09}$	29	709
EF_g100_loose	$105 < E_{\mathrm{T}}^{\gamma} < 125$	$99.32^{+0.08}_{-0.08}$	13	1552
EF_g120_loose	$125 < E_{\mathrm{T}}^{\gamma}$	$99.19^{+0.08}_{-0.09}$	1	20.2×10^3

are used in exclusive ranges of E_{T}^{γ} in order to simplify the treatment of the integrated luminosity in the measurement of the cross section as a function of E_{T}^{γ}. Table 5–2 lists the trigger criteria with the E_{T}^{γ} range in which they are used and their associated average prescale factors and integrated luminosities. The trigger efficiencies measured at the lower boundaries of the E_{T}^{γ} ranges are also shown in the table.

3. Photon preselection

Reconstructed photons are required to satisfy the photon preselection. The photon preselection requires that photons satisfy cuts on the discriminating identification variables that are common to both the tight and the relaxed tight sets of cuts. These variables are nominally $w_{\mathrm{s,tot}}$, R_{η}, R_{ϕ}, w_{η_2} and R_{had}.

Events are selected if there is at least one reconstructed photon that satisfies the preselection.

4. **Photon particle-level matching**

   Reconstructed photons in simulated events are required to be matched geometrically in (η, ϕ) to a particle-level prompt photon. Reconstructed and particle-level photons are considered matched if their angular distance is less than 0.2: $\Delta R < 0.2$.

   Simulated events are selected if there is at least one reconstructed photon that is matched to a particle-level prompt photon.

5. **Photon E_{T} acceptance**

   Reconstructed photons are required to satisfy $E_{\mathrm{T}}^{\gamma} > 25$ GeV. This cut ensures that the trigger efficiency is above 99%.

   Events are selected if there is at least one reconstructed photon in this acceptance region.

6. **Photon η acceptance**

   Reconstructed photons are required to satisfy $|\eta^{\gamma}| < 1.37$ or $1.56 < |\eta^{\gamma}| < 2.37$. The separation of the pseudorapidity values in two ranges is motivated by the transition region between the barrel and the end-caps of the electromagnetic calorimeter, spanning $1.37 < |\eta| < 1.56$ as discussed in Section 3.2.2. The upper boundary of the acceptance range is determined by the region where finely segmented strip cells are present in the calorimeter.

   Events are selected if there is at least one reconstructed photon in either of these acceptance regions.

7. Photon identification

Events are selected if the leading reconstructed photon passes the tight set of identification cuts, defined in Section 4.2.2.

8. Photon isolation

Events are selected if the isolation energy of the leading reconstructed photon satisfies $E_{\mathrm{T}}^{\mathrm{iso}} < 4.8\ \mathrm{GeV} + 0.0042 \times E_{\mathrm{T}}^{\gamma}$. The specific values of the isolation cut were optimized to provide the best signal-to-background ratio in selected events [35].

The dependence of the requirement on E_{T}^{γ} is to improve the isolation efficiency at large E_{T}^{γ} values. The isolation efficiency is defined as the ratio of the number of events satisfying the complete event selection at the detector level to the number of events satisfying the complete event selection at the detector level but without the isolation cut. Figure 5–4 shows the isolation efficiencies of different isolation cuts in the SHERPA and PYTHIA samples. It can be seen that the efficiencies of the fixed-value isolation cuts decrease as a function of E_{T}^{γ}. The decrease is due to an imperfect correction of the leakage of the photon energy outside of the photon window. Adding a term dependent on E_{T}^{γ} in the definition of the isolation cut allows to reduce this decrease. Also, the isolation efficiency is lower in the PYTHIA samples than in the SHERPA samples. This is due to the emission of bremsstrahlung photons in the parton shower in the PYTHIA samples, which on average results in larger values of $E_{\mathrm{T}}^{\mathrm{iso}}$.

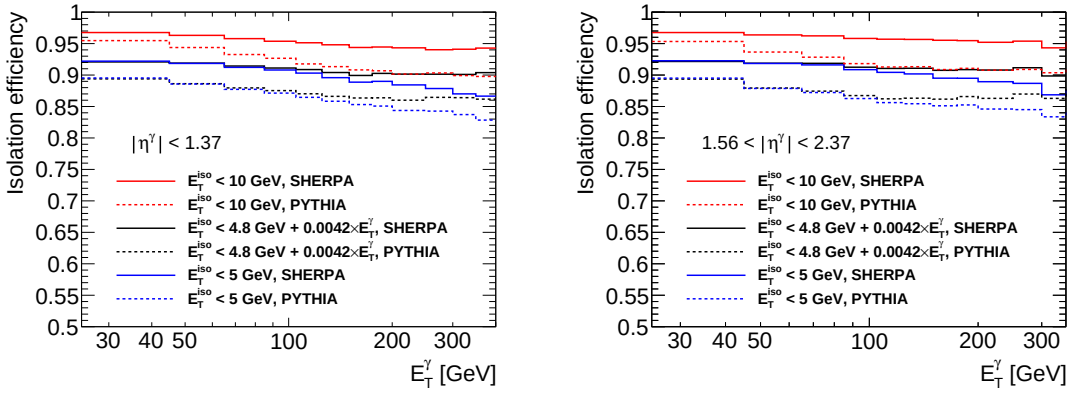

(a) (b)

Figure 5–4 – Isolation efficiency in the SHERPA and PYTHIA samples as a function of the photon transverse energy for (a) the central region and (b) the forward region. Isolation efficiencies for different requirements on the isolation energy are displayed.

9. Jet vertex fraction requirement

Reconstructed jets within the phase-space region defined by $p_{\mathrm{T}}^{\mathrm{jet}} < 50$ GeV and $|\eta^{\mathrm{jet}}| < 2.4$ are required to satisfy $|\mathrm{JVF}| > 0.5$. The value of this cut on the JVF corresponds to an efficiency of selecting jets produced in the hard vertex of about 90% and to a rejection factor of about 50 for jets produced in additional pp collisions.

Events are selected if there is at least one reconstructed jet that satisfies the JVF cut or that is outside of the phase-space region defined above.

10. Jet–photon overlap removal

Reconstructed jets are required to be located at an angular distance of $\Delta R > 0.4$ from the leading reconstructed photon. Reconstruction algorithms of physical objects are independent of each other. This has the consequence that energy

deposits in the calorimeters can be reconstructed as both a photon and a jet. With the leading photon already identified and selected, jets that are within an angular distance of 0.4 of the leading photon are considered to be overlapping the leading photon.

Events are selected if there is at least one reconstructed jet that does not overlap the leading reconstructed photon.

11. Jet p_{T} acceptance

Events are selected if the leading reconstructed jet satisfies $p_{\mathrm{T}}^{\mathrm{jet}} > 20$ GeV. The value of the requirement on the jet transverse momentum is chosen to be smaller than that of the photon. This allows for a possible decrease in jet transverse momentum due to hadronization effects.

12. Jet η acceptance

Events are selected if the leading reconstructed jet satisfies $|\eta^{\mathrm{jet}}| < 2.5$. This cut is required to ensure that the leading jet is within the coverage of the Inner Detector, such as to make possible the use of the b-tagging algorithms.

13. Jet–photon separation

Events are selected if the leading reconstructed jet is located at an angular distance of $\Delta R > 1$ from the leading reconstructed photon. The jet area has a radius of 0.4 and the radius of the region in which the isolation energy of the photon is measured is 0.4. Requiring an angular distance of at least 1 ensures

Table 5–3 – Number of data, SHERPA and PYTHIA events satisfying the detector-level selection cuts described in the text. A dash indicates that the selection cut is not applied. The total numbers of SHERPA and PYTHIA events are the number of generated events before the stitching of the filtered samples. The effect of the stitching on the number of selected events is included in the photon preselection cut.

#	Detector-level selection cut	Data	SHERPA	PYTHIA
0	Total	729,720,140	61,958,741	20,373,297
1	Hard scattering vertex	699,781,767	61,958,601	20,373,288
2	Trigger selection	57,022,566	–	–
3	Photon preselection	30,314,757	5,777,026	4,013,596
4	Photon particle-level matching	–	4,968,236	3,575,264
5	Photon E_{T} acceptance	16,818,097	4,923,631	3,547,416
6	Photon η acceptance	16,239,775	4,790,290	3,448,668
7	Photon identification	7,489,875	4,589,944	3,298,820
8	Photon isolation	4,945,136	4,154,080	2,879,730
9	Jet vertex fraction requirement	4,945,074	4,153,960	2,879,648
10	Jet–photon overlap removal	4,944,990	4,153,855	2,879,598
11	Jet p_{T} acceptance	4,830,027	3,900,668	2,741,702
12	Jet η acceptance	4,493,408	3,577,088	2,526,891
13	Jet–photon separation	4,482,887	3,553,236	2,515,753

that the leading jet does not contribute to the isolation energy of the leading photon, keeping the two objects independent.

The impact of each detector-level selection cut on the number of data and simulated events is given in Table 5–3. About 4.5 million recorded events satisfy the selection criteria. It is worth noting that no b-tagging on the jets is performed and thus the tagging has no effect on the number of events selected.

The $\gamma + b$ production cross section is measured differentially as a function of the photon transverse energy. This observable is chosen instead of the jet transverse

momentum since the energy resolution of the reconstructed photons is better than that of jets, as mentioned in Section 4.3.1. The widths of the E_{T}^{γ} bins follow that of the trigger E_{T}^{γ} ranges for the prescaled trigger criteria. For $E_{\mathrm{T}}^{\gamma} > 125$ GeV, the bin widths are chosen to increase with E_{T}^{γ} such as to compensate for the decreasing number of events in each bin. As a result, the E_{T}^{γ} bins used in the cross-section measurement have widths of 20 GeV in the E_{T}^{γ} range 25–125 GeV, 25 GeV in the E_{T}^{γ} range 125–200 GeV and 50 GeV in the E_{T}^{γ} range 200–400 GeV. Although there are selected events with $E_{\mathrm{T}}^{\gamma} > 400$ GeV, the uncertainty in the measurement effectively limits the range to 400 GeV in the central region, $|\eta^{\gamma}| < 1.37$, and to 350 GeV in the forward region, $1.56 < |\eta^{\gamma}| < 2.37$.

Figures 5–5, 5–6 and 5–7 show the correlation between the kinematics of the selected leading photon and jet. The distributions between the recorded and the simulated events do not agree perfectly since the selected recorded events contain background events that also pass the selection cuts. The figures show that in the samples of selected events, the leading photon and jet are typically produced back-to-back and with similar transverse energies and pseudorapidities. The distributions in Figure 5–6 have different shapes in the central and forward regions. This is because the central and forward regions are defined by the pseudorapidity of the photon.

Figure 5–8 shows a computer event display of a typical recorded event passing the selection cuts. In addition to the selection cuts, the leading jet satisfies the most stringent requirement on the MV1c value, corresponding to the b-jet b-tagging efficiency of 50%. The event exhibits the expected features of a $\gamma + b$ event, including that the photon and the jet have opposite directions in the transverse plane and

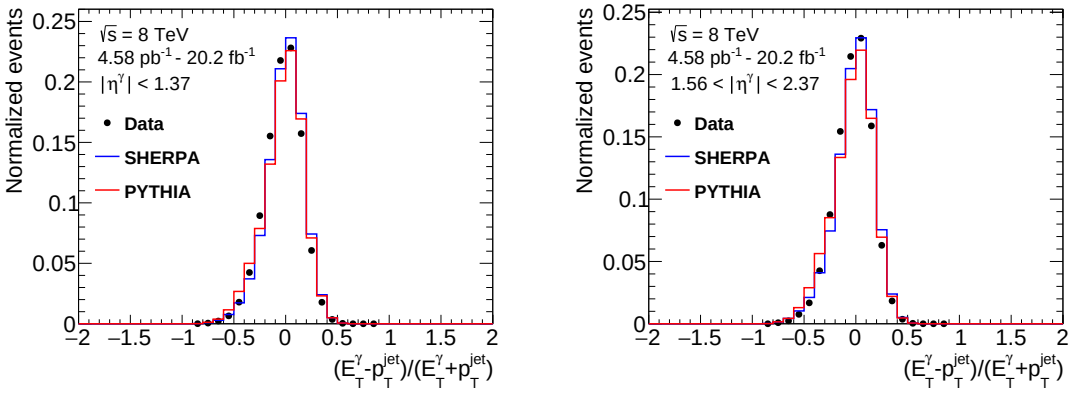

(a) (b)

Figure 5–5 – Normalized data, SHERPA and PYTHIA distributions of the ratio of the difference between the transverse momenta of the leading photon and the leading jet to the sum of their transverse momenta for (a) the central region and (b) the forward region. The data distribution contains background events. The statistical uncertainty in the data distribution is too small to be visible.

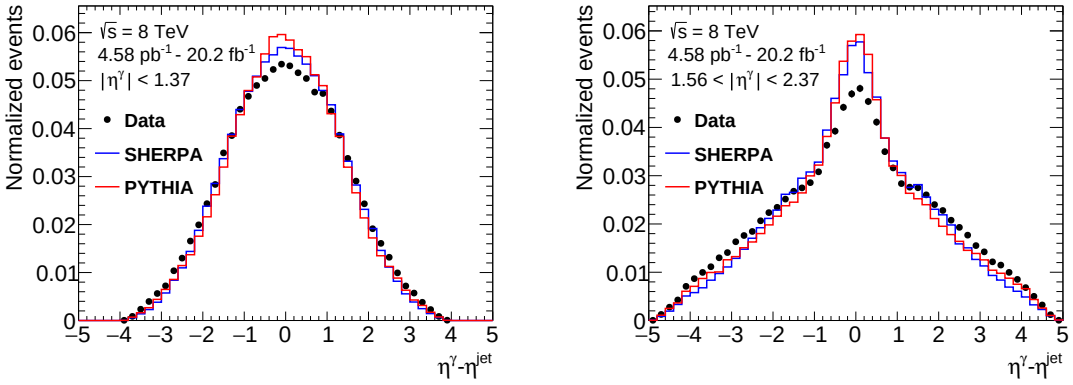

(a) (b)

Figure 5–6 – Normalized data, SHERPA and PYTHIA distributions of the difference in pseudorapidities between the leading photon and the leading jet for (a) the central region and (b) the forward region. The data distribution contains background events. The statistical uncertainty in the data distribution is too small to be visible.

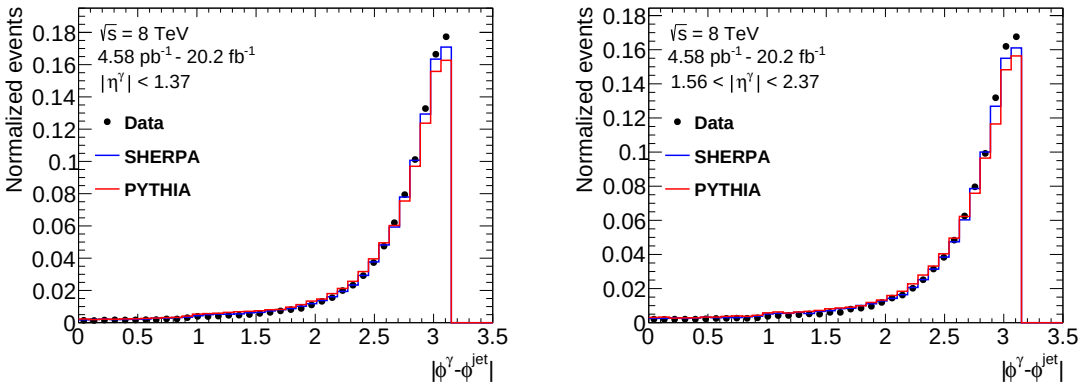

(a) (b)

Figure 5–7 – Normalized data, SHERPA and PYTHIA distributions of the absolute value of the difference in azimuthal angles between the leading photon and the leading jet for (a) the central region and (b) the forward region. The data distribution contains background events. The statistical uncertainty in the data distribution is too small to be visible.

that the photon shower is narrower and shorter than the one produced by the jet. Furthermore, the secondary vertex, located at about $(-0.5, -0.3, 40.2)$ mm in (x, y, z) is displaced by about one millimeter from the hard vertex, located at $(-0.3, 0.5, 39.8)$ mm, which is of the order of the displacement expected from a b-hadron lifetime and subsequent decay.

5.3 Particle-level Selection

A particle-level selection applied to MC events is necessary to define the fiducial phase-space of the cross-section measurement. It is independent of the detector-level selection. The particle-level selection is also needed to study the reconstruction and selection efficiency of the detector-level selection, to assess the calibration of

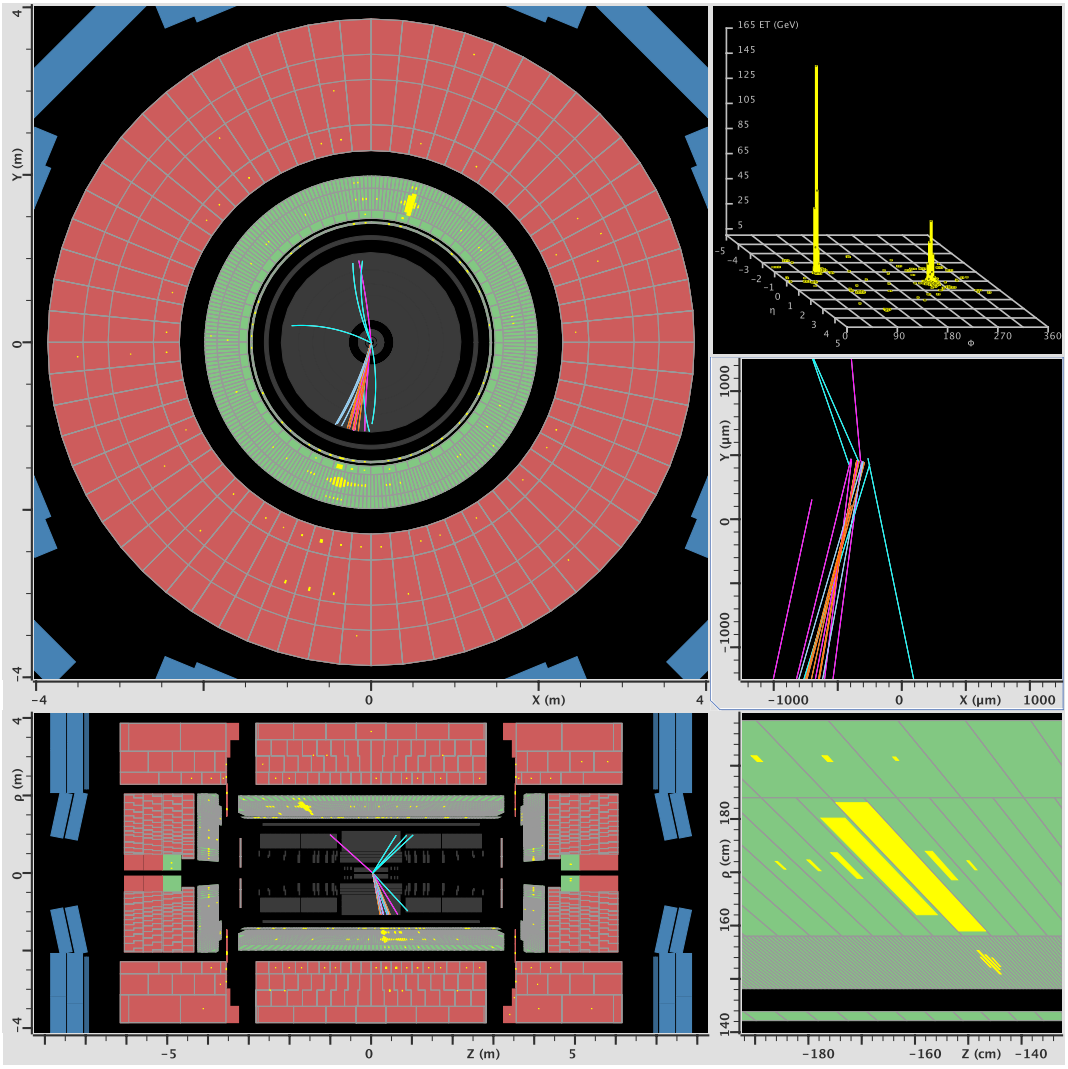

Figure 5–8 – Event display of a selected recorded event with a leading jet satisfying MV1c $>$ 0.9195. The event was recorded on 2012-12-05. The electromagnetic and hadronic calorimeters are displayed in green and red respectively. The muon spectrometer is in blue. The tracks in the Inner Detector are colored according to their transverse momenta, the colors being cyan, blue, magenta and orange for p_{T} values greater than 1 GeV, 2 GeV, 4 GeV and 8 GeV, respectively. Only tracks with $p_{\mathrm{T}} > 1$ GeV and $|z_0| < 2.5$ mm with respect to the hard vertex are shown. The yellow rectangles are indicative of energy deposits in the calorimeters, with their sizes being an indication of the amount of energy deposited. A two-dimensional histogram of the energy deposits is displayed in the top right panel.

the physical objects and to gain knowledge on the resolutions of the reconstructed kinematic quantities.

With the aim of maximizing the reconstruction and selection efficiency, the particle-level selection mimics the detector-level selection. Events are considered at the particle level only after they pass the cut on the hard-vertex tracks at the detector level. The ordered selection criteria on the events that survive that cut follow.

1. **Photon E_{T} acceptance**

   Particle-level photons are required to satisfy $E_{\mathrm{T}}^{\gamma} > 25$ GeV.

   Events are selected if there is at least one particle-level photon in this acceptance region.

2. **Photon η**

   Particle-level photons are required to satisfy $|\eta^{\gamma}| < 1.37$ or $1.56 < |\eta^{\gamma}| < 2.37$.

   Events are selected if there is at least one particle-level photon in either of these acceptance regions.

3. **Photon isolation**

   Events are selected if the particle-level isolation energy of the leading particle-level photon satisfies $E_{\mathrm{T}}^{\mathrm{iso}} < 4.8 \text{ GeV} + 0.0042 \times E_{\mathrm{T}}^{\gamma}$.

   The isolation energy at particle level is defined in a similar way as the detector-level isolation energy, including the correction for the ambient transverse-momentum density. The particle-level four-momenta of long-lived particles,

except those of muons and neutrinos, within an angular distance of 0.4 of the prompt photon are summed. The four-momentum of the prompt photon itself is excluded from that summation. The transverse energy of the resulting four-momentum is taken as the particle-level isolation energy. The particle-level ambient transverse-momentum density is determined from the median value of the ratio of the particle-level jet transverse momentum divided by the jet area for jets built using the k_t algorithm with parameter $R = 0.5$ taking as input all long-lived particles, except muons and neutrinos. The particle-level ambient transverse momentum density is then multiplied by a circular area of radius $R = 0.4$ to obtain the correction. This correction is derived in coarse pseudorapidity bins. Pileup is not considered at any stage of this correction, as such this corrects only for contributions to the isolation energy from the underlying event.

The cross section does not depend strongly on the specific values of the cut on the isolation energy as long as the angular region in which the isolation energy is measured is large enough to include the effects of photon fragmentation, while being not too large to avoid being sensitive to activity in the rest of the event. A radius parameter of 0.4 is adequate in that respect [186].

4. Jet–photon overlap removal

Particle-level jets are required to be located at an angular distance of $\Delta R > 0.4$ from the leading particle-level photon. Particle-level jets are defined here with the same jet algorithm and the same parameter value as those used to

reconstruct jets at the detector-level but by using as input objects all long-lived particles, including muons and neutrinos. Muons and neutrinos are included in the definition of particle-level jets as they are expected to carry a non-negligible amount of energy, since they can be produced in the decay of the b and c hadrons via the decay of W bosons.

Events are selected if there is at least one particle-level jet that does not overlap the leading particle-level photon.

5. **Jet p_{T} acceptance**

   Events are selected if the leading particle-level jet satisfies $p_{\mathrm{T}} > 20$ GeV.

6. **Jet rapidity acceptance**

   Events are selected if the rapidity of the leading particle-level jet satisfies $|y| < 2.5$.

7. **Jet–photon separation**

   Events are selected if the leading particle-level jet is located at an angular distance of $\Delta R > 1$ from the leading particle-level photon.

8. ***b*-jet label**

   Events are selected if the leading particle-level jet is labelled as a b-jet, as dicussed in Section 4.3.3.

Table 5–4 – Number of SHERPA and PYTHIA events satisfying the particle-level selection cuts described in the text. The total numbers of events are the number of generated events before the stitching of the filtered samples. The effect of the stitching on the number of selected events is included in the photon E_{T} acceptance cut.

#	Particle-level selection cut	SHERPA	PYTHIA
0	Total	61,958,741	20,373,297
1	Photon E_{T} acceptance	7,291,048	4,810,341
2	Photon η acceptance	5,419,503	4,087,552
3	Photon isolation	4,818,921	3,329,573
4	Jet–photon overlap removal	4,818,841	3,329,558
5	Jet p_{T} acceptance	4,516,478	3,147,322
6	Jet y acceptance	4,192,922	2,925,311
7	Jet–photon separation	4,173,875	2,916,194
8	b-jet label	782,874	71,697

The reduction in the number of MC events selected at each step of the particle-level selection is given in Table 5–4. In contrast to the detector-level selection, the particle-level jet is selected only if it is labelled as a b-jet. The b-jet label cut is not as severe on the SHERPA samples as it is on the PYTHIA samples, since the SHERPA samples are filtered to contain a higher number of events with b hadrons.

CHAPTER 6
Signal Extraction

This chapter describes how signal events are extracted from the selected events. The fraction of selected events in which the selected photon is a prompt photon, called the photon purity, and the fraction of selected events in which the selected jet is a b-jet, called the b-jet fraction, are extracted sequentially. The extraction of prompt photons is necessary as a significant number of events that do not contain prompt photons are selected. The extraction of b-jets is necessary as the event selection does not distinguish between different jet flavours. The first and second sections describe how the photon purity and the b-jet fraction are extracted from the selected events.

6.1 Prompt-photon Signal

The event selection discussed in the previous chapter aims to select $\gamma + \text{jet}$ events among all the pp collisions provided by the LHC. Some background events that do not contain a prompt photon and a jet are still selected.

Background objects that can be mis-reconstructed and selected as prompt photons include electrons and jets. The stringent photon reconstruction process, particularly the resolution of the ambiguity between electrons and photons, reduces the impact of the electron background contribution. Electrons reconstructed as photons contribute less than 1% of the reconstructed prompt photons in the phase space that is investigated [35]. This source of background is thus negligible and not discussed further.

The jet background contribution is however not negligible. Although the photon identification criteria result in a jet background rejection factor of about 5×10^3, the ratio of the number of jets that are produced in proton–proton collisions in the phase space that is explored to the number of prompt photons produced is also of the same order of magnitude. The requirement on the isolation energy helps reduce the jet background further but a non-negligible number of background jet events are still selected.

To extract the prompt-photon signal from the selected $\gamma +$ jet events, a data-driven procedure based on a two-dimensional sideband is used. This procedure extracts the prompt-photon signal statistically, i.e. not on a per-event basis, from the recorded event sample by using mainly the recorded events themselves. The idea behind the procedure is to exploit two measurable quantities that both define the phase space of the signal events and that are not correlated to each other for background events. Since the quantities are not correlated, the number of events in the background phase-space region of one quantity, relative to the number of events in its signal region, will not change if that number is evaluated in the signal region or in the background region of the other quantity. Therefore, the numbers of events in the background regions can be used to determine the number of background events in the signal region.

In practice, the two quantities used are the isolation energy of the leading photon and the set of photon identification discriminating variables. The signal region of these quantities are those used in the event selection, i.e. $E_{\mathrm{T}}^{\mathrm{iso}} < 4.8 \text{ GeV} + 0.0042 \times E_{\mathrm{T}}^{\gamma}$ and the tight set of identification cuts. The background regions of these quantities

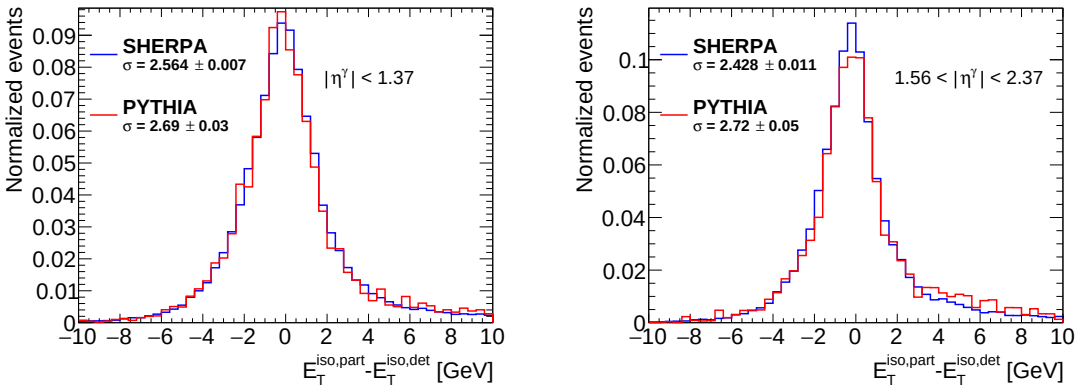

(a) (b)

Figure 6–1 – Normalized SHERPA and PYTHIA distributions of the difference between the particle- and the detector-level isolation energies for (a) the central region and (b) the forward region. The standard deviations of the distributions are displayed in the legend.

are defined as $E_{\mathrm{T}}^{\mathrm{iso}} > 6.8\ \mathrm{GeV} + 0.0042 \times E_{\mathrm{T}}^{\gamma}$ and the relaxed tight identification. These definitions of the background regions have been chosen such as to minimize the amount of signal events satisfying them while maximizing the number of background events.

The gap of 2 GeV between the signal and the background regions of the isolation energy reduces the amount of prompt photons, compared to having no gap, that would get categorized in the background region due to the resolution of the measurement of the isolation energy. Figure 6–1 shows the distribution of the difference in isolation energy between the particle and the detector levels for prompt photons. A standard deviation of about 2 GeV is observed. A wider gap is not used to avoid decreasing further the number of background events in the background region.

The use of the relaxed tight identification cuts to define the background region related to the photon identification is motivated by the fact that π^0 mesons, and other neutral mesons, can pass the tight identification cuts, as mentioned in Section 4.2.2. The data-driven two-dimensional sideband method is only sensitive to the background events in the signal region that have a similar origin as those in the background regions. To ensure that events in which the selected photons originate from the decays of neutral mesons are not considered as signal events, this type of events must be accepted into the background region. The relaxed tight definition is designed for such a task since it vetoes the discriminating identification variables based on the first layer of the electromagnetic calorimeter, which are the most sensitive to the presence of photons produced in the decays of neutral mesons. Events with neutral mesons will thus be found in the background regions and be properly subtracted from the signal region via the sideband procedure.

In the context of the photon identification and the isolation energy, the two assumptions that underlie the sideband method can be stated as follow.

- There is no correlation in the background events between the isolation energy and the identification variables based on the first layer of the electromagnetic calorimeter.
- No prompt-photon events satisfy $E_{\mathrm{T}}^{\mathrm{iso}} > 6.8\ \mathrm{GeV} + 0.0042 \times E_{\mathrm{T}}^{\gamma}$ or the relaxed tight identification.

The first assumption is reasonable because the energy deposits contributing to the variables based on the information of the first calorimeter layer are different than

those contributing to the isolation energy, since the former are inside of the photon cluster while the latter are outside of it. The second assumption does not necessarily hold however and needs to be addressed.

The sideband method can be applied on distributions of the isolation energy of the selected photon in the signal and background regions of the photon identification variables or on the integrated numbers of events of these distributions. The approach based on the distributions of the isolation energy allows to assess the validity of the method in removing background events from the signal region. However, it does not allow to assess the impact of the two assumptions that underlie the method. The approach based on the integrated numbers allows to assess the assumptions. Therefore, these two approaches are complementary.

Figure 6–2 shows the impact of the two-dimensional sideband method on the distribution of the isolation energy of the selected photon for the lowest-E_{T}^{γ} bin. Figure 6–3 similarly shows the impact in the highest-E_{T}^{γ} bin. The sideband method concretely consists in scaling the distribution of the isolation energy of relaxed-tight photons such that its integral in the background region of the isolation energy matches that of the tight photons in that background region. The scaled number of relaxed-tight events in the signal region of the isolation energy is then subtracted from that of the tight events to give the distribution of the prompt-photon events. It can be seen in those figures that the shape of the data distribution after this subtraction mostly agrees with that of the MC distributions, which only contain prompt photons. This level of agreement gives confidence that the method does indeed remove the

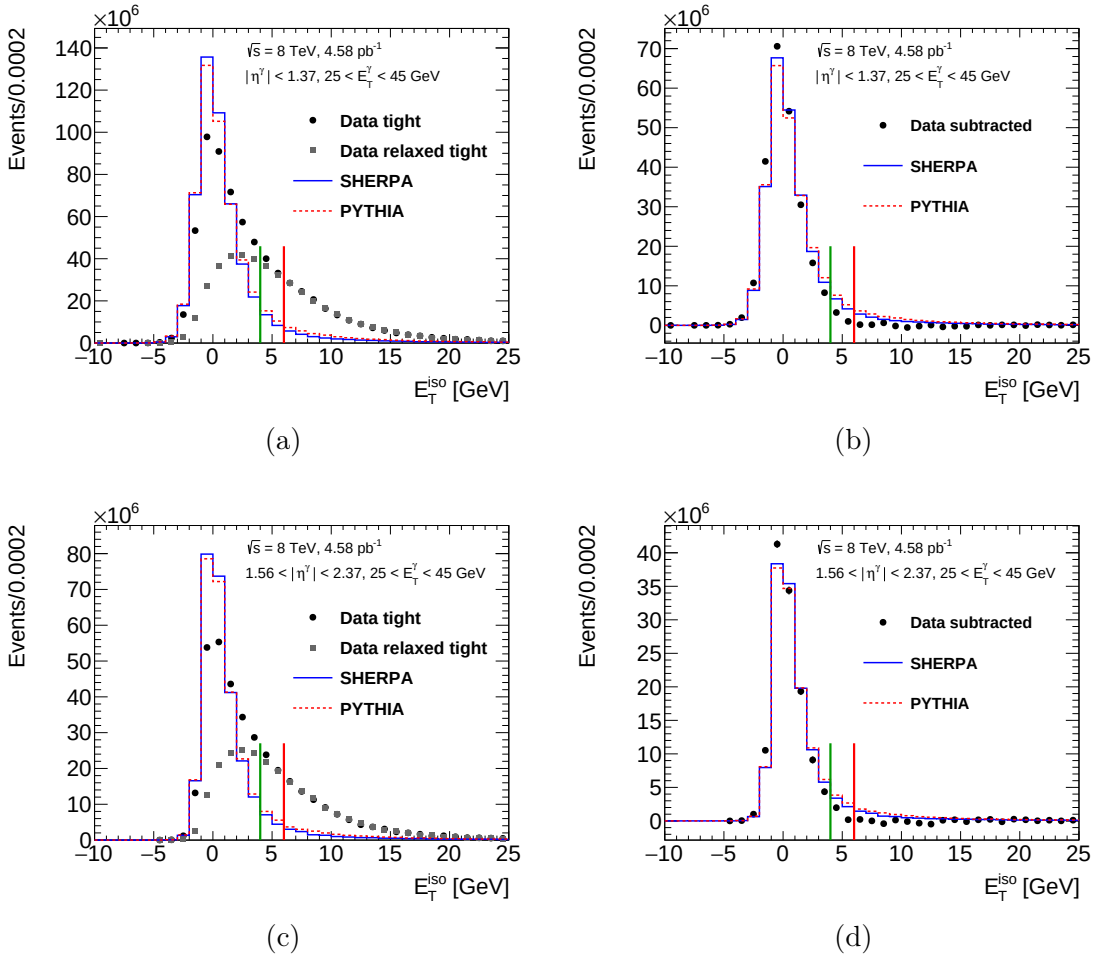

Figure 6–2 – Data, SHERPA and PYTHIA distributions of the isolation energy in the lowest-E_{T}^{γ} bin of (a) the central region before the background subtraction, (b) the central region after the background subtraction, (c) the forward region before the background subtraction and (d) the forward region after the background subtraction. The data events are weighted by the prescale factor associated to the E_{T}^{γ} bin to bring their numbers to those corresponding to an integrated luminosity of 20.2 fb^{-1}. The signal region of the isolation energy is to the left of the green line while the background region is to the right of the red line. The relaxed-tight distribution is scaled such that its integral to the right of the red line correspond to that of the tight distribution. The MC distributions are scaled such that their integrals to the left of the green line correspond to that of the tight or the subtracted distributions. The statistical uncertainties in the data distribution are too small to be visible.

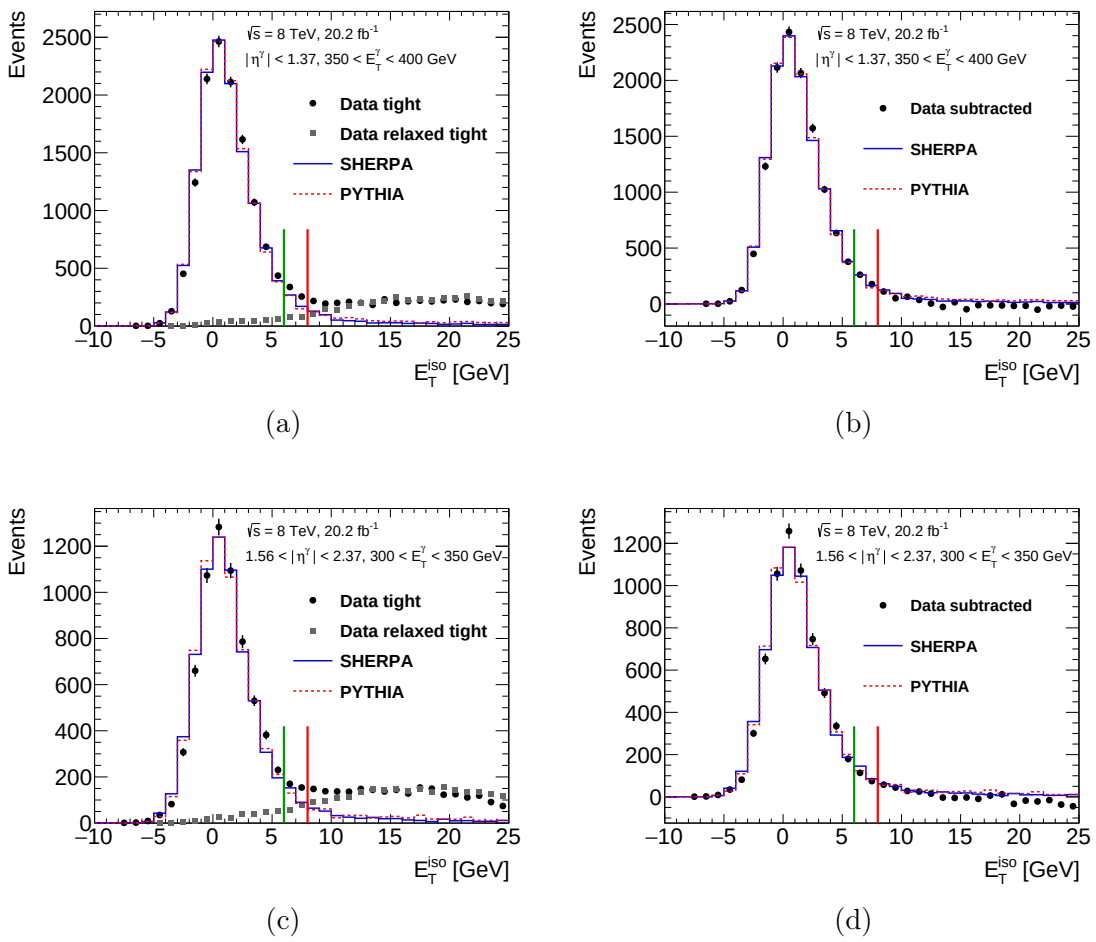

Figure 6–3 – Data, SHERPA and PYTHIA distributions of the isolation energy in the highest-E_{T}^{γ} bin of (a) the central region before the background subtraction, (b) the central region after the background subtraction, (c) the forward region before the background subtraction and (d) the forward region after the background subtraction. The signal region of the isolation energy is to the left of the green line while the background region is to the right of the red line. The relaxed-tight distribution is scaled such that its integral to the right of the red line correspond to that of the tight distribution. The MC distributions are scaled such that their integrals to the left of the green line correspond to that of the tight or the subtracted distributions. The error bars in the data distribution correspond to the statistical uncertainty.

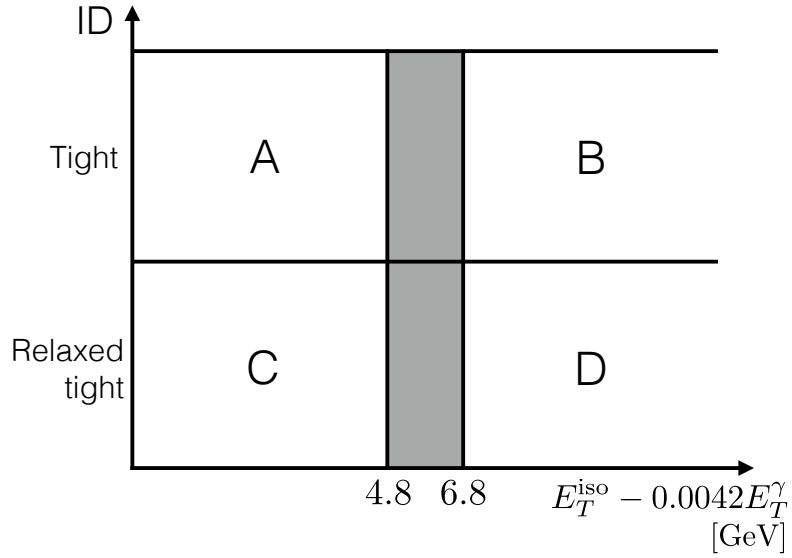

Figure 6–4 – Diagram of the regions defined in the two-dimensional sideband method as a function of the isolation energy and the photon identification (ID). The grey regions are not associated to any sideband region.

background events from the signal region. Imperfections in the agreement can be caused by the breakdown of the assumptions that underlie the sideband method.

The approach of the sideband method using the total numbers of events in each background and signal regions can be expressed in terms of the regions defined in Figure 6–4. Region A represents the signal region and regions B, C and D represent respectively the background regions of the isolation energy, of the photon identification and of both the isolation energy and the photon identification.

The relation between the numbers of background events in the regions can be stated as

$$\frac{N_A^{\rm bkg}}{N_B^{\rm bkg}} = R_{\rm bkg}\frac{N_C^{\rm bkg}}{N_D^{\rm bkg}}, \tag{6.1}$$

where R_{bkg} is a factor that relates the two ratios. It is a measure of the correlation between the isolation energy and the photon identification in the background events. The assumption that there is no correlation in the background events between the photon identification and the isolation energy is equivalent to having $R_{\text{bkg}} = 1$. The assumption that there is no signal events in the background regions is equivalent to having $N_X = N_X^{\text{bkg}}$, for $X \in \{B, C, D\}$. The quantity N_i is the total number of events in region i and can be decomposed into signal and background events: $N_i = N_i^{\text{sig}} + N_i^{\text{bkg}}$. Under these two assumptions, the previous equation becomes

$$\frac{N_A^{\text{bkg}}}{N_B} = \frac{N_C}{N_D}. \tag{6.2}$$

The prompt-photon event purity is defined as $p^{\text{prompt-}\gamma} = N_A^{\text{sig}}/N_A$. A knowledge of it allows to obtain the number of prompt-photon events from the number of selected events. Using the previous equation, it is given by

$$p^{\text{prompt-}\gamma} = \frac{N_A - N_A^{\text{bkg}}}{N_A} = 1 - \frac{N_B N_C}{N_A N_D}. \tag{6.3}$$

This equation is equivalent to the procedure used to subtract the background events in the distribution of the isolation energy .

If the assumption that there are no signal events in the background regions is not expected to hold, the photon purity becomes

$$p^{\text{prompt-}\gamma} = 1 - \frac{N_B^{\text{bkg}} N_C^{\text{bkg}}}{N_A N_D^{\text{bkg}}}. \tag{6.4}$$

Since in data only the total number of events in a region is known, i.e. it is not known in data if an event is a signal or a background event, the previous equation can be

transformed to make use of the total numbers of events:

$$p^{\text{prompt-}\gamma} = 1 - \frac{(N_B - c_B N_A^{\text{sig}})(N_C - c_C N_A^{\text{sig}})}{N_A(N_D - c_D N_A^{\text{sig}})} \tag{6.5}$$

with

$$c_B = \frac{N_B^{\text{sig}}}{N_A^{\text{sig}}}, \quad c_C = \frac{N_C^{\text{sig}}}{N_A^{\text{sig}}}, \quad c_D = \frac{N_D^{\text{sig}}}{N_A^{\text{sig}}}. \tag{6.6}$$

The c_X factors represent the number of signal events in the background regions relative to the signal region, i.e. the amount of signal leaking into the background regions. These factors cannot be obtained from data. However, they can be obtained from the signal MC samples. By construction of the background regions, the values for these leakage factors are expected to be small such that they are used as a small MC correction to an otherwise data-driven procedure.

Figure 6–5 shows the values of the factors. It can be seen that the values in the SHERPA samples are below 10%. The values of c_B and c_D are different between the SHERPA and PYTHIA samples because the PYTHIA samples includes bremsstrahlung photons, which have larger $E_{\text{T}}^{\text{iso}}$ values. The values of c_C are larger at low E_{T}^{γ} since the efficiency of the photon identification is lower at these low values. The values of c_D are the smallest since the prompt photon has to fail the requirements on both the isolation energy and the tight photon identification.

Equation 6.5 gives the purity once N_A^{sig} is known, which is not the case in data. However, since $p^{\text{prompt-}\gamma} = N_A^{\text{sig}}/N_A$, the equation can be interpreted as a quadratic

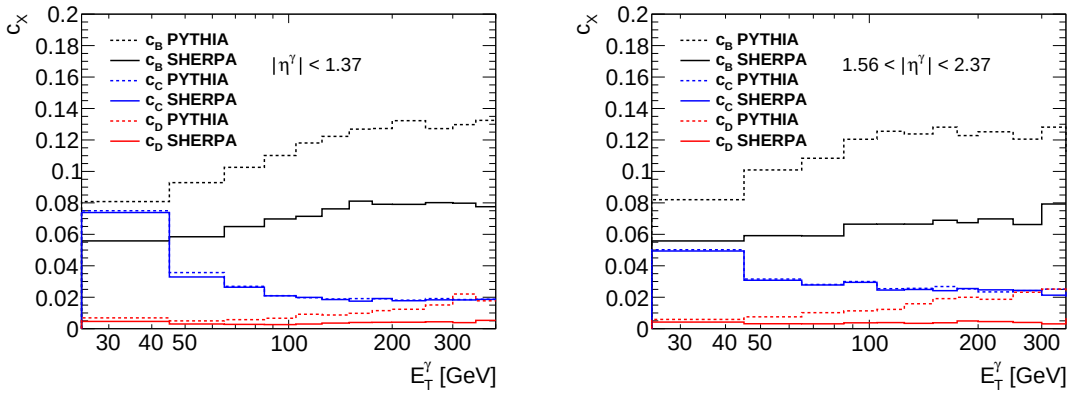

(a) (b)

Figure 6–5 – Leakage correction factors c_B, c_C and c_D in the SHERPA and PYTHIA samples as a function of the photon transverse energy for (a) the central region and (b) the forward region.

equation in N_A^{sig}, which can be solved via the usual quadratic formula to give

$$p^{\text{prompt-}\gamma} = \frac{1}{2N_A(c_B c_C - c_D)}\Big\{ c_B N_C + c_C N_B - N_D - c_D N_A + \Big[(c_B N_C + c_C N_B - N_D - c_D N_A)^2 - 4(c_B c_C - c_D)(N_B N_C - N_A N_D)\Big]^{1/2}\Big\}. \tag{6.7}$$

The other solution of the quadratic formula is rejected since it gives unphysical purity values, i.e. values outside the range 0 to 1. This equation expresses the purity in terms of quantities that are accessible in data. It is this equation that is used to extract the contribution of prompt-photon events in the selected events.

Figure 6–6 shows the prompt-photon purity in each E_{T}^γ bin as obtained with Equations 6.3 and 6.7. The effect of the MC correction is to increase the estimated purity.

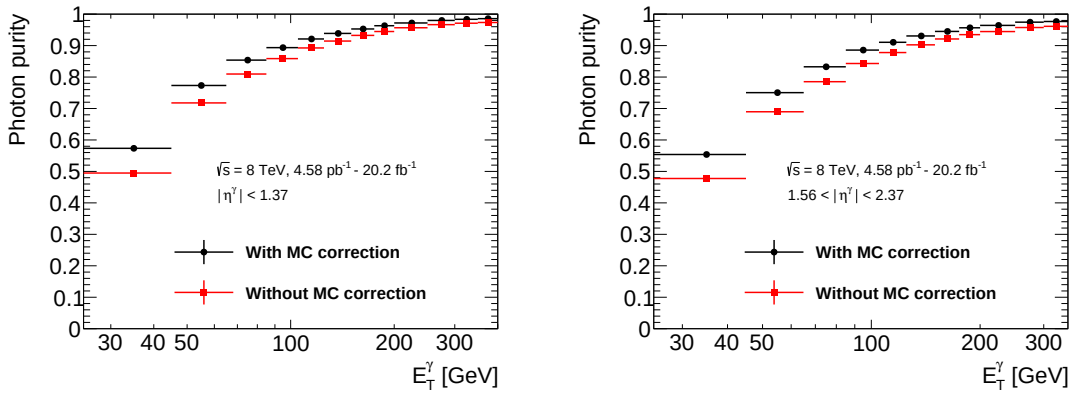

(a) (b)

Figure 6–6 – Prompt-photon purity in the selected recorded events as a function of the photon transverse energy for (a) the central region and (b) the forward region. The prompt-photon purity is shown with and without the MC correction for the signal leakage, which is obtained from the SHERPA samples. The statistical uncertainties in the distributions are specified with vertical error bars, but they are too small to be visible.

The correction is obtained from the SHERPA samples. The purity is observed to increase from about 50% to 100% as a function of E_{T}^{γ}.

The purity is measured in each E_{T}^{γ} bin to allow for a measurement of the cross section in each E_{T}^{γ} bin. However, the photon purity does not determine the flavour of the selected jet in the event. This is done by making use of the MV1c distribution. To properly take into account the photon purity in the extraction of the jet flavour, the purity needs to be measured also as a function of the MV1c weight. This is necessary as a slight dependence of the purity on the MV1c weight of the selected jet is observed.

Figure 6–7 displays the dependence of the photon purity as a function of the MV1c weight, using the values listed in Table 4–2 as bin boundaries, in the lowest-E_{T}^{γ} bin

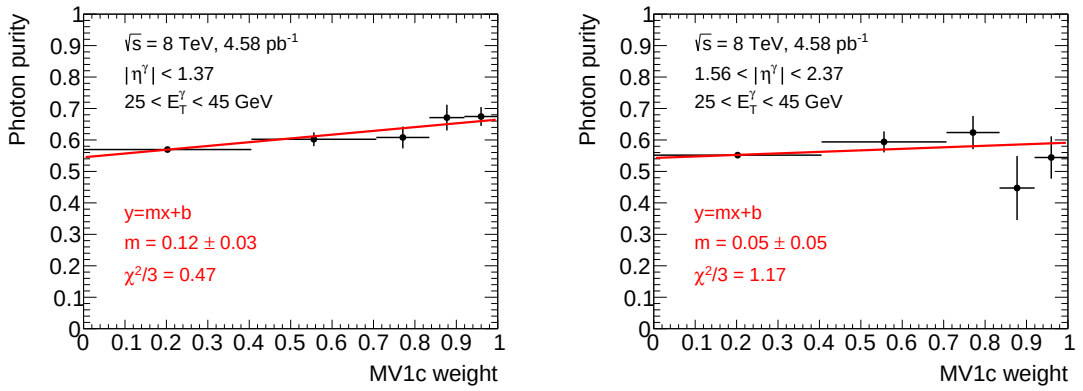

(a) (b)

Figure 6–7 – Measured prompt-photon purity with the MC correction obtained from the SHERPA samples as a function of the MV1c weight for (a) the central region and (b) the forward region. The vertical error bars correspond to the statistical uncertainty in the purity. A first-order polynomial is fitted to the measured values. The values of the fitted slope and of the reduced chi-squared are displayed.

as an example. A least-square fit of a first-order polynomial to the measured purity is performed to quantify the dependence. A statistically significant non-zero value for the slope is obtained in the central region, indicating an observable dependence of the purity on the MV1c weight, but not in the forward region.

The slope of the fitted polynomial in each E_{T}^{γ} bin is reported in Figure 6–8. It can be seen that, in the central region at low E_{T}^{γ} and in the forward region at high E_{T}^{γ}, a statistically significant dependence of the purity on the MV1c weight is observed. The cause of the dependence of the photon purity on the MV1c weight is not investigated further due to the lack of background MC samples, which prevents a study of the relation between the purity and the flavour of the selected jet. Therefore, to be as general as possible and to take into account the effects on the measured cross section

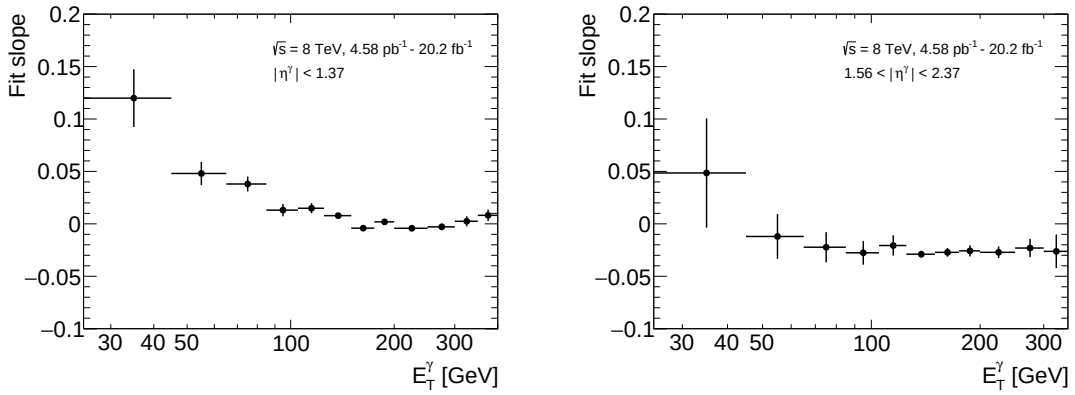

(a) (b)

Figure 6–8 – Fitted values of the slope of the first-order polynomials as a function of the transverse photon energy for (a) the central region and (b) the forward region. The vertical error bars represent the statistical uncertainty in the fitted slope.

of such a dependence, the purity is measured simultaneously as a function of E_{T}^{γ} and the MV1c weight. This two-dimensional purity is shown in Figure 6–9. The values of the MV1c weight are categorized according to the working points such as to correspond to the MV1c b-jet b-tagging efficiencies, i.e. the categories are equivalent to the bins in Figure 6–7. It is these values of the photon purity that are used to measure the $\gamma + b$ production cross section.

6.2 *b*-jet Signal

The product of the number of selected events in the recorded dataset with the prompt-photon purity results in the number of events containing a prompt photon and a jet. From this number of events, the number of events in which the selected jet is a b-jet needs to be extracted. The background of b-jets can be either c-jets or light jets. The

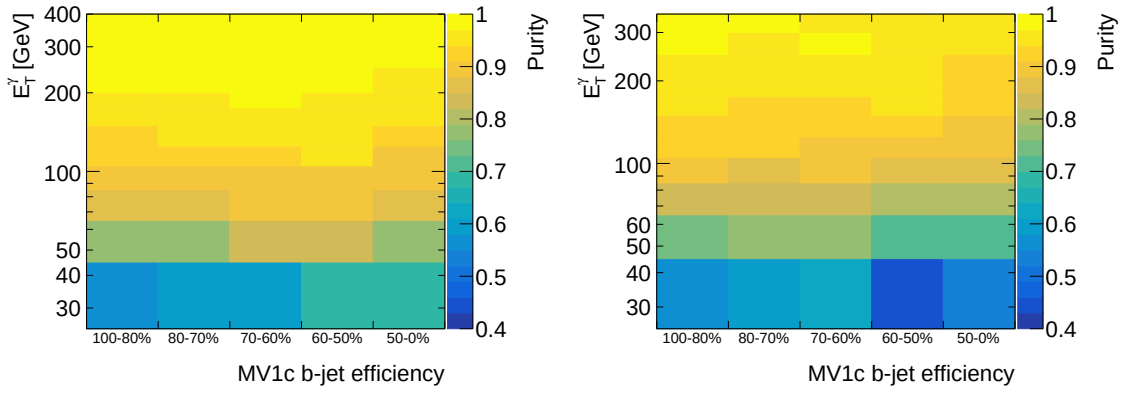

(a) (b)

Figure 6–9 – Measured prompt-photon purity with the MC correction obtained from the SHERPA samples in the selected recorded events as a function of the MV1c b-jet b-tagging efficiency and the photon transverse energy for (a) the central region and (b) the forward region.

b-jet signal is extracted statistically from the recorded events by using information about the jet flavours from the MC samples.

A procedure based on a template fit is used to separate the b-jet signal from the c- and light jets. The template fit involves the use of known distributions, the templates, to fit a distribution that is an admixture of the known ones, i.e. the data distribution. The template fit keeps the shapes of the templates intact but changes their normalizations such that their sum agrees with the data. The templates are obtained from MC events passing the event selection and are separated according to the flavour of the selected jet. A calibration of the shapes of the templates is required to ensure that the templates can properly describe the data.

The template fit relies on the differing shapes of the templates to determine their fractions. An observable sensitive to the b-jet flavour is required, such that the

shape of the b-jet template is different from the shapes of the other templates. This observable is chosen to be the MV1c weight that is usually used for tagging jets. The templates are separated into five bins with the bin boundaries given by the values listed in Table 4–2. This choice of binning permits the use of the continuous calibration, discussed at the end of Section 4.3.3. Each bin of the template can be individually calibrated. This use of per-bin scale factors allows to calibrate the shape of the template.

This approach, which does not tag jets and instead uses the tagging weight itself as the observable for the template fit, is different than that used in the Tevatron $\gamma + b$ measurements [47, 49]. In these measurements, the jets were tagged using an observable sensitive to the b-jet properties and a template fit is performed on these tagged jets using a different observable sensitive to the b-jet properties. In general, this different observable is likely to be based on the same properties of b-jets as the tagging weight, i.e. the track impact parameters, the secondary vertex and the line of flight of the decay chain. If a calibration of the shapes of the templates is necessary, it will be affected by similar sources of uncertainty as those affecting the calibration of the b-tagging efficiency. Non-trivial correlations between these related sources have to be understood. To avoid such studies and to simplify the analysis, jets are not tagged and the continuously calibrated MV1c distributions are used as templates. This approach has been used previously for the measurement of the cross section of the production of $t\bar{t}$ in association with b-jets in proton–proton collisions at $\sqrt{s} = 8$ TeV [187]. The measurement presented in this thesis marks the first time that this approach is used for the measurement of a differential cross section.

Concretely, the template fit is performed via a binned maximum likelihood fit. The fractions of the three jet-flavour templates are fitted to the data. The sum of all three fractions must sum to unity: the third fraction is fully determined from the first two. These two fractions, f_1 and f_2, are the two fit parameters.

The probability for an event to appear in bin i of the distribution of the MV1c weight, $S_i(f_1, f_2)$, is obtained from the sum of the templates and is

$$S_i(f_1, f_2) = f_1 B_i + (1 - f_1)[f_2 C_i + (1 - f_2) L_i]. \tag{6.8}$$

The quantities B_i, C_i and L_i are the values in bin i of the b-, c- and light-jet templates respectively. They are unit-normalized across all bins such that S_i is also unit-normalized and describes a proper probability density function. The relations of these fractions to the physical b-, c- and light-jet fractions are respectively $f^{b\text{-jet}} = f_1$, $f^{c\text{-jet}} = (1 - f_1) f_2$ and $f^{\text{light-jet}} = (1 - f_1)(1 - f_2) = 1 - f^{b\text{-jet}} - f^{c\text{-jet}}$. This particular choice of parameterization allows both fitted fractions to be varied independently in the range 0 to 1 without mathematical inconsistencies.

The binned likelihood function to be maximized is $L(f_1, f_2)$. The total number of events, N, is fixed, i.e. it is the product of the photon purity with the number of selected events. Only the fitted fraction of each template is of interest to the cross-section measurement. The numbers of events in the bins of the MV1c distribution are thus constrained by $\sum_i n_i = N$, where n_i is the number of events in bin i. The measured distribution in data follows a multinomial distribution with a likelihood

given by

$$L(f_1, f_2) = N! \prod_{i=1}^{5} \frac{[S_i(f_1, f_2)]^{n_i}}{n_i!}. \tag{6.9}$$

The negative log-likelihood to be minimized is given by

$$-\ln L(f_1, f_2) = -\sum_{i=1}^{5} n_i \ln S_i(f_1, f_2), \tag{6.10}$$

where the terms that do not depend on the parameters to be fitted are omitted. The product and the sum run over the five bins of the MV1c distribution. The statistical uncertainties in the data and in the MC distributions are not taken directly into account in the fit.

Figure 6–10 shows the templates and the data distribution before and after the template fit in the lowest-E_{T}^{γ} bin, while Figure 6–11 shows the impact of the fit in the highest-E_{T}^{γ} bin. The agreement between the data and the Sherpa distributions is also displayed in those figures. All sources of uncertainties, which are discussed in Chapter 8, are taken into account, including their correlations. The data and the Sherpa distributions are not expected to agree before the template fit is performed because large theoretical uncertainties are expected in the Sherpa distributions. After the template fit is performed, a good agreement is observed, given the considered uncertainties. The bins driving the fit, and hence those with the smallest uncertainties, are the 100–80% MV1c bin, due to its large number of events, and the 50–0% MV1c bin, due to its b-jet discriminating power. These bins respectively drive the fit of the light-jet and of the b-jet templates. The good agreement of the fit results with the data gives confidence that the fitted Sherpa distributions describe adequately the data.

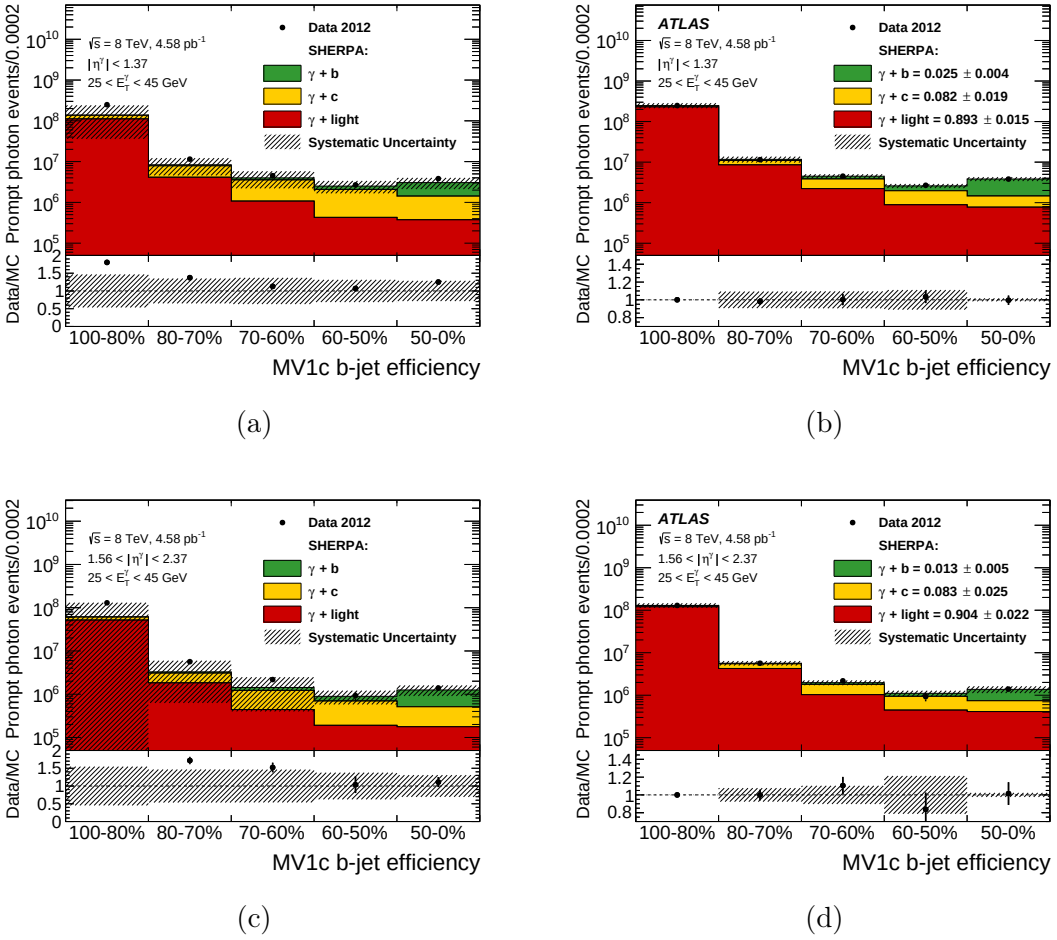

Figure 6–10 – Data and SHERPA distributions of the MV1c weight in γ + jet events in the lowest-E_{T}^{γ} bin of (a) the central region before the template fit, (b) the central region after the template fit, (c) the forward region before the template fit and (d) the forward region after the template fit. The ratio of the data distribution to that of SHERPA is shown in the bottom panel. The data distribution has been subtracted of background photons with the prompt-photon purity and is weighted by the prescale factor associated to the E_{T}^{γ} bin to bring the numbers of events to those corresponding to an integrated luminosity of 20.2 fb^{-1}. The error bars in the data correspond to the statistical uncertainty. The uncertainty band includes all sources of systematic uncertainties that are discussed in Chapter 8. The numbers in the legend are the fitted fractions of each template and their statistical uncertainties.

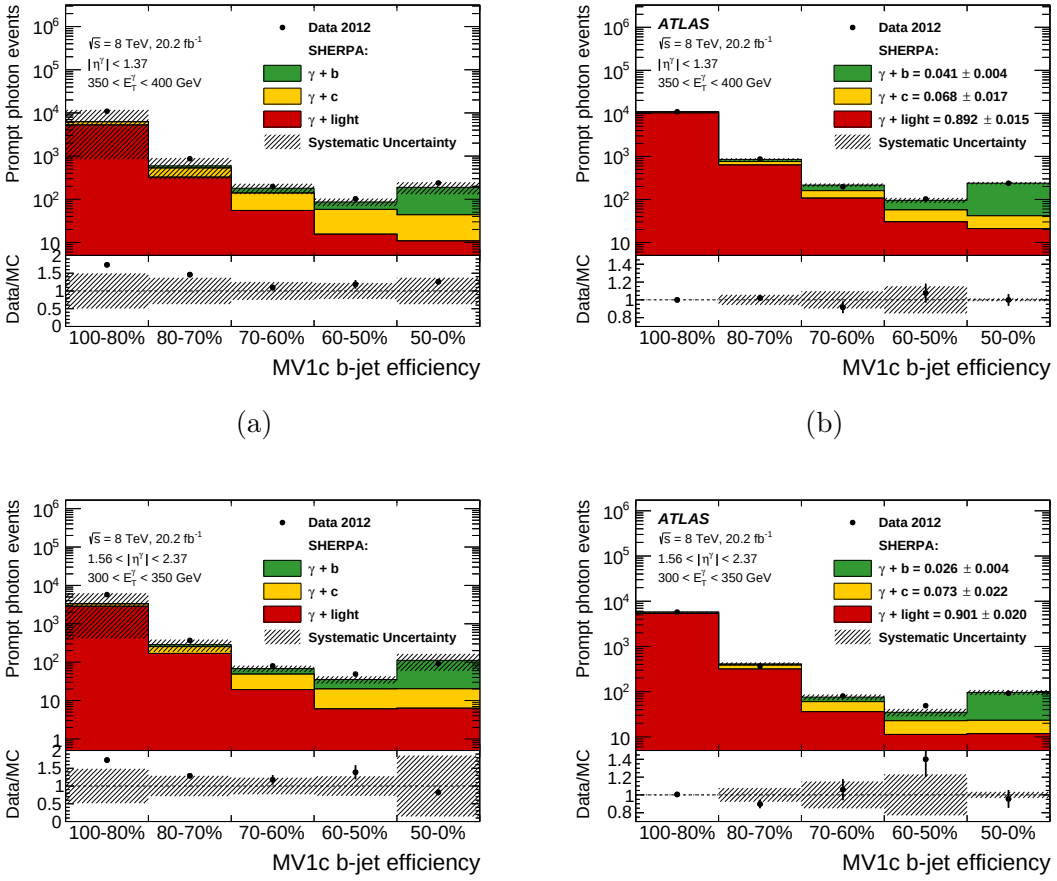

Figure 6–11 – Data and SHERPA distributions of the MV1c weight in γ + jet events in the highest-E_{T}^{γ} bin of (a) the central region before the template fit, (b) the central region after the template fit, (c) the forward region before the template fit and (d) the forward region after the template fit. The ratio of the data distribution to that of SHERPA is shown in the bottom panel. The data distribution has been subtracted of background photons with the prompt-photon purity. The error bars in the data correspond to the statistical uncertainty. The uncertainty band includes all sources of systematic uncertainties that are discussed in Chapter 8. The numbers in the legend are the fitted fractions of each template and their statistical uncertainties.

Several studies performed to inspect the validity of the fit give further confidence in the accuracy of the values of the flavour fractions obtained with the template fit. For example, Figure 6–12 shows the distributions of the negative log-likelihood for the lowest- and the highest-E_{T}^{γ} bins. It can be seen that each of the distributions has a clear minimum at the fitted values of the fractions. Additionally, the partial anticorrelation between $f^{b\text{-jet}}$ and $f^{c\text{-jet}}$, due to the constraint on the sum of the fractions, can be seen from the contour levels of the distributions.

The closure of the template fit among the MC samples has also been investigated, in which the templates of one MC sample, for example those of Sherpa, are used to fit the event distribution of another sample, for example that of Pythia. It is found that the flavour fractions obtained with the template fit describe accurately the flavour fractions of the sample at the particle level.

To inspect the stability of the template fit with respect to background events, the template fit has been performed anew but without considering the 100–80% MV1c bin. The choice of removing this specific bin stems from the fact that this bin contains the largest amount of events and that these events are mostly light-jet background events. Removing this bin allows to alleviate the dependence of the fitting procedure on the background events. It is found that the fitted values in this approach do not change significantly with respect to those obtained when fitting the whole MV1c distribution, indicating that the values are indeed stable and are not dominated by background events.

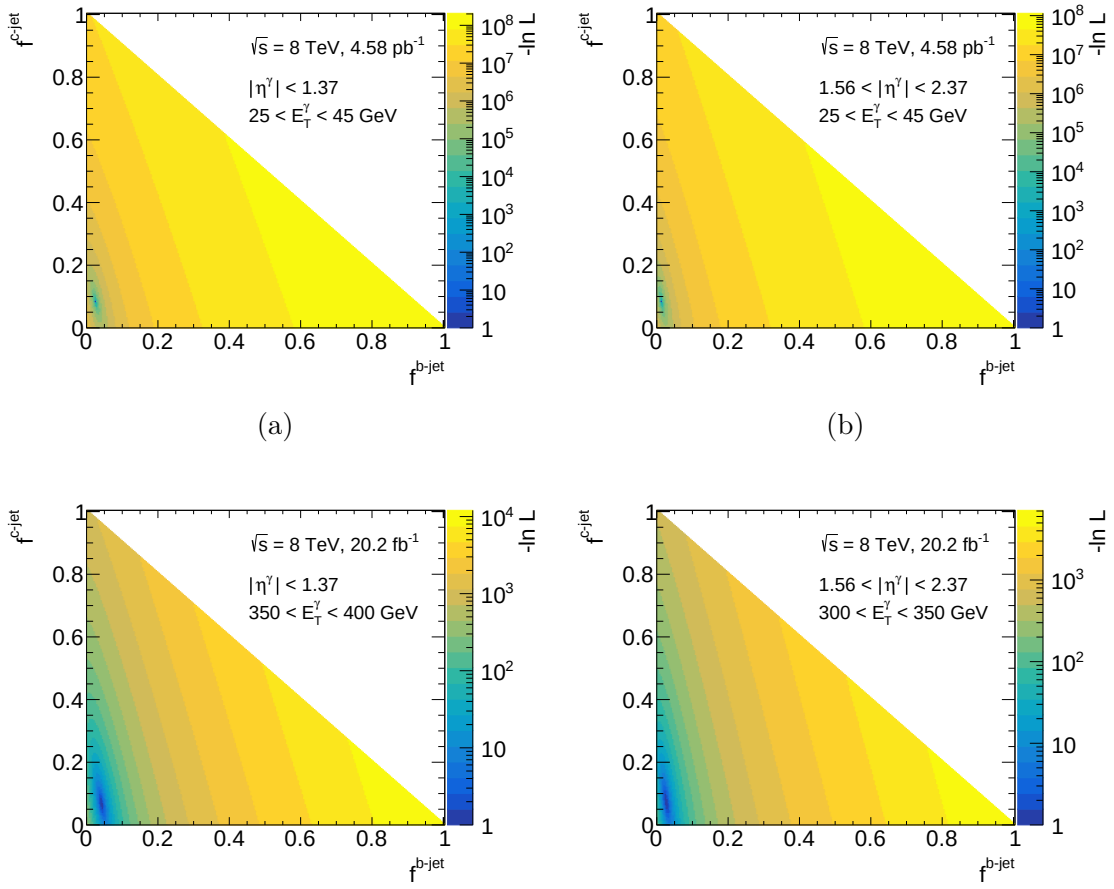

Figure 6–12 – Distribution of the negative log-likelihood as a function of the fitted fractions in (a) the lowest-E_{T}^{γ} bin of the central region, (b) the lowest-E_{T}^{γ} bin of the forward region, (c) the highest-E_{T}^{γ} bin of the central region and (d) the highest-E_{T}^{γ} bin of the forward region. The values of the distribution have been shifted such that the minimum value is 1.

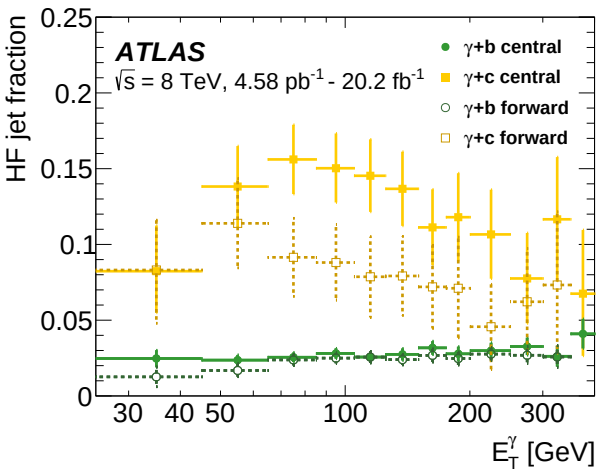

Figure 6–13 – Measured b- and c-jet fractions, i.e. the fitted heavy-flavour (HF) jet fractions, as a function of the transverse photon energy for both the central and the forward regions, as published in Ref. [188]. The fractions are defined with respect to recorded events containing a prompt photon and a jet. The vertical error bars correspond to the total uncertainty in the fractions, including the statistical uncertainty and all sources of systematic uncertainties that are discussed in Chapter 8.

The b- and c-jet fractions in data as a function of E_{T}^{γ} are given in Figure 6–13. These are the fractions of $\gamma + b$ and $\gamma + c$ events in the selected and purity-corrected $\gamma +$ jet recorded events. The light-jet fraction can be obtained via $f^{\text{light-jet}} = 1 - f^{b\text{-jet}} - f^{c\text{-jet}}$. The values of the b-jet fraction are observed to be about 3%. Since the scales of the momentum exchange in the proton–proton collisions measured in this analysis are well above the values of the b- and c-quark masses, the matrix elements for $\gamma + b$ and $\gamma + c$ processes are similar. Differences in the production of these types of events then come from differences in the b-quark and c-quark PDFs. Due to the heavier mass of the b quark compared to that of the c quark, the b-quark PDF is smaller than that of the c quark, resulting in smaller values of the b-jet fraction compared to those of the c-jet fraction. The values of the b-jet fraction are indeed observed to be smaller.

Concerning the dependence of the flavour fractions on E_{T}^{γ}, the b- and c-quark PDFs increase as a function of the energy scale of the hard scattering. The E_{T}^{γ} value of the event can be used as an approximation of the energy scale of the hard interaction since it is a boost-invariant energy scale. However, larger E_{T}^{γ} values correspond not only to higher interaction energy scales but also to larger values of the fraction x of the proton momentum, as derived in Appendix A. Although the b- and c-quark PDFs increase with the interaction energy, the PDFs decrease as a function of x. The net effect on the PDFs of these opposite trends as a function of E_{T}^{γ} depends on the precise interplay between the dependences of the PDFs on the interaction energy scale and on the fraction of the proton momentum. The overall shapes of the fractions are similar to what is seen in the MC samples at the particle level, giving confidence in the accuracy of the measurement of the fractions.

CHAPTER 7
Data Unfolding

This chapter covers the data unfolding procedure, which produces a particle-level distribution from a given detector-level distribution. This procedure is necessary to take the measured detector-level distribution of $\gamma + b$ events to the particle level, such as to obtain the particle-level cross section. The unfolding procedure hinges on the accurate simulation of the detector. The detector simulation allows to describe how effects specific to the detector transform a particle-level distribution into the corresponding detector-level distribution. The first section describes these detectors effects. The second section discusses the implementation of two unfolding methods that are used to unfold the measured E_{T}^{γ} distribution of $\gamma + b$ events and thus produce the differential cross section of the production of $\gamma + b$ events as a function of E_{T}^{γ}.

7.1 Detector Effects

Following the event selection and the signal extraction, the distribution of recorded $\gamma + b$ events at the detector level is obtained. However, this distribution cannot be used directly as is to determine the number of $\gamma + b$ events at the particle level because of detector effects that affect this distribution. These detector effects distort the particle-level distribution to produce the one that is measured at the detector level.

Mathematically, the distortion is given by the integral equation

$$g(d) = \int R(d,p) f(p) dp, \tag{7.1}$$

where $f(p)$ is the particle-level distribution of interest, $R(d,p)$ is the response function of the detector and $g(d)$ is the detector-level distribution that is measured. The response function serves as the kernel of the integral equation and is specific to the detector and to a given physics analysis. In practice, due to the finite detector resolution and the finite number of events, the distributions are discretized in bins. The previous equation becomes then

$$N_{D_j} = \sum_i R_{ji} N_{P_i}, \tag{7.2}$$

with N_{P_i} being the number of events in bin i of the particle-level distribution, R_{ji} being the response matrix and N_{D_j} being the number of events in bin j of the detector-level distribution.

The response matrix can be interpreted as the conditional probability

$$R_{ji} = P(D_j|P_i). \tag{7.3}$$

It is the probability of measuring an event in bin j of the detector-level distribution given that it is found in bin i of the particle-level distribution.

The detector effects that are included in the detector response can be categorized into three types:

- **Non-linear response:** This category includes non-linear effects in the detector response, reconstruction algorithms of physical objects and potential biases introduced by the selection cuts of the physics analysis. A variable at the particle level is transformed into a different quantity at the detector level. This type of effect results in a distortion of the particle-level distribution.

- **Detector resolution:** The finite resolution of the detector in the measurement of particle kinematics has the effect of smearing distributions. This type of effect results in events migrating from one bin of the particle-level distribution to different bins of the corresponding detector-level distribution.

- **Efficiency:** This effect encompasses detector, reconstruction and selection inefficiencies. This type of effect results in a reduction in the number of events in the detector-level distribution compared to that in the particle-level distribution.

These detector effects are investigated by using simulated event samples that include a full simulation of the ATLAS detector response. Selected events at the detector level can then be compared to those selected at the particle level to investigate the detector effects.

The detector effects can be investigated via the transfer matrix, which is the two-dimensional distribution of events satisfying both the detector- and the particle-level selections as a function of the detector-level and particle-level quantities. The transfer matrix is related to the response matrix via a normalization of its elements. Figure 7–1 shows the transfer matrix of the photon transverse energy, i.e. the distribution of

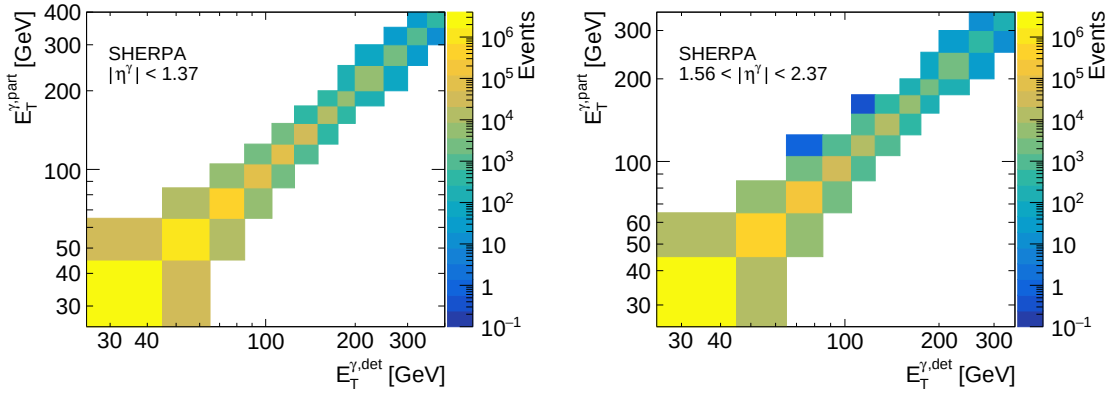

(a) (b)

Figure 7–1 – Distribution of SHERPA events satisfying both the detector- and the particle-level selections as a function of the detector-level and the particle-level photon transverse energies for (a) the central region and (b) the forward region.

events that satisfy both the detector- and the particle-level selections as a function of both the particle-level and detector-level E_{T}^{γ}. Here, the event selection at the detector level requires that the selected jet be b-jet in addition to the criteria discussed in Section 5.2. This is necessary in order to be representative of the recorded events after the signal extraction. It can be seen that the matrix is nearly diagonal, with off-diagonal elements whose values are around 5% of the values of the neighbouring diagonal elements. This indicates a good linear detector response and that few events are migrating across bins.

The small amount of event migrating between bins is due to the small resolution of the photon transverse energy compared to the chosen widths of the bins of the E_{T}^{γ} distribution. Figure 7–2 shows the distribution of the relative difference in the detector- and particle-level E_{T}^{γ}. A relative energy resolution of about 3% is observed. This is to be compared to the widths of the E_{T}^{γ} bins, which are typically 20% of the

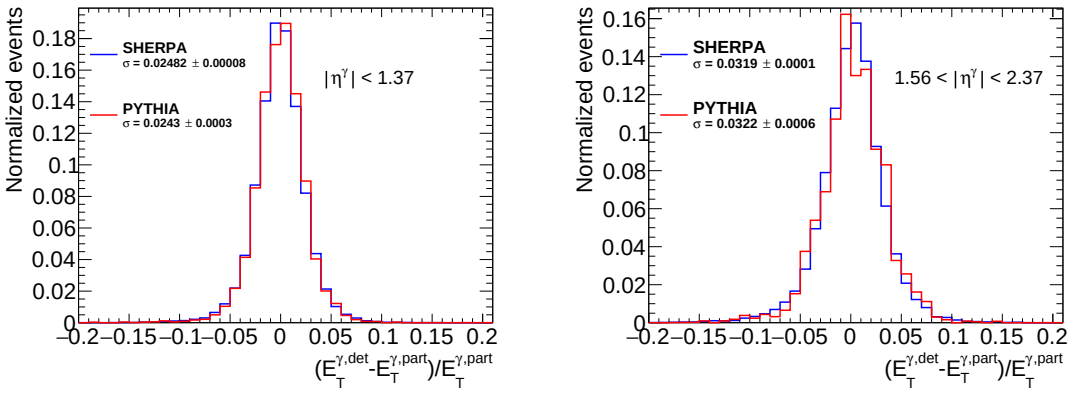

(a) (b)

Figure 7–2 – Normalized SHERPA and PYTHIA distributions of the relative difference between the detector- and the particle-level photon transverse energies for (a) the central region and (b) the forward region. The standard deviations of the distributions are displayed in the legend.

value of the lower E_{T}^{γ} boundary. Figure 7–3 shows the distribution of the difference between the photon pseudorapidities at the detector and the particle levels. A resolution of about 0.02 is observed. This is smaller than the width in pseudorapidity of 0.19 of the transition region between the central and the forward regions. As such, this motivates the ability to study the detector effects separately in the central and forward regions.

The combined reconstruction and selection efficiency of $\gamma + b$ events at the detector level in bin i, ϵ_i is defined as

$$\epsilon_i = \frac{\sum_j N_{P_i D_j}}{N_{P_i}}, \tag{7.4}$$

where $N_{P_i D_j}$ is the number of events associated to the element of the transfer matrix corresponding to bin i and j of the particle-level and detector-level quantities respectively. The efficiency includes the effects of all efficiencies related to the reconstruction

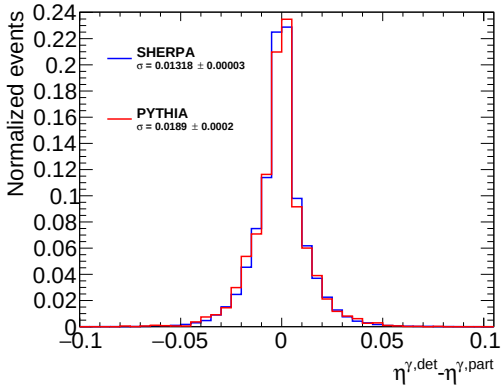

Figure 7–3 – Normalized SHERPA and PYTHIA distributions of the difference between the detector- and the particle-level photon pseudorapidities. The standard deviations of the distributions are displayed in the legend.

or the selection of events. In addition, resolution effects can have an impact on the efficiency. When a value of a given quantity at the particle level is close to a cut value of the event selection, the event can pass the particle-level cut but fail the detector-level cut due to the finite detector resolution.

In the case of the photon transverse energy, the resolution can cause a reduced efficiency in the lowest-E_{T}^{γ} bin. Also, since the transverse momenta of the selected jet and of the selected photon tend to have the same values, the efficiency measured in the low-E_{T}^{γ} bins are decreased by a similar effect related to the jet p_{T}. This effect is bigger than that related to E_{T}^{γ}, since $p_{\mathrm{T}}^{\mathrm{jet}}$ has a worse resolution. The effect is amplified further due to the calibration of the jet energy. The calibration is done with respect to particle jets that do not contain muons or neutrinos, while the particle jets investigated in the analysis do contain these particles. Therefore, in the analysis, the particle-level jets will have larger values of transverse momentum than

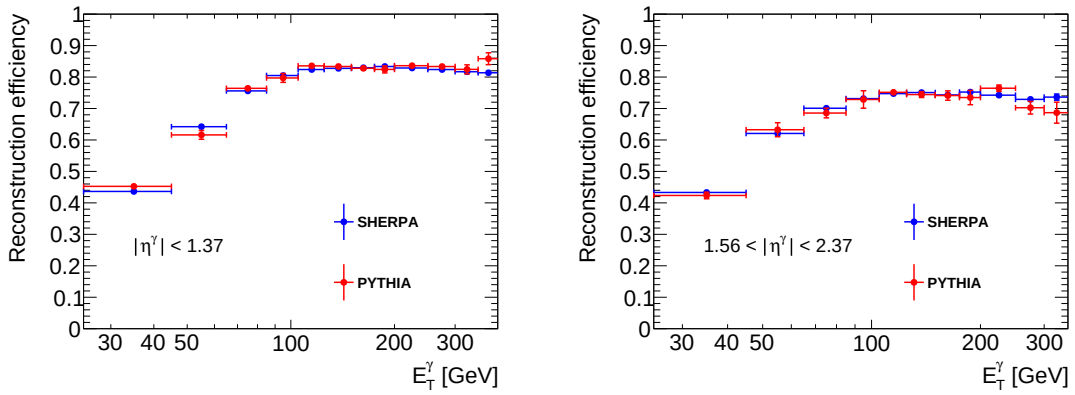

(a) (b)

Figure 7–4 – Combined reconstruction and selection efficiency in the SHERPA and PYTHIA samples as a function of the particle-level photon transverse energy for (a) the central region and (b) the forward region. The vertical error bars correspond to the statistical uncertainty in the efficiency.

the corresponding detector-level jets. The particle jets are more likely to satisfy the $p_{\mathrm{T}}^{\mathrm{jet}}$ cut than the detector-level jets. Also contributing to the inefficiency at low E_{T}^{γ} is the additional requirement of the JVF cut for jets with $p_{\mathrm{T}} < 50$ GeV. Furthermore, the photon identification efficiency is smaller at low E_{T}^{γ} than at high E_{T}^{γ}.

Figure 7–4 shows the combined reconstruction and selection efficiency obtained using simulated signal events. The combination of all the effects at low-E_{T}^{γ} discussed above reduces the combined efficiency to about 45% in the lowest-E_{T}^{γ} bin. In contrast, the efficiency is about 80% (75%) in the highest-E_{T}^{γ} bins of the central (forward) region. In those bins, the dominant sources of inefficiencies are from the photon reconstruction, identification and isolation. The forward region has a lower combined efficiency due to the lower efficiency of the photon reconstruction in that region.

The resolution effects related to the crossing of a selection cut threshold, such as that on E_{T}^{γ} mentioned above, can reduce the efficiency if the event satisfies the particle-level cut but not the detector-level cut. The opposite effect, i.e. an event that does not satisfy the particle-level cut but does satisfy the detector-level cut, produces background events from the perspective of the fiducial phase space. This background contribution can be quantified by the combined reconstruction and selection purity in a bin j, p_j, which is defined as

$$p_j = \frac{\sum_i N_{P_i D_j}}{N_{D_j}}. \tag{7.5}$$

Figure 7–5 shows the combined reconstruction and selection purity obtained using simulated signal events. The purity at high E_{T}^{γ} is about 96%. The remaining 4% of background contamination is primarily due to resolution effects related to the isolation energy. At low E_{T}^{γ}, the purity is approximately 85%, lower than that at high E_{T}^{γ} values. Background contamination at low E_{T}^{γ} is primarily due to resolution effects related to the jet transverse momentum.

7.2 Data Unfolding Methods

To compare theory predictions against data, generated events can be interfaced to a detector simulation to produce detector-level distributions. These samples can then be compared to the measured detector-level distribution, allowing to test the theoretical model that generated the samples. An approach that is more versatile is instead to unfold the detector effects from the measured detector-level distribution, bringing it to the particle level. This is desirable since it makes the measurement independent

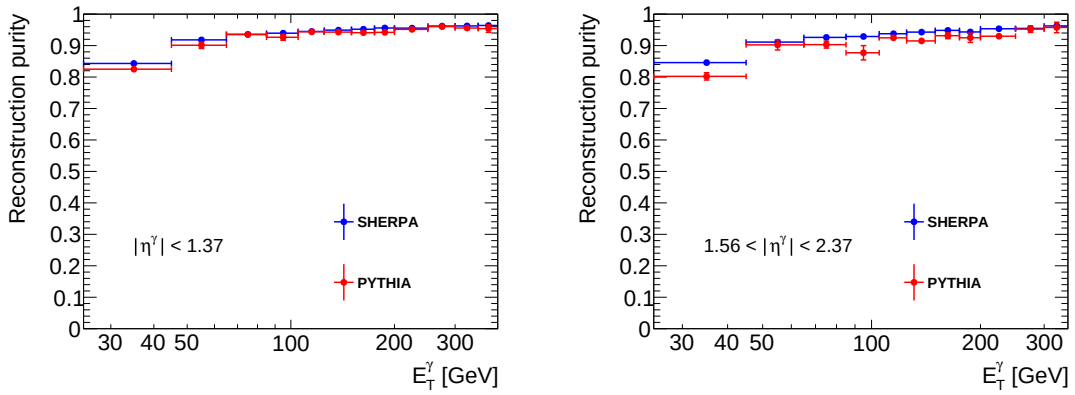

(a) (b)

Figure 7–5 – Combined reconstruction and selection purity in the SHERPA and PYTHIA samples as a function of the detector-level photon transverse energy for (a) the central region and (b) the forward region. The vertical error bars correspond to the statistical uncertainty in the purity.

of the detector. The measured distribution can then be compared directly to the distributions of generated samples or to unfolded measurements obtained using other detectors.

The data unfolding procedure corresponds to solving Equation 7.2 for N_{P_i} given a measured N_{D_j}, and a R_{ji} obtained using simulated events. The procedure is not simply the inversion of the response matrix since the response matrix can be singular. Additionally, measured distributions and the response matrix are affected by statistical fluctuations since they are obtained from samples with finite amounts of events. The unfolding procedure should avoid being sensitive to these fluctuations. Several unfolding techniques have been developed [189]. Two techniques have been investigated for the case of the measurement of the $\gamma + b$ cross section: the bin-by-bin method and the iterative Bayesian method. Their implementations are now discussed.

7.2.1 Bin-by-bin Method

The bin-by-bin data unfolding method consists in the use of simple multiplicative correction factors that are derived and applied individually in each bin of a given detector-level distribution to bring it to the particle level. It is this unfolding method that is used to measure the $\gamma + b$ cross section.

The correction factor in bin i of a distribution, C_i^{unf}, is defined such that its product with the detector-level distribution gives the particle-level distribution:

$$C_i^{\text{unf}} = \frac{N_{P_i}}{N_{D_i}}. \tag{7.6}$$

To determine these correction factors, the quantities N_{P_i} and N_{D_i} are taken from simulated event samples. As such, the correction factors are sensitive to a possible mismodelling of the detector response in the simulated samples.

The correction factor corrects for signal events that have not been selected and for events that have been selected but which do not satisfy the particle-level cuts defining the fiducial phase space. If the transfer matrix is symmetric, then $C_i^{\text{unf}} = p_i/\epsilon_i$.

In the case of the measurement of the differential $\gamma + b$ cross section as a function of E_{T}^{γ}, the use of the bin-by-bin correction factors is motivated by the good resolution of the photon transverse energy, since it results in a small number of events migrating across E_{T}^{γ} bins. A small number of migrating events is necessary to ensure the accuracy of the unfolded distribution since the transfer matrix is not used in the calculation of the correction factors. In other words, the bin-by-bin data unfolding procedure does not properly take into account event migrations between bins.

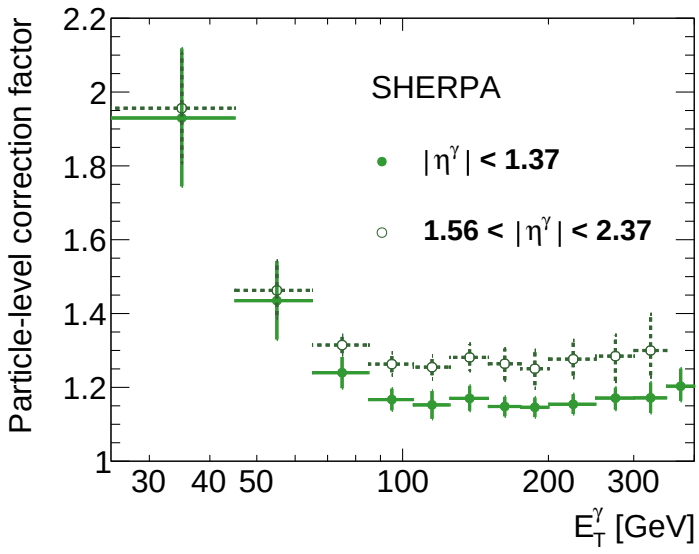

Figure 7–6 – Bin-by-bin particle-level correction factors obtained from SHERPA $\gamma + b$ events as a function of the reconstructed photon transverse energy in both the central and forward regions. The vertical error bars correspond to the total uncertainty in the factors, including the statistical uncertainty and all sources of systematic uncertainties that are discussed in Chapter 8.

Figure 7–6 shows the correction factors as a function of E_{T}^{γ} for $\gamma + b$ events. Since the E_{T}^{γ} transfer matrix is approximately symmetric, the correction factors correspond approximately to the ratio of the combined reconstruction and selection purity to the combined reconstruction and selection efficiency. The values of the efficiency are farther from unity than those of the purity. Thus, the correction factors are dominated by the inefficiency of the reconstruction and selection. The values and dependence of the correction factors as a function of E_{T}^{γ} can be explained in a similar way to those of the efficiency distribution shown in Figure 7–4.

Using the particle-level correction factors, the measured detector-level E_{T}^{γ} distribution of $\gamma + b$ events is unfolded to the particle level. The differential $\gamma + b$ cross section

can then be obtained by dividing by the integrated luminosity, as specified by Equation 3.1. The following equation summarizes all the quantities that are involved in the measurement of the $\gamma + b$ differential cross section in bin i of E_{T}^{γ} with the bin-by-bin data unfolding method:

$$\left(\frac{d\sigma^{\gamma+b}}{dE_{\mathrm{T}}^{\gamma}}\right)_i = \frac{1}{(\Delta E_{\mathrm{T}}^{\gamma})_i}\frac{1}{(\mathcal{L}_{\mathrm{int}}^{\mathrm{trig}})_i}\frac{1}{\epsilon_i^{\mathrm{trig}}}C_i^{\mathrm{unf}} f_i^{b\text{-jet}} \sum_{j\in \mathrm{MV1c}} p_{ij}^{\text{prompt-}\gamma} N_{ij}^{\gamma+\mathrm{jet}}, \tag{7.7}$$

where $(\Delta E_{\mathrm{T}}^{\gamma})_i$ is the width of the E_{T}^{γ} bin i, $(\mathcal{L}_{\mathrm{int}}^{\mathrm{trig}})_i$ is the integrated luminosity of the trigger criterion associated to the E_{T}^{γ} bin i, $\epsilon_i^{\mathrm{trig}}$ is the trigger efficiency of the trigger criterion associated to the E_{T}^{γ} bin i, C_i^{unf} is the particle-level correction factor in the E_{T}^{γ} bin i, $f_i^{b\text{-jet}}$ is the b-jet fraction in the E_{T}^{γ} bin i, $p_{ij}^{\text{prompt-}\gamma}$ is the prompt-photon purity in bin i of E_{T}^{γ} and bin j of the MV1c weight and $N_{ij}^{\gamma+\mathrm{jet}}$ is the number of events satisfying the detector-level selection in bin i of E_{T}^{γ} and bin j of the MV1c weight. It is this equation that is used to measure the differential $\gamma + b$ production cross section.

7.2.2 Iterative Bayesian Method

The iterative Bayesian data unfolding method consists in the repeated usage of Bayes' theorem [190]. It makes use of the transfer matrix and is thus of general applicability, i.e. it does not require that the number of events at the particle-level migrating into a different bin at the detector-level be small, in contrast to the bin-by-bin data unfolding method. The iterative Bayesian method is however more complex than the bin-by-bin method and it can be affected by large statistical uncertainties. This method is used to investigate the impact of event migrations on the unfolded distribution. Furthermore,

this unfolding method is less sensitive to the choice of simulated samples used to unfold distributions.

The unfolded number of events in bin i, $\hat{N}_{P_i}$, can be obtained from the measured detector-level distribution by using the equation [190]

$$\epsilon_i \hat{N}_{P_i} = \sum_{j=1}^{n_D} P(P_i|D_j) p_j N_{D_j}, \tag{7.8}$$

where ϵ_i is the combined reconstruction and selection efficiency, n_D is the number of bins in the detector-level distribution, $P(P_i|D_j)$ is the conditional probability that an event measured in bin j of the detector-level distribution is found in bin i of the particle-level distribution, p_j is the combined reconstruction and selection purity and N_{D_j} is the number of events in bin j of the detector-level distribution. The presence of the efficiency and of the purity in the equation is required as the conditional probability is only valid for events that satisfy both the detector- and the particle-level selections. The conditional probability is given by Bayes' theorem:

$$P(P_i|D_j) = \frac{P(D_j|P_i)P(P_i)}{\sum_{k=1}^{n_P} P(D_j|P_k)P(P_k)}, \tag{7.9}$$

where n_P is the number of bins in the particle-level distribution, $P(D_j|P_i)$ is an element in the response matrix and $P(P_i)$ is the prior probability that an event is found in bin i of the particle-level distribution. The prior can be obtained from the particle-level distribution via

$$P(P_i) = \frac{N_{P_i}}{N_{\text{tot}}}, \tag{7.10}$$

where N_{P_i} is the number of events in bin i of the particle-level distribution and N_{tot} is the total number of events that pass either the particle- or the detector-level

distribution. It is given by

$$N_{\text{tot}} = \sum_{i=1}^{n_P} N_{P_i} + \sum_{j=1}^{n_D} N_{D_j} - \sum_{j=1}^{n_D} \sum_{i=1}^{n_P} N_{P_i D_j}, \tag{7.11}$$

where $N_{P_i D_j}$ is an element in the transfer matrix.

The response matrix is related to the transfer matrix through

$$P(D_j|P_i) = \frac{P(P_i, D_j)}{P(P_i)} = \frac{N_{P_i D_j}}{N_{P_i}}. \tag{7.12}$$

The last equality of the previous equation holds since the joint probability is simply the normalized transfer matrix:

$$P(P_i, D_j) = \frac{N_{P_i D_j}}{N_{\text{tot}}}. \tag{7.13}$$

As a consequence of Equations 7.8 and 7.9, the unfolded distribution is directly dependent on the choice of the prior. The prior is obtained from the MC signal samples. After the application of Equation 7.8, the unfolded distribution, which has knowledge of both the MC and the data samples, can be normalized and taken as the new prior. This can be iterated, each time reducing the dependence of the unfolded distribution on the original MC prior. Each iteration however increases the statistical uncertainty in the unfolded distribution. An optimization of the number of iteration must be performed. The response matrix stays the same for all iterations.

Equation 7.8 can be written as

$$\hat{N}_{P_i} = \sum_{j=1}^{n_D} U_{ij} N_{D_j}, \tag{7.14}$$

where U_{ij} is called the unfolding matrix and is given by

$$U_{ij} = \frac{p_j}{\epsilon_i} P(P_i|D_j) = \frac{p_j}{\epsilon_i} \frac{N_{P_i D_j}}{\sum_{i=1}^{n_P} N_{P_i D_j}}. \tag{7.15}$$

The unfolding matrix corresponds to the bin-by-bin correction factors if the transfer matrix is diagonal. In other words, the bin-by-bin method and the first iteration of the Bayesian method with any diagonal transfer matrix produce the same unfolded distribution.

Since the prior is updated after each iteration, the unfolding matrix needs to be expressed as a function of it. The reconstruction efficiency and the reconstruction purity can be expressed in terms of the event probabilities as

$$\epsilon_i = \frac{\sum_{j=1}^{n_D} N_{P_i D_j}}{N_{P_i}} = \frac{\sum_{j=1}^{n_D} P(D_j|P_i) P(P_i)}{P(P_i)} = \sum_{j=1}^{n_D} P(D_j|P_i) \tag{7.16}$$

and

$$p_j = \frac{\sum_{i=1}^{n_P} N_{P_i D_j}}{N_{D_j}} = \frac{\sum_{i=1}^{n_P} P(D_j|P_i) P(P_i)}{P(D_j)}. \tag{7.17}$$

The efficiency does not depend on the prior but the purity does depend on it. The purity needs to be updated after each iteration.

A way of updating the purity is to include it in the definition of the conditional probability, giving the following new conditional probability

$$P'(P_i|D_j) = p_j P(P_i|D_j) = \frac{P(D_j|P_i) P(P_i)}{\sum_{k=1}^{n_P+1} P(D_j|P_k) P(P_k)}, \tag{7.18}$$

where the denominator of the fraction is a way of considering $P(D_j)$ as a function of the prior. It is achieved by including an additional bin in the particle-level distribution.

This bin corresponds to events that satisfy the detector-level selection but fail the particle-level selection. Doing this allows to treat those events at the particle level on the same footing as the other ones. The values of the additional elements of the transfer matrix, i.e. those at $i = n_P + 1$, are given by

$$N_{P_{n_P+1}D_j} = N_{D_j} - \sum_{i=1}^{n_P} N_{P_i D_j} \tag{7.19}$$

and the number of events in the additional bin of the particle-level distribution is

$$N_{P_{n_P+1}} = \sum_{j=1}^{n_D} N_{P_{n_P+1}D_j}, \tag{7.20}$$

such that $\sum_{i=1}^{n_P+1} N_{P_i} = N_{\text{tot}}$.

With the definition of this new conditional probability, the unfolding matrix becomes

$$U_{ij} = \frac{P'(P_i|D_j)}{\epsilon_i}. \tag{7.21}$$

It can be used in Equation 7.14 to obtain the unfolded distribution. After an iteration, the assignment $\hat{N}_{P_i} \to N_{P_i}$ can be done, giving the new prior

$$P(P_i) = \frac{\hat{N}_{P_i}}{\sum_{i=1}^{n_P+1} \hat{N}_{P_i}}. \tag{7.22}$$

This new prior is to be used in Equation 7.18 to give a new unfolding matrix and thus a new unfolded distribution. This can be iterated an arbitrary amount of times.

The differential $\gamma+b$ cross section in bin i of E_{T}^{γ} calculated using the iterative Bayesian data unfolding method is given by

$$\left(\frac{d\sigma^{\gamma+b}}{dE_{\mathrm{T}}^{\gamma}}\right)_i = \frac{1}{(\Delta E_{\mathrm{T}}^{\gamma})_i}\frac{1}{(\mathcal{L}_{\mathrm{int}}^{\mathrm{trig}})_i}\sum_j U_{ij}^{\mathrm{unf}}\frac{1}{\epsilon_j^{\mathrm{trig}}}f_j^{b\text{-jet}}\sum_{k\in\mathrm{MV1c}} p_{jk}^{\text{prompt-}\gamma}N_{jk}^{\gamma+\mathrm{jet}}, \tag{7.23}$$

where U_{ij}^{unf} is the unfolding matrix of the previous iteration.

In general, few iterations of the Bayesian data unfolding procedure are necessary [190]. Since the E_{T}^{γ} transfer matrix is nearly diagonal, it is expected that the unfolded distribution is stable against variations in the number of iterations. It is preferable to choose a number of iterations as small as possible, since larger numbers of iterations increase the statistical uncertainty in the unfolded distribution. There is however a qualitative difference between using a single iteration and two iterations of the unfolding procedure. Using a single iteration of the unfolding procedure results in an unfolded distribution that is directly dependent on the MC prior. Using two iterations of the unfolding procedure results in a reduced dependence of the unfolded distribution on the MC samples. Therefore, two iterations are considered to be optimal for the Bayesian data unfolding of the E_{T}^{γ} distribution of $\gamma + b$ events.

Figure 7–7 shows the unfolding matrix after two iterations of the iterative Bayesian data unfolding procedure. As for the case of the transfer matrix, it is nearly diagonal with the value of the off-diagonal elements being typically 5% of that of the diagonal elements.

The unfolded E_{T}^{γ} distribution of $\gamma + b$ events can be divided by the detector-level distribution to provide similar unfolding correction factors as the bin-by-bin method.

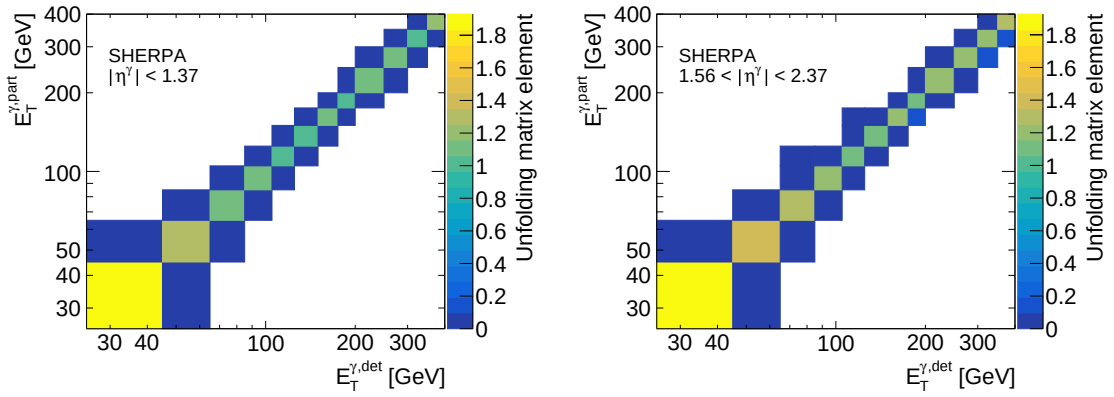

(a) (b)

Figure 7–7 – Unfolding matrix of the E_{T}^{γ} distribution of SHERPA $\gamma + b$ events after two iterations of Bayes' theorem for (a) the central region and (b) the forward region.

This allows to compare the two unfolding methods. Figure 7–8 gives the comparison of the bin-by-bin correction factors with those of the iterative Bayesian method with one, two and three iterations.

The comparison of the bin-by-bin correction factors with those of the Bayesian approach with one iteration allows to quantify the impact of neglecting the off-diagonal elements of the transfer matrix in the bin-by-bin unfolding process. It is seen that these factors are in agreement and thus the impact of event migrations is not significant. Similarly, the factors of the Bayesian approach with two iterations agree with those using three iterations, as expected from the stability of the unfolded distribution on the number of iterations beyond the first iteration. However, statistically significant differences can be observed between the bin-by-bin correction factors and those obtained using the Bayesian approach with two iterations. Such differences quantify the mismodelling of detector effects by the simulated event samples. Since the

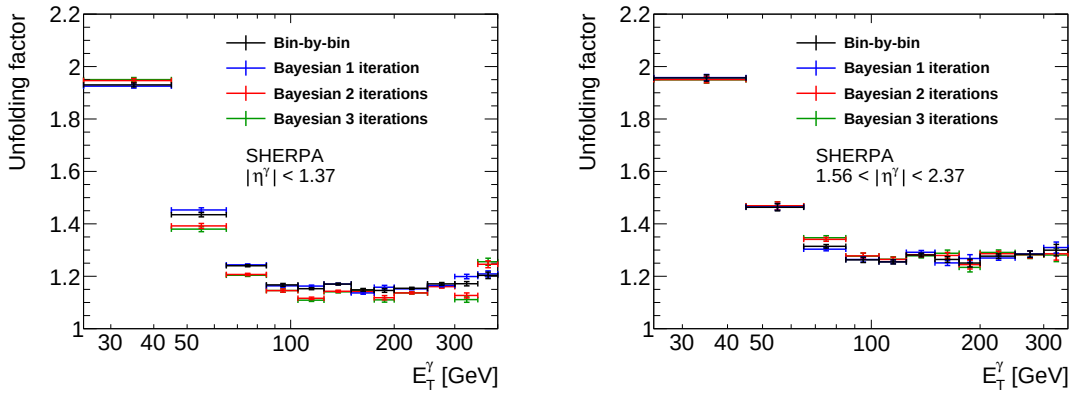

(a) (b)

Figure 7–8 – Unfolding correction factors of the bin-by-bin and of the 1-, 2- and 3-iteration Bayesian unfolding methods obtained from SHERPA $\gamma + b$ events as a function of the photon transverse energy in (a) the central region and (b) the forward region. The vertical error bars correspond to the statistical uncertainty in the factors.

differences are small, at most 5%, the bin-by-bin method is kept as the nominal approach as it is simpler to implement and to interpret.

CHAPTER 8
Uncertainties

This chapter provides a description of the uncertainties that have been evaluated in the measured values of the $\gamma + b$ differential cross section as a function of E_{T}^{γ} for the central and the forward regions. Uncertainties arise from the finite size of the event samples, from the calibration of the reconstructed objects, from the modelling of the signal events and from the choice of analysis techniques. Since the measurement is to be compared to theoretical predictions, uncertainties in the theoretical predictions are also described. The uncertainties in the theoretical predictions arise from the truncation of the infinite perturbative QCD series to a finite order and from the uncertainties in the quantities that are used as input to the calculations. To reduce the size of both the uncertainties in the measurement and in the theoretical predictions, the ratio of the cross section in the central region to that in the forward region is measured. The uncertainties in the measured and predicted values of the cross-section ratio are also presented. The first section of this chapter discusses the measurement uncertainties, while the second section discusses the theoretical uncertainties.

8.1 Measurement Uncertainties

The measurement of the cross section as given by Equation 7.7 depends on several different ingredients: physical objects that are reconstructed from detector signals, different theoretical models in the generation of simulated signal samples and analysis

techniques chosen to make the measurement. Each of these ingredients are affected by uncertainties, the systematic uncertainties, that in turn affect the measured values of the cross section. In addition, the measured values are affected by statistical uncertainties since both the recorded and the simulated event samples contain a finite number of events.

Most sources of systematic uncertainties are positively correlated across the central and the forward regions. Since a ratio of positively correlated quantities has a lower variance than either of the quantities, the ratio of the cross section in these regions is measured to obtain a more precisely measured quantity against which to compare theoretical predictions.

The determination of the statistical uncertainties is explained in the next section. Sources of systematic uncertainties are described in the following section. Also discussed are cross-check studies, which do not result in uncertainties. The presentation of the size of the uncertainties and of the total uncertainty in the measured values then follows.

8.1.1 Statistical Uncertainty

Due to the use of event samples with finite numbers of events, measured quantities are affected by a statistical uncertainty. The source of this statistical uncertainty can be attributed to the Poisson process of selecting an event in a given bin of a distribution. For example, the number of selected events in a given bin of the E_{T}^{γ} distribution, N, is the sum of N independent Poisson distributions of mean one, which is itself a Poisson distribution of mean N. The statistical uncertainty in that number, ΔN,

is given by the standard deviation of the Poisson distribution of mean N, that is $\Delta N = \sqrt{N}$. Such a statistical uncertainty is present in both the recorded and the simulated event samples. The statistical uncertainty in the MC event samples is categorized as a systematic uncertainty of the measurement.

To propagate these Poisson uncertainties through each step of the analysis up to the measured values of the cross section and cross-section ratio, the bootstrap resampling technique is used [191]. This technique is preferred to the traditional formula for the propagation of uncertainties due to the complexity of the analysis, particularly the use of the prompt-photon purity and the b-jet fraction. The bootstrap technique makes it possible to assess the asymmetry in the uncertainty, does not require the linearization of the dependence of the cross section on the number of selected events and does not require the derivation of partial derivatives. In particular, the mathematical expressions for the partial derivatives would necessitate the decomposition of events into exclusive categories to avoid the double counting of events that are used in more than one quantity of the cross-section equation, which would be non-trivial.

The bootstrap resampling technique consists in assigning a weight to each recorded or simulated event. The value of the weight is randomly picked from a Poisson distribution of mean one. Such a random weight assignment resamples the sample of events. The complete physics analysis is repeated on this new sample of events. The new measured values of the cross section and cross-section ratio differ from those measured with the original event sample due to the event weights. The mean of the resampled values however coincide with the value measured with the original

sample. Therefore, this resampling technique makes it possible to assess the impact of statistical variations on a measured quantity.

A particular resampling of the original event sample is called a replica, while the original sample is called the nominal sample. The resampling described above can be done multiple times, each time with a different weight assignment. A distribution of replicas is thus created. The replica distribution of a measured quantity follows the underlying statistical distribution of the quantity. The statistical uncertainty is defined as the two-sided 68% confidence interval of this distribution of replicas. The statistical uncertainty obtained this way can be asymmetric.

In the context of this analysis, one thousand replicas are used, as a compromise between the precise description of the underlying statistical distribution and computer processing time. Data and MC statistical uncertainties are determined separately by resampling the data and the MC samples one after the other.

As an example, Figure 8–1 shows the replica distribution of the measured cross-section ratio obtained in the lowest-E_{T}^{γ} bin and also in the lowest-E_{T}^{γ} bin that is associated to an unprescaled trigger selection. The underlying statistical distributions as obtained from the bootstrap technique and from an MC toy study are compared. The MC toy study corresponds to the generation of one thousand random numbers for each of the numerator and denominator of the ratio. A pair of numbers correspond to a replica of the data. The random numbers follow the Gaussian distributions of the measured values of the cross section.

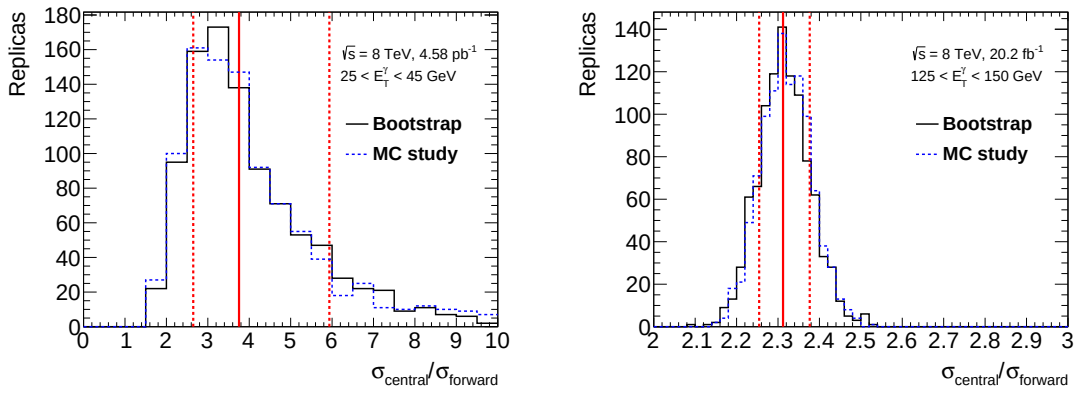

(a) (b)

Figure 8–1 – Replica distributions of the measured central-to-forward cross-section ratio obtained from the bootstrap technique and the MC toy study for (a) the lowest-E_{T}^{γ} bin and (b) the lowest-E_{T}^{γ} bin that is associated to an unprescaled trigger selection. The solid red line corresponds to the nominal value of the ratio while the dashed red lines delimit the two-sided 68% confidence interval.

It can be seen that the two methods produce a similar distribution for the ratio. The ratio in the lowest-E_{T}^{γ} unprescaled bin is Gaussian, while that in the lowest-E_{T}^{γ} bin is not. The asymmetry of the latter distribution is due to the large relative uncertainties that affect the numerator and the denominator. As a comparison, the asymmetry of the distribution would not have been captured by the traditional formula for the propagation of uncertainties since the linear approximation under which it is derived breaks down for these large relative uncertainties. The bootstrap technique allows to preserve the asymmetry of the statistical uncertainty.

8.1.2 Systematic Uncertainties

All systematic uncertainties in the measured values of the cross section and of the cross-section ratio are estimated using a similar approach. For each individual

source of uncertainty, the quantities in the analysis that are affected by it are varied simultaneously and the complete physics analysis is repeated with these varied quantities. For most sources of uncertainties, quantities are varied in the nominal SHERPA simulated samples. The difference between a measured value obtained with the systematic variation and that obtained without the systematic variation is taken as the systematic uncertainty in that measured value. Asymmetric systematic uncertainties are assessed by considering individual upward and downward variations of the quantities. Since systematic variations are evaluated using finite-size event samples, the impact of these variations is affected by statistical fluctuations. A smoothing procedure is performed on every systematic variation to remove the statistical fluctuations.

The smoothing procedure depends on the statistical uncertainty in the systematic variation. This statistical uncertainty is determined by using the same bootstrap technique as explained in the previous section. For each systematic variation, one thousand replicas are produced by varying the event weights of the SHERPA events. For each replica, the relative systematic variation in a measured value is evaluated with respect to the nominal measured value. The standard deviation of the replica distribution of this relative variation is taken as the statistical uncertainty in the variation. As a consequence, the statistical uncertainty in a systematic variation is related to the statistical uncertainty in the SHERPA samples.

The smoothing procedure is accomplished in two steps. The first step consists in rebinning the E_{T}^{γ} distribution of a relative systematic variation by merging bins until the value of the relative variation in each new bin is greater than two times the size

of its statistical uncertainty. If this condition cannot be satisfied, the systematic variation is set to zero. The rebinning procedure is attempted starting from both the lowest-E_{T}^{γ} bin and the highest-E_{T}^{γ} bin, using whichever way produces the largest number of significant bins. Afterwards, the values of the new bins are given to each of the original bins that were merged, that is the binning of the original distribution is used but with the values associated to the rebinned distribution. The second step of the smoothing procedure is a sliding average over the E_{T}^{γ} bins with a Gaussian kernel. Assuming that the distribution of the relative systematic variation is smooth as a function of E_{T}^{γ}, this step extracts this smooth distribution while avoiding a significant change to the values of the relative systematic variation. The relative systematic variation that results from these two smoothing steps is taken as the relative systematic uncertainty in the measured quantity.

Figure 8–2 shows the effect of the smoothing procedure on two systematic variations, described later in this section, chosen for illustration purposes. In Figure 8–2(a), the effect of the rebinning step can be seen at low E_{T}^{γ} while that of the sliding-average step has no impact. Conversely, Figure 8–2(b) shows that the rebinning step has no impact while the sliding-average step changes slightly the values at high E_{T}^{γ}.

The systematic uncertainties that are considered in this analysis are divided into categories according to what part of the analysis they affect. The systematic uncertainties are now discussed in the following order: uncertainties related to the photon reconstruction, to the jet reconstruction, to the signal modelling and to the analysis techniques.

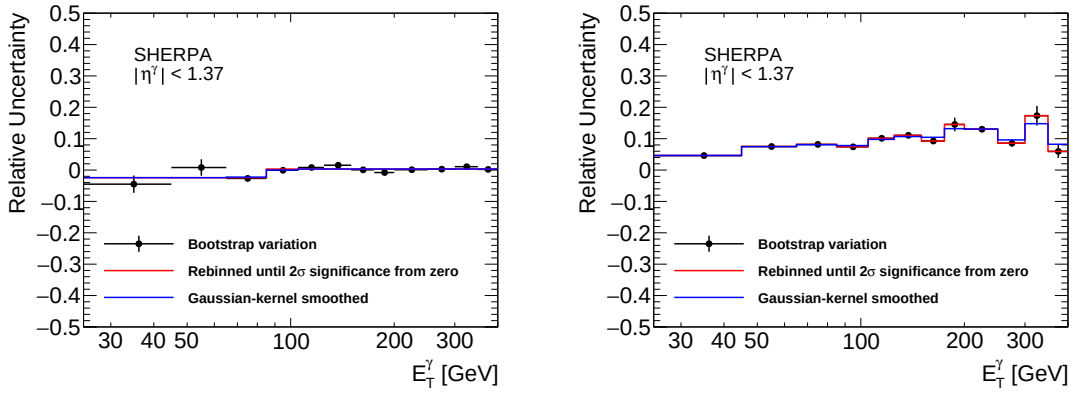

(a) (b)

Figure 8–2 – Relative systematic uncertainty in the differential cross section for the central region as a function of E_{T}^{γ} related to an upward variation in the SHERPA events of (a) the jet energy resolution and (b) the first eigenvector of the c-jet b-tagging efficiency. The states of the relative uncertainty before the smoothing, after the rebinning and after the Gaussian-kernel sliding average are displayed. The vertical error bars correspond to the statistical uncertainty in the relative systematic variation before the smoothing, as obtained from the bootstrap replicas.

Photon Energy Scale

The energy calibration of the reconstructed photons is affected by several uncertainties [169]. A total of 20 independent uncertainty sources are considered, related to the following aspects of the calibration of the photon energy scale: the relative calibration between the layers of the electromagnetic calorimeter, the description of the detector material upstream of the calorimeter cells, the knowledge of the calorimeter geometry, the simulation of the physical interactions, the dependence of the energy response on the amplifier gains, the modelling of the photon energy leaking outside the photon cluster, the misclassification of photons as unconverted or converted and the physics analysis performed to determine the electron energy scale from $Z \to ee$ decays. The

individual uncertainty with the largest impact on the measured cross-section values is the dependence of the energy response on the amplifier gains in the second layer of the electromagnetic calorimeter.

Most of the uncertainties are correlated across the barrel and the end-cap electromagnetic calorimeters. However, uncertainties related to the relative layer calibration, the material description upstream of the calorimeter cells and the knowledge of the calorimeter geometry are taken to be uncorrelated across the barrel and the end-cap electromagnetic calorimeters. This has the implication that they do not cancel in the central-to-forward ratio of the cross section.

Photon Identification

The calibration of the efficiency of the tight photon identification in simulated events is affected by various sources of uncertainties [166]. The total uncertainty in the scale factors is propagated up to the measured values of the cross section and cross-section ratio. The impact of having scale factors derived using an isolation energy cut of 4 GeV instead of the nominal E_{T}^{γ} dependent cut value has been assessed and has been found to be negligible.

Jet Energy Scale

The calibration of the jet energy scale (JES) is affected by uncertainties [175]. The JES uncertainties not only affect the selected jets in this physics analysis but also the derivation of the scale factors of the b-tagging efficiency, since this efficiency is measured from jets with a calibrated energy. As such, the individual JES uncertainties are varied simultaneously in this analysis and in the derivation of the b-tagging scale

factors of the b-jets. However, this simultaneous variation is not technically possible for the b-tagging scale factors of c- and light jets. For those, the total JES uncertainty is varied as part of the uncertainties specific to the b-tagging scale factors.

Most of the JES uncertainties are related to the absolute in situ calibration analyses. There are 56 uncertainties related to these analyses. To reduce the number of uncertainties to assess, the principal component analysis (PCA), described in Appendix D, is used.[1] The eigenvectors with the five largest eigenvalues are kept and the remaining ones are combined into a residual uncertainty. The correlations in the JES calibration factors obtained with this reduced set of uncertainties differ by about 5% from those obtained with the complete set.

With the reduced set of in situ uncertainties and the uncertainties in the JES calibration factors that are not related to the in situ analyses, a total of 18 independent uncertainties affect the JES calibration. They are related to the absolute in situ calibration analyses, the corrections dependent on the pileup, the corrections for jets that punch through the calorimeters and the differences in response between the jet flavours. These uncertainties are all considered in this analysis. The uncertainty with the largest impact on the measured values of the cross section and cross-section ratio is the uncertainty in the response of the b-jets, which is related to the modelling of the fragmentation of the b quarks into b hadrons.

[1]The PCA replaces the variations of possibly correlated sources of uncertainties in a set of quantities, in this case the JES calibration factors, by variations of the uncorrelated eigenvectors of their covariance matrix.

Jet Energy Resolution

The measurement of the jet energy resolution is affected by the uncertainties related to the in situ analyses [175]. The uncertainty in the jet energy resolution is assessed by applying a Gaussian smearing correction to the four-momentum of the jets in simulated events, such as to vary the resolution within its uncertainty. The differences in the measured values of the cross section and cross-section ratio that are obtained with the smeared jets, compared to those without the smearing correction, are taken as the uncertainty due to the jet energy resolution. This uncertainty is assessed simultaneously in the jets of this physics analysis and in the derivation of the scale factors of the b-tagging efficiency of all three jet flavours.

b-tagging Identification

The scale factors of the b-tagging efficiency are obtained from calibration analyses specific to b-, c- and light jets, discussed in Section 4.3.3. Each analysis has its own set of uncertainties. As these analyses all deal with jets, they are affected by uncertainties pertaining to the reconstruction and selection of jets. These uncertainties are assessed simultaneously in this physics analysis and in the derivation of the b-tagging efficiency scale factors, as mentioned previously.

There are a multitude of uncertainties specifically affecting each of the calibration analyses specifically. There are 41 independent sources of systematic uncertainties in the derivation of the b-jet scale factors. These are related to the modelling of signal and background events in the $t\bar{t}$ selection, and to the calibration of the kinematics of the electrons and muons that are selected [181]. There are 17 independent sources

of systematic uncertainties in the derivation of the c-jet scale factors. These are related to the template fit distinguishing between the b- and the c-jets, and to the extrapolation of the scale factors measured for c-jets containing D^{*+} mesons to those obtained for inclusive c-jets [182]. There are 13 independent sources of systematic uncertainties in the derivation of the light-jet scale factors. These are related to the modelling of the tracks that are associated to jets, and to the modelling of the contamination due to b and c hadrons, hyperons and material interactions [182].

In addition to these various sources of systematic uncertainties, the statistical uncertainties in the scale factors have to be assessed. Since the MV1c weight distribution is normalized to unity, the statistical uncertainty in the number of events in a given bin of that distribution is not independent of that in other bins and instead follows a multinomial distribution as a function of the MV1c weight.

To take into account the correlations in the statistical uncertainties, the PCA is used and applied taking also into account the sources of systematic uncertainties discussed above. The eigenvectors that are obtained are ordered by decreasing eigenvalue. An eigenvector is considered in this analysis only if its eigenvalue is larger than 10^{-20}. Out of the 30 possible eigenvectors for the b-jet scale factors, 26 of them are considered. Every eigenvector of the c-jet and the light-jet scale factors is considered. There are 20 and 60 of them respectively for the c-jet and the light-jet scale factors.

There is an additional uncertainty in the b-tagging efficiency scale factors that is assessed independently for each jet flavour. It is related to the limited reach at high $p_{\mathrm{T}}^{\mathrm{jet}}$ of the calibration analyses, due to a lack of recorded events in that region of

phase space. For the b- and c-jet scale factors, values of scale factors can only be derived up to a jet p_{T} of 300 GeV, while those for light jets do not extend beyond 750 GeV. Beyond these values, the b-tagging efficiency scale factors are taken to be those of the highest-$p_{\mathrm{T}}^{\mathrm{jet}}$ bins available. An extrapolation uncertainty accounting for the possible differences in the actual scale factors at high $p_{\mathrm{T}}^{\mathrm{jet}}$, compared to the ones that are used, is obtained from the simulated samples.

The source of uncertainty related to the b-jet scale factors that has the largest impact on the measured values of the cross section and cross-section ratio is the one related to the jet energy scale. As described previously, the impact of the jet energy scale is assessed separately in the analysis. The second leading source of uncertainty in the b-jet scale factors, which is considered in this present uncertainty category, is due to differences in the modelling of background events in the $t\bar{t}$ selection between different generators. For the c-jet scale factors, the dominant uncertainty is related to the template fit that separates the c-jets from the b-jets. This uncertainty is also the largest single one among all the uncertainties that are considered in this physics analysis. For the light-jet scale factors, there are two dominant uncertainties: one related to the modelling of the number of tracks that are associated to jets and one related to the c-jet b-tagging efficiency.

The variations of the b-tagging efficiency scale factors according to their uncertainties distort the shapes of the templates in the MV1c template fit. These variations assess the dependence of the results of the template fit on the shapes of the templates. This is an advantage of using templates that are continuously calibrated. Furthermore, the dependence of the results of the template fit on the overall normalizations of

the fitted data and MC distributions is taken into account through the bootstrap replicas that are used to estimate statistical uncertainties. As such, no additional uncertainties related to the technique of the template fit are necessary.

Photon Sideband Definition

The two-dimensional sideband method is used to obtain the purity of prompt photons in the event selection. The purity depends on the definitions of the background regions of the photon identification and of the isolation energy.

To assess the impact of the chosen background region for the photon identification, the definition of the relaxed tight identification is made tighter and looser by respectively requiring an additional tight photon discriminating variable and by removing such a requirement, as specified in Table 4–1. Changing this definition also allows to assess partially a possible mismodelling of the efficiency of the relaxed tight identification. A mismodelling is possible since this identification efficiency in simulated events is not calibrated to that in recorded events.

To assess the impact of the requirement on the isolation energy for the background region of the isolation energy, the isolation cut is made tighter and looser by the size of the resolution of the isolation energy, i.e. by 2 GeV. This uncertainty has a larger impact on the measured values of the cross section and cross-section ratio than the uncertainty related to the definition of the background region of the photon identification.

Photon Sideband Correlation

One of the assumptions in the two-dimensional sideband method is that the two quantities that define the sidebands are not correlated in background events. In other words, that the following equality holds for the correlation factor:

$$R_{\text{bkg}} \equiv \frac{N_A^{\text{bkg}} N_D^{\text{bkg}}}{N_B^{\text{bkg}} N_C^{\text{bkg}}} = 1. \tag{8.1}$$

Determining if this assumption holds is not possible due to the lack of background simulated samples. Instead, the quantity R'_{bkg} is used as a proxy to R_{bkg} and is measured in data. This new quantity is defined similarly to the correlation factor and is

$$R'_{\text{bkg}} \equiv \frac{N_{A'}^{\text{bkg}} N_{D'}^{\text{bkg}}}{N_{B'}^{\text{bkg}} N_{C'}^{\text{bkg}}}, \tag{8.2}$$

where the definition of the prime regions is shown in Figure 8–3.

The four prime regions are located at larger values of $E_{\text{T}}^{\text{iso}}$ than the corresponding four non-prime regions and thus should all be dominated by background events. These four prime regions are corrected for signal events leaking into them via similar MC leakage correction factors as those used for the non-prime regions. The R'_{bkg} quantity is measured as a function of both E_{T}^{γ} and the MV1c weight according to the bins of the two-dimensional purity. Figure 8–4 shows an example of measured R'_{bkg} values in a bin of the MV1c distribution as a function of E_{T}^{γ}. The values are within 10% of unity, taking into account the statistical uncertainty.

The uncertainty in the purity due to the correlation of the two quantities that define the sidebands in the background events is therefore assessed by varying R_{bkg} by 10%

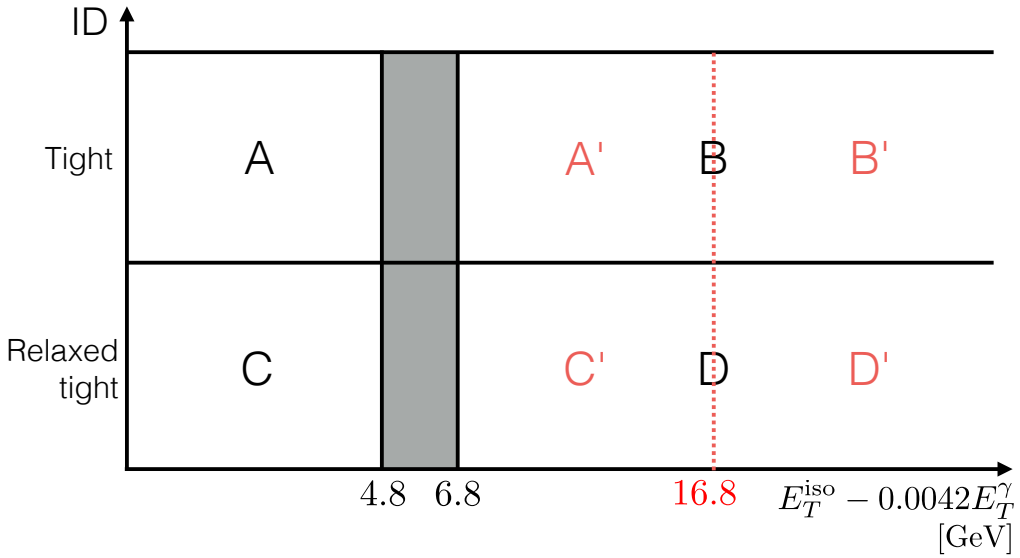

Figure 8–3 – Diagram of the non-prime and prime regions as a function of the isolation energy and the photon identification (ID). The dashed line separates both regions B and D into two prime regions. The grey regions are not associated to any sideband region.

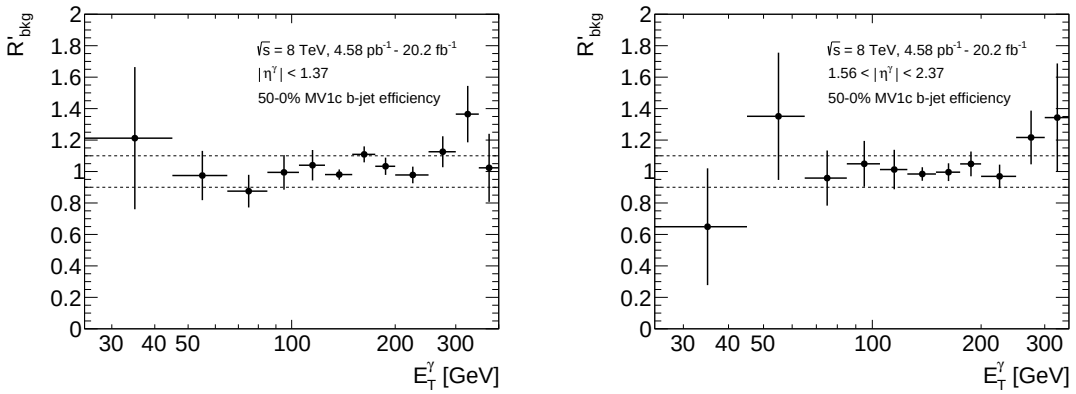

(a) (b)

Figure 8–4 – Correlation factor in the prime regions measured in recorded events in the 50–0% MV1c b-jet b-tagging efficiency bin as a function of E_{T}^{γ} for (a) the central region and (b) the forward region. The signal leakage in the prime regions has been corrected with a correction factor obtained from the SHERPA samples. The vertical error bars correspond to the statistical uncertainty in the correlation factor.

from unity. The equation of the photon purity has to be modified to allow a non-unity value for the correlation factor. The equation becomes

$$p^{\gamma\text{-prompt}} = \frac{1}{2N_A(c_B c_C R_{\text{bkg}} - c_D)}\Big\{c_B N_C R_{\text{bkg}} + c_C N_B R_{\text{bkg}} - N_D - c_D N_A + \Big[(c_B N_C R_{\text{bkg}} + c_C N_B R_{\text{bkg}} - N_D - c_D N_A)^2 - 4(c_B c_C R_{\text{bkg}} - c_D)(N_B N_C R_{\text{bkg}} - N_A N_D)\Big]^{1/2}\Big\}. \tag{8.3}$$

This equation is used to assess the impact of this background-correlation uncertainty on the measured values of the cross section and cross-section ratio.

Prompt-photon Modelling

As PYTHIA is a $2 \to 2$ event generator, the contributions of the initial- and final-state radiated photons and of the fragmentation photons to the production of prompt photons are approximated via the emissions of bremsstrahlung photons in the parton shower. Events containing bremsstrahlung photons can be distinguished from those containing direct photons that are generated in the hard process through the different final states of their matrix elements. As such, it is possible to reweight the relative contributions of events containing bremsstrahlung and direct, also called hard, photons according to what is observed in data. The difference between this optimal admixture and the admixture of bremsstrahlung and hard photons set by default in PYTHIA is taken as an uncertainty pertaining to the modelling of the prompt photons.

To find the optimal admixture of bremsstrahlung and hard photons that best describes the data, a least-square fit of the selected PYTHIA events containing bremsstrahlung

and hard photons to the selected data events is performed. The function to minimize is

$$\chi^2 = \sum_{i,j} \left(\frac{N_{ij}^{\text{data}}(\alpha) - N_{ij}^{\text{MC}}(\alpha)}{\Delta N_{ij}^{\text{data}}(\alpha)} \right)^2 , \tag{8.4}$$

with

$$N_{ij}^{\text{MC}}(\alpha) = \frac{\sum_{i,j} N_{ij}^{\text{data}}(\alpha)}{\sum_{i,j}[\alpha N_{ij}^{\text{MC,hard}} + (1-\alpha) N_{ij}^{\text{MC,brem}}]} \left(\alpha N_{ij}^{\text{MC,hard}} + (1-\alpha) N_{ij}^{\text{MC,brem}} \right), \tag{8.5}$$

where i is a bin in E_{T}^{γ}, j is a bin in the MV1c weight and α is the relative weight applied to the hard contribution and is the fit parameter. The numbers of PYTHIA events with a hard photon and with a bremsstrahlung photon in bin (i, j) are respectively $N_{ij}^{\text{MC,hard}}$ and $N_{ij}^{\text{MC,brem}}$. This formula considers only events with prompt photons that pass the detector-level selection. Thus, $N_{ij}^{\text{data}}(\alpha)$ is the number of recorded events in bin (i, j) after the application of the photon purity and $\Delta N_{ij}^{\text{data}}(\alpha)$ is its statistical uncertainty. These quantities depend on α since the signal leakage correction factors used in the sideband method depend on the reweighted MC events. The ratio in Equation 8.5 is used to normalize the sum of the two PYTHIA distributions to the data distribution.

The distribution of the reduced χ^2 is shown in Figure 8–5. The actual values of the reduced χ^2 are not meaningful since the distributions of prompt photons in data and in the PYTHIA samples are not expected to agree because systematic uncertainties are not considered in the least-square fit. Only the shape of the distribution of the reduced χ^2 is of relevance. It can be seen that it admits a single minimum, giving confidence in the accuracy of the fitted value.

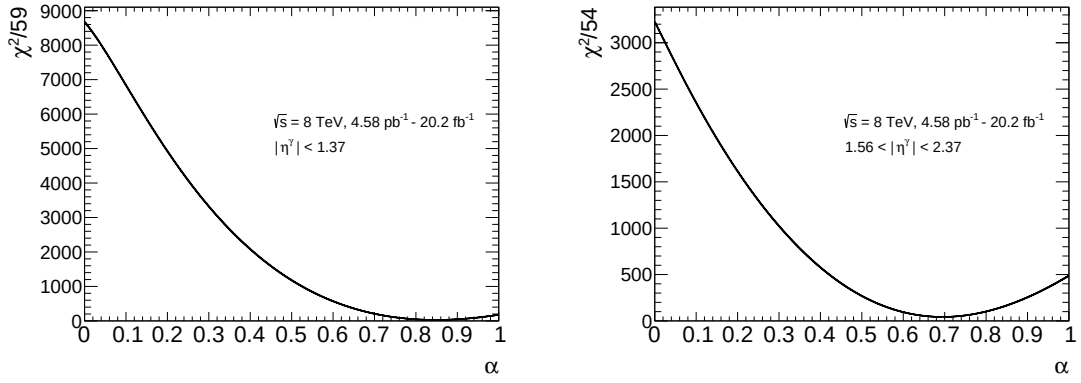

(a) (b)

Figure 8–5 – Reduced χ^2 of the reweighted contributions of the PYTHIA events containing bremsstrahlung and hard photons, compared to the recorded events that contain prompt photons, as a function of the weight parameter α for (a) the central region and (b) the forward region.

The distributions of the selected events that contain hard and bremsstrahlung photons before and after the fit are shown in Figure 8–6. The projection of the two-dimensional distributions onto the E_{T}^{γ} axis has been performed. The photon purity that is applied to the data distribution makes use of leakage correction factors that have been obtained from the PYTHIA samples. Bremsstrahlung photons are relatively more abundant at low E_{T}^{γ} than at high E_{T}^{γ} compared to hard photons, i.e. the distribution of bremsstrahlung photons is more steeply decreasing as a function of E_{T}^{γ} than that of the hard photons. These different shapes in the distributions make the fit of their contributions to the data possible. It is observed that the data is better described by an increased relative contribution of events containing hard photons compared to the default PYTHIA admixture.

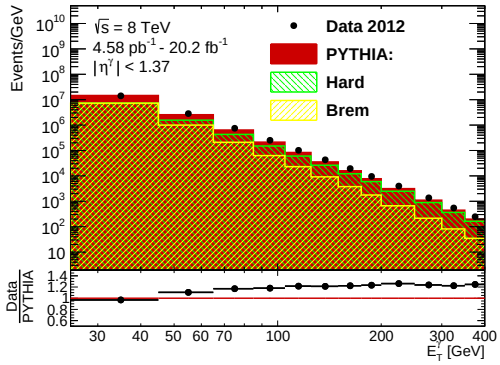

(a)

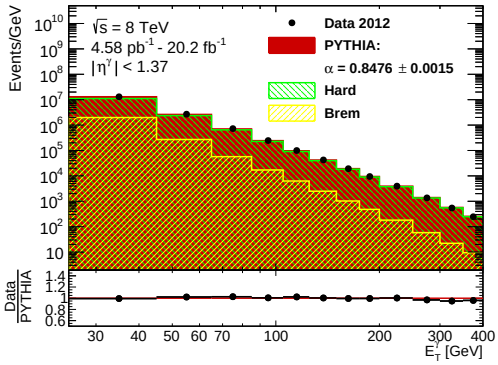

(b)

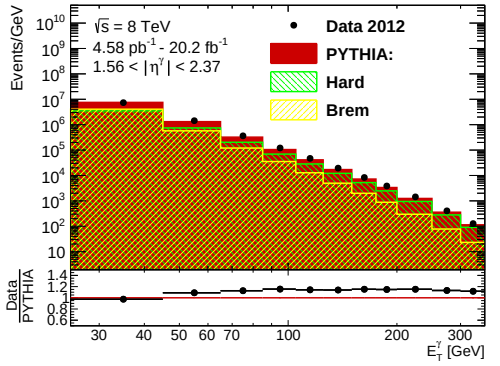

(c)

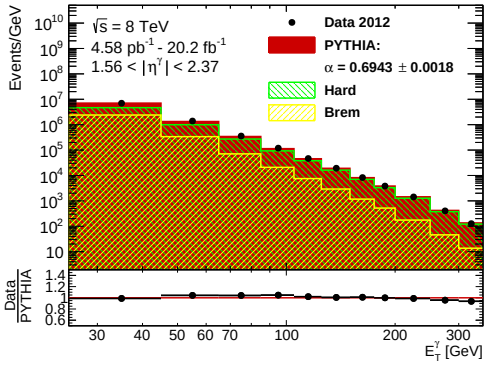

(d)

Figure 8–6 – Distributions of selected events containing prompt photons in data and in the PYTHIA samples as a function of E_{T}^{γ} for (a) the central region before the least-square fit, (b) the central region after the least-square fit, (c) the forward region before the least-square fit and (d) the forward region after the least-square fit. The decomposition of the PYTHIA distribution into events containing bremsstrahlung photons (Brem) and direct photons (Hard) is also displayed. The distributions displayed are projections of the corresponding two-dimensional distributions onto the E_{T}^{γ} axis. The number of events in each bin has been divided by the width of the bin. The ratio of the data distribution to that of PYTHIA is shown in the bottom panel. The statistical uncertainty in the data distribution is too small to be visible. The numbers in the legend are the fitted value of α and its statistical uncertainty.

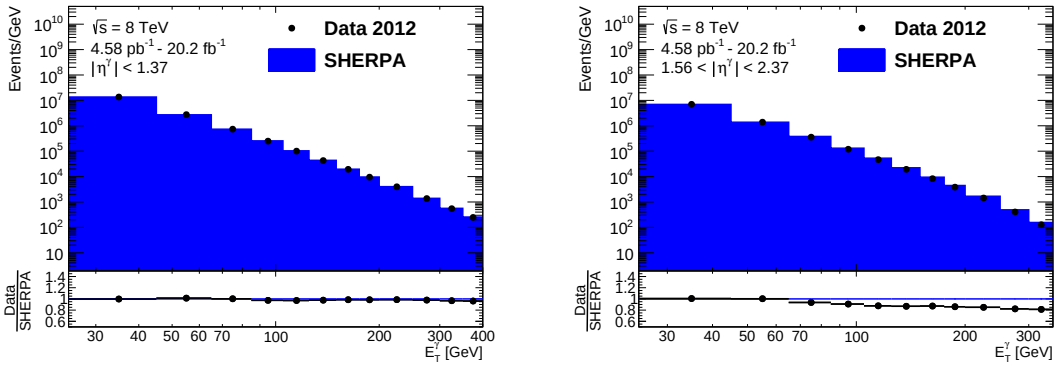

(a) (b)

Figure 8–7 – Distributions of selected events containing prompt photons in data and in the SHERPA samples as a function of E_{T}^{γ} for (a) the central region and (b) the forward region. The distributions displayed are projections of the corresponding two-dimensional distributions onto the E_{T}^{γ} axis. The number of events in each bin has been divided by the width of the bin. The ratio of the data distribution to that of SHERPA is shown in the bottom panel. The statistical uncertainty in the data distribution is too small to be visible.

For comparison purposes, Figure 8–7 shows the E_{T}^{γ} distribution of selected events in the SHERPA samples. The data distribution that is compared to the SHERPA distribution makes use of a photon purity that has been corrected with signal leakage correction factors that have been obtained from the SHERPA samples. It can be seen from the ratio of the data distribution to that of the simulated samples that the fitted PYTHIA distribution is in closer agreement with the data, compared to that of the PYTHIA distribution before the fit, and that the agreement obtained is similar to that of the SHERPA distribution.

The product of the fitted α value with the ratio of the integrals of the data distribution to that of the sum of the PYTHIA distributions produces event weights. The values

of the weights are 1.43 and 0.26 respectively for the distributions of the hard and bremsstrahlung events in the central region and 1.28 and 0.56 respectively for the distributions of the hard and bremsstrahlung events in the forward region. The application of these event weights to the hard and bremsstrahlung events produces the optimal PYTHIA admixture that can be used in the physics analysis.

The difference between the measured values of the cross section and cross-section ratio that are obtained by using the optimal and the default PYTHIA admixtures is taken as the uncertainty related to the prompt-photon modelling. To evaluate this uncertainty, the PYTHIA samples are used in the analysis instead of the SHERPA samples, which are not used here. There is only one systematic variation associated to this uncertainty. As such, the variation is symmetrized with respect to zero to obtain a positive uncertainty and a negative uncertainty.

Non-Perturbative QCD Models

An uncertainty related to the modelling of the parton shower, the hadronisation and the hadron decays, i.e. the non-perturbative QCD models, used to generate the signal events, is considered. The difference between the measured values of the cross section and cross-section ratio that are obtained by using the SHERPA and the PYTHIA samples, which make use of different models, is taken as the uncertainty. In the evaluation of this difference, the PYTHIA samples with the optimal admixture of events containing bremsstrahlung and direct photons is used. This avoids the double counting of the uncertainty in the prompt-photon modelling, since the PYTHIA samples with the optimal admixture are more similar to the SHERPA samples than

those with the default admixture. For the smoothing procedure of this systematic variation, the statistical uncertainties related to the finite sizes of the PYTHIA and SHERPA samples are added in quadrature and used as the statistical uncertainty in the variation. The variation is symmetrized to produce a positive uncertainty and a negative uncertainty.

Particle-level Bin Migration Effects

As can be seen in Figure 7–8, statistically significant differences exist in the unfolding correction factors obtained using the bin-by-bin approach and the Bayesian approach with two iterations. The difference between the measured values of the cross section and cross-section ratio obtained using the Bayesian unfolding with two iterations and the nominal bin-by-bin unfolding is taken as the uncertainty related to the particle-level bin migration effects. These effects include the impact of neglecting the off-diagonal elements of the transfer matrix in the unfolding procedure and the mismodelling of the detector effects by the MC samples. This variation is symmetrized to produce a positive uncertainty and a negative uncertainty.

Luminosity

The relative uncertainty in the integrated luminosity is determined to be 1.9% [147]. This uncertainty is dominated by the uncertainties related to the calibration of the absolute luminosity via the van der Meer beam scans and also by the uncertainties related to the differences between the conditions of the beams during these scans and those during the *pp* collisions that are recorded for physics analysis. As the integrated luminosity is a multiplicative factor in the equation used to measure the cross section,

Equation 7.7, the relative uncertainty in the measured values of the cross section has the same value as that in the luminosity. It is independent of E_{T}^{γ}. Also, this uncertainty cancels completely in the cross-section ratio.

8.1.3 Cross-checks

Possible sources of systematic uncertainties different from those already discussed in this section have been investigated. They result in no statistically significant differences in the measured values of the cross section and cross-section ratio and thus are not considered as additional sources of uncertainties. These sources of uncertainties are those related to the calibration of the photon energy resolution, the corrections that are applied to the isolation energy and the efficiency of the JVF selection.

Additionally, the impact of several choices in the physics analysis, different than those already discussed in this section, have been studied. These changes in the analysis do not result in statistically significant differences in the measured values of the cross section and cross-section ratio and thus serve as cross-checks. These studies include the comparison of the measured cross section with the sum of the separately measured cross sections for unconverted and converted photons, the comparison of the b-jet b-tagging efficiencies derived in $t\bar{t}$ simulated events with those derived in γ + jet simulated events, and the comparison of the measured b-jet fractions using different parameterizations of the sum of the MV1c templates in Equation 6.8. Also studied is the comparison of the measured cross section obtained using MC samples that are weighted with respect to the amount of pileup with that obtained using

MC samples that are weighted with respect to the number of reconstructed primary vertices.

8.1.4 Total Measurement Uncertainty

The smoothed systematic uncertainties and the statistical uncertainty in the measured values of the cross section and cross-section ratio are all added in quadrature to produce the total uncertainty in that quantity. To preserve the asymmetry in the uncertainties, the sum in quadrature is done separately for the positive and the negative variations. About 160 independent sources of systematic uncertainties are considered. The total uncertainty and its breakdown into the category uncertainties are shown in Figures 8–8 and 8–9 for the $\gamma + b$ cross section in the central and forward regions respectively and in Figure 8–10 for the cross-section ratio. Table 8–1 lists the range of the size of various uncertainties per category.

Most uncertainties are Gaussian in nature, and thus symmetric as can be seen from the figures. The total relative uncertainty in the differential cross section is around 20% for both the central and the forward regions, although the total uncertainty increases at low and high E_{T}^{γ} for the forward region. This increase is due to the larger statistical uncertainty that is associated to those regions of the phase space. The statistical uncertainty is large at low E_{T}^{γ} due to the prescaled trigger selection which reduces the number of recorded events compared to the unprescaled trigger selection. The statistical uncertainty is large at high E_{T}^{γ} due to the low amount of $\gamma + b$ events produced, owing to the steeply decreasing production cross section of $\gamma + b$ events as a function of E_{T}^{γ}. Additionally, the number of produced events is smaller in the

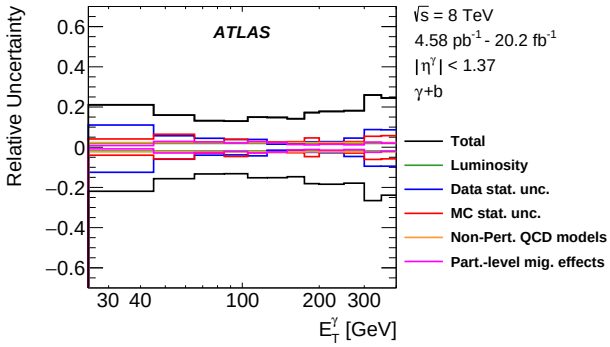

(a)

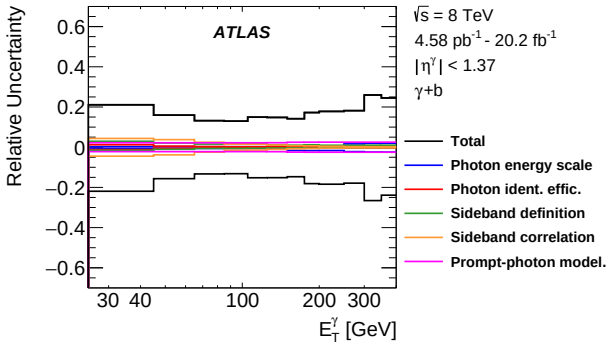

(b)

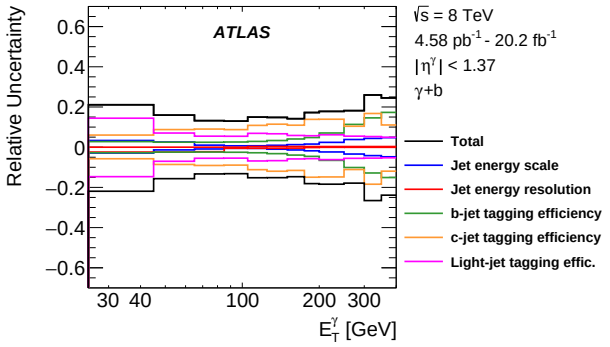

(c)

Figure 8–8 – Total relative uncertainty in the measured values of the differential $\gamma + b$ cross section for the central region as a function of E_{T}^{γ} and its breakdown into (a) the event-related uncertainties, (b) the photon-related uncertainties and (c) the jet-related uncertainties. The total uncertainty is reported in all three plots for comparison purposes.

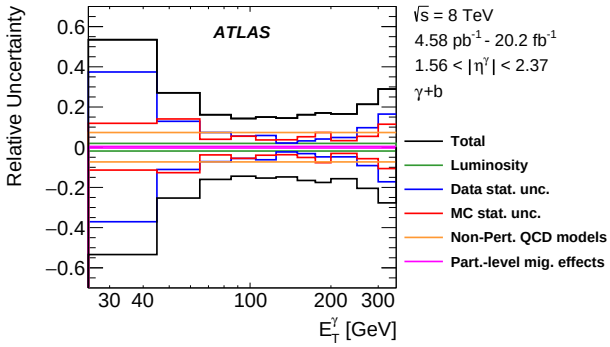

(a)

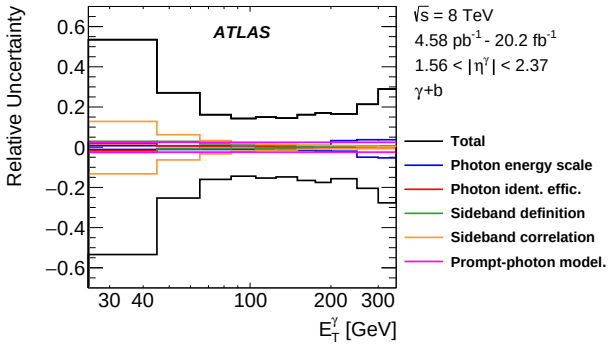

(b)

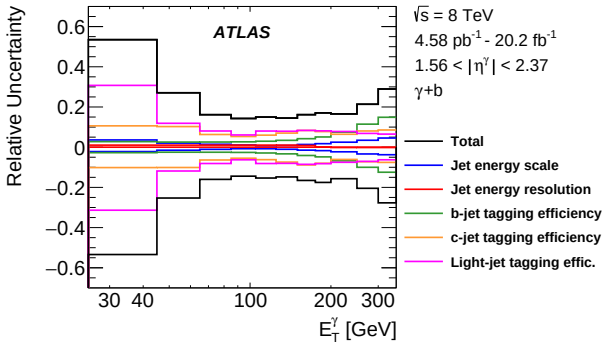

(c)

Figure 8–9 – Total relative uncertainty in the measured values of the differential $\gamma + b$ cross section for the forward region as a function of E_{T}^{γ} and its breakdown into (a) the event-related uncertainties, (b) the photon-related uncertainties and (c) the jet-related uncertainties. The total uncertainty is reported in all three plots for comparison purposes.

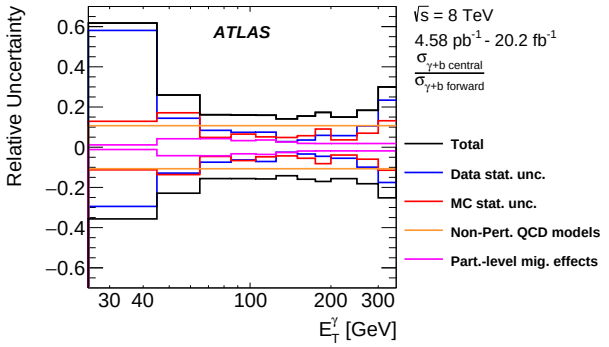

(a)

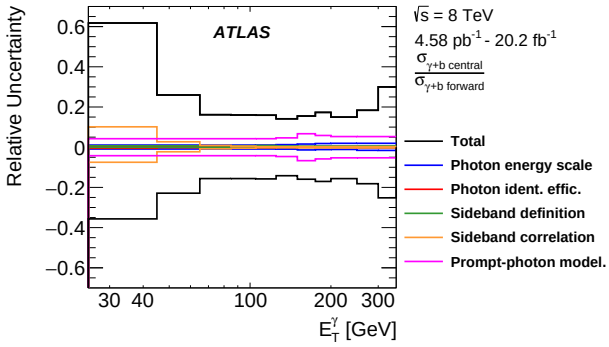

(b)

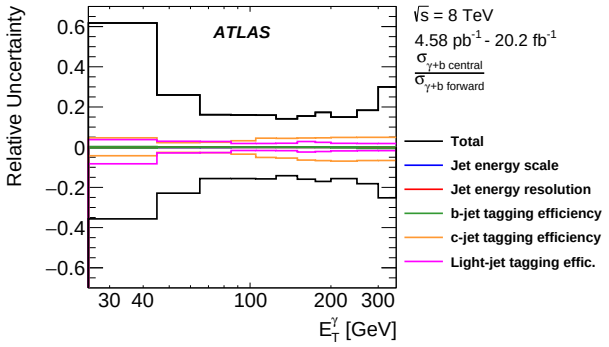

(c)

Figure 8–10 – Total relative uncertainty in measured values of the central-to-forward cross-section ratio as a function of E_{T}^{γ} and its breakdown into (a) the event-related uncertainties, (b) the photon-related uncertainties and (c) the jet-related uncertainties. The total uncertainty is reported in all three plots for comparison purposes.

Table 8–1 – Range of the size of the relative uncertainties in the measured differential $\gamma + b$ cross section and in the cross-section ratio as a function of E_{T}^{γ} for the different uncertainty categories. Adapted from Ref. [188].

	Uncertainty [%]		
Uncertainty source	$d\sigma_{\mathrm{central}}/dE_{\mathrm{T}}^{\gamma}$	$\mathrm{d}\sigma_{\mathrm{forward}}/dE_{\mathrm{T}}^{\gamma}$	$\sigma_{\mathrm{central}}/\sigma_{\mathrm{forward}}$
MC statistical uncertainty	1.9 – 6.4	3.1 – 14	3.6 – 17
Photon energy scale	0.2 – 2.5	0.7 – 5.3	0.9 – 1.9
Photon identification efficiency	0.2 – 1.2	0.4 – 1.8	0.1 – 0.5
Jet energy scale	0.6 – 4.8	0.7 – 4.6	0.1 – 0.2
Jet energy resolution	0.0 – 2.4	0.0 – 1.0	0.0 – 0.1
b-jet b-tagging efficiency	2.4 – 17	2.5 – 15	0.1 – 0.6
c-jet b-tagging efficiency	5.7 – 18	5.3 – 11	2.3 – 6.9
Light-jet b-tagging efficiency	4.9 – 15	6.1 – 31	1.6 – 8.3
Sideband definition	0.2 – 3.0	0.2 – 2.9	0.1 – 0.8
Sideband correlation	0.2 – 4.5	0.4 – 13	0.2 – 10
Prompt-photon modelling	2.2 – 2.5	2.4	4.2 – 6.7
Non-perturbative QCD models	2.3	7.3	11
Particle-level bin migration effects	0.8 – 2.9	0.4	1.2 – 4.3
Luminosity	1.9	1.9	0
Total systematic uncertainty	12 – 25	13 – 38	14 – 22
Data statistical uncertainty	1.5 – 13	2.1 – 37	2.5 – 58
Total uncertainty	13 – 27	14 – 54	14 – 62

forward region than in the central region. For a given E_{T}^{γ} value, events produced in the forward region, compared to those in the central region, require a larger difference between the fractions of the proton momentum carried by the two colliding partons, x_1 and x_2, as can be inferred by Equation A.17. This larger difference implies that one of the momentum fractions has a large value, which is less probable.

On Figures 8–8, 8–9 and 8–10, the MC statistical uncertainty can be observed not to be smooth as a function of E_{T}^{γ}. This is due to the use of different filters for the MC samples, as discussed in Section 5.1. The MC statistical uncertainty that is considered in the figures and in the table is that of the SHERPA samples.

In most E_{T}^{γ} bins, the total uncertainty in the measured values of the cross section is dominated by the systematic uncertainties. The largest uncertainties affecting the measured values, other than the data and MC statistical uncertainties, are uncertainties related to the b-tagging efficiencies. They are the limiting factor in the precision of the measurement at high E_{T}^{γ}. At higher E_{T}^{γ} values than those for which the cross section is measured, the uncertainties related to the b-tagging become excessively large. This is due to the extrapolation uncertainty in the scale factors of the b-tagging efficiencies, which significantly increases as a function of $p_{\mathrm{T}}^{\mathrm{jet}}$, and correspondingly has the largest impact at high values of E_{T}^{γ}. The highest E_{T}^{γ} values at which the cross section is measured are chosen to be those for which the size of the total uncertainty stays approximately constant as a function of E_{T}^{γ}, i.e. 400 GeV for the central region and 350 GeV for the forward region.

Since the precision of the measured cross-section values is systematically limited and most of the uncertainties are positively correlated in pseudorapidity, the ratio of the cross section in the central region to that in the forward region is measured. Most of the systematic uncertainties in the ratio are indeed smaller than those in the cross section in either region. The relative statistical uncertainty in the ratio is however larger than that in the cross sections. It is larger as it corresponds to the sum in quadrature of their relative statistical uncertainties, since the events in one region are independent of the events in the other one. This increase in the statistical uncertainty counteracts the decrease in the systematic uncertainty and produces a total uncertainty that is approximately the same size as that in the cross section for the forward region. Although the total uncertainty in the ratio is not reduced compared to that in the cross section, its composition in terms of statistical and systematic components is different.

Keeping in mind the possibility that the measured values of the cross section could be used as input to some future analysis, the correlations of their systematic uncertainties need to be provided. The correlations can be provided either as the sum of the covariance matrices of each uncertainty or as signed upward and downward variations of each systematic uncertainty. The latter option is chosen since it allows to keep knowledge on the physical origin of the uncertainties and also since it allows to correlate the uncertainties across different observables. The signed systematic uncertainties in the cross section for the central and the forward regions are provided in Appendix E. They can be used to obtain the systematic uncertainties in the central-to-forward cross-section ratio, for example, or any other quantity that depends on these values.

8.2 Theoretical Uncertainties

The theoretical predictions of the $\gamma + b$ production cross section in pp collisions that are discussed in Section 2.3.3 are affected by uncertainties. These theoretical uncertainties arise from the truncation of the infinite pQCD series at a given order, from the uncertainty in the parton distribution functions, from the uncertainty in the measured parameters of the Standard Model and from the modelling of the non-perturbative QCD effects.

The impact of the truncation of the perturbative series is assessed via the renormalization and the factorization scales. The PDF uncertainty is assessed according to the recommendations of the collaborations that produced them. The uncertainty in the measured parameters of the Standard Model is only assessed by varying the value of the strong coupling constant. Since the predictions are to be compared to the particle-level cross-section measurement, the uncertainty related to the non-perturbative QCD models is not considered in the predictions as this uncertainty is already taken into account in the measurement uncertainties. The theoretical uncertainties are evaluated only for the NLO predictions obtained from MadGraph5_aMC@NLO using the NNPDF3.0 PDF sets in the 5F and in the 4F schemes.

The theoretical uncertainties are assessed in a similar manner as the measurement systematic uncertainties. For each independent source of uncertainty, the relevant parameters are varied upwards and downwards and the change in the predictions, relative to those obtained without any variation, are taken as the uncertainty in the

predictions. Variations are taken to be fully correlated between the central and the forward regions. No smoothing of the theoretical uncertainties is performed.

The three categories of uncertainties that are considered and the total theoretical uncertainty are discussed in the following sections.

8.2.1 Renormalization and Factorization Scales

The predicted cross section of a process in pp collisions is given by Equation 2.5. It is dependent on the unphysical renormalization and factorization scales μ_{R} and μ_{F}. The parton-level cross section has an explicit dependence on these scales to compensate the dependences of the strong coupling constant and of the parton distribution functions on them, which themselves appear to provide finite values in the calculations in the presence of ultraviolet and infrared divergences.

The physical cross section is not dependent on the renormalization and the factorization scales, i.e. an all-order calculation is independent of these scales. However, at a finite pQCD order, the dependence is present and values must be chosen for these scales. Therefore, there is an uncertainty related to the arbitrary choice of their nominal values μ_{R}^{0} and μ_{F}^{0}.

A variation in the chosen values of these scales is related to the higher-order pQCD terms that are missing from a calculation at a finite order. Indeed, since the all-order calculation has no dependence on the scales and since the higher-order terms have an increasingly smaller contribution to the cross section, an interplay exists between the scale dependence and the terms at different orders. Specifically, the lower-order terms contribute partially to the higher-order terms. Thus, given some known lower-order

terms, the size of the impact on the cross section due to a variation in the scales is representative of a part of the size of the contribution of the higher-order terms to the cross section. Since the variation is only sensitive to a part of the higher-order contributions, the uncertainty related to the scales is only an approximation of the complete impact of the truncation of the infinite pQCD series. This approximation becomes better as the pQCD order of the calculation increases.

The correspondence between the scale variation and the higher-order terms exist only if the lower-order terms have an explicit dependence on the scales. This is the case for the NLO terms but not for the LO terms, since these are not affected by ultraviolet and infrared divergences. As such, the variation of the scales is not physically meaningful for the LO predictions and is not performed.

The scale uncertainty in the NLO predictions is assessed by varying the nominal scale values by a factor of two upwards and downwards: $\mu = 2\mu^0$ and $\mu = \mu^0/2$. The factor of two is a common choice to evaluate the scale uncertainties but is arbitrary, owing to the approximate nature of the uncertainty. The scales μ_{R} and μ_{F} can be varied either simultaneously in the same direction, simultaneously in opposite directions or independently. These possibilities result in eight independent variations of the values of the scales. The scale uncertainty in the predictions is taken as the largest variation among these eight variations.

8.2.2 Parton Distribution Functions

There are uncertainties in the parton distribution functions that are used in the theoretical calculations. The PDF uncertainties arise from the uncertainties in the

measured values of the cross sections from which the PDFs are extracted, from the uncertainties in the theory predictions that are fitted to the measurements and from the uncertainties in the fitting procedure. The sources of PDF uncertainties that are considered depend on the PDF set. The procedure to propagate the PDF uncertainties to the predictions also depend on the PDF set.

For the NNPDF3.0 PDF set, the uncertainties that are related to the measured values of the cross sections from which the PDFs are extracted are considered. The propagation of these uncertainties relies on MC replicas generated based on these measured values. For each replica, a different PDF set is extracted. In the context of the predictions of the $\gamma + b$ cross section, one hundred PDF replicas are considered. Each of these PDF replicas are used to produce theoretical predictions of the $\gamma + b$ cross section. The PDF uncertainty in a predicted cross-section value is taken to be the two-sided 68% confidence interval of the replica distribution of that predicted value [192].

8.2.3 Strong Coupling Constant

The strong coupling constant is a parameter that is present in every term of the theoretical calculations. The variation of its value according to its uncertainty is thus expected to have the largest impact on the predictions among the parameters of the Standard Model. The value of the strong coupling constant at the energy scale of the mass of the Z boson is $\alpha_{\mathrm{S}}(m_Z) = 0.118 \pm 0.002$ at the 90% confidence level [54, 77].

The impact of the uncertainty in the strong coupling constant on the predictions is assessed by varying this value according to its uncertainty simultaneously in the

calculations of the matrix elements and in the PDFs.[2] This results in an uncertainty in the predictions at the 90% confidence level. To properly compare to the other uncertainties, this uncertainty is reported at the 68% confidence level by dividing its size by 1.645.

8.2.4 Total Theoretical Uncertainty

The total theoretical uncertainty in the predicted values is obtained by adding in quadrature the three individual uncertainties listed in the previous sections. This is done separately for positive and negative variations, allowing for the possibility of an asymmetric total uncertainty. The total uncertainties in the NLO predictions obtained from MadGraph5_aMC@NLO in the 5F and in the 4F schemes are assessed. Figures 8–11 and 8–12 show the total relative theoretical uncertainty in the predicted values of the $\gamma + b$ differential cross section for the central and the forward regions, and also for the cross-section ratio, in the 5F and 4F schemes respectively. The figures also show the breakdown of the total uncertainty into the three individual uncertainty components.

[2]For technical reasons, this uncertainty is assessed by using the NNPDF3.1 PDF set, although the proper assessment would require the use of the NNPDF3.0 PDF set. Both PDF sets produce a similar PDF uncertainty in the predictions, such that the α_S uncertainty in the predictions evaluated with the former set is expected to be also similar to that using the latter PDF set.

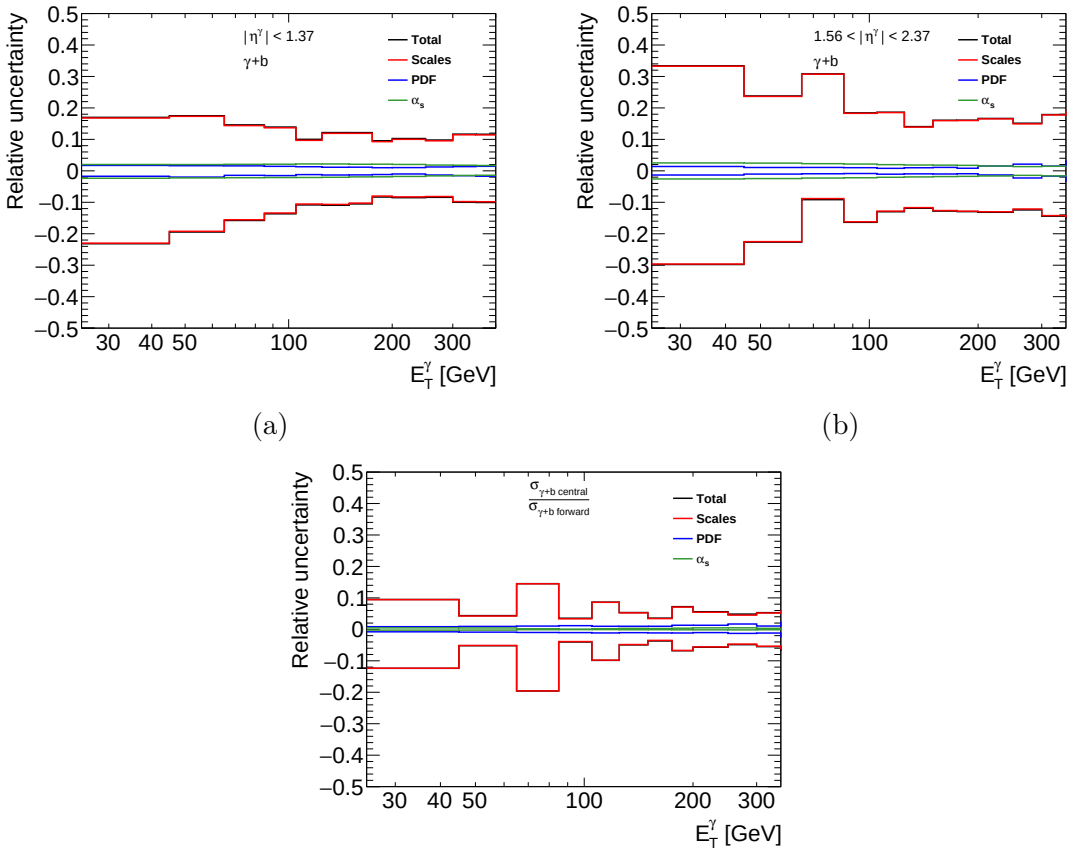

Figure 8–11 – Total relative uncertainty in the predicted values obtained from MadGraph5_aMC@NLO in the 5F scheme as a function of E_{T}^{γ} of (a) the differential $\gamma + b$ cross section for the central region, (b) the differential $\gamma + b$ cross section for the forward region and (c) the central-to-forward cross-section ratio. Also displayed is the breakdown of the total theoretical uncertainty into individual components.

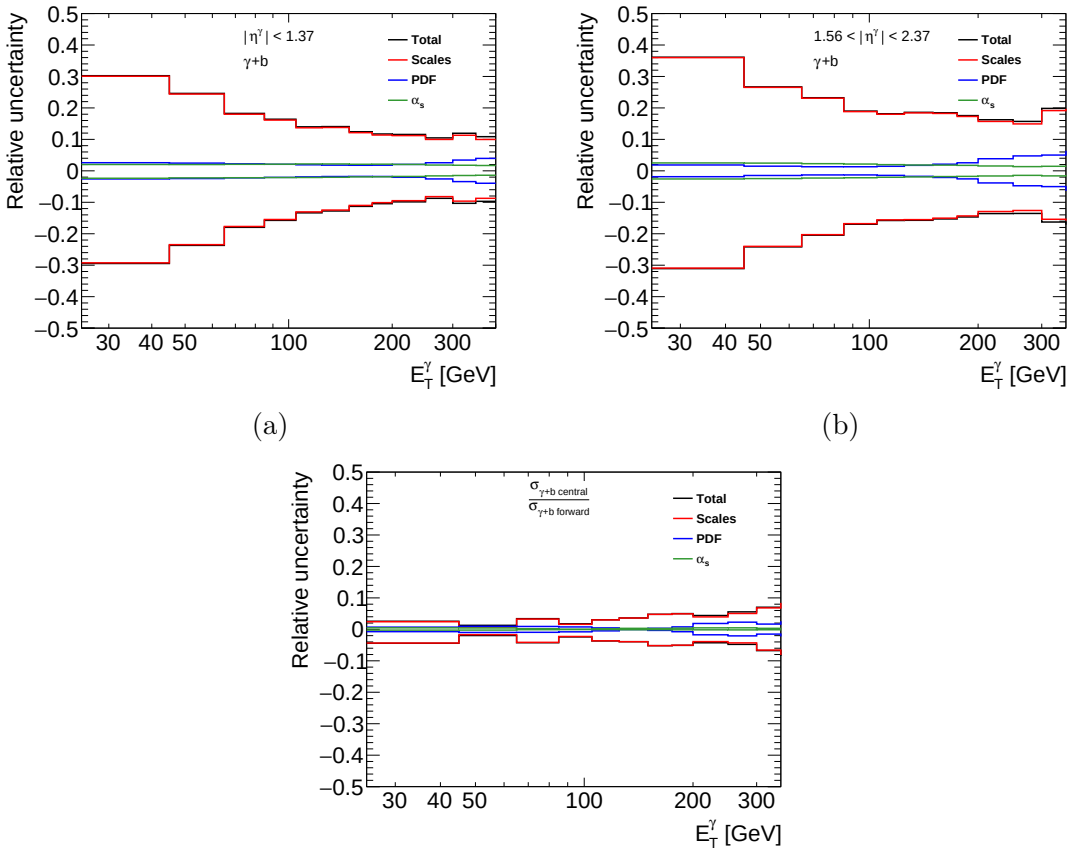

Figure 8–12 – Total relative uncertainty in the predicted values obtained from MadGraph5_aMC@NLO in the 4F scheme as a function of E_{T}^{γ} of (a) the differential $\gamma + b$ cross section for the central region, (b) the differential $\gamma + b$ cross section for the forward region and (c) the central-to-forward cross-section ratio. Also displayed is the breakdown of the total theoretical uncertainty into individual components.

The uncertainties in the 5F predictions are affected by statistical fluctuations related to the fact that not all generated events are $\gamma+b$ events. Thus, a compromise between the computer processing time and the accuracy of the uncertainties reduces the latter.

The total relative uncertainty in the predicted $\gamma + b$ cross-section values is largest at low E_{T}^{γ} and decreases as a function of E_{T}^{γ}. In the central region, the total uncertainty in the 5F (4F) predictions decreases from about 25% (30%) to about 10% in the E_{T}^{γ} range of the measurement, while that in the forward region is about 5% larger throughout the range. It is observed that the dominant theoretical uncertainty comes from the choice of the values of the renormalization and factorization scales, or in other words from the missing higher-order terms of the pQCD series. It is this uncertainty that decreases as a function of E_{T}^{γ}. The uncertainties related to the PDFs and to α_s are smaller and of a comparable size to one another. They are mostly independent of E_{T}^{γ}.

The total relative uncertainty in the predicted cross-section ratio is mostly independent of E_{T}^{γ}. It is about 5%.[3] This independence on E_{T}^{γ} is due to the partial cancellation of the scale uncertainty. Even with this partial cancellation, the scale uncertainty still dominates the total theoretical uncertainty in the predicted cross-section ratio.

[3]For technical reasons, the uncertainties in the predicted values of the cross-section ratio in the 4F scheme are obtained directly from the overall uncertainties in the cross section for the central and the forward regions, in contrast to the propagation of every individual uncertainty to the ratio. This can cause an underestimation of the uncertainties.

Overall, the size of the total theoretical uncertainty in the 5F predictions is similar to that in the 4F predictions. The size of the total theoretical uncertainty in the cross section is roughly similar to the size of the total measurement uncertainty in the cross section. Although the size of the measurement uncertainty is not reduced in the cross-section ratio in comparison to that in the cross section, the size of the theoretical uncertainty is reduced. Thus, the ratio allows for a more stringent comparison of the predictions against the measurement.

Theoretical uncertainties are not assessed for the LO predictions because the dominant uncertainty, the scale uncertainty, does not correspond to the missing higher-order pQCD terms. However, since the LO predictions are less precise than the NLO predictions, it is expected that their total theoretical uncertainties are larger than those shown in Figures 8–11 and 8–12.

CHAPTER 9
Results

This chapter presents the measured values of the differential fiducial $\gamma + b$ production cross section as a function of E_{T}^{γ} in proton–proton collisions for the central and forward pseudorapidity regions, and of the central-to-forward cross-section ratio. These values are compared to the predicted values and the level of agreement between them is interpreted in terms of the underlying physical processes. For completeness, the integrated fiducial $\gamma + b$ production cross section in proton–proton collisions is also presented. The first and second sections present respectively the differential and integrated $\gamma + b$ cross-section measurements.

9.1 Differential Fiducial Cross Section

The differential fiducial cross section of the associated production of a photon and a bottom quark as a function of E_{T}^{γ} is measured through Equation 7.7. Theoretical predictions of this cross section are obtained from Sherpa, Pythia and MadGraph5_aMC@NLO in the 5F and 4F schemes as described in Section 2.3.3. The evaluation of the uncertainties in the measurement and in the predictions was presented in Chapter 8. The results in the central and in the forward regions are shown in Figure 9–1. From that figure it can be seen that the differential cross section is steeply decreasing as a function of E_{T}^{γ}, decreasing by about five orders of magnitude in the E_{T}^{γ} range considered.

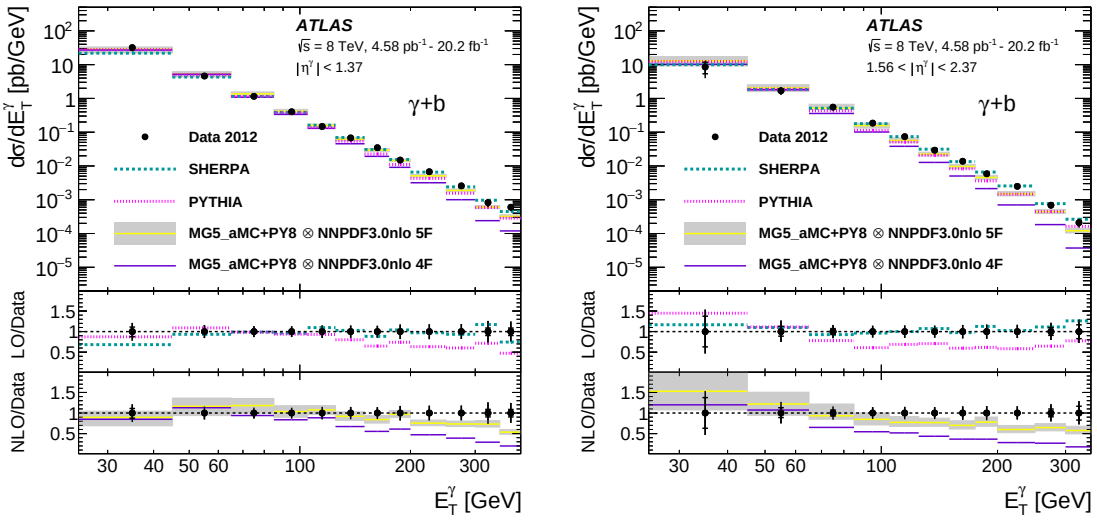

(a) (b)

Figure 9–1 – Differential fiducial cross section of the associated production of a photon and a bottom quark as a function of E_{T}^{γ} as measured and as predicted by SHERPA, PYTHIA and MADGRAPH5_aMC@NLO in the 5F and 4F schemes for (a) the central region and (b) the forward region, as published in Ref. [188]. The ratios of the LO predictions to the measurement are displayed in the middle panel, while the ratios of the NLO predictions to the measurement are displayed in the bottom panel. The error bars correspond to the total uncertainty in the measurement, while the horizontal marks on the bars represent the contribution of the statistical uncertainty. The label MG5_aMC+PY8 refers to predictions obtained from the interface of MADGRAPH5_aMC@NLO to PYTHIA. The total uncertainty in the MADGRAPH5_aMC@NLO prediction in the 5F scheme is displayed as a band. The total uncertainty in the 4F prediction is not displayed but has a similar size to that in the 5F prediction. No uncertainties are displayed or considered for the SHERPA and PYTHIA predictions.

The LO predictions provide a good description of the data at low E_{T}^{γ}. Although no theoretical uncertainties are assessed for the LO predictions, the PYTHIA prediction appear to underestimate the data above 150 GeV (85 GeV) in E_{T}^{γ} for the central (forward) region, given the measurement uncertainties. On the other hand, the SHERPA prediction agrees with the data across the whole E_{T}^{γ} range considered. The smaller predicted values from PYTHIA compared to those from SHERPA have also been reported in the analysis measuring the inclusive production cross section of prompt photons in pp collisions at $\sqrt{s} = 8$ TeV in the E_{T}^{γ} range that is considered in the present measurement [35]. As such, the underestimation of the data by the PYTHIA prediction is possibly related to the modelling of the prompt photon.

The NLO predictions also provide a good description of the data at low E_{T}^{γ}. However, above 125 GeV (85 GeV) in the central (forward) region, the 4F prediction increasingly underestimates the data as a function of E_{T}^{γ}. The 5F prediction agrees with the data up to larger E_{T}^{γ} values than the 4F prediction, but still underestimates the data above 350 GeV (200 GeV) in the central (forward) region. At high E_{T}^{γ}, the predicted values in the 5F scheme underestimate by up to a factor of two the measured values. The observation that the 5F prediction provides a better description of the data at larger E_{T}^{γ} values than the 4F prediction is consistent with the expectation that the 4F scheme is better suited for energy scales close to the b quark mass, while the 5F scheme is better suited for larger energy scales.

The NLO prediction in the 5F scheme uses the NNPDF3.0 PDF set. The description of the $\gamma + b$ production in the 5F scheme depends directly on the PDF of the b quark. Therefore, the 5F prediction, and its agreement with the data, could depend on the

choice of the PDF set. To assess the sensitivity of the prediction to the choice of the PDF set, a 5F prediction using the CT14 PDF set has been produced, including the evaluation of its total theoretical uncertainty.[1] The prediction that is obtained with that PDF set does not differ significantly from the one obtained with the NNPDF3.0 PDF set. The 5F NLO prediction is not sensitive to the choice of the PDF set and thus neither is its agreement with the data.

The underestimation of the data by the 5F NLO prediction at high E_{T}^{γ} occurs in the region of phase space where the contribution of the Compton scattering subprocess, $gb \to \gamma b$, starts to become less dominant as a function of E_{T}^{γ} in favour of gluon splitting in the quark–antiquark annihilation subprocess, $q\bar{q} \to \gamma g$, as can be seen in Figure 9–2(a). Since the gluon-splitting subprocess is not present at $O(\alpha\alpha_{\mathrm{S}})$ and only starts to contribute at $O(\alpha\alpha_{\mathrm{S}}^{2})$, this subprocess does not receive real and virtual contributions in the 5F NLO prediction, in contrast to the Compton scattering subprocess. In other words, the description of the Compton scattering subprocess is more accurate than the gluon-splitting subprocess in the 5F NLO prediction. Therefore, the 5F NLO prediction is expected to become less accurate as a function of E_{T}^{γ}. In comparison, the SHERPA prediction takes into account real contributions up to $O(\alpha\alpha_{\mathrm{S}}^{4})$ and thus include real contributions to the gluon-splitting subprocess. It is observed that this prediction agrees with the data. These observations indicate that

[1]The PDF uncertainty in the CT14 PDF set is propagated to the measured quantities in a different way from that in the NNPDF3.0 PDF set. The Hessian matrix of the fitted PDFs is diagonalized to provide eigenvectors that are to be propagated to the measured quantities [193].

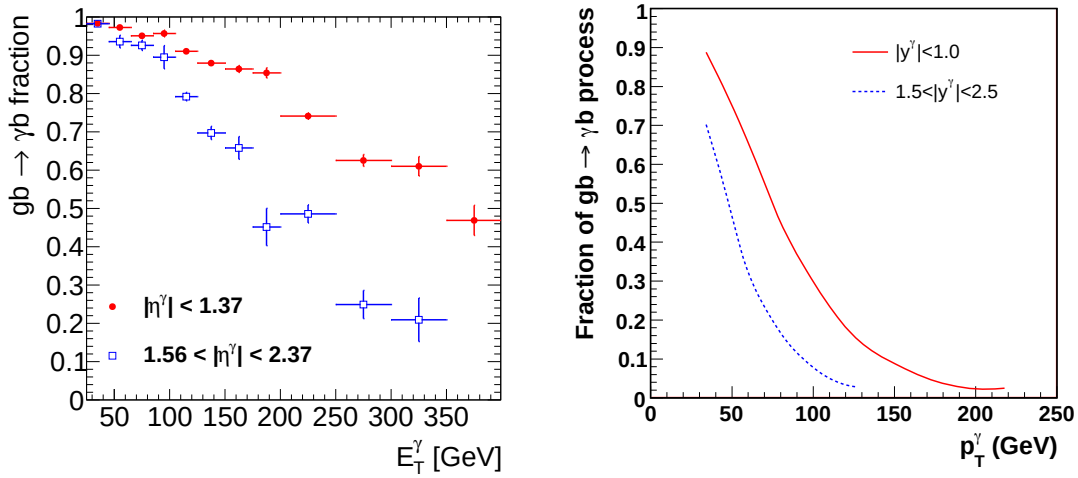

(a) (b)

Figure 9–2 – Fraction of the subprocess $gb \to \gamma b$ in the sum of the subprocesses $gb \to \gamma b$ and $q\bar{q} \to \gamma g$ in PYTHIA events selected at the particle level for two regions of the photon rapidity as a function of E_{T}^{γ} in (a) proton–proton collisions at $\sqrt{s} = 8$ TeV and (b) proton–antiproton collisions at $\sqrt{s} = 1.96$ TeV. The vertical error bars in (a) represent the statistical uncertainty in the fractions. Figure (b) is reproduced with permission from Ref. [49].

the underestimation of the data by the 5F NLO prediction is seemingly caused by the lack of higher-order terms in the truncated pQCD series. The impact of these terms is not assessed as part of the scale uncertainty since the gluon-splitting subprocess is essentially at LO in the 5F NLO prediction. The variation of the scale values does not account for its contribution in the higher-order terms. The scale uncertainty underestimates the complete impact of the missing higher-order terms at high E_{T}^{γ}.

Figure 9–2 shows the fraction of the Compton scattering subprocess in the sum of the Compton scattering and the gluon-splitting annihilation subprocesses in the PYTHIA samples in pp collisions at $\sqrt{s} = 8$ TeV, relevant to this measurement, and in $p\bar{p}$

collisions at $\sqrt{s} = 1.96$ TeV, relevant to the D0 measurement presented in Figure 1–1. In both cases, the contribution of the Compton scattering subprocess decreases as a function of E_{T}^{γ} since it depends directly on the b-quark and gluon PDFs, which steeply decrease as a function of the momentum fraction of the proton, x, or similarly E_{T}^{γ}. In parallel, the annihilation subprocess becomes relatively more dominant as a function of E_{T}^{γ} since it directly depends on the PDFs of any pair of quarks and antiquarks, in particular the valence quarks whose PDFs are relatively large at large values of x, or E_{T}^{γ}. For a similar reason, the forward region, which requires larger values of x, has a lower relative contribution of the Compton scattering subprocess than the central region.

The relative contribution of the Compton scattering subprocess is more important in pp collisions than in $p\bar{p}$ collisions for a given E_{T}^{γ} value, as can be seen in Figure 9–2, because valence antiquarks are present in the latter type of collision. This results in an enhanced contribution of the quark–antiquark annihilation subprocess in $p\bar{p}$ collisions. The 5F NLO predictions are thus expected to describe the $\gamma + b$ production process in the collisions provided by the LHC up to larger E_{T}^{γ} values than those provided by the Tevatron.

The comparison of the D0 measurement to the NLO prediction of the differential $\gamma + b$ cross section in $p\bar{p}$ collisions, displayed in Figure 1–1, shows that the NLO prediction underestimates the data for E_{T}^{γ} values above 70 GeV. This underestimation occurs in the phase-space region in which the Compton scattering subprocess is less dominant compared to the gluon-splitting subprocess, similarly to the measurement presented in this thesis. The underestimation of the D0 data occurs for lower values

of E_{T}^{γ} than the underestimation related to the measurement presented in Figure 9–1. This is compatible with the expectation that the NLO predictions should provide a good description of the data up to larger E_{T}^{γ} values at the LHC than at the Tevatron. Additionally, it is observed that the SHERPA prediction provides a good description of the D0 measurement. The previous observations give confidence that the discrepancy between the NLO prediction and the D0 data is due to missing higher-order contributions related to the gluon-splitting quark–antiquark annihilation subprocess and that a similar, albeit smaller, effect is observed in the measurement presented in this thesis.

In addition to the measurement of the differential fiducial cross section as a function of E_{T}^{γ} in the central and the forward regions, the ratio of the cross section in those regions is measured. The measured and predicted values of the ratio are shown in Figure 9–3.

The ratio is greater than one due to the smaller cross section in the forward region compared to that in the central region, as explained in Section 8.1.4. Also, the value of the ratio increases as a function of E_{T}^{γ} since the cross section in the forward region is more steeply decreasing than that in the central region. This is due to the fact that the PDF values corresponding to the x values probed in the forward region decrease more rapidly as a function of x than those corresponding to the x values probed in the central region.

A similar conclusion regarding the agreement between the predictions and the measurement of the differential cross section applies to the ratio. The SHERPA prediction

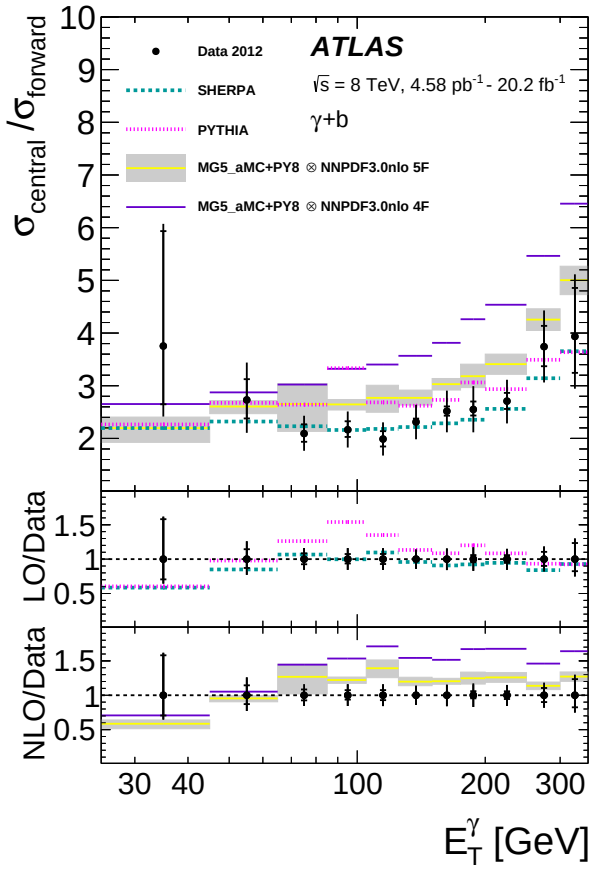

Figure 9–3 – Ratio of the fiducial cross section in the central region to that in the forward region of the associated production of a photon and a bottom quark as a function of E_{T}^{γ} as measured and as predicted by SHERPA, PYTHIA and MADGRAPH5_aMC@NLO in the 5F and 4F schemes, as published in Ref. [188]. The ratios of the LO predictions to the measurement are displayed in the middle panel, while the ratios of the NLO predictions to the measurement are displayed in the bottom panel. The error bars correspond to the total uncertainty in the measurement, while the horizontal marks on the bars represent the contribution of the statistical uncertainty. The label MG5_aMC+PY8 refers to predictions obtained from the interface of MADGRAPH5_aMC@NLO to PYTHIA. The total uncertainty in the MADGRAPH5_aMC@NLO prediction in the 5F scheme is displayed as a band. The total uncertainty in the 4F prediction is not displayed but has a similar size to that in the 5F prediction. No uncertainties are displayed or considered for the SHERPA and PYTHIA predictions.

provides the best description of the data among the considered predictions. The 4F NLO prediction overestimates and does not agree with the data above 65 GeV in E_{T}^{γ}. The 5F NLO prediction overestimates the measurement above 85 GeV in most bins, but are within approximately two standard deviations of the measurement. Also, the PYTHIA prediction, in contrast to the case of the differential cross section, agrees with the data in most bins. This suggests that the underestimation of these predictions at high E_{T}^{γ} is similar in the central and in the forward regions, such that effect cancels in the ratio.

The measurement of the differential cross section and of the cross-section ratio of the production of $\gamma + b$ events in pp collisions is sensitive to the modelling of the b quarks, as can be seen by the differing levels of agreement with the data between the 5F and the 4F NLO predictions. This measurement allows to assess which treatment of the mass effects related to the bottom quark provides the best description of the physical processes at energy scales larger than the b-quark mass.

To allow for the comparison of the measurement with future theoretical predictions, which could improve the treatment of the mass effects, a number of actions have been taken. The numerical values of the measurement of the differential cross section and of the cross-section ratio, including the systematic uncertainties listed in Appendix E, have been made publicly available in HEPData [194]. The numerical values of the measurement, including the statistical uncertainty, the total systematic uncertainty and the total measurement uncertainty, are also reported in Appendix F. This appendix also lists the numerical values of the predictions, including the total

theoretical uncertainties. Furthermore, software that takes as input generated particle-level events and outputs predictions that can be compared to the measured values of the differential cross section has been made publicly available in Rivet [195]. This software allows to accurately reproduce the particle-level selection of Section 5.3, which defines the fiducial region of the cross section. These actions have been taken to facilitate the production of new predictions and their comparisons to the data.

9.2 Integrated Fiducial Cross Section

The measurement of the integrated fiducial cross section of the associated production of a photon and a bottom quark in the central and the forward regions is discussed. The ratio of the integrated cross section in the central region to that in the forward region is also considered. The measured values are obtained by integrating the differential fiducial cross section. The uncertainties in the measured values are obtained by propagating the systematic and the statistical uncertainties in the differential cross section, listed respectively in Appendices E and F, to the integrated cross section. The statistical uncertainty in the cross-section ratio is obtained from an MC toy study similar to that discussed in Section 8.1.1. Predictions of the measured quantities are similarly obtained by integrating the differential cross section and by propagating the individual variations up to these quantities.

Figure 9–4 shows the measured and the predicted values of the integrated cross section in the central and the forward regions and of the ratio of the integrated cross section in those regions. In the case of the integrated cross section, it can be seen that every prediction agrees with the measurement for both the central and the forward regions.

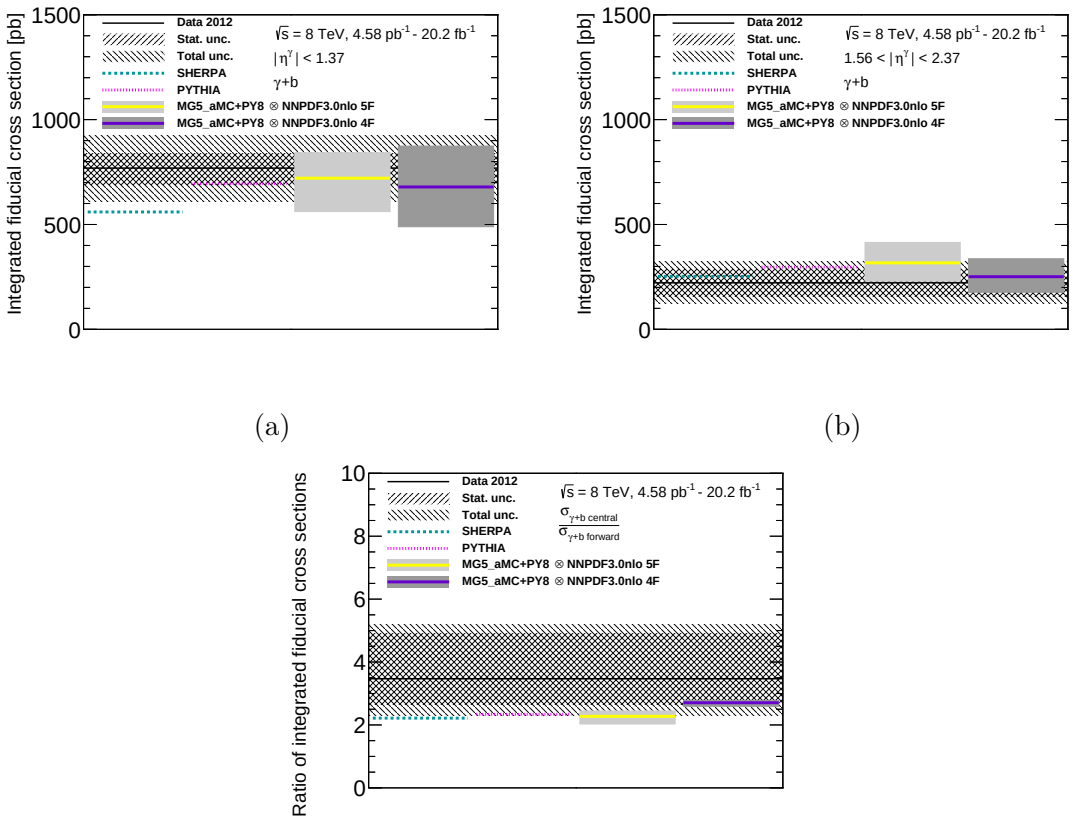

Figure 9–4 – Integrated fiducial cross section of the associated production of a photon and a bottom quark as measured and as predicted by SHERPA, PYTHIA and MADGRAPH5_aMC@NLO in the 5F and 4F schemes for (a) the central region and (b) the forward region, and also (c) the central-to-forward cross-section ratio. The label MG5_aMC+PY8 refers to predictions obtained from the interface of MADGRAPH5_aMC@NLO to PYTHIA. The total uncertainties in the MADGRAPH5_aMC@NLO predictions are displayed as bands. No uncertainties are displayed or considered for the SHERPA and PYTHIA predictions.

Although the SHERPA prediction for the central region appears to underestimate significantly the measurement, the size of its uncertainty is expected to be larger than that in the NLO predictions and, consequently, is expected to cover the difference in values. The integrated cross section is dominated by the differential cross section in the lowest-E_{T}^{γ} bin. As such, the 4F NLO prediction, which is better suited at low energy scales, provides a good description of the measurement. Also, the Compton scattering subprocess dominates the cross section in the lowest-E_{T}^{γ} bin. Therefore, the agreement between the other predictions and the data is a reflection of the good theoretical description of the Compton scattering subprocess.

In the case of the cross-section ratio, the predictions agree with the measurement within approximately one standard deviation. This appears to be caused by an upward variation of the ratio in the dominating lowest-E_{T}^{γ} bin, as can be interpreted from the size of the statistical uncertainty in the ratio in that E_{T}^{γ} bin and from the shape of the measured distribution of the ratio in Figure 9–3.

The numerical values of the integrated cross section in the central and the forward regions and of the central-to-forward ratio of the integrated cross section are provided in HEPData and in Appendix F.

CHAPTER 10
Conclusion

The measurement of the inclusive differential cross section of the associated production of a photon and a bottom quark as a function of E_{T}^{γ} in proton–proton collisions at a center-of-mass energy of 8 TeV was presented. The measurement uses the ATLAS detector at the LHC and a dataset corresponding to an integrated luminosity of up to 20.2 fb^{-1}. It is the first measurement of this physical process in proton–proton collisions. This process is sensitive to the modelling of bottom quarks in perturbative QCD calculations and to the b-quark parton distribution function.

The cross section is measured in fiducial regions of the kinematic phase space at the particle level. It is measured in two regions of $|\eta^{\gamma}|$: the central region, $|\eta^{\gamma}| < 1.37$, and the forward region, $1.56 < |\eta^{\gamma}| < 2.37$. The measurement covers the ranges $25 < E_{\mathrm{T}}^{\gamma} < 400$ GeV and $25 < E_{\mathrm{T}}^{\gamma} < 350$ GeV respectively for the two pseudorapidity regions. The photon considered in this analysis is the leading prompt photon in an event. The isolation energy of that photon is required to satisfy $E_{\mathrm{T}}^{\mathrm{iso}} < 4.8\ \mathrm{GeV} + 0.0042 \times E_{\mathrm{T}}^{\gamma}$. The bottom quark in the event is identified via the jet that it produces. The jet considered in this analysis is the leading jet in an event. This leading jet is required to contain a b hadron. This leading jet is also required to have $p_{\mathrm{T}}^{\mathrm{jet}} > 20$ GeV and $|y| < 2.5$. The angular distance between the leading photon and the leading jet is required to be greater than one.

At the detector level, recorded events are selected with analogous criteria on the leading photon and on the leading jet as those at the particle level, with the exception that no requirement is imposed on the flavour of the leading jet. The selected events are statistically subtracted from events containing background prompt photons via the two-dimensional sideband method, which is based on the photon identification and on the isolation energy of the photon. The selected events are statistically reduced to events in which the leading jet contains a b hadron via the template fit method, which is based on the continuously calibrated distributions of the MV1c tagging weight. The detector-level events are corrected for reconstruction and selection inefficiencies and other detector effects by the bin-by-bin data unfolding method, which brings the measurement to the particle level.

The uncertainties in the measured values of the cross section are dominated by systematic uncertainties, which are themselves dominated by uncertainties related to the b-tagging efficiencies and the Monte Carlo statistical uncertainty. The data statistical uncertainty in the measurement is also important at low and at high E_{T}^{γ}. The typical value of the total relative uncertainty in the measured cross section is approximately 20%.

To reduce the contribution of the systematic uncertainties, which are for the most part positively correlated between the central and the forward regions, the central-to-forward cross-section ratio is measured. The systematic uncertainties in the ratio are indeed decreased but the statistical uncertainties are increased, such that the size of the total relative uncertainty is similar to that in the differential cross section.

The numerical values of the measured quantities and of their uncertainties are publicly available in the HEPData repository and software that reproduces the particle-level event selection is provided in the Rivet repository.

The differential cross section and the cross-section ratio are compared to leading-order predictions in perturbative QCD from Sherpa and Pythia and to next-to-leading-order predictions from MadGraph5_aMC@NLO. For the next-to-leading-order predictions, two different calculation schemes are considered, the five-flavour and four-flavour schemes. The two schemes have a different treatment of the terms in perturbative QCD that are dependent on the mass of the bottom quark. The total uncertainty in the predictions are dominated by the scale uncertainty, which assesses the impact of the truncation of the perturbative QCD series to a given finite order. The total relative theoretical uncertainty in the cross-section ratio is reduced in comparison to that in the differential cross section.

Among the theoretical predictions considered, the Sherpa prediction, which takes partially into account terms of higher orders than those in the next-to-leading-order predictions, provides the overall best description of the measured values. The four-flavour next-to-leading-order prediction provides the overall worst description of the measured values. This calculation scheme is better suited for energy scales close to the mass of the bottom quark.

The five-flavour next-to-leading-order prediction, which should provide a priori the best description of the data among the different theoretical predictions considered, agrees with the measured values of the differential cross section at low E_{T}^{γ}. However,

this prediction underestimates the measured values of the differential cross section at high E_{T}^{γ} by up to a factor of two. The difference in the levels of agreement between the four- and the five-flavour predictions indicate that the measurement is sensitive to the treatment of the mass terms in perturbative QCD and that it can be used to improve the modelling of the bottom quarks in perturbative QCD. Also, although the five-flavour prediction is sensitive to the b-quark parton distribution function, no significant differences are observed in the predictions that use parton distribution functions provided by different collaborations.

The disagreement at high E_{T}^{γ} between the five-flavour prediction and the data occurs in the region of phase-space where the gluon-splitting quark–antiquark annihilation subprocess is dominant in comparison to the Compton scattering subprocess. The gluon-splitting subprocess is not as well theoretically described by the predictions since it does not occur at the leading order in perturbative QCD, in contrast to the Compton scattering subprocess. This lack of agreement at high E_{T}^{γ} has been observed between the D0 measurement and the next-to-leading-order prediction of the differential production cross section of $\gamma + b$ events in proton–antiproton collisions. In this process, the gluon-splitting subprocess dominates the Compton scattering subprocess at a lower E_{T}^{γ} than in the proton–proton process. The disagreement between the measurement and the prediction occurs also at a lower E_{T}^{γ}. These observations indicate that a good theoretical description of these physical processes requires that the predictions must be at a higher order than the next-to-leading order to properly take into account the gluon-splitting effects. These effects are related

to the b-jet definition that is used, which is not infrared safe with respect to the jet flavour.

This first measurement of the $pp \to \gamma bX$ process paves the way towards more refined analyses. Several aspects can be improved. From the point of view of the theoretical predictions, SHERPA 2 could be used to obtain a five-flavour next-to-leading-order prediction that also takes partially into account the higher-order effects, via the use of the MEPS@NLO scheme. This prediction should provide a more accurate description of the data than any of those that have been considered. Additionally, these predictions could be obtained at the parton level, which would enable the data to be included in a global fit of the parton distribution functions.

From the point of view of the measurement, it would be desirable to produce simulated background samples of adequate size as they would allow to understand the physical cause of the dependence of the prompt-photon purity on the MV1c weight of the leading jet. Also, the analysis could be extended to measure the cross section differentially as a function of additional observables, such as $|\eta^{\gamma}|$, $p_{\mathrm{T}}^{\mathrm{jet}}$, $|y^{\mathrm{jet}}|$ and the angular distance between the leading photon and the leading jet, among others, which would bring complementary information on the $\gamma + b$ production process. In addition, the analysis could measure the production of an additional b quark, producing a subleading b-jet. These events could be identified by an additional template in the MV1c template fit. A better understanding of the production of a photon in association with two b quarks could help reduce the modelling uncertainty in the background jet events of the production of $t\bar{t}H$ in proton–proton collisions with the

Higgs boson decaying into two b quarks, which is the dominant uncertainty in the search for this process [196].

The measurement would benefit from a calibration of the b-tagging efficiencies that would extend beyond the current $p_{\mathrm{T}}^{\mathrm{jet}}$ values of 300 GeV for the b- and c-jets and of 750 GeV for the light jets. Such a calibration would allow to extend the measurement up to larger E_{T}^{γ} values. Furthermore, although the continuously calibrated MV1c templates allow to assess straightforwardly the uncertainty in the template fit, they anticorrelate the uncertainties in the calibration of the b-tagging efficiencies. A fitting procedure which would decouple the b-tagging uncertainties from the uncertainty in the shapes of the templates would allow for a precise measurement of the ratio of the $\gamma + c$ cross section to the $\gamma + b$ cross section. Such a ratio would allow to decrease the size of most of the uncertainties, similarly to the central-to-forward cross-section ratio, but without the increase in the size of the statistical uncertainties. This ratio in $p\bar{p}$ collisions has been measured by the D0 experiment [197]. The ratio is sensitive to c-quark parton distribution function. In particular, it is sensitive to the possible presence of intrinsic charm quarks in the proton [198].

The sensitivity of the measurement of the $\gamma + b$ cross section to the b-quark parton distribution function can be increased by removing the contribution of the gluon-splitting subprocess. This can be achieved by using a b-jet definition that is infrared safe with respect to the jet flavour. Such a definition is provided by the flavour-k_t jet algorithm. This algorithm is experimentally difficult to use as it requires the knowledge of whether a b quark is present or not in every input object. An idea on how to achieve this is via jet reclustering, i.e. forming large-radius jets from

small-radius jets. For example, b-tagging could be performed on anti-k_t jets of radius 0.2. These jets, for which the presence of a b quark is known through the b-tagging procedure, could then be used as input to the flavour-k_t algorithm with a parameter $R = 1$. This innovative idea would however require detailed performance studies to ensure its feasibility.

APPENDIX A
Parton Kinematics

This Appendix aims to motivate the choice of observables used in the measurement presented in this thesis. It also describes them in terms of parton-level quantities.

The particle kinematics in the laboratory frame of a $2 \to 2$ parton-level process in proton–proton collisions at a center-of-mass (COM) energy of $\sqrt{s}$, where s is the Mandelstam variable, is schematized in Figure A–1. It is assumed that $\sqrt{s}$ is much greater than the mass of the proton or that of the partons such that the masses can be neglected. The z-axis is aligned to correspond to the momentum axis of the protons. For such a frame, in which the colliding partons have a momentum fraction x_1 and x_2 of their respective proton, the four-momenta of the partons are

$$P_1 = \left(x_1 \frac{\sqrt{s}}{2},\, 0,\, 0,\, x_1 \frac{\sqrt{s}}{2}\right) \quad \text{and} \quad P_2 = \left(x_2 \frac{\sqrt{s}}{2},\, 0,\, 0,\, -x_2 \frac{\sqrt{s}}{2}\right). \tag{A.1}$$

The two particles that are produced have the four-momenta

$$P_3 = (E_3,\, p_3^x,\, p_3^y,\, p_3^z) \quad \text{and} \quad P_4 = (E_4,\, p_4^x,\, p_4^y,\, p_4^z). \tag{A.2}$$

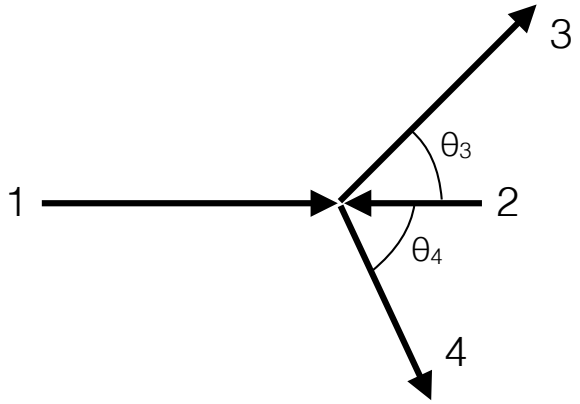

Figure A–1 – Parton-level kinematic diagram of a collision between two hadrons producing two particles in the laboratory frame. Partons 1 and 2 collide to produce particles 3 and 4. The z-axis points to the right.

The conservation of four-momentum between the initial and final states implies

$$\begin{aligned} E_3 + E_4 &= (x_1 + x_2)\frac{\sqrt{s}}{2}, \\ p_3^x + p_4^x &= 0, \\ p_3^y + p_4^y &= 0, \\ p_3^z + p_4^z &= (x_1 - x_2)\frac{\sqrt{s}}{2}. \end{aligned} \tag{A.3}$$

The two produced particles have their x- and y-components of their momenta opposite of each other. These components are also independent of the x_1 and x_2 momentum fractions. This is an important observation as those momentum fractions are experimental unknowns: each collision has random x_1 and x_2 following the parton distribution functions, which are discussed in Section 2.2.1. The transverse component of the momentum, $p_{\mathrm{T}} = \sqrt{(p^x)^2 + (p^y)^2}$, is thus an observable that can be interpreted independently of the details specific to a given proton–proton collision. Also, it has the same value for the two produced particles. The four-momenta can be expressed

in terms of this quantity explicitly by using spherical coordinates. The four-momenta are then

$$\begin{aligned} P_3 &= (E_3,\, p_\mathrm{T}\cos\phi,\, p_\mathrm{T}\sin\phi,\, p_3\cos\theta_3)\,, \\ P_4 &= (E_4,\, p_\mathrm{T}\cos(\phi+\pi),\, p_\mathrm{T}\sin(\phi+\pi),\, p_4\cos\theta_4)\,, \end{aligned} \tag{A.4}$$

where p_i is the magnitude of $\vec{p}_i$, ϕ is the azimuthal angle of particle 3 around the z-axis and θ is the polar angle from the positive z-direction. As ϕ only depends on p_x and p_y, it is also independent of x_1 and x_2.

In contrast to the azimuthal angle, the polar angle does depend on x_1 and x_2. A change in the relative values of the momentum fractions induces a Lorentz boost along the z-axis. With the goal of minimizing the sensitivity of the observables to boosts, the best that can be done is thus to choose an angle whose measure is boost invariant. To construct such an angle, considering the COM frame proves to be useful. The COM frame of the partonic system requires that $(p_1^z)^* = -(p_2^z)^*$, where the asterisks mean that the quantities are in the COM frame. A boost of parameters β and $\gamma = (1-\beta^2)^{-\frac{1}{2}}$ can be applied on the parton four-momenta in the laboratory frame to get the four-momenta in the COM frame:

$$\begin{aligned} P_1^* &= \left(\gamma x_1 \frac{\sqrt{s}}{2}(1-\beta),\, 0,\, 0,\, \gamma x_1 \frac{\sqrt{s}}{2}(1-\beta)\right), \\ P_2^* &= \left(\gamma x_2 \frac{\sqrt{s}}{2}(1+\beta),\, 0,\, 0,\, -\gamma x_2 \frac{\sqrt{s}}{2}(1+\beta)\right). \end{aligned} \tag{A.5}$$

The COM frame requirement implies that $x_1(1-\beta) = x_2(1+\beta)$, giving $\beta = \frac{x_1 - x_2}{x_1 + x_2}$. Applying the same boost on the four-momenta of the produced particles gives

$$\begin{aligned} P_3^* &= (\gamma(E_3 - \beta p_3 \cos\theta_3),\, p_\mathrm{T}\cos\phi,\, p_\mathrm{T}\sin\phi,\, \gamma(p_3\cos\theta_3 - \beta E_3))\,, \\ P_4^* &= (\gamma(E_4 - \beta p_4 \cos\theta_4),\, p_\mathrm{T}\cos(\phi+\pi),\, p_\mathrm{T}\sin(\phi+\pi),\, \gamma(p_4\cos\theta_4 - \beta E_4))\,. \end{aligned} \tag{A.6}$$

The tangent of the polar angle is defined directly in terms of the components p_T and $p_z = p\cos\theta$ of the four-momentum and its transformation rule is thus simple to write:

$$\tan\theta \to \tan\theta^* = \frac{p_\mathrm{T}^*}{p^*\cos\theta^*} = \frac{p_\mathrm{T}}{\gamma(p\cos\theta - \beta E)} = \frac{\tan\theta}{\gamma(1 - \beta E/(p\cos\theta))}. \tag{A.7}$$

Since the transformed polar angle depends on both the energy and the momentum, it cannot have a boost-invariant measure. This is because the polar angle is defined by a component of the four-momentum that transforms under a boost and one that does not.

An angle that would be defined in terms of components that both transform under a boost could have a boost-invariant measure. The quantity $\alpha = p_z/E$ follows that idea and transforms as

$$\alpha \to \alpha^* = \frac{p_z^*}{E^*} = \frac{\gamma(p_z - \beta E)}{\gamma(E - \beta p_z)} = \frac{\frac{p_z}{E} - \beta}{1 - \beta\frac{p_z}{E}} = \frac{\alpha - \beta}{1 - \alpha\beta}. \tag{A.8}$$

Comparing to the hyperbolic identity $\tanh(y+z) = \frac{\tanh(y)+\tanh(z)}{1+\tanh(y)\tanh(z)}$, the following identifications can be made: $\alpha = \tanh(y)$ and $\beta = -\tanh(z)$. The transformation rule becomes

$$\tanh(y) \to \tanh(y+z). \tag{A.9}$$

The hyperbolic angle y, known as the rapidity, thus transforms as

$$y \to y^* = y - \operatorname{artanh}\beta. \tag{A.10}$$

The transformation rule of the rapidity depends on the boost parameter, such that the rapidity is not boost invariant. However, its measure is boost-invariant:

$$\Delta y \to \Delta y^* = y_2^* - y_1^* = y_2 - \operatorname{artanh}\beta - (y_1 - \operatorname{artanh}\beta) = \Delta y. \tag{A.11}$$

This property makes the rapidity a useful observable to define regions of size Δy. Regions defined that way will have the same size in all frames. Such regions can thus be used to describe every proton–proton collision even if each collision has a different boost.

The rapidity can be written as $y = \operatorname{artanh}\frac{p_z}{E}$. Making use of the hyperbolic identity $\operatorname{artanh} x = \frac{1}{2}\ln\left(\frac{1+x}{1-x}\right)$, the rapidity can also be written $y = \frac{1}{2}\ln\left(\frac{E+p_z}{E-p_z}\right)$.

The energy and the longitudinal momentum can be expressed in terms of the rapidity through the use of the identity $1 - \tanh^2 y = \operatorname{sech}^2 y$:

$$\begin{aligned} \cosh y &= \frac{1}{\sqrt{1-\tanh^2 y}} = \frac{1}{\sqrt{1-\left(\frac{p_z}{E}\right)^2}} = \frac{E}{\sqrt{E^2-p_z^2}}, \\ \sinh y &= \tanh y \cosh y = \frac{p_z}{\sqrt{E^2-p_z^2}}. \end{aligned} \tag{A.12}$$

Defining the transverse mass as $m_\mathrm{T} = \sqrt{E^2 - p_z^2} = \sqrt{m^2 + p_\mathrm{T}^2}$, the energy can be expressed as $E = m_\mathrm{T}\cosh y$ and the longitudinal momentum as $p_z = m_\mathrm{T}\sinh y$.

In terms of m_{T}, p_{T}, ϕ and y, the four-momenta of the produced particles are

$$\begin{aligned} P_3 &= (m_{\mathrm{T},3}\cosh y_3,\, p_{\mathrm{T}}\cos\phi,\, p_{\mathrm{T}}\sin\phi,\, m_{\mathrm{T},3}\sinh y_3)\,, \\ P_4 &= (m_{\mathrm{T},4}\cosh y_4,\, p_{\mathrm{T}}\cos(\phi+\pi),\, p_{\mathrm{T}}\sin(\phi+\pi),\, m_{\mathrm{T},4}\sinh y_4)\,. \end{aligned} \tag{A.13}$$

Approximating that the produced particles are massless, such that $m_{\mathrm{T}} = p_{\mathrm{T}}$, the conservation of four-momentum implies

$$\begin{aligned} p_{\mathrm{T}}(\cosh y_3 + \cosh y_4) &= (x_1 + x_2)\frac{\sqrt{s}}{2}, \\ p_{\mathrm{T}}(\sinh y_3 + \sinh y_4) &= (x_1 - x_2)\frac{\sqrt{s}}{2}. \end{aligned} \tag{A.14}$$

The addition and subtraction of these equations give respectively

$$\begin{aligned} x_1 &= \frac{p_{\mathrm{T}}}{\sqrt{s}}(\cosh y_3 + \sinh y_3 + \cosh y_4 + \sinh y_4) = \frac{p_{\mathrm{T}}}{\sqrt{s}}(e^{y_3} + e^{y_4}), \\ x_2 &= \frac{p_{\mathrm{T}}}{\sqrt{s}}(\cosh y_3 - \sinh y_3 + \cosh y_4 - \sinh y_4) = \frac{p_{\mathrm{T}}}{\sqrt{s}}(e^{-y_3} + e^{-y_4}). \end{aligned} \tag{A.15}$$

Therefore, measuring the rapidities and the transverse momenta of the produced particles gives a handle on the proton momentum fractions of the partons.

Working under the additional approximation that the produced particles have the same rapidity gives

$$\begin{aligned} x_1 &= \frac{2p_{\mathrm{T}}}{\sqrt{s}}e^{y}, \\ x_2 &= \frac{2p_{\mathrm{T}}}{\sqrt{s}}e^{-y}. \end{aligned} \tag{A.16}$$

Multiplying and dividing these equations to solve respectively for the transverse momentum and rapidity yields

$$\begin{aligned} p_{\mathrm{T}} &= \frac{1}{2}\sqrt{x_1 x_2 s}, \\ y &= \frac{1}{2}\ln\frac{x_1}{x_2}. \end{aligned} \tag{A.17}$$

These results are valid under the approximations that only two particles are produced in the collision, that they have the same rapidity and that all particles are massless. These are good approximations for the production of a photon and a b-quark in proton–proton collisions at $\sqrt{s} = 8$ TeV.

Notwithstanding any approximation, the transverse energy, E_{T}, is defined as $E_{\mathrm{T}} = \frac{E}{p} p_{\mathrm{T}}$. For a photon, which is massless and thus $E = p$, the transverse energy is equal to the transverse momentum, $E_{\mathrm{T}} = p_{\mathrm{T}}$. Consequently, the transverse energy for a photon can also be expressed as $E_{\mathrm{T}} = E/\cosh y$. Therefore, small values of E_{T} can be measured either for small to moderate values of E at large y or for small values of E at small values of y, while large values of E_{T} can be obtained for high values of E at small values of y.

The transverse momentum p_{T}, or equivalently the transverse energy E_{T} for a photon, the rapidity y and the azimuthal angle ϕ are thus theoretically interesting observables that are used to define the kinematics of the measurement presented in this thesis. They are also used to define the partonic phase-space of the measurement.

APPENDIX B
Jet Definitions

Colored particles that are produced in a high-energy collision are not directly detectable due to color confinement, cf. Section 2.2.4. Instead, they form hadrons, which are the particles that are detected. The hadron formation cannot be described by pQCD and instead non-perturbative QCD models are used. These hadrons collectively carry the momentum of the original colored particle and are thus collimated. It becomes interesting to describe this collection of particles as a unique object with properties that can be related to the original colored particle. Such an object is called a jet, as a reference to the collimated spray of particles it describes.

Jets are not particles and as such they have a finite extension in space. Therefore, they can be defined in different ways through the use of different algorithms that build jets from a given list of constituents. Certain definitions will have some properties that could be better suited to describe specific phenomena than other definitions. However, one property of a jet algorithm that is paramount is that it needs to be insensitive to the production of colored particles at collinear angles and of gluons at low energy. This property of the jet definition is called infrared safe. If the algorithm is not infrared safe, a different configuration of jets could be built if low-energy gluons or collinear colored particles were produced. This would imply that the infrared divergences would not cancel one another in the perturbative expansion of QCD and

would lead to a divergent cross section for the production of jets. In other words, a jet definition that is infrared safe assures that the same jets are built whether the input to the algorithm are the partons in the matrix element at LO or NLO in pQCD or even the particles after the parton shower and hadronization steps of the event generation.

Jet algorithms can be separated into two categories: cone algorithms and sequential recombination algorithms. Both categories build jets in the two-dimensional plane defined by the rapidity and the azimuthal angle of the particles, since distances in those variables are boost-invariant and can thus be used consistently for all proton–proton collisions. Algorithms in the former class attempt to build cones containing the spray of particles, which are then identified as jets. These algorithms are mostly not infrared safe and thus were mainly used when infrared safe algorithms had not been conceived. However, a modern cone algorithm, SISCone [199], is infrared safe. It is seldom used as its implementation requires a larger number of computations compared to the sequential recombination algorithms. These algorithms instead build jets by progressively adding particles to the jet. They are the main jet algorithms used in modern experiments as they are infrared safe and can be implemented to run quickly.

The popular sequential recombination algorithms in proton–proton collisions can be described with the two following quantities [200]:

$$d_{ij} = \min(p_{\mathrm{T},i}^{2p}, p_{\mathrm{T},j}^{2p})\frac{(\Delta R_{ij})^2}{R^2}, \qquad d_{iB} = p_{\mathrm{T},i}^{2p}, \tag{B.1}$$

where $\Delta R_{ij} = \sqrt{(y_i - y_j)^2 + (\phi_i - \phi_j)^2}$ is the distance between particles i and j in the rapidity–azimuthal angle plane and R and p are parameters. The quantity d_{ij} is thus the normalized angular distance between two particles weighted by some function of the transverse momentum. The use of the transverse momentum keeps the algorithm boost-invariant. The quantity d_{ij} is related to the component of the momentum of one particle that is transverse to the momentum of the other particle. The second quantity, d_{iB} is used as a way to stop the jet building. The subscript B refers to the beam since the quantity is related to the component of the momentum of the particle that is transverse to the axis of the colliding protons, which corresponds to the usual definition of the transverse momentum. The algorithm computes d_{ij} for all possible pairs, finds the minimum value among those and adds together the four-momenta of the two particles in that pair, thus defining a new particle. If d_{iB} is smaller than every d_{ij}, the particle i is called a jet and is removed from the list of particles. This is repeated until all particles are associated to a jet.

The parameters R and p control the behaviour of the algorithm. Larger values of R will increase the angular extent of the jet. This can be desirable to encompass more of the activity associated to the original colored particle. However, larger values will increase the activity not associated to the original particle. Algorithms with values of p satisfying $p > 0$, $p = 0$ and $p < 0$ have qualitatively different behaviours. Algorithms with $p = 1$, $p = 0$ and $p = -1$ are respectively called the k_t, Cambridge/Aachen and anti-k_t algorithms. Their differences are highlighted as follows.

k_t The k_t algorithm [171, 172] first combines particles with low transverse momentum and builds towards larger momentum. The jets it builds are more sensitive to

particles with low energy. The algorithm is particularly useful to quantify the activity coming from the underlying event or from proton–proton collisions that did not have a large-momentum exchange. The jets have an irregular circular shape of radius R in the y–ϕ plane.

Cambridge/Aachen The Cambridge/Aachen algorithm [201] combines particles based purely on their angular distance. This feature is interesting for studies of jet substructure, for example a boosted massive boson whose decay products are collimated thus forming a jet. The jets are described in the y–ϕ plane by a irregular circle of radius R.

anti-k_t The anti-k_t algorithm [173] combines the particles with the largest transverse momentum first. It is well suited to build jets from particles originating from hard proton–proton collisions while being robust against soft particles. The jets it builds are circular in the y–ϕ plane and have a radius R.

Jet algorithms can take as input any object described by a four-momentum. These objects include not only particles, but also calorimeter cells for example. The same jet definition can thus be used in theoretical and experimental contexts, making possible a direct comparison of predictions and measurements.

Quarks do not give rise to low-energy divergences in contrast to gluons. When distinguishing quarks from gluons, or equivalently b quarks from the other partons, the jet algorithm must be designed to keep track of this difference in divergences to be infrared safe. The formation of b-jets, here defined as jets initiated by b quarks, with no distinction between b and $\bar{b}$ quarks, thus requires a modification of the jet

algorithms. This modified algorithm, called flavour-k_t [129], requires that each input object be identified as either a b quark or not. The main modification is the change of the minimum function to a maximum function in Equation B.1, if the parton with smaller p_{T} is a b quark. The result of the combination of two b quarks is considered as not containing any b quarks. This is compatible with the idea that a jet containing two b quarks from gluon splitting is not a jet that was initiated by a b quark but rather by a gluon. However, the identification of each input object as a b quark or not is experimentally difficult to achieve, for example that information is not readily available for calorimeter cells. Therefore, this approach is not currently viable for a proper comparison between theory and measurement.

However, a different definition of b-jets can be used with the algorithms described previously. Using this different definition, the jets are identified as b-jets if they simply contain at least one b quark, or similarly one b hadron. This definition of b-jets however implies that most b-jets at high energy will be identified as such due to the presence of b quarks that were created in gluon splitting and not from b quarks that participated in the large-momentum exchange described by the matrix element [129]. Furthermore, this b-jet definition is not infrared safe since a collinear gluon could split into a pair of b quarks thus changing a non b-jet into a b-jet. This definition cannot be safely used with partons, only with particles after the parton shower and hadronization steps, since for those particles the infrared effects have already been resummed.

APPENDIX C
b-tagging Algorithms

The main jet b-tagging algorithm used in the measurement presented in this thesis is the MV1c algorithm, an artificial neural network, discussed in Section 4.3.3. The output of three b-tagging algorithms, IP3D [180], SV1 [180] and JetFitter [180], are used as input to the MV1c algorithm. The description of these input algorithms follows.

IP3D This algorithm makes use of the large impact parameter that the tracks coming from the secondary vertex have relative to the primary vertex. There is an impact parameter in the transverse plane and also a longitudinal one along the z-direction. The transverse impact parameter is signed: positive if the track crosses the jet axis between the primary vertex and the jet direction and negative if not. The b-jets contain more tracks that have a positive transverse impact parameter than light jets, as the transverse impact parameters of tracks coming from the primary vertex have an approximately equal probability of being positive or negative due to the tracking resolution. IP3D uses both the transverse and longitudinal impact parameters in a log-likelihood ratio to associate a tagging weight to the jet. In more details, it compares the impact parameter significance, that is the value of the signed impact parameter divided by its uncertainty, of both the transverse and longitudinal impact parameters of

a track to probability density functions obtained from simulated events for b-, c- and light jets. The b-tagging probability for a given jet flavour, p_b, p_c and p_l, for respectively b-, c- and light jets, is the product of the likelihood values of its associated tracks. The IP3D tagging weight is $\ln(p_b/p_l)$. It is used as an input to MV1c. This algorithm does not have discrimination power against c-jets.

SV1 This algorithm reconstructs explicitly a secondary vertex. It builds all possible secondary vertices using pairs of tracks that are close to each other at a point. Based on the invariant mass of the tracks, assuming they are pions, and on the position of the vertex, it rejects vertices compatible with the decays of hyperons or compatible with interactions with the detector material. The tracks associated to the surviving vertices are combined into a single vertex. SV1 uses quantities related to that secondary vertex in a log-likelihood ratio. The quantities used are the invariant mass of the secondary vertex, the ratio of the energy sum of its associated tracks to the energy sum of all the tracks associated to the jet, the number of two-track vertices and the angular distance between the jet axis and the axis passing through both the primary and secondary vertices. The probability density functions for the three jet flavours are obtained from simulated events. For each jet, the likelihoods of each of the above quantities are multiplied to give the jet-flavour probabilities p_b, p_c and p_l. The SV1 tagging weight is $\ln(p_b/p_l)$. It is used as an input to MV1c. This algorithm does not have discrimination power against c-jets.

JetFitter This algorithm uses the topology of the sequential decays of the b and c hadrons. A Kalman filter finds the best axis for the line of flight, aligning

the primary, secondary and tertiary vertices. In contrast to SV1, this filter has the capability of not merging the secondary and tertiary vertices, even if they only each have one track associated to them. The output of the filter includes six quantities based on the decay topology and based on the vertices. The quantities are the number of vertices with at least two tracks, the total number of tracks associated to these vertices, the number of single-track vertices along the line of flight, the invariant mass of the tracks involved in the decay chain, the ratio of the energy sum of the tracks involved in the decay chain to the energy sum of all the tracks associated to the jet and the average signed decay-length significance of the vertices, i.e. the ratio of the distance between the primary vertex and a given vertex to the uncertainty in this distance. These quantities, and also the IP3D tagging weight, are used as input to an artificial neural network which is trained to discriminate between the jet flavours using simulated events. Since the above quantities depend on the jet transverse momentum and pseudorapidity, these two kinematic quantities are also used as input to the neural network. The output of the neural network are the three jet flavour probabilities: p_b, p_c and p_l. They are used as input to MV1c.

The transverse momentum and the pseudorapidity of the jet are also used as input to the MV1c algorithm in addition to the IP3D, SV1 and JetFitter input quantities mentioned above.

APPENDIX D
Principal Component Analysis

The principal component analysis (PCA), also known as the eigenvector decomposition method, is a technique to simplify the treatment of uncertainties. It is based on the idea of transforming the basis of the vector space spanned by the uncertainties into a basis in which the uncertainties are uncorrelated. In other words, it is based on the diagonalization of the covariance matrix. The method has two advantages: it produces uncorrelated uncertainties and it can reduce the number of uncertainties. An introduction to the PCA and its use in the context of the measurement presented in this thesis follow.

Given a set of quantities x_i with standard deviations σ_i, the elements of their covariance matrix, Σ, are

$$\Sigma_{ij} = \mathrm{cov}(x_i, x_j) \equiv \mathrm{E}[(x_i - \mathrm{E}[x_i])(x_j - \mathrm{E}[x_j])] \tag{D.1}$$

where $\mathrm{E}[x_i]$ is the expectation value of x_i. In matrix notation, the previous equation becomes

$$\Sigma = \mathrm{cov}(\vec{x}) \equiv \mathrm{E}\left[(\vec{x} - \mathrm{E}[\vec{x}])(\vec{x} - \mathrm{E}[\vec{x}])^{\mathrm{T}}\right]. \tag{D.2}$$

A diagonal element of the covariance matrix is given by the variance of the corresponding x_i, $\Sigma_{ii} = \sigma_i^2$, while an off-diagonal element is given by the covariance between the corresponding x_i and x_j, $\Sigma_{ij} = \sigma_{ij}$. Uncorrelated quantities have $\Sigma_{ij} = 0$.

Now considering a set of quantities y_i dependent on x_i, a linearization of their dependence around $\vec{x}_0$ is

$$y_i(\vec{x}) \approx y_i(\vec{x}_0) + \sum_j x_j \frac{\partial y_i}{\partial x_j}\bigg|_{x_j = x_{j0}} \tag{D.3}$$

or, in matrix notation,

$$\vec{y}(\vec{x}) \approx \vec{y}(\vec{x}_0) + J\vec{x}, \tag{D.4}$$

where J is the matrix of partial derivatives, i.e. the Jacobian matrix. Making use of that approximation and of the following property of the covariance matrix

$$\mathrm{cov}(A\vec{x} + \vec{b}) = A\,\mathrm{cov}(\vec{x})A^{\mathrm{T}}, \tag{D.5}$$

the covariance matrix of $\vec{y}$ as a function of that of $\vec{x}$ is

$$\Sigma_y = J\Sigma_x J^{\mathrm{T}}. \tag{D.6}$$

The previous equation, which is the well-known formula for the propagation of uncertainties, is valid as long as the linearization approximation of Equation D.3 is valid. Although it is often the case, there are some situations for which it is not, such as for a ratio of quantities when their standard deviations are large, as discussed in Section 8.1.1.

Considering the case where a variable z depends on two variables, y_1 and y_2, the variance of z is given by Equation D.6 and is

$$\sigma_z^2 = \left(\frac{\partial z}{\partial y_1}\right)^2 \sigma_{y_1}^2 + \left(\frac{\partial z}{\partial y_2}\right)^2 \sigma_{y_2}^2 + 2\frac{\partial z}{\partial y_1}\frac{\partial z}{\partial y_2}\sigma_{y_1 y_2}. \tag{D.7}$$

Furthermore, if the variables y_1 and y_2 are themselves dependent on two other variables, x_1 and x_2, that are uncorrelated, the covariance matrix of $\vec{y}$ is

$$\Sigma_y = \begin{bmatrix} \left(\frac{\partial y_1}{\partial x_1}\right)^2 \sigma_{x_1}^2 + \left(\frac{\partial y_1}{\partial x_2}\right)^2 \sigma_{x_2}^2 & \frac{\partial y_1}{\partial x_1}\frac{\partial y_2}{\partial x_1}\sigma_{x_1}^2 + \frac{\partial y_1}{\partial x_2}\frac{\partial y_2}{\partial x_2}\sigma_{x_2}^2 \\ \frac{\partial y_1}{\partial x_1}\frac{\partial y_2}{\partial x_1}\sigma_{x_1}^2 + \frac{\partial y_1}{\partial x_2}\frac{\partial y_2}{\partial x_2}\sigma_{x_2}^2 & \left(\frac{\partial y_2}{\partial x_1}\right)^2 \sigma_{x_1}^2 + \left(\frac{\partial y_2}{\partial x_2}\right)^2 \sigma_{x_2}^2 \end{bmatrix}. \tag{D.8}$$

Combining Equations D.7 and D.8 gives the following relation between the variance of z and the variances of x_1 and x_2, after simplification:

$$\begin{aligned} \sigma_z^2 &= \left(\frac{\partial z}{\partial y_1}\frac{\partial y_1}{\partial x_1} + \frac{\partial z}{\partial y_2}\frac{\partial y_2}{\partial x_1}\right)^2 \sigma_{x_1}^2 + \left(\frac{\partial z}{\partial y_1}\frac{\partial y_1}{\partial x_2} + \frac{\partial z}{\partial y_2}\frac{\partial y_2}{\partial x_2}\right)^2 \sigma_{x_2}^2 \\ &= \left(\frac{\partial z}{\partial x_1}\right)^2 \sigma_{x_1}^2 + \left(\frac{\partial z}{\partial x_2}\right)^2 \sigma_{x_2}^2. \end{aligned} \tag{D.9}$$

In particular, the covariance term is not present, as it should be since x_1 and x_2 are uncorrelated. Inversely, although x_1 and x_2 are uncorrelated, the covariance term between y_1 and y_2 must be taken into account to obtain the proper variance on z. In other words, the dependent variables can be correlated even if the independent variables are not.

The function composition as illustrated above is common in the context of the measurement presented in this thesis, due to the separation of performance studies and physics analysis. As a concrete example, the independent variables x_i could represent the quantities used as input to measure the b-tagging efficiency and which are directly affected by independent sources of uncertainties, y_i would then be the different kinematic bins in which the calibration factors of the efficiency are measured and z could be one bin of the differential $\gamma + b$ cross section that is measured.

If there are fewer y_i than x_i, as is often the case, it becomes advantageous to determine the uncertainty on z directly from that on y_i instead of that on x_i. Having fewer uncertainty sources simplifies the treatment of the uncertainties on z, while reducing the consumption of computing resources. However, a difficulty arises in using the y_i instead of the x_i. The covariance terms among all the y_i need to be taken into account. This is in contrast to being able to simply sum in quadrature the various uncertainties, as is possible with the x_i.

The PCA simplifies the treatment of the covariance terms. As the covariance matrix is real and symmetric, it can be diagonalized and an orthonormal set of eigenvectors can be found. Furthermore, the covariance matrix is positive semi-definite, such that the eigenvalues will be non-negative. Thus, the eigenvectors describe the covariance matrix in a basis in which the covariance terms are zero and the eigenvalues are identified as the variances in this new basis. The uncertainties in this basis can be summed in quadrature.

Mathematically, the diagonalization of the covariance matrix means obtaining D via $D = P^{-1}\Sigma P$, where D is the diagonal matrix of eigenvalues and P is the matrix whose columns are given by the corresponding eigenvectors. As the eigenvectors can be built to be orthonormal, P can be taken to be orthogonal, giving $D = P^{\mathrm{T}}\Sigma P$. Comparing this relation to Equation D.6, the matrix D is identified to be the covariance matrix in the eigenvector basis since the Jacobian matrix of the transformation rule of the change of basis is given by P^{T}.

A change of basis from $\vec{y}$ to $\vec{y}'$, following the transformation described above, does not change the covariance matrix of a set of dependent variables z_i. Indeed, the transpose of the Jacobian matrix of the dependence of z_i on y_i, J^{T}, can be identified to be the matrix whose columns are given by the components of the variables z_i in the original basis. The transpose of the Jacobian matrix of the dependence of z_i on y'_i, J'^{T}, is thus related to the original one by the action of the inverse of the matrix built from the eigenvectors, i.e. P^{T}: $J'^{\mathrm{T}} = P^{\mathrm{T}} J^{\mathrm{T}}$. Explicitly, the covariance of $\vec{z}$ in the transformed basis, Σ'_z, in terms of that in the original basis, Σ_z, is

$$\begin{aligned}
\Sigma'_z &= J' \Sigma_{y'} J'^{\mathrm{T}} \\
&= (P^{\mathrm{T}} J^{\mathrm{T}})^{\mathrm{T}} \Sigma_{y'} (P^{\mathrm{T}} J^{\mathrm{T}}) \\
&= JP(P^{\mathrm{T}} \Sigma_y P) P^{\mathrm{T}} J^{\mathrm{T}} \\
&= J \Sigma_y J^{\mathrm{T}} \\
&= \Sigma_z
\end{aligned} \tag{D.10}$$

Therefore, the change of basis in the PCA keeps the covariance of $\vec{z}$ invariant. This important property makes the PCA a viable procedure for assessing properly the uncertainty on the z_i and their correlations.

To show visually the transformation induced by the PCA, an example to consider is $z = 3y_1 + y_2$ with a covariance matrix

$$\Sigma_y = \begin{bmatrix} 4 & 3 \\ 3 & 4 \end{bmatrix}. \tag{D.11}$$

The variance of z is, from Equation D.7:

$$\sigma_z^2 = 3^2 \cdot 4 + 1 \cdot 4 + 2 \cdot 3 \cdot 1 \cdot 3 = 58. \tag{D.12}$$

Using the PCA to simplify this last expression, the diagonalization of the covariance matrix gives the following eigenvalues and orthonormal eigenvectors:

$$\lambda_1 = 7,\ \hat{y}_1' = \frac{1}{\sqrt{2}}\begin{bmatrix}1\\1\end{bmatrix}; \qquad \lambda_2 = 1,\ \hat{y}_2' = \frac{1}{\sqrt{2}}\begin{bmatrix}1\\-1\end{bmatrix}. \tag{D.13}$$

In matrix notation, the previous quantities become

$$\Sigma_{y'} = D = \begin{bmatrix}7 & 0\\0 & 1\end{bmatrix} \quad \text{and} \quad P = \frac{1}{\sqrt{2}}\begin{bmatrix}1 & 1\\1 & -1\end{bmatrix} \tag{D.14}$$

In the new basis, z is given by $z = 2\sqrt{2}y_1' + \sqrt{2}y_2'$, giving a variance of

$$\sigma_z^2 = 8 \cdot 7 + 2 \cdot 1 = 58, \tag{D.15}$$

which is indeed the same value as obtained in the original basis but without the covariance term. Figure D–1 gives a graphical interpretation of the effect of the basis change for an underlying bivariate Gaussian probability distribution with a covariance matrix given by either Equation D.11 or D.14. It can be seen in Figure D–1(a), where a non-zero correlation exists, that the eigenvectors, at a plus or minus 45-degree angle with respect to the unit vectors of the basis, are aligned with the symmetry axes of the distribution. In the eigenvector basis shown in Figure D–1(b), where there is no correlation, the symmetry axes are aligned with the unit vectors of the basis.

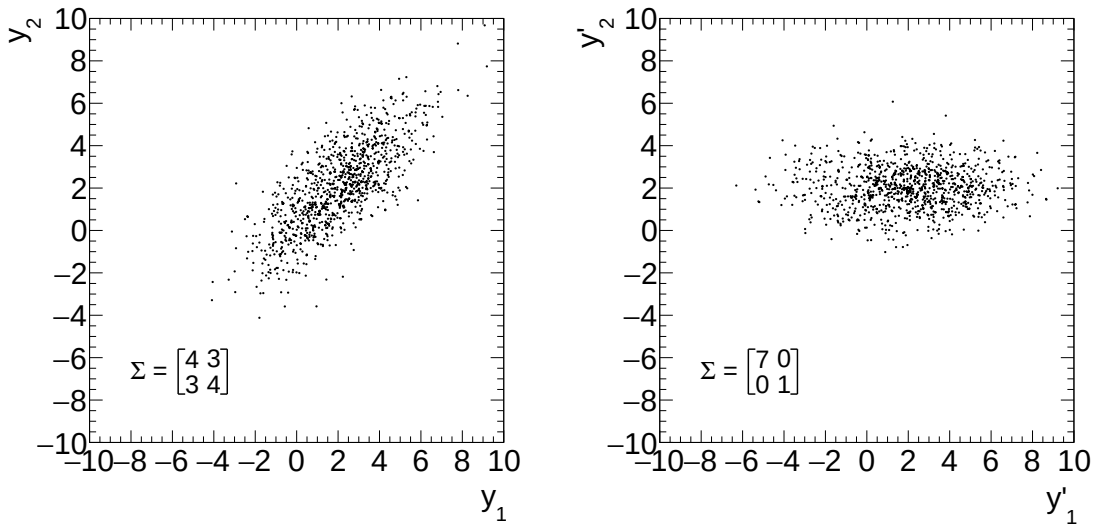

(a) (b)

Figure D–1 – Bivariate Gaussian probability distribution in (a) the original basis and (b) the eigenvector basis.

With the PCA, an uncertainty in the transformed basis is given simply by

$$\sigma'_i = \sqrt{\lambda_i}\hat{y}'_i, \tag{D.16}$$

where there is one such uncertainty for each eigenvalue. Furthermore, the effect of these uncertainty variations can be ordered by decreasing eigenvalue and the smallest ones can be neglected, or combined, if they are below some arbitrary threshold. This can decrease further the number of uncertainty sources.

In the context of the measurement presented in this thesis, the PCA is used for the uncertainties in the calibration of the jet energy scale and of the b-tagging efficiency. In each of these cases, multiple sources of uncertainty affect each kinematic bin in which the calibration is derived. Each source of uncertainty affects the calibration

bins with its own covariance matrix. These uncertainty sources are taken to be independent of each other, such that the overall covariance matrix between the bins is given by the sum of the individual covariance matrices:

$$\Sigma = \sum_i \Sigma_i \tag{D.17}$$

where i runs over all the uncertainty sources. The PCA is then performed on this summed covariance matrix. The uncertainty described by the eigenvalues are thus a linear combination of the total uncertainty in each of the calibration bin. Such a combination cannot be assigned a physical description, in contrast to the sources of uncertainties. Therefore, the simplicity of the treatment of the uncertainties provided by the PCA comes at the cost of losing the knowledge of the physical origin of the uncertainties.

To keep partial knowledge of the physical origin of the uncertainties, which is important when determining how to reduce the uncertainty contributions for instance, the PCA can be performed in different categories of uncertainties. The categories can be defined, for example, for uncertainties having a related physical origin. In this approach, the sum of the individual covariance matrices of Equation D.17 runs only over the uncertainties associated to that category, thus producing a summed covariance matrix for each category. Compared to the application of the PCA to the total covariance matrix, this hybrid approach increases the number of uncertainties to consider, but keeps some information on their physical origin via the categories.

APPENDIX E
Tables of Systematic Uncertainties

Table E–1 – Signed relative variations of the individual systematic uncertainties in the measured values of the differential fiducial $\gamma+b$ cross section in the central region, $|\eta^\gamma| < 1.37$. The top (bottom) value is the effect of an up (down) variation of the uncertainty. The uncertainties related to the prompt photon modelling, the non-perturbative QCD models and the particle-level migration effects are only varied once and not up and down by their nature, but are to be symmetrized in the final results. A number following the name of an uncertainty refers to an individual component of that uncertainty category. Only uncertainties which produce at least a 1% variation in at least one bin of the cross section in either the central or the forward region, or in the central-to-forward ratio, are listed. The others are summed in quadrature and are listed as a single entry. Each bin of the MC statistical uncertainty is independent of every other bin. The first four components of the photon energy scale uncertainty are specific to this $|\eta^\gamma|$ region, are indicated as such in the name and are uncorrelated to the components in the other region.

Uncertainty [%] — E_{T}^{γ} bin [GeV]	25–45	45–65	65–85	85–105	105–125	125–150	150–175	175–200	200–250	250–300	300–350	350–400
MC statistical uncertainty	+4.11 −3.98	+6.44 −5.85	+2.62 −2.91	+3.94 −4.63	+2.72 −2.73	+2.70 −2.57	+2.75 −2.73	+4.62 −4.68	+1.91 −2.14	+2.81 −2.92	+5.43 −6.08	+5.75 −5.79
Photon energy scale 1 central	+0.00 −0.15	+0.00 −0.15	+0.00 −0.15	+0.00 −0.15	+0.00 −0.15	+0.00 −0.15	+0.00 −0.15	+0.00 −0.15	+0.00 −0.17	+0.00 −0.62	+0.00 −1.09	+0.00 −1.16
Photon energy scale 2 central	−0.12 +0.00	−0.12 +0.00	−0.12 +0.00	−0.12 +0.00	−0.12 +0.00	−0.12 +0.00	−0.12 +0.00	−0.12 +0.00	−0.12 +0.00	−0.12 +0.00	−0.12 +0.00	−0.12 +0.00
Photon energy scale 3 central	+0.00 −0.17	+0.00 −0.17	+0.00 −0.17	+0.00 −0.17	+0.00 −0.17	+0.00 −0.22	+0.00 −0.51	+0.00 −0.58	+0.00 −0.59	+0.00 −1.02	+0.00 −1.09	+0.00 −1.10
Photon energy scale 4 central	+0.17 −0.32	+0.17 −0.32	+0.17 −0.32	+0.17 −0.32	+0.17 −0.32	+0.17 −0.43	+0.17 −0.95	+0.17 −0.66	+0.17 −0.50	+0.17 −0.50	+0.17 −0.50	+0.17 −0.50
Photon energy scale 5	+0.00 +0.02	+0.00 +0.02	+0.00 +0.02	+0.00 +0.02	+0.00 +0.02	+0.00 −0.15	+0.00 −1.12	+0.00 −1.35	+0.05 −1.37	+1.62 −1.71	+1.76 −1.74	+1.76 −1.74
Photon identification efficiency	−1.19 +1.21	−0.55 +0.55	−0.32 +0.32	−0.23 +0.23	−0.20 +0.20	−0.21 +0.21	−0.30 +0.30	−0.29 +0.29	−0.28 +0.28	−0.32 +0.33	−0.33 +0.33	−0.33 +0.33
Jet energy scale 1	−0.58 +1.35	−0.58 +1.33	−0.53 +0.52	+0.12 +0.25	+0.21 −0.06	+0.26 −0.39	+0.50 −0.59	+0.61 −0.79	+1.04 −1.02	+1.72 −1.55	+1.99 −1.96	+2.26 −2.32
Jet energy scale 2	+1.01 −1.46	+1.04 −0.33	+0.41 −0.29	+0.11 −0.13	−0.09 +0.06	−0.16 +0.28	−0.44 +0.36	−0.69 +0.51	−0.99 +0.98	−1.44 +1.59	−1.73 +1.76	−1.98 +1.91
Jet energy scale 3	−0.07 +0.05	−0.07 +0.05	−0.07 +0.05	−0.04 +0.05	−0.03 +0.03	+0.01 +0.02	+0.02 −0.01	+0.02 −0.02	+0.10 −0.09	+0.19 −0.18	+0.24 −0.23	+0.26 −0.26
Jet energy scale 4	+0.08 +0.76	+0.08 −0.09	+0.08 −0.11	+0.08 −0.11	+0.08 −0.11	+0.08 −0.11	+0.08 −0.11	+0.10 −0.13	+0.39 −0.37	+0.72 −0.75	+1.15 −1.11	+1.10 −1.20
Jet energy scale 5	+0.06 +0.12	+0.06 +0.12	+0.06 +0.12	+0.06 +0.12	+0.06 +0.11	+0.06 −0.00	+0.06 −0.03	+0.03 −0.03	+0.02 −0.02	−0.06 +0.13	−0.13 +0.14	−0.17 +0.16
Jet energy scale 6	+0.27 +0.94	+0.27 +0.91	+0.27 −0.14	+0.27 −0.21	+0.29 −0.24	+0.44 −0.44	+0.56 −0.59	+0.62 −0.74	+0.91 −0.89	+1.39 −1.17	+1.47 −1.40	+1.60 −1.59
Jet energy scale 7	−0.56 +0.57	−0.15 +0.16	+0.07 −0.07	+0.19 −0.18	+0.28 −0.26	+0.40 −0.39	+0.56 −0.55	+0.68 −0.68	+0.96 −0.94	+1.50 −1.32	+1.62 −1.56	+1.81 −1.77
Jet energy scale 8	−0.15 +1.20	−0.15 +1.18	−0.16 +0.32	−0.29 +0.36	−0.39 +0.40	−0.60 +0.48	−0.57 +0.49	−0.61 +0.47	−0.41 +0.37	−0.16 +0.19	−0.14 +0.18	−0.14 +0.18
Jet energy scale 9	−2.18 +2.06	−1.11 +1.14	−0.54 +0.54	−0.23 +0.27	+0.09 −0.03	+0.20 −0.15	+0.49 −0.53	+0.76 −0.75	+1.20 −1.19	+1.98 −1.76	+2.32 −2.12	+2.41 −2.35

Jet energy resolution	$^{-2.43}_{-0.54}$	$^{-2.43}_{-0.54}$	$^{-2.25}_{-0.54}$	$^{+0.00}_{-0.54}$	$^{+0.32}_{-0.54}$	$^{+0.32}_{-0.54}$	$^{+0.32}_{-0.46}$	$^{+0.32}_{-0.18}$	$^{+0.32}_{-0.07}$	$^{+0.32}_{-0.07}$	$^{+0.32}_{-0.07}$	$^{+0.32}_{-0.07}$
b-jet tagging efficiency 1	$^{+1.49}_{-1.46}$	$^{+1.63}_{-1.59}$	$^{+1.83}_{-1.79}$	$^{+2.02}_{-1.96}$	$^{+2.30}_{-2.21}$	$^{+2.68}_{-2.58}$	$^{+3.37}_{-3.21}$	$^{+4.09}_{-3.85}$	$^{+6.50}_{-5.97}$	$^{+10.49}_{-9.27}$	$^{+13.32}_{-11.47}$	$^{+15.51}_{-13.20}$
b-jet tagging efficiency 2	$^{-0.91}_{+0.91}$	$^{-0.69}_{+0.69}$	$^{-0.64}_{+0.64}$	$^{-0.68}_{+0.68}$	$^{-0.81}_{+0.81}$	$^{-1.01}_{+1.02}$	$^{-1.19}_{+1.21}$	$^{-1.13}_{+1.14}$	$^{-0.40}_{+0.40}$	$^{+1.39}_{-1.26}$	$^{+2.63}_{-2.56}$	$^{+3.59}_{-3.49}$
b-jet tagging efficiency 3	$^{-1.04}_{+1.05}$	$^{-0.87}_{+0.88}$	$^{-0.83}_{+0.84}$	$^{-0.91}_{+0.92}$	$^{-1.01}_{+1.02}$	$^{-1.19}_{+1.21}$	$^{-1.45}_{+1.48}$	$^{-1.61}_{+1.65}$	$^{-1.74}_{+1.77}$	$^{-1.80}_{+1.92}$	$^{-1.86}_{+1.84}$	$^{-2.07}_{+2.01}$
b-jet tagging efficiency 4	$^{+0.06}_{-0.06}$	$^{+0.14}_{-0.14}$	$^{+0.20}_{-0.19}$	$^{+0.23}_{-0.23}$	$^{+0.29}_{-0.29}$	$^{+0.39}_{-0.38}$	$^{+0.57}_{-0.57}$	$^{+0.79}_{-0.78}$	$^{+1.23}_{-1.22}$	$^{+2.11}_{-2.06}$	$^{+2.19}_{-2.27}$	$^{+2.15}_{-2.31}$
b-jet tagging efficiency 5	$^{+0.12}_{-0.12}$	$^{-0.12}_{+0.12}$	$^{-0.13}_{+0.13}$	$^{-0.20}_{+0.20}$	$^{-0.27}_{+0.28}$	$^{-0.39}_{+0.39}$	$^{-0.56}_{+0.57}$	$^{-0.70}_{+0.72}$	$^{-0.92}_{+0.93}$	$^{-1.06}_{+1.15}$	$^{-1.30}_{+1.26}$	$^{-1.38}_{+1.27}$
b-jet tagging efficiency 6	$^{+0.34}_{-0.34}$	$^{+0.24}_{-0.24}$	$^{+0.17}_{-0.17}$	$^{+0.13}_{-0.13}$	$^{+0.12}_{-0.12}$	$^{+0.11}_{-0.11}$	$^{+0.16}_{-0.16}$	$^{+0.29}_{-0.29}$	$^{+1.00}_{-0.99}$	$^{+2.27}_{-2.19}$	$^{+3.27}_{-3.15}$	$^{+3.73}_{-3.63}$
b-jet tagging efficiency 7	$^{+0.42}_{-0.42}$	$^{+0.36}_{-0.35}$	$^{+0.25}_{-0.25}$	$^{+0.14}_{-0.14}$	$^{-0.01}_{+0.02}$	$^{-0.10}_{+0.23}$	$^{-0.50}_{+0.53}$	$^{-0.73}_{+0.74}$	$^{-0.85}_{+0.86}$	$^{-0.68}_{+0.84}$	$^{-0.50}_{+0.53}$	$^{-0.39}_{+0.39}$
b-jet tagging efficiency 8	$^{-0.00}_{+0.00}$	$^{-0.00}_{+0.00}$	$^{-0.00}_{+0.00}$	$^{-0.00}_{+0.00}$	$^{-0.00}_{+0.00}$	$^{-0.03}_{+0.03}$	$^{-0.06}_{+0.06}$	$^{-0.08}_{+0.10}$	$^{-0.24}_{+0.25}$	$^{-0.89}_{+1.07}$	$^{-2.46}_{+2.71}$	$^{-4.07}_{+4.63}$
c-jet tagging efficiency 1	$^{+4.63}_{-4.36}$	$^{+7.45}_{-7.26}$	$^{+8.08}_{-8.12}$	$^{+7.80}_{-7.97}$	$^{+9.78}_{-10.15}$	$^{+10.67}_{-11.23}$	$^{+10.44}_{-11.06}$	$^{+13.19}_{-14.27}$	$^{+13.06}_{-13.90}$	$^{+9.61}_{-10.32}$	$^{+14.78}_{-16.52}$	$^{+8.22}_{-9.46}$
c-jet tagging efficiency 2	$^{-1.87}_{+2.04}$	$^{+0.12}_{+0.57}$	$^{+0.17}_{-0.18}$	$^{+0.22}_{-0.38}$	$^{+0.66}_{-0.53}$	$^{+1.45}_{-1.44}$	$^{+2.33}_{-2.47}$	$^{+3.55}_{-3.86}$	$^{+3.99}_{-4.46}$	$^{+3.03}_{-3.42}$	$^{+4.83}_{-5.61}$	$^{+2.86}_{-3.43}$
c-jet tagging efficiency 3	$^{+2.28}_{-2.26}$	$^{+2.11}_{-2.11}$	$^{+0.41}_{-0.37}$	$^{-0.31}_{+0.35}$	$^{-0.59}_{+0.62}$	$^{-0.32}_{+0.34}$	$^{+0.31}_{-0.28}$	$^{+0.68}_{-0.60}$	$^{+0.82}_{-0.69}$	$^{+0.82}_{-0.63}$	$^{+0.50}_{-0.29}$	$^{+0.44}_{-0.23}$
c-jet tagging efficiency 4	$^{+0.20}_{-0.18}$	$^{-0.31}_{+0.34}$	$^{-0.33}_{+0.35}$	$^{-0.29}_{+0.33}$	$^{-0.13}_{+0.16}$	$^{+0.11}_{-0.12}$	$^{+0.43}_{-0.46}$	$^{+0.73}_{-0.76}$	$^{+0.83}_{-0.90}$	$^{+0.59}_{-0.68}$	$^{+1.08}_{-1.19}$	$^{+0.70}_{-0.79}$
c-jet tagging efficiency 5	$^{+0.51}_{-0.46}$	$^{+0.60}_{-0.59}$	$^{-0.06}_{+0.07}$	$^{-0.49}_{+0.50}$	$^{-0.67}_{+0.69}$	$^{-0.61}_{+0.62}$	$^{-0.29}_{+0.24}$	$^{+0.02}_{+0.15}$	$^{+0.13}_{+0.15}$	$^{+0.13}_{+0.15}$	$^{+0.19}_{+0.15}$	$^{+0.47}_{+0.15}$
c-jet tagging efficiency 6	$^{+0.43}_{-0.34}$	$^{+0.25}_{+0.31}$	$^{-0.48}_{+0.37}$	$^{-0.87}_{+0.87}$	$^{-0.96}_{+1.01}$	$^{-0.62}_{+0.68}$	$^{+0.18}_{-0.10}$	$^{+0.36}_{-0.27}$	$^{+0.37}_{-0.28}$	$^{+0.65}_{-0.46}$	$^{+1.15}_{-1.00}$	$^{+0.89}_{-0.81}$
c-jet tagging efficiency 7	$^{-1.48}_{+1.45}$	$^{-1.40}_{+1.38}$	$^{-0.73}_{+0.73}$	$^{-0.37}_{+0.38}$	$^{-0.23}_{+0.23}$	$^{-0.05}_{+0.01}$	$^{+0.13}_{-0.08}$	$^{+0.28}_{-0.26}$	$^{+0.27}_{-0.26}$	$^{+0.29}_{-0.20}$	$^{+0.25}_{-0.25}$	$^{+0.24}_{-0.26}$
c-jet tagging efficiency 8	$^{-0.92}_{+0.92}$	$^{-2.12}_{+2.10}$	$^{-2.06}_{+2.04}$	$^{-1.73}_{+1.72}$	$^{-1.88}_{+1.86}$	$^{-1.78}_{+1.76}$	$^{-1.37}_{+1.35}$	$^{-1.34}_{+1.35}$	$^{-1.56}_{+1.53}$	$^{-1.12}_{+1.03}$	$^{-0.89}_{+0.92}$	$^{-0.86}_{+0.91}$
c-jet tagging efficiency 9	$^{+0.29}_{-0.29}$	$^{+0.63}_{-0.63}$	$^{+1.39}_{-1.41}$	$^{+1.64}_{-1.65}$	$^{+1.79}_{-1.81}$	$^{+1.20}_{-1.17}$	$^{+0.06}_{+0.05}$	$^{-0.22}_{+0.50}$	$^{-0.81}_{+1.10}$	$^{-0.81}_{+1.21}$	$^{-0.52}_{+0.87}$	$^{-0.48}_{+0.82}$
c-jet tagging efficiency 10	$^{-1.19}_{+1.17}$	$^{-2.02}_{+1.98}$	$^{+0.03}_{-0.01}$	$^{+0.37}_{-0.35}$	$^{+1.55}_{-1.54}$	$^{+1.74}_{-1.76}$	$^{+1.28}_{-1.30}$	$^{+1.20}_{-1.18}$	$^{+1.27}_{-1.25}$	$^{+0.95}_{-0.87}$	$^{+0.75}_{-0.69}$	$^{+0.72}_{-0.67}$
c-jet tagging efficiency 11	$^{+0.63}_{-0.65}$	$^{+2.05}_{-2.16}$	$^{+2.66}_{-2.82}$	$^{+2.53}_{-2.69}$	$^{+2.66}_{-2.81}$	$^{+1.97}_{-2.06}$	$^{+0.79}_{-0.82}$	$^{+0.30}_{-0.30}$	$^{-0.04}_{+0.05}$	$^{-0.17}_{+0.26}$	$^{-0.40}_{+0.39}$	$^{-0.26}_{+0.25}$
c-jet tagging efficiency 12	$^{+0.42}_{-0.35}$	$^{+0.98}_{-0.81}$	$^{+1.07}_{-0.96}$	$^{+0.67}_{-0.62}$	$^{+0.68}_{-0.64}$	$^{+0.49}_{-0.48}$	$^{+0.24}_{-0.23}$	$^{+0.07}_{-0.06}$	$^{+0.01}_{-0.01}$	$^{+0.01}_{-0.01}$	$^{+0.01}_{-0.01}$	$^{+0.01}_{-0.01}$
c-jet tagging efficiency 13	$^{-0.14}_{+0.13}$	$^{-0.14}_{+0.13}$	$^{-0.14}_{+0.15}$	$^{-0.20}_{+0.48}$	$^{-0.55}_{+0.62}$	$^{-0.48}_{+0.49}$	$^{-0.20}_{+0.20}$	$^{-0.09}_{+0.09}$	$^{+0.00}_{-0.00}$	$^{+0.06}_{-0.06}$	$^{+0.07}_{-0.07}$	$^{+0.08}_{-0.08}$
c-jet tagging efficiency 14	$^{-0.12}_{+0.13}$	$^{-0.19}_{+0.19}$	$^{+0.29}_{-0.28}$	$^{+0.65}_{-0.65}$	$^{+0.98}_{-0.99}$	$^{+0.84}_{-0.85}$	$^{+0.45}_{-0.46}$	$^{+0.26}_{-0.27}$	$^{+0.12}_{-0.12}$	$^{+0.02}_{-0.02}$	$^{+0.01}_{-0.01}$	$^{+0.01}_{-0.01}$
c-jet tagging efficiency 15	$^{+0.08}_{-0.08}$	$^{-0.15}_{+0.15}$	$^{-0.71}_{+0.75}$	$^{-0.81}_{+0.91}$	$^{-1.17}_{+1.29}$	$^{-1.01}_{+1.10}$	$^{-0.60}_{+0.64}$	$^{-0.35}_{+0.36}$	$^{-0.18}_{+0.18}$	$^{-0.03}_{+0.03}$	$^{+0.05}_{-0.05}$	$^{+0.06}_{-0.06}$
c-jet tagging efficiency 16	$^{+0.08}_{-0.08}$	$^{+0.11}_{-0.11}$	$^{-0.07}_{+0.13}$	$^{-0.08}_{+0.15}$	$^{-0.08}_{+0.15}$	$^{-0.06}_{+0.16}$	$^{+0.07}_{+0.00}$	$^{+0.06}_{-0.03}$	$^{+0.04}_{-0.04}$	$^{+0.04}_{-0.04}$	$^{+0.03}_{-0.03}$	$^{+0.03}_{-0.03}$
c-jet tagging efficiency 17	$^{+0.00}_{-0.00}$	$^{+0.00}_{-0.00}$	$^{+0.00}_{-0.00}$	$^{+0.00}_{-0.00}$	$^{+0.00}_{-0.00}$	$^{+0.00}_{-0.00}$	$^{+0.00}_{-0.00}$	$^{+0.00}_{-0.00}$	$^{-0.03}_{+0.03}$	$^{-1.23}_{+1.43}$	$^{-5.54}_{+5.84}$	$^{-6.20}_{+6.52}$
Light-jet tagging efficiency 1	$^{+9.58}_{-10.07}$	$^{-3.47}_{+3.45}$	$^{-3.83}_{+3.82}$	$^{-4.23}_{+4.23}$	$^{-5.40}_{+5.43}$	$^{-5.19}_{+5.17}$	$^{-4.42}_{+4.41}$	$^{-4.11}_{+4.08}$	$^{-4.42}_{+4.38}$	$^{-3.70}_{+3.60}$	$^{-3.36}_{+3.21}$	$^{-3.18}_{+3.05}$
Light-jet tagging efficiency 2	$^{-7.84}_{+7.96}$	$^{-4.36}_{+4.39}$	$^{-1.76}_{+1.76}$	$^{-0.74}_{+0.74}$	$^{-0.82}_{+0.82}$	$^{-0.93}_{+0.92}$	$^{-1.00}_{+1.01}$	$^{-1.10}_{+1.13}$	$^{-1.41}_{+1.42}$	$^{-1.63}_{+1.63}$	$^{-2.15}_{+2.09}$	$^{-2.38}_{+1.97}$
Light-jet tagging efficiency 3	$^{-3.06}_{+3.09}$	$^{-2.02}_{+2.03}$	$^{-2.52}_{+2.50}$	$^{-2.42}_{+2.40}$	$^{-3.06}_{+3.05}$	$^{-3.16}_{+3.14}$	$^{-2.89}_{+2.89}$	$^{-3.03}_{+3.03}$	$^{-3.30}_{+3.31}$	$^{-2.90}_{+2.88}$	$^{-2.65}_{+2.63}$	$^{-2.53}_{+2.38}$
Light-jet tagging efficiency 4	$^{-1.30}_{+1.27}$	$^{-0.56}_{+0.56}$	$^{-0.55}_{+0.54}$	$^{-0.60}_{+0.60}$	$^{-0.93}_{+0.94}$	$^{-0.89}_{+0.87}$	$^{-0.62}_{+0.62}$	$^{-0.46}_{+0.49}$	$^{-0.30}_{+0.41}$	$^{-0.28}_{+0.13}$	$^{-0.28}_{+0.11}$	$^{-0.28}_{+0.11}$
Light-jet tagging efficiency 5	$^{-2.34}_{+2.36}$	$^{-1.87}_{+1.87}$	$^{-1.23}_{+1.22}$	$^{-0.37}_{+0.36}$	$^{-0.23}_{+0.23}$	$^{+0.07}_{-0.07}$	$^{+0.15}_{-0.15}$	$^{+0.15}_{-0.15}$	$^{+0.15}_{-0.15}$	$^{+0.35}_{-0.36}$	$^{+0.54}_{-0.55}$	$^{+0.66}_{-0.70}$
Light-jet tagging efficiency 6	$^{+5.61}_{-5.57}$	$^{+2.61}_{-2.60}$	$^{+0.87}_{-0.88}$	$^{+0.54}_{-0.54}$	$^{+0.69}_{-0.68}$	$^{+0.69}_{-0.69}$	$^{+0.65}_{-0.65}$	$^{+0.66}_{-0.64}$	$^{+0.74}_{-0.74}$	$^{+0.74}_{-0.71}$	$^{+0.66}_{-0.67}$	$^{+0.56}_{-0.57}$
Light-jet tagging efficiency 7	$^{-1.21}_{+1.19}$	$^{-0.60}_{+0.60}$	$^{-0.41}_{+0.41}$	$^{-0.48}_{+0.48}$	$^{-0.41}_{+0.41}$	$^{-0.25}_{+0.24}$	$^{+0.01}_{-0.01}$	$^{+0.07}_{-0.07}$	$^{+0.07}_{-0.07}$	$^{+0.17}_{+0.08}$	$^{-0.20}_{+0.10}$	$^{-0.25}_{+0.10}$
Light-jet tagging efficiency 8	$^{+0.83}_{-0.85}$	$^{+0.55}_{-0.55}$	$^{+0.43}_{-0.43}$	$^{+0.57}_{-0.57}$	$^{+0.66}_{-0.66}$	$^{+0.69}_{-0.69}$	$^{+0.63}_{-0.63}$	$^{+0.71}_{-0.69}$	$^{+0.72}_{-0.72}$	$^{+0.77}_{-0.74}$	$^{+0.72}_{-0.73}$	$^{+0.65}_{-0.66}$
Light-jet tagging efficiency 9	$^{-1.10}_{+1.09}$	$^{-1.54}_{+1.53}$	$^{-1.66}_{+1.64}$	$^{-1.79}_{+1.78}$	$^{-2.08}_{+2.08}$	$^{-1.92}_{+1.92}$	$^{-1.56}_{+1.55}$	$^{-1.49}_{+1.50}$	$^{-1.47}_{+1.45}$	$^{-1.36}_{+1.27}$	$^{-1.23}_{+1.18}$	$^{-1.03}_{+0.99}$
Light-jet tagging efficiency 10	$^{-0.11}_{+0.38}$	$^{-0.12}_{+0.38}$	$^{-0.55}_{+0.40}$	$^{-0.66}_{+0.64}$	$^{-0.91}_{+0.92}$	$^{-0.99}_{+0.98}$	$^{-0.97}_{+0.97}$	$^{-1.05}_{+1.07}$	$^{-1.19}_{+1.18}$	$^{-1.28}_{+1.24}$	$^{-1.46}_{+1.43}$	$^{-1.34}_{+1.29}$
Light-jet tagging efficiency 11	$^{-0.12}_{+0.10}$	$^{+0.18}_{+0.10}$	$^{-0.09}_{+0.10}$	$^{-0.11}_{+0.10}$	$^{-0.14}_{+0.13}$	$^{-0.34}_{+0.34}$	$^{-0.50}_{+0.49}$	$^{-0.67}_{+0.67}$	$^{-0.78}_{+0.78}$	$^{-0.96}_{+1.01}$	$^{-1.16}_{+1.15}$	$^{-1.05}_{+1.03}$
Light-jet tagging efficiency 12	$^{-0.60}_{+0.60}$	$^{+0.04}_{+0.06}$	$^{+0.05}_{+0.04}$	$^{+0.05}_{+0.04}$	$^{+0.03}_{+0.04}$	$^{-0.10}_{+0.04}$	$^{-0.15}_{+0.08}$	$^{-0.25}_{+0.22}$	$^{-0.36}_{+0.36}$	$^{-0.38}_{+0.47}$	$^{-0.34}_{+0.35}$	$^{-0.29}_{+0.28}$

Light-jet tagging efficiency 13	$^{+0.15}_{-0.15}$	$^{+0.22}_{-0.22}$	$^{+0.23}_{-0.23}$	$^{+0.31}_{-0.30}$	$^{+0.32}_{-0.31}$	$^{+0.29}_{-0.28}$	$^{+0.18}_{-0.18}$	$^{+0.06}_{-0.06}$	$^{+0.02}_{-0.02}$	$^{+0.02}_{-0.02}$	$^{+0.02}_{-0.02}$	$^{+0.02}_{-0.02}$
Light-jet tagging efficiency 14	$^{-0.08}_{+0.08}$	$^{-0.08}_{+0.08}$	$^{-0.09}_{+0.09}$	$^{-0.19}_{+0.19}$	$^{-0.25}_{+0.27}$	$^{-0.27}_{+0.27}$	$^{-0.24}_{+0.24}$	$^{-0.24}_{+0.24}$	$^{-0.24}_{+0.25}$	$^{-0.24}_{+0.39}$	$^{-0.17}_{+0.19}$	$^{-0.16}_{+0.16}$
Light-jet tagging efficiency 15	$^{-0.21}_{+0.21}$	$^{+0.08}_{-0.08}$	$^{+0.09}_{-0.09}$	$^{+0.15}_{-0.15}$	$^{+0.24}_{-0.22}$	$^{+0.25}_{-0.25}$	$^{+0.24}_{-0.24}$	$^{+0.24}_{-0.24}$	$^{+0.26}_{-0.26}$	$^{+0.36}_{-0.25}$	$^{+0.26}_{-0.25}$	$^{+0.21}_{-0.22}$
Light-jet tagging efficiency 16	$^{-0.24}_{+0.24}$	$^{-0.23}_{+0.23}$	$^{-0.07}_{+0.07}$	$^{+0.05}_{-0.04}$	$^{+0.11}_{-0.09}$	$^{+0.11}_{-0.10}$	$^{+0.09}_{-0.09}$	$^{+0.08}_{-0.08}$	$^{+0.09}_{-0.09}$	$^{+0.06}_{-0.06}$	$^{+0.06}_{-0.06}$	$^{+0.06}_{-0.06}$
Light-jet tagging efficiency 17	$^{-0.32}_{+0.31}$	$^{-0.22}_{+0.22}$	$^{-0.12}_{+0.12}$	$^{-0.11}_{+0.12}$	$^{-0.12}_{+0.15}$	$^{-0.12}_{+0.13}$	$^{-0.10}_{+0.10}$	$^{-0.08}_{+0.08}$	$^{-0.08}_{+0.08}$	$^{-0.02}_{+0.02}$	$^{-0.01}_{+0.01}$	$^{-0.01}_{+0.01}$
Sideband isolation definition	$^{-1.55}_{+2.64}$	$^{-1.03}_{+1.77}$	$^{-0.57}_{+1.04}$	$^{-0.52}_{+0.95}$	$^{-0.36}_{+0.70}$	$^{-0.29}_{+0.61}$	$^{-0.23}_{+0.43}$	$^{-0.14}_{+0.29}$	$^{-0.09}_{+0.22}$	$^{-0.06}_{+0.14}$	$^{-0.03}_{+0.09}$	$^{-0.02}_{+0.08}$
Sideband identification definition	$^{-0.18}_{+1.33}$	$^{-0.18}_{+1.11}$	$^{-0.18}_{+1.14}$	$^{-0.23}_{+1.65}$	$^{-0.33}_{+1.45}$	$^{-0.25}_{+1.05}$	$^{-0.28}_{+0.90}$	$^{-0.48}_{+1.18}$	$^{-0.26}_{+0.93}$	$^{-0.18}_{+0.92}$	$^{-0.19}_{+0.98}$	$^{-0.19}_{+0.99}$
Sideband correlation	$^{-4.46}_{+4.36}$	$^{-3.82}_{+3.77}$	$^{-2.47}_{+2.44}$	$^{-1.52}_{+1.51}$	$^{-1.42}_{+1.43}$	$^{-1.09}_{+1.09}$	$^{-0.76}_{+0.76}$	$^{-0.65}_{+0.65}$	$^{-0.47}_{+0.46}$	$^{-0.27}_{+0.27}$	$^{-0.23}_{+0.23}$	$^{-0.23}_{+0.22}$
Prompt photon modelling	-2.20	-2.20	-2.20	-2.20	-2.20	-2.24	-2.46	-2.51	-2.51	-2.51	-2.51	-2.51
Non-perturbative QCD models	-2.32	-2.32	-2.32	-2.32	-2.32	-2.32	-2.32	-2.32	-2.32	-2.32	-2.32	-2.32
Particle-level migration effects	$+0.84$	-2.87	-2.64	-2.11	-2.86	-2.34	-1.33	-1.15	-1.46	-1.18	-2.52	$+2.04$
Luminosity	$^{+1.90}_{-1.90}$	$^{+1.90}_{-1.90}$	$^{+1.90}_{-1.90}$	$^{+1.90}_{-1.90}$	$^{+1.90}_{-1.90}$	$^{+1.90}_{-1.90}$	$^{+1.90}_{-1.90}$	$^{+1.90}_{-1.90}$	$^{+1.90}_{-1.90}$	$^{+1.90}_{-1.90}$	$^{+1.90}_{-1.90}$	$^{+1.90}_{-1.90}$
Other sources combined	$^{+2.13}_{-2.21}$	$^{+1.62}_{-1.63}$	$^{+1.34}_{-1.41}$	$^{+1.22}_{-1.28}$	$^{+1.28}_{-1.27}$	$^{+1.20}_{-1.24}$	$^{+1.03}_{-1.10}$	$^{+0.91}_{-1.05}$	$^{+0.81}_{-0.93}$	$^{+0.84}_{-0.90}$	$^{+1.17}_{-1.04}$	$^{+1.31}_{-1.17}$

Table E–2 – Signed relative variations of the individual systematic uncertainties in the measured values of the differential fiducial $\gamma + b$ cross section in the forward region, $1.56 \leq |\eta^{\gamma}| < 2.37$. The top (bottom) value is the effect of an up (down) variation of the uncertainty. The uncertainties related to the prompt photon modelling, the non-perturbative QCD models and the particle-level migration effects are only varied once and not up and down by their nature, but are to be symmetrized in the final results. A number following the name of an uncertainty refers to an individual component of that uncertainty category. Only uncertainties which produce at least a 1% variation in at least one bin of the cross section in either the central or the forward region, or in the central-to-forward ratio, are listed. The others are summed in quadrature and are listed as a single entry. Each bin of the MC statistical uncertainty is independent of every other bin. The first four components of the photon energy scale uncertainty are specific to this $|\eta^{\gamma}|$ region, are indicated as such in the name and are uncorrelated to the components in the other region.

Uncertainty [%] — E_{T}^{γ} bin [GeV]	25–45	45–65	65–85	85–105	105–125	125–150	150–175	175–200	200–250	250–300	300–350
MC statistical uncertainty	+11.89 −11.37	+14.06 −12.67	+3.95 −3.82	+5.46 −5.53	+3.62 −3.98	+3.70 −3.73	+5.21 −5.10	+7.33 −7.70	+3.27 −3.08	+5.40 −5.70	+11.44 −10.62
Photon energy scale 1 forward	+0.22 +0.00	+0.22 +0.00	+0.22 +0.00	+0.22 +0.00	+0.22 +0.00	+0.22 +0.00	+0.22 +0.00	+0.22 +0.00	+0.22 +0.00	+0.22 +0.00	+0.22 +0.00
Photon energy scale 2 forward	−0.51 +0.42	−0.51 +0.42	−0.51 +0.42	−0.51 +0.42	−0.51 +0.42	−0.58 +0.42	−0.97 +0.42	−1.06 +0.44	−1.06 +0.77	−1.06 +0.82	−1.06 +0.82
Photon energy scale 3 forward	+0.00 −0.41	+0.00 −0.41	+0.00 −0.41	+0.00 −0.41	+0.00 −0.41	+0.00 −0.41	+0.00 −0.41	+0.00 −0.41	+0.00 −0.41	+0.00 −0.41	+0.00 −0.41
Photon energy scale 4 forward	+0.00 −0.46	+0.00 −0.46	+0.00 −0.46	+0.00 −0.46	+0.00 −0.46	+0.00 −0.46	+0.00 −0.58	+0.00 −1.03	+0.00 −1.21	+0.00 −1.21	+0.00 −1.21
Photon energy scale 5	+0.28 −0.18	+0.28 −0.18	+0.28 −0.18	+0.28 −0.18	+0.28 −0.18	+0.28 −0.18	+0.28 −0.18	+0.47 −0.18	+3.13 −0.32	+3.58 −4.55	+3.58 −4.93
Photon identification efficiency	−1.70 +1.76	−0.63 +0.64	−0.58 +0.58	−0.73 +0.74	−0.48 +0.48	−0.37 +0.37	−0.40 +0.40	−0.41 +0.42	−0.41 +0.42	−0.59 +0.60	−0.60 +0.60
Jet energy scale 1	−0.73 +0.79	−0.73 +0.79	−0.69 +0.72	−0.20 −0.09	+0.04 −0.21	+0.14 −0.26	+0.52 −0.57	+0.69 −0.66	+1.05 −0.93	+1.59 −1.49	+2.28 −1.70
Jet energy scale 2	+0.95 −0.41	+0.94 −0.41	+0.55 −0.39	+0.12 −0.11	−0.12 +0.13	−0.31 +0.21	−0.50 +0.46	−0.71 +0.73	−1.01 +1.08	−1.37 +1.45	−1.40 +2.13
Jet energy scale 3	−0.04 +0.13	−0.04 +0.13	−0.04 +0.12	−0.04 +0.04	−0.03 +0.03	−0.03 +0.02	+0.02 −0.02	+0.06 −0.05	+0.11 −0.09	+0.17 −0.15	+0.22 −0.38
Jet energy scale 4	−0.56 −0.29	−0.54 −0.29	+0.14 −0.29	+0.19 −0.29	+0.19 −0.29	+0.19 −0.29	+0.19 −0.29	+0.20 −0.29	+0.43 −0.30	+0.71 −0.76	+0.73 −0.80
Jet energy scale 5	+1.03 +0.19	+1.01 +0.19	+0.30 +0.19	−0.04 +0.17	−0.08 +0.03	−0.08 −0.00	−0.08 −0.00	−0.08 −0.00	−0.08 −0.00	−0.08 −0.00	−0.08 −0.00
Jet energy scale 6	+0.17 +0.45	+0.17 +0.45	+0.17 +0.40	+0.17 −0.19	+0.19 −0.30	+0.35 −0.44	+0.54 −0.65	+0.66 −0.67	+0.92 −0.85	+1.28 −1.22	+1.82 −1.35
Jet energy scale 7	−0.58 +0.59	−0.14 +0.14	+0.08 −0.08	+0.20 −0.20	+0.30 −0.29	+0.41 −0.41	+0.58 −0.57	+0.71 −0.71	+0.97 −0.96	+1.31 −1.24	+1.50 −1.46
Jet energy scale 8	−0.22 +1.65	−0.22 +0.47	−0.22 +0.47	−0.25 +0.79	−0.42 +0.47	−0.54 +0.41	−0.47 +0.49	−0.34 +0.35	−0.32 +0.29	−0.33 +0.20	−0.33 +0.19
Jet energy scale 9	−1.80 +2.55	−1.05 +0.91	−0.55 +0.67	−0.49 +0.59	+0.00 −0.10	+0.18 −0.31	+0.61 −0.63	+0.91 −0.83	+1.27 −1.18	+1.75 −1.77	+2.10 −1.99
Jet energy resolution	+1.03 +0.00	+1.03 +0.00	+1.03 +0.00	+1.03 +0.00	+1.03 +0.00	+1.03 +0.00	+0.83 +0.00	+0.12 +0.00	−0.16 +0.00	−0.16 +0.00	−0.16 +0.00
b-jet tagging efficiency 1	+1.40 −1.37	+1.72 −1.68	+1.96 −1.91	+2.12 −2.06	+2.38 −2.31	+2.78 −2.68	+3.53 −3.39	+4.41 −4.13	+6.90 −6.20	+10.67 −9.19	+13.56 −11.28
b-jet tagging efficiency 2	−0.84 +0.84	−0.75 +0.75	−0.69 +0.70	−0.72 +0.73	−0.84 +0.85	−1.03 +1.04	−1.21 +1.20	−1.08 +1.09	−0.55 +0.55	+0.88 −0.83	+1.99 −1.95
b-jet tagging efficiency 3	−1.00 +1.01	−0.85 +0.86	−0.83 +0.84	−0.90 +0.91	−1.03 +1.05	−1.20 +1.22	−1.49 +1.49	−1.63 +1.66	−1.62 +1.64	−1.26 +1.28	−1.12 +1.07
b-jet tagging efficiency 4	+0.18 −0.18	+0.11 −0.11	+0.19 −0.19	+0.23 −0.23	+0.30 −0.30	+0.40 −0.40	+0.60 −0.62	+0.76 −0.76	+1.29 −1.17	+1.71 −1.75	+1.79 −1.87
b-jet tagging efficiency 5	−0.10 +0.09	−0.10 +0.09	−0.10 +0.10	−0.20 +0.20	−0.29 +0.29	−0.39 +0.40	−0.57 +0.58	−0.75 +0.75	−1.00 +1.00	−1.52 +1.60	−1.79 +2.33
b-jet tagging efficiency 6	+0.35 −0.35	+0.26 −0.26	+0.19 −0.19	+0.15 −0.15	+0.13 −0.13	+0.13 −0.13	+0.20 −0.20	+0.39 −0.38	+1.20 −1.05	+2.75 −2.42	+3.98 −3.39
b-jet tagging efficiency 7	+0.50 −0.50	+0.34 −0.34	+0.23 −0.23	+0.11 −0.11	−0.03 +0.03	−0.13 +0.13	−0.58 +0.57	−0.78 +0.85	−0.91 +1.06	−0.94 +0.86	−0.62 +0.61

b-jet tagging efficiency 8	$^{-0.00}_{+0.00}$	$^{-0.00}_{+0.00}$	$^{-0.00}_{+0.00}$	$^{-0.00}_{+0.00}$	$^{-0.01}_{+0.01}$	$^{-0.04}_{+0.04}$	$^{-0.07}_{+0.07}$	$^{-0.13}_{+0.13}$	$^{-0.26}_{+0.26}$	$^{-1.08}_{+1.07}$	$^{-2.07}_{+2.76}$
c-jet tagging efficiency 1	$^{+8.64}_{-8.20}$	$^{+8.44}_{-8.20}$	$^{+5.61}_{-5.65}$	$^{+4.77}_{-4.93}$	$^{+5.42}_{-5.65}$	$^{+6.65}_{-7.00}$	$^{+7.90}_{-8.39}$	$^{+7.24}_{-7.46}$	$^{+5.74}_{-5.46}$	$^{+6.77}_{-5.84}$	$^{+6.88}_{-5.90}$
c-jet tagging efficiency 2	$^{-3.22}_{+3.48}$	$^{+0.13}_{-0.06}$	$^{+0.22}_{-0.15}$	$^{+0.26}_{-0.15}$	$^{+0.27}_{-0.26}$	$^{+0.48}_{-1.07}$	$^{+1.70}_{-1.98}$	$^{+1.90}_{-2.07}$	$^{+1.95}_{-1.98}$	$^{+2.82}_{-3.08}$	$^{+2.68}_{-3.18}$
c-jet tagging efficiency 3	$^{+2.75}_{-2.56}$	$^{+2.79}_{-2.84}$	$^{+0.54}_{-0.51}$	$^{-0.24}_{+0.25}$	$^{-0.30}_{+0.32}$	$^{-0.11}_{+0.11}$	$^{+0.29}_{-0.28}$	$^{+0.59}_{-0.45}$	$^{+0.68}_{-0.48}$	$^{+0.70}_{-0.48}$	$^{+0.70}_{-0.48}$
c-jet tagging efficiency 4	$^{+0.78}_{-0.76}$	$^{-0.59}_{+0.63}$	$^{-0.18}_{+0.20}$	$^{+0.04}_{-0.04}$	$^{+0.06}_{-0.07}$	$^{+0.07}_{-0.07}$	$^{+0.11}_{-0.12}$	$^{+0.26}_{-0.28}$	$^{+0.46}_{-0.34}$	$^{+0.71}_{-0.49}$	$^{+0.93}_{-0.50}$
c-jet tagging efficiency 5	$^{+0.88}_{-0.81}$	$^{+0.73}_{-0.73}$	$^{-0.12}_{+0.04}$	$^{-0.19}_{+0.14}$	$^{-0.18}_{+0.40}$	$^{-0.14}_{+0.23}$	$^{-0.14}_{+0.17}$	$^{-0.14}_{+0.17}$	$^{-0.14}_{+0.17}$	$^{-0.14}_{+0.17}$	$^{-0.14}_{+0.17}$
c-jet tagging efficiency 6	$^{-0.20}_{+0.24}$	$^{-0.20}_{+0.24}$	$^{-0.20}_{+0.24}$	$^{-0.26}_{+0.29}$	$^{-0.58}_{+0.60}$	$^{-0.31}_{+0.36}$	$^{+0.27}_{-0.16}$	$^{+0.39}_{-0.27}$	$^{+0.43}_{-0.30}$	$^{+1.36}_{-1.11}$	$^{+1.78}_{-1.23}$
c-jet tagging efficiency 7	$^{-2.79}_{+2.72}$	$^{-1.63}_{+1.61}$	$^{-0.56}_{+0.56}$	$^{-0.19}_{+0.20}$	$^{-0.05}_{+0.05}$	$^{-0.02}_{+0.02}$	$^{-0.02}_{+0.02}$	$^{-0.02}_{+0.02}$	$^{-0.02}_{+0.02}$	$^{-0.02}_{+0.02}$	$^{-0.02}_{+0.02}$
c-jet tagging efficiency 8	$^{-1.67}_{+1.67}$	$^{-2.70}_{+2.66}$	$^{-1.52}_{+1.51}$	$^{-0.96}_{+0.97}$	$^{-0.96}_{+0.96}$	$^{-1.10}_{+1.08}$	$^{-1.25}_{+1.18}$	$^{-1.33}_{+1.27}$	$^{-1.26}_{+1.36}$	$^{-1.90}_{+1.86}$	$^{-2.24}_{+2.09}$
c-jet tagging efficiency 9	$^{+0.53}_{-0.53}$	$^{+0.62}_{-0.62}$	$^{+0.86}_{-0.87}$	$^{+0.91}_{-0.92}$	$^{+0.97}_{-0.98}$	$^{+0.58}_{-0.55}$	$^{-0.37}_{+0.53}$	$^{-0.58}_{+0.77}$	$^{-0.61}_{+0.81}$	$^{-1.33}_{+1.69}$	$^{-1.70}_{+2.44}$
c-jet tagging efficiency 10	$^{-1.93}_{+1.91}$	$^{-2.90}_{+2.84}$	$^{-0.44}_{+0.45}$	$^{+0.54}_{-0.54}$	$^{+0.97}_{-0.98}$	$^{+1.04}_{-1.07}$	$^{+1.04}_{-1.10}$	$^{+1.08}_{-1.07}$	$^{+1.08}_{-0.95}$	$^{+1.47}_{-1.28}$	$^{+1.98}_{-1.57}$
c-jet tagging efficiency 11	$^{+1.37}_{-1.42}$	$^{+2.48}_{-2.62}$	$^{+1.88}_{-2.00}$	$^{+1.61}_{-1.74}$	$^{+1.53}_{-1.63}$	$^{+1.11}_{-1.17}$	$^{+0.56}_{-0.61}$	$^{+0.14}_{-0.16}$	$^{+0.01}_{-0.01}$	$^{+0.00}_{-0.01}$	$^{+0.00}_{-0.01}$
c-jet tagging efficiency 12	$^{+0.48}_{-0.45}$	$^{+0.93}_{-0.45}$	$^{+0.77}_{-0.67}$	$^{+0.35}_{-0.32}$	$^{+0.29}_{-0.27}$	$^{+0.28}_{-0.27}$	$^{+0.21}_{-0.21}$	$^{+0.13}_{-0.13}$	$^{+0.04}_{-0.05}$	$^{+0.03}_{+0.11}$	$^{+0.03}_{+0.12}$
c-jet tagging efficiency 13	$^{+0.76}_{-0.67}$	$^{-0.12}_{+0.16}$	$^{-0.15}_{+0.18}$	$^{-0.15}_{+0.18}$	$^{-0.16}_{+0.19}$	$^{-0.25}_{+0.24}$	$^{-0.14}_{+0.04}$	$^{-0.02}_{-0.01}$	$^{+0.03}_{-0.02}$	$^{+0.04}_{-0.02}$	$^{+0.13}_{-0.02}$
c-jet tagging efficiency 14	$^{-0.47}_{+0.47}$	$^{+0.22}_{-0.22}$	$^{+0.25}_{-0.25}$	$^{+0.44}_{-0.45}$	$^{+0.54}_{-0.55}$	$^{+0.47}_{-0.49}$	$^{+0.37}_{-0.40}$	$^{+0.27}_{-0.23}$	$^{+0.11}_{-0.08}$	$^{+0.06}_{-0.06}$	$^{+0.06}_{-0.06}$
c-jet tagging efficiency 15	$^{-0.09}_{+0.10}$	$^{-0.10}_{+0.11}$	$^{-0.43}_{+0.46}$	$^{-0.36}_{+0.43}$	$^{-0.37}_{+0.45}$	$^{-0.54}_{+0.59}$	$^{-0.58}_{+0.59}$	$^{-0.38}_{+0.44}$	$^{-0.10}_{+0.12}$	$^{-0.07}_{+0.07}$	$^{-0.07}_{+0.07}$
c-jet tagging efficiency 16	$^{+0.12}_{-0.04}$	$^{+0.04}_{-0.04}$	$^{+0.03}_{-0.04}$	$^{+0.03}_{-0.04}$	$^{+0.03}_{-0.04}$	$^{+0.03}_{-0.04}$	$^{+0.03}_{-0.04}$	$^{+0.03}_{-0.04}$	$^{+0.03}_{-0.04}$	$^{+0.03}_{-0.04}$	$^{+0.03}_{-0.04}$
c-jet tagging efficiency 17	$^{+0.00}_{+0.00}$	$^{+0.00}_{+0.00}$	$^{+0.00}_{+0.00}$	$^{+0.00}_{+0.00}$	$^{+0.00}_{+0.00}$	$^{+0.00}_{+0.00}$	$^{+0.00}_{+0.00}$	$^{+0.00}_{+0.00}$	$^{+0.00}_{+0.00}$	$^{+0.00}_{+0.00}$	$^{+0.00}_{+0.00}$
Light-jet tagging efficiency 1	$^{+22.03}_{-23.17}$	$^{-5.99}_{+5.92}$	$^{-6.57}_{+6.52}$	$^{-5.14}_{+4.97}$	$^{-6.83}_{+6.76}$	$^{-6.70}_{+6.61}$	$^{-6.93}_{+6.81}$	$^{-6.56}_{+6.49}$	$^{-5.85}_{+5.90}$	$^{-5.51}_{+5.07}$	$^{-4.37}_{+4.14}$
Light-jet tagging efficiency 2	$^{-16.40}_{+16.73}$	$^{-8.40}_{+8.51}$	$^{-2.76}_{+2.75}$	$^{-1.59}_{+1.57}$	$^{-1.92}_{+1.92}$	$^{-1.95}_{+1.95}$	$^{-2.08}_{+2.05}$	$^{-2.36}_{+2.39}$	$^{-2.27}_{+2.47}$	$^{-2.36}_{+2.44}$	$^{-2.37}_{+2.44}$
Light-jet tagging efficiency 3	$^{-6.15}_{+6.21}$	$^{-2.28}_{+2.25}$	$^{-2.15}_{+2.12}$	$^{-1.93}_{+1.86}$	$^{-2.59}_{+2.53}$	$^{-2.87}_{+2.81}$	$^{-3.49}_{+3.41}$	$^{-3.28}_{+3.27}$	$^{-3.33}_{+3.55}$	$^{-3.05}_{+2.97}$	$^{-2.73}_{+2.68}$
Light-jet tagging efficiency 4	$^{-2.36}_{+2.33}$	$^{-2.31}_{+2.28}$	$^{-0.65}_{+0.65}$	$^{-0.53}_{+0.53}$	$^{-0.53}_{+0.53}$	$^{-0.53}_{+0.52}$	$^{-0.61}_{+0.58}$	$^{-0.27}_{+0.33}$	$^{-0.13}_{+0.22}$	$^{-0.12}_{+0.22}$	$^{-0.12}_{+0.22}$
Light-jet tagging efficiency 5	$^{-4.12}_{+4.17}$	$^{-3.30}_{+3.30}$	$^{-1.89}_{+1.89}$	$^{-0.73}_{+0.73}$	$^{-0.72}_{+0.71}$	$^{-0.33}_{+0.33}$	$^{-0.23}_{+0.23}$	$^{-0.22}_{+0.23}$	$^{-0.22}_{+0.23}$	$^{-0.22}_{+0.23}$	$^{-0.22}_{+0.23}$
Light-jet tagging efficiency 6	$^{+10.18}_{-10.10}$	$^{+2.22}_{-2.22}$	$^{+1.08}_{-1.08}$	$^{+0.69}_{-0.70}$	$^{+0.93}_{-0.94}$	$^{+0.92}_{-0.93}$	$^{+0.94}_{-0.99}$	$^{+0.97}_{-0.98}$	$^{+1.01}_{-0.86}$	$^{+1.01}_{-0.81}$	$^{+1.47}_{-0.94}$
Light-jet tagging efficiency 7	$^{-1.84}_{+1.82}$	$^{-0.46}_{+0.46}$	$^{-0.44}_{+0.43}$	$^{-0.55}_{+0.55}$	$^{-0.34}_{+0.31}$	$^{-0.22}_{+0.03}$	$^{+0.01}_{-0.03}$	$^{+0.07}_{-0.03}$	$^{+0.07}_{-0.03}$	$^{+0.07}_{-0.03}$	$^{+0.07}_{-0.03}$
Light-jet tagging efficiency 8	$^{+1.94}_{-1.96}$	$^{+0.82}_{-0.82}$	$^{+0.37}_{-0.38}$	$^{+0.42}_{-0.42}$	$^{+0.42}_{-0.42}$	$^{+0.51}_{-0.52}$	$^{+0.61}_{-0.65}$	$^{+0.77}_{-0.76}$	$^{+0.90}_{-0.76}$	$^{+0.76}_{-0.59}$	$^{+1.01}_{-0.58}$
Light-jet tagging efficiency 9	$^{-2.15}_{+2.12}$	$^{-2.32}_{+2.31}$	$^{-2.05}_{+2.02}$	$^{-1.94}_{+1.89}$	$^{-2.23}_{+2.20}$	$^{-2.12}_{+2.09}$	$^{-2.07}_{+2.00}$	$^{-1.96}_{+1.93}$	$^{-1.53}_{+1.66}$	$^{-1.16}_{+1.43}$	$^{-1.66}_{+2.03}$
Light-jet tagging efficiency 10	$^{-0.50}_{+0.49}$	$^{-0.50}_{+0.49}$	$^{-0.51}_{+0.50}$	$^{-0.65}_{+0.63}$	$^{-1.03}_{+1.01}$	$^{-1.05}_{+1.03}$	$^{-1.18}_{+1.13}$	$^{-1.22}_{+1.21}$	$^{-1.16}_{+1.30}$	$^{-1.09}_{+1.31}$	$^{-1.43}_{+1.89}$
Light-jet tagging efficiency 11	$^{+0.14}_{-0.14}$	$^{+0.14}_{-0.14}$	$^{+0.12}_{-0.12}$	$^{-0.07}_{+0.07}$	$^{-0.10}_{+0.10}$	$^{-0.14}_{+0.13}$	$^{-0.39}_{+0.37}$	$^{-0.61}_{+0.65}$	$^{-0.74}_{+0.87}$	$^{-0.81}_{+0.79}$	$^{-0.84}_{+0.83}$
Light-jet tagging efficiency 12	$^{-0.92}_{+0.92}$	$^{-0.10}_{+0.13}$	$^{-0.08}_{+0.11}$	$^{-0.08}_{+0.11}$	$^{-0.08}_{+0.11}$	$^{-0.08}_{+0.11}$	$^{-0.08}_{+0.11}$	$^{-0.08}_{+0.11}$	$^{-0.09}_{+0.12}$	$^{-0.42}_{+0.35}$	$^{-0.41}_{+0.40}$
Light-jet tagging efficiency 13	$^{+0.24}_{-0.24}$	$^{+0.24}_{-0.24}$	$^{+0.26}_{-0.26}$	$^{+0.55}_{-0.55}$	$^{+0.57}_{-0.57}$	$^{+0.41}_{-0.40}$	$^{+0.11}_{-0.10}$	$^{+0.05}_{-0.03}$	$^{+0.05}_{-0.03}$	$^{+0.05}_{-0.03}$	$^{+0.05}_{-0.03}$
Light-jet tagging efficiency 14	$^{-0.07}_{+0.06}$	$^{-0.07}_{+0.06}$	$^{-0.07}_{+0.07}$	$^{-0.16}_{+0.15}$	$^{-0.26}_{+0.26}$	$^{-0.29}_{+0.28}$	$^{-0.31}_{+0.28}$	$^{-0.31}_{+0.35}$	$^{-0.25}_{+0.26}$	$^{-0.20}_{+0.25}$	$^{-0.20}_{+0.25}$
Light-jet tagging efficiency 15	$^{-0.39}_{+0.38}$	$^{+0.13}_{-0.13}$	$^{+0.14}_{-0.15}$	$^{+0.19}_{-0.19}$	$^{+0.28}_{-0.28}$	$^{+0.29}_{-0.29}$	$^{+0.22}_{-0.26}$	$^{+0.22}_{-0.23}$	$^{+0.23}_{-0.23}$	$^{+0.20}_{-0.19}$	$^{+0.26}_{-0.18}$
Light-jet tagging efficiency 16	$^{-0.40}_{+0.40}$	$^{-0.25}_{+0.25}$	$^{-0.12}_{+0.12}$	$^{+0.04}_{-0.04}$	$^{+0.07}_{-0.07}$	$^{+0.10}_{-0.10}$	$^{+0.13}_{-0.16}$	$^{+0.13}_{-0.14}$	$^{+0.10}_{-0.10}$	$^{+0.14}_{-0.09}$	$^{+0.13}_{-0.13}$
Light-jet tagging efficiency 17	$^{-0.65}_{+0.64}$	$^{-0.42}_{+0.42}$	$^{-0.17}_{+0.16}$	$^{-0.13}_{+0.13}$	$^{-0.15}_{+0.15}$	$^{-0.16}_{+0.15}$	$^{-0.15}_{+0.12}$	$^{-0.10}_{+0.09}$	$^{-0.08}_{+0.08}$	$^{-0.08}_{+0.09}$	$^{-0.08}_{+0.09}$
Sideband isolation definition	$^{-2.53}_{+2.81}$	$^{-0.42}_{+2.78}$	$^{-0.37}_{+1.53}$	$^{-0.35}_{+0.90}$	$^{-0.35}_{+0.70}$	$^{-0.35}_{+0.56}$	$^{-0.25}_{+0.42}$	$^{-0.25}_{+0.35}$	$^{-0.19}_{+0.33}$	$^{-0.09}_{+0.24}$	$^{-0.08}_{+0.18}$
Sideband identification definition	$^{-0.67}_{+0.86}$	$^{-0.67}_{+0.85}$	$^{-0.65}_{+0.54}$	$^{-0.41}_{+0.52}$	$^{-0.35}_{+0.51}$	$^{-0.21}_{+0.45}$	$^{-0.17}_{+0.30}$	$^{-0.17}_{+0.27}$	$^{-0.17}_{+0.26}$	$^{-0.17}_{+0.26}$	$^{-0.17}_{+0.26}$
Sideband correlation	$^{-13.26}_{+12.81}$	$^{-6.33}_{+6.19}$	$^{-3.33}_{+3.28}$	$^{-2.00}_{+1.98}$	$^{-1.48}_{+1.47}$	$^{-1.42}_{+1.41}$	$^{-1.07}_{+1.06}$	$^{-0.90}_{+0.89}$	$^{-0.81}_{+0.80}$	$^{-0.57}_{+0.57}$	$^{-0.42}_{+0.42}$

Prompt photon modelling	+2.45	+2.45	+2.45	+2.45	+2.45	+2.45	+2.45	+2.45	+2.45	+2.45	+2.45
Non-perturbative QCD models	+7.31	+7.31	+7.31	+7.31	+7.31	+7.31	+7.31	+7.31	+7.31	+7.31	+7.31
Particle-level migration effects	+0.39	+0.39	+0.39	+0.39	+0.39	+0.39	+0.39	+0.39	+0.39	+0.39	+0.39
Luminosity	$^{+1.90}_{-1.90}$	$^{+1.90}_{-1.90}$	$^{+1.90}_{-1.90}$	$^{+1.90}_{-1.90}$	$^{+1.90}_{-1.90}$	$^{+1.90}_{-1.90}$	$^{+1.90}_{-1.90}$	$^{+1.90}_{-1.90}$	$^{+1.90}_{-1.90}$	$^{+1.90}_{-1.90}$	$^{+1.90}_{-1.90}$
Other sources combined	$^{+2.41}_{-2.39}$	$^{+1.80}_{-1.86}$	$^{+1.54}_{-1.59}$	$^{+1.31}_{-1.45}$	$^{+1.36}_{-1.51}$	$^{+1.30}_{-1.59}$	$^{+1.16}_{-1.55}$	$^{+1.06}_{-1.45}$	$^{+0.99}_{-1.35}$	$^{+0.90}_{-1.31}$	$^{+0.94}_{-1.34}$

APPENDIX F
Tables of Measured and Predicted Cross Sections

Table F–1 – Measured values of the fiducial integrated $\gamma + b$ cross section in the central and forward regions, including their statistical and systematic uncertainties. The quadrature sum of the uncertainties is also given as the total uncertainty. The central region is defined as $|\eta^\gamma| < 1.37$ and covers $25 < E_{\mathrm{T}}^\gamma < 400$ GeV and the forward region is defined as $1.56 < |\eta^\gamma| < 2.37$ and covers $25 < E_{\mathrm{T}}^\gamma < 350$ GeV. The order-of-magnitude factor multiplies all values in the corresponding row.

Quantity	Value	Stat. unc.	Syst. unc.	Total unc.	[pb]
$\sigma_{\mathrm{central}}$	7.7	$^{+0.7}_{-0.8}$	$^{+1.4}_{-1.4}$	$^{+1.6}_{-1.6}$	$\times 10^2$
$\sigma_{\mathrm{forward}}$	2.2	$^{+0.6}_{-0.6}$	$^{+0.8}_{-0.8}$	$^{+1.0}_{-1.0}$	$\times 10^2$
$\sigma_{\mathrm{central}}/\sigma_{\mathrm{forward}}$	3.5	$^{+1.4}_{-0.8}$	$^{+0.9}_{-0.8}$	$^{+1.7}_{-1.2}$	–

Table F–2 – Predicted values of the fiducial integrated $\gamma + b$ cross section in the central and forward regions by SHERPA, PYTHIA and MADGRAPH5_aMC@NLO (MG5_aMC). The theoretical uncertainties related to the NLO predictions are given, while no uncertainties are provided for the LO predictions. The central region is defined as $|\eta^{\gamma}| < 1.37$ and covers $25 < E_{\mathrm{T}}^{\gamma} < 400$ GeV and the forward region is defined as $1.56 < |\eta^{\gamma}| < 2.37$ and covers $25 < E_{\mathrm{T}}^{\gamma} < 350$ GeV. The order-of-magnitude factor multiplies all values in the corresponding row.

Quantity	SHERPA	PYTHIA	MG5_aMC 5F	MG5_aMC 4F	[pb]
$\sigma_{\mathrm{central}}$	5.60	6.94	$7.2\ ^{+1.2}_{-1.6}$	$6.8\ ^{+2.0}_{-1.9}$	$\times 10^2$
$\sigma_{\mathrm{forward}}$	2.53	2.97	$3.2\ ^{+1.0}_{-0.9}$	$2.5\ ^{+0.9}_{-0.7}$	$\times 10^2$
$\sigma_{\mathrm{central}}/\sigma_{\mathrm{forward}}$	2.22	2.34	$2.27^{+0.17}_{-0.24}$	$2.71^{+0.07}_{-0.11}$	–

Table F–3 – Measured values of the fiducial differential $\gamma+b$ cross section in the central region as a function of E_{T}^{γ}, including their statistical and systematic uncertainties. The quadrature sum of the uncertainties is also given as the total uncertainty. The central region is defined as $|\eta^{\gamma}| < 1.37$. The order-of-magnitude factor multiplies all values in the corresponding row, except for the E_{T}^{γ} bin range.

E_{T}^{γ} bin [GeV]	$d\sigma_{\mathrm{central}}/dE_{\mathrm{T}}^{\gamma}$	Stat. unc.	Syst. unc.	Total unc.	[pb/GeV]
25–45	3.20	$^{+0.35}_{-0.40}$	$^{+0.58}_{-0.58}$	$^{+0.67}_{-0.70}$	$\times 10^{1}$
45–65	4.60	$^{+0.26}_{-0.27}$	$^{+0.68}_{-0.67}$	$^{+0.73}_{-0.72}$	$\times 10^{0}$
65–85	1.15	$^{+0.05}_{-0.05}$	$^{+0.14}_{-0.15}$	$^{+0.15}_{-0.15}$	$\times 10^{0}$
85–105	4.02	$^{+0.15}_{-0.15}$	$^{+0.50}_{-0.51}$	$^{+0.52}_{-0.53}$	$\times 10^{-1}$
105–125	1.47	$^{+0.06}_{-0.06}$	$^{+0.21}_{-0.21}$	$^{+0.22}_{-0.22}$	$\times 10^{-1}$
125–150	6.8	$^{+0.1}_{-0.1}$	$^{+1.0}_{-1.0}$	$^{+1.0}_{-1.0}$	$\times 10^{-2}$
150–175	3.48	$^{+0.06}_{-0.06}$	$^{+0.49}_{-0.51}$	$^{+0.49}_{-0.51}$	$\times 10^{-2}$
175–200	1.49	$^{+0.04}_{-0.04}$	$^{+0.25}_{-0.27}$	$^{+0.26}_{-0.27}$	$\times 10^{-2}$
200–250	6.8	$^{+0.2}_{-0.2}$	$^{+1.2}_{-1.2}$	$^{+1.2}_{-1.2}$	$\times 10^{-3}$
250–300	2.58	$^{+0.12}_{-0.12}$	$^{+0.45}_{-0.45}$	$^{+0.47}_{-0.46}$	$\times 10^{-3}$
300–350	8.3	$^{+0.7}_{-0.8}$	$^{+2.0}_{-2.0}$	$^{+2.1}_{-2.2}$	$\times 10^{-4}$
350–400	6.0	$^{+0.5}_{-0.6}$	$^{+1.4}_{-1.3}$	$^{+1.5}_{-1.4}$	$\times 10^{-4}$

Table F–4 – Predicted values of the fiducial differential $\gamma + b$ cross section in the central region as a function of E_{T}^{γ} by SHERPA, PYTHIA and MADGRAPH5_aMC@NLO (MG5_aMC). The theoretical uncertainties related to the NLO predictions are given, while no uncertainties are provided for the LO predictions. The central region is defined as $|\eta^{\gamma}| < 1.37$. The order-of-magnitude factor multiplies all values in the corresponding row, except for the E_{T}^{γ} bin range.

E_{T}^{γ} bin [GeV]	$d\sigma_{\mathrm{central}}/dE_{\mathrm{T}}^{\gamma}$				[pb/GeV]
	SHERPA	PYTHIA	MG5_aMC 5F	MG5_aMC 4F	
25–45	2.2	2.8	$2.9\ ^{+0.5}_{-0.7}$	$2.7\ ^{+0.8}_{-0.8}$	$\times 10^{1}$
45–65	4.3	5.0	$5.3\ ^{+0.9}_{-1.0}$	$5.2\ ^{+1.3}_{-1.2}$	$\times 10^{0}$
65–85	1.14	1.14	$1.36^{+0.20}_{-0.21}$	$1.08^{+0.20}_{-0.19}$	$\times 10^{0}$
85–105	3.9	3.8	$4.2\ ^{+0.6}_{-0.6}$	$3.4\ ^{+0.5}_{-0.5}$	$\times 10^{-1}$
105–125	1.61	1.37	$1.58^{+0.15}_{-0.17}$	$1.30^{+0.18}_{-0.17}$	$\times 10^{-1}$
125–150	7.0	5.4	$6.2\ ^{+0.7}_{-0.7}$	$4.5\ ^{+0.6}_{-0.6}$	$\times 10^{-2}$
150–175	3.08	2.25	$2.92^{+0.35}_{-0.30}$	$1.92^{+0.24}_{-0.21}$	$\times 10^{-2}$
175–200	1.55	1.11	$1.45^{+0.14}_{-0.12}$	$0.91^{+0.10}_{-0.09}$	$\times 10^{-2}$
200–250	6.56	4.28	$5.1\ ^{+0.5}_{-0.4}$	$3.18^{+0.36}_{-0.31}$	$\times 10^{-3}$
250–300	2.41	1.55	$1.89^{+0.18}_{-0.16}$	$1.00^{+0.10}_{-0.09}$	$\times 10^{-3}$
300–350	9.67	5.92	$6.0\ ^{+0.7}_{-0.6}$	$2.40^{+0.28}_{-0.25}$	$\times 10^{-4}$
350–400	4.48	2.85	$3.21^{+0.37}_{-0.32}$	$1.19^{+0.13}_{-0.11}$	$\times 10^{-4}$

Table F–5 – Measured values of the fiducial differential $\gamma+b$ cross section in the forward region as a function of E_{T}^{γ}, including their statistical and systematic uncertainties. The quadrature sum of the uncertainties is also given as the total uncertainty. The forward region is defined as $1.56 < |\eta^{\gamma}| < 2.37$. The order-of-magnitude factor multiplies all values in the corresponding row, except for the E_{T}^{γ} bin range.

E_{T}^{γ} bin [GeV]	$d\sigma_{\mathrm{forward}}/dE_{\mathrm{T}}^{\gamma}$	Stat. unc.	Syst. unc.	Total unc.	[pb/GeV]
25–45	8.5	$^{+3.2}_{-3.2}$	$^{+3.3}_{-3.3}$	$^{+4.6}_{-4.5}$	$\times 10^{0}$
45–65	1.68	$^{+0.22}_{-0.19}$	$^{+0.40}_{-0.38}$	$^{+0.46}_{-0.43}$	$\times 10^{0}$
65–85	5.5	$^{+0.4}_{-0.4}$	$^{+0.8}_{-0.8}$	$^{+0.9}_{-0.9}$	$\times 10^{-1}$
85–105	1.86	$^{+0.10}_{-0.10}$	$^{+0.24}_{-0.25}$	$^{+0.27}_{-0.27}$	$\times 10^{-1}$
105–125	7.4	$^{+0.4}_{-0.5}$	$^{+1.0}_{-1.0}$	$^{+1.1}_{-1.1}$	$\times 10^{-2}$
125–150	2.93	$^{+0.06}_{-0.07}$	$^{+0.42}_{-0.43}$	$^{+0.42}_{-0.43}$	$\times 10^{-2}$
150–175	1.38	$^{+0.04}_{-0.04}$	$^{+0.22}_{-0.22}$	$^{+0.22}_{-0.23}$	$\times 10^{-2}$
175–200	5.9	$^{+0.2}_{-0.3}$	$^{+1.0}_{-1.0}$	$^{+1.0}_{-1.0}$	$\times 10^{-3}$
200–250	2.49	$^{+0.12}_{-0.12}$	$^{+0.39}_{-0.37}$	$^{+0.41}_{-0.39}$	$\times 10^{-3}$
250–300	6.9	$^{+0.7}_{-0.6}$	$^{+1.3}_{-1.3}$	$^{+1.5}_{-1.4}$	$\times 10^{-4}$
300–350	2.10	$^{+0.35}_{-0.36}$	$^{+0.50}_{-0.46}$	$^{+0.61}_{-0.58}$	$\times 10^{-4}$

Table F–6 – Predicted values of the fiducial differential $\gamma+b$ cross section in the forward region as a function of E_{T}^{γ} by SHERPA, PYTHIA and MADGRAPH5_aMC@NLO (MG5_aMC). The theoretical uncertainties related to the NLO predictions are given, while no uncertainties are provided for the LO predictions. The forward region is defined as $1.56 < |\eta^{\gamma}| < 2.37$. The order-of-magnitude factor multiplies all values in the corresponding row, except for the E_{T}^{γ} bin range.

E_{T}^{γ} bin [GeV]	$d\sigma_{\mathrm{forward}}/dE_{\mathrm{T}}^{\gamma}$				[pb/GeV]
	SHERPA	PYTHIA	MG5_aMC 5F	MG5_aMC 4F	
25–45	9.9	12.3	$13\ ^{+4}_{-4}$	$10.2\ ^{+3.7}_{-3.2}$	$\times 10^{0}$
45–65	1.9	1.9	$2.1\ ^{+0.5}_{-0.5}$	$1.8\ ^{+0.5}_{-0.4}$	$\times 10^{0}$
65–85	5.1	4.3	$5.1\ ^{+1.6}_{-0.5}$	$3.6\ ^{+0.8}_{-0.7}$	$\times 10^{-1}$
85–105	1.79	1.13	$1.57^{+0.29}_{-0.26}$	$1.01^{+0.19}_{-0.17}$	$\times 10^{-1}$
105–125	7.4	5.1	$5.7\ ^{+1.1}_{-0.7}$	$3.8\ ^{+0.7}_{-0.6}$	$\times 10^{-2}$
125–150	3.14	2.07	$2.25^{+0.31}_{-0.26}$	$1.27^{+0.24}_{-0.20}$	$\times 10^{-2}$
150–175	1.35	0.82	$0.97^{+0.15}_{-0.12}$	$0.50^{+0.09}_{-0.08}$	$\times 10^{-2}$
175–200	6.60	3.61	$4.6\ ^{+0.7}_{-0.6}$	$2.14^{+0.37}_{-0.31}$	$\times 10^{-3}$
200–250	2.56	1.46	$1.49^{+0.25}_{-0.20}$	$0.70^{+0.11}_{-0.09}$	$\times 10^{-3}$
250–300	7.66	4.45	$4.4\ ^{+0.7}_{-0.5}$	$1.83^{+0.29}_{-0.25}$	$\times 10^{-4}$
300–350	2.65	1.63	$1.21^{+0.22}_{-0.17}$	$0.37^{+0.07}_{-0.06}$	$\times 10^{-4}$

Table F–7 – Measured values of the ratio of the fiducial $\gamma + b$ cross section in the central region to that of the forward region as a function of E_{T}^{γ}, including their statistical and systematic uncertainties. The quadrature sum of the uncertainties is also given as the total uncertainty. The central region is defined as $|\eta^{\gamma}| < 1.37$ and covers $25 < E_{\mathrm{T}}^{\gamma} < 400$ GeV and the forward region is defined as $1.56 < |\eta^{\gamma}| < 2.37$ and covers $25 < E_{\mathrm{T}}^{\gamma} < 350$ GeV.

E_{T}^{γ} bin [GeV]	$\sigma_{\mathrm{central}}/\sigma_{\mathrm{forward}}$	Stat. unc.	Syst. unc.	Total unc.
25–45	3.8	$^{+2.2}_{-1.1}$	$^{+0.8}_{-0.8}$	$^{+2.3}_{-1.3}$
45–65	2.73	$^{+0.39}_{-0.35}$	$^{+0.59}_{-0.52}$	$^{+0.71}_{-0.62}$
65–85	2.09	$^{+0.18}_{-0.16}$	$^{+0.29}_{-0.29}$	$^{+0.34}_{-0.33}$
85–105	2.17	$^{+0.16}_{-0.14}$	$^{+0.31}_{-0.31}$	$^{+0.35}_{-0.34}$
105–125	1.99	$^{+0.15}_{-0.14}$	$^{+0.28}_{-0.28}$	$^{+0.32}_{-0.31}$
125–150	2.31	$^{+0.06}_{-0.06}$	$^{+0.32}_{-0.32}$	$^{+0.33}_{-0.33}$
150–175	2.52	$^{+0.09}_{-0.09}$	$^{+0.38}_{-0.39}$	$^{+0.39}_{-0.40}$
175–200	2.55	$^{+0.15}_{-0.12}$	$^{+0.42}_{-0.42}$	$^{+0.44}_{-0.43}$
200–250	2.71	$^{+0.16}_{-0.15}$	$^{+0.37}_{-0.40}$	$^{+0.41}_{-0.42}$
250–300	3.7	$^{+0.4}_{-0.4}$	$^{+0.6}_{-0.6}$	$^{+0.7}_{-0.7}$
300–350	3.9	$^{+0.9}_{-0.7}$	$^{+0.7}_{-0.7}$	$^{+1.2}_{-1.0}$

Table F–8 – Predicted values of the ratio of the fiducial $\gamma+b$ cross section in the central region to that of the forward region as a function of E_{T}^{γ} by SHERPA, PYTHIA and MADGRAPH5_aMC@NLO (MG5_aMC). The theoretical uncertainties related to the NLO predictions are given, while no uncertainties are provided for the LO predictions. The central region is defined as $|\eta^{\gamma}| < 1.37$ and covers $25 < E_{\mathrm{T}}^{\gamma} < 400$ GeV and the forward region is defined as $1.56 < |\eta^{\gamma}| < 2.37$ and covers $25 < E_{\mathrm{T}}^{\gamma} < 350$ GeV.

E_{T}^{γ} bin [GeV]	$\sigma_{\mathrm{central}}/\sigma_{\mathrm{forward}}$			
	SHERPA	PYTHIA	MG5_aMC 5F	MG5_aMC 4F
25–45	2.20	2.27	$2.20^{+0.21}_{-0.27}$	$2.65^{+0.07}_{-0.12}$
45–65	2.32	2.68	$2.61^{+0.11}_{-0.14}$	$2.87^{+0.03}_{-0.06}$
65–85	2.23	2.64	$2.7^{+0.4}_{-0.5}$	$3.02^{+0.10}_{-0.13}$
85–105	2.16	3.33	$2.65^{+0.09}_{-0.11}$	$3.32^{+0.06}_{-0.08}$
105–125	2.18	2.68	$2.77^{+0.24}_{-0.27}$	$3.40^{+0.10}_{-0.13}$
125–150	2.22	2.62	$2.77^{+0.15}_{-0.14}$	$3.57^{+0.13}_{-0.14}$
150–175	2.29	2.73	$3.03^{+0.11}_{-0.11}$	$3.81^{+0.18}_{-0.20}$
175–200	2.35	3.06	$3.18^{+0.23}_{-0.22}$	$4.26^{+0.21}_{-0.22}$
200–250	2.56	2.94	$3.41^{+0.19}_{-0.19}$	$4.54^{+0.20}_{-0.19}$
250–300	3.14	3.49	$4.26^{+0.21}_{-0.21}$	$5.46^{+0.30}_{-0.26}$
300–350	3.66	3.64	$5.00^{+0.27}_{-0.27}$	$6.46^{+0.45}_{-0.44}$

References

[1] S. W. Herb et al., *Observation of a Dimuon Resonance at 9.5 GeV in 400-GeV Proton-Nucleus Collisions*, Phys. Rev. Lett. **39** (1977) 252.

[2] M. Kobayashi and T. Maskawa, *CP Violation in the Renormalizable Theory of Weak Interaction*, Prog. Theor. Phys. **49** (1973) 652.

[3] J. Yoh, *The Discovery of the b Quark at Fermilab in 1977: The Experiment Coordinator's Story*, AIP Conf. Proc. **424** (1998) 29.

[4] M. L. Perl et al., *Evidence for Anomalous Lepton Production in e^+–e^- Annihilation*, Phys. Rev. Lett. **35** (1975) 1489.

[5] BABAR Collaboration, *The BABAR detector*, Nucl. Instrum. Meth. A **479** (2002) 1, arXiv: hep-ex/0105044.

[6] Belle Collaboration, *The Belle detector*, Nucl. Instrum. Meth. A **479** (2002) 117.

[7] Belle II Collaboration, *Belle II Technical Design Report*, (2010), arXiv: 1011.0352 [physics.ins-det].

[8] CDF Collaboration, *The CDF detector: an overview*, Nucl. Instrum. Meth. A **271** (1988) 387.

[9] DØ Collaboration, *The DØ detector*, Nucl. Instrum. Meth. A **338** (1994) 185.

[10] Fermilab, *TEVATRON Phase 1, February, 1980*, FERMILAB-DESIGN-1980-01.

[11] CDF Collaboration, *Observation of Top Quark Production in $\bar{p}p$ Collisions with the Collider Detector at Fermilab*, Phys. Rev. Lett. **74** (1995) 2626, arXiv: hep-ex/9503002.

[12] D0 Collaboration, *Observation of the Top Quark*, Phys. Rev. Lett. **74** (1995) 2632, arXiv: hep-ex/9503003.

[13] L. Evans and P. Bryant, *LHC Machine*, JINST **3** (2008) S08001.

[14] ATLAS Collaboration, *The ATLAS Experiment at the CERN Large Hadron Collider*, JINST **3** (2008) S08003.

[15] CMS Collaboration, *The CMS Experiment at the CERN LHC*, JINST **3** (2008) S08004.

[16] ATLAS Collaboration, *Evidence for the $H \to b\bar{b}$ decay with the ATLAS detector*, JHEP **12** (2017) 024, arXiv: 1708.03299 [hep-ex].

[17] CMS Collaboration, *Evidence for the Higgs boson decay to a bottom quark-antiquark pair*, Phys. Lett. B **780** (2018) 501, arXiv: 1709.07497 [hep-ex].

[18] U. Baur, M. Spira, and P. M. Zerwas, *Excited-quark and -lepton production at hadron colliders*, Phys. Rev. D **42** (1990) 815.

[19] G. R. Farrar and P. Fayet, *Phenomenology of the production, decay, and detection of new hadronic states associated with supersymmetry*, Phys. Lett. B **76** (1978) 575.

[20] Z. Sullivan, *Fully differential W' production and decay at next-to-leading order in QCD*, Phys. Rev. D **66** (2002) 075011, arXiv: hep-ph/0207290.

[21] ATLAS Collaboration, *Measurement of the inclusive and dijet cross-sections of b^- jets in pp collisions at $\sqrt{s} = 7$ TeV with the ATLAS detector*, Eur. Phys. J. C **71** (2011) 1846, arXiv: 1109.6833 [hep-ex].

[22] ATLAS Collaboration, *Measurement of the $b\bar{b}$ dijet cross section in pp collisions at $\sqrt{s} = 7$ TeV with the ATLAS detector*, Eur. Phys. J. C **76** (2016) 670, arXiv: 1607.08430 [hep-ex].

[23] CMS Collaboration, *Inclusive b-jet production in pp collisions at $\sqrt{s} = 7$ TeV*, JHEP **04** (2012) 084, arXiv: 1202.4617 [hep-ex].

[24] ATLAS Collaboration, *Measurement of differential production cross-sections for a Z boson in association with b-jets in 7 TeV proton-proton collisions with the ATLAS detector*, JHEP **10** (2014) 141, arXiv: 1407.3643 [hep-ex].

[25] CMS Collaboration, *Measurement of the production cross sections for a Z boson and one or more b jets in pp collisions at $\sqrt{s} = 7$ TeV*, JHEP **06** (2014) 120, arXiv: 1402.1521 [hep-ex].

[26] CMS Collaboration, *Measurements of the associated production of a Z boson and b jets in pp collisions at $\sqrt{s} = 8$ TeV*, Eur. Phys. J. C **77** (2017) 751, arXiv: 1611.06507 [hep-ex].

[27] LHCb Collaboration, *The LHCb Detector at the LHC*, JINST **3** (2008) S08005.

[28] LHCb Collaboration, *Measurement of the Z+b-jet cross-section in pp collisions at $\sqrt{s} = 7$ TeV in the forward region*, JHEP **01** (2015) 064, arXiv: 1411.1264 [hep-ex].

[29] ATLAS Collaboration, *Measurement of the cross-section for W boson production in association with b-jets in pp collisions at* $\sqrt{s} = 7$ *TeV with the ATLAS detector*, JHEP **06** (2013) 084, arXiv: 1302.2929 [hep-ex].

[30] CMS Collaboration, *Measurement of the production cross section for a W boson and two b jets in pp collisions at* $\sqrt{s} = 7$ *TeV*, Phys. Lett. B **735** (2014) 204, arXiv: 1312.6608 [hep-ex].

[31] CMS Collaboration, *Measurement of the production cross section of a W boson in association with two b jets in pp collisions at* $\sqrt{s} = 8$ TeV, Eur. Phys. J. C **77** (2017) 92, arXiv: 1608.07561 [hep-ex].

[32] LHCb Collaboration, *Study of W boson production in association with beauty and charm*, Phys. Rev. D **92** (2015) 052001, arXiv: 1505.04051 [hep-ex].

[33] LHCb Collaboration, *Measurement of forward* $t\bar{t}$, $W+b\bar{b}$ *and* $W+c\bar{c}$ *production in pp collisions at* $\sqrt{s} = 8$ *TeV*, Phys. Lett. B **767** (2017) 110, arXiv: 1610.08142 [hep-ex].

[34] ATLAS Collaboration, *Measurement of the inclusive isolated prompt photons cross section in pp collisions at* $\sqrt{s} = 7$ *TeV with the ATLAS detector using 4.6* fb^{-1}, Phys. Rev. D **89** (2014) 052004, arXiv: 1311.1440 [hep-ex].

[35] ATLAS Collaboration, *Measurement of the inclusive isolated prompt photon cross section in pp collisions at* $\sqrt{s} = 8$ *TeV with the ATLAS detector*, JHEP **08** (2016) 005, arXiv: 1605.03495 [hep-ex].

[36] ATLAS Collaboration, *Measurement of the cross section for inclusive isolated-photon production in pp collisions at* $\sqrt{s} = 13$ *TeV using the ATLAS detector*, Phys. Lett. B **770** (2017) 473, arXiv: 1701.06882 [hep-ex].

[37] CMS Collaboration, *Measurement of the Differential Cross Section for Isolated Prompt Photon Production in pp Collisions at 7 TeV*, Phys. Rev. D **84** (2011) 052011, arXiv: 1108.2044 [hep-ex].

[38] ATLAS Collaboration, *Measurement of the production cross section of an isolated photon associated with jets in proton-proton collisions at $\sqrt{s} = 7$ TeV with the ATLAS detector*, Phys. Rev. D **85** (2012) 092014, arXiv: 1203.3161 [hep-ex].

[39] ATLAS Collaboration, *Dynamics of isolated-photon plus jet production in pp collisions at $\sqrt{s} = 7$ TeV with the ATLAS detector*, Nucl. Phys. B **875** (2013) 483, arXiv: 1307.6795 [hep-ex].

[40] ATLAS Collaboration, *High-E_T isolated-photon plus jets production in pp collisions at $\sqrt{s} = 8$ TeV with the ATLAS detector*, Nucl. Phys. B **918** (2017) 257, arXiv: 1611.06586 [hep-ex].

[41] CMS Collaboration, *Rapidity distributions in exclusive Z + jet and γ + jet events in pp collisions at $\sqrt{s} = 7$ TeV*, Phys. Rev. D **88** (2013) 112009, arXiv: 1310.3082 [hep-ex].

[42] CMS Collaboration, *Measurement of the triple-differential cross section for photon+jets production in proton-proton collisions at $\sqrt{s} = 7$ TeV*, JHEP **06** (2014) 009, arXiv: 1311.6141 [hep-ex].

[43] CMS Collaboration, *Comparison of the Z/γ^* + jets to γ + jets cross sections in pp collisions at $\sqrt{s} = 8$ TeV*, JHEP **10** (2015) 128, Erratum: JHEP **04** (2016) 010, arXiv: 1505.06520 [hep-ex].

[44] ATLAS Collaboration, *Search for new phenomena in high-mass final states with a photon and a jet from pp collisions at* $\sqrt{s} = 13$ *TeV with the ATLAS detector*, Eur. Phys. J. C **78** (2018) 102, arXiv: 1709.10440 [hep-ex].

[45] CMS Collaboration, *Search for excited quarks of light and heavy flavor in* γ*+jet final states in proton-proton collisions at* $\sqrt{s} = 13$ *TeV*, Phys. Lett. B **781** (2018) 390, arXiv: 1711.04652 [hep-ex].

[46] CDF Collaboration, *Study of the associated production of photons and b-quark jets in* $p\bar{p}$ *collisions at* $\sqrt{s} = 1.96$ *TeV*, Phys. Rev. D **81** (2010) 052006, arXiv: 0912.3453 [hep-ex].

[47] CDF Collaboration, *Measurement of the cross section for direct-photon production in association with a heavy quark in* $p\bar{p}$ *collisions at* $\sqrt{s} = 1.96$ *TeV*, Phys. Rev. Lett. **111** (2013) 042003, arXiv: 1303.6136 [hep-ex].

[48] D0 Collaboration, *Measurement of* $\gamma + b + X$ *and* $\gamma + c + X$ *Production Cross Sections in* $p\bar{p}$ *Collisions at* $\sqrt{s} = 1.96$ *TeV*, Phys. Rev. Lett. **102** (2009) 192002, arXiv: 0901.0739 [hep-ex].

[49] D0 Collaboration, *Measurement of the photon+b-jet production differential cross section in* $p\bar{p}$ *collisions at* $\sqrt{s} = 1.96$ *TeV*, Phys. Lett. B **714** (2012) 32, arXiv: 1203.5865 [hep-ex].

[50] S. L. Glashow, *Partial-symmetries of weak interactions*, Nucl. Phys. **22** (1961) 579.

[51] S. Weinberg, *A Model of Leptons*, Phys. Rev. Lett. **19** (1967) 1264.

[52] A. Salam, *Weak and electromagnetic interactions*, Conf. Proc. C680519 (1968) 367.

[53] S. L. Glashow, J. Iliopoulos, and L. Maiani, *Weak Interactions with Lepton-Hadron Symmetry*, Phys. Rev. D **2** (1970) 1285.

[54] C. Patrignani et al., *Review of Particle Physics*, Chin. Phys. C **40** (2016) 100001.

[55] F. Englert and R. Brout, *Broken Symmetry and the Mass of Gauge Vector Mesons*, Phys. Rev. Lett. **13** (1964) 321.

[56] P. W. Higgs, *Broken Symmetries and the Masses of Gauge Bosons*, Phys. Rev. Lett. **13** (1964) 508.

[57] C. P. Burgess and G. D. Moore, *The Standard Model: A Primer*, Cambridge University Press, 2006, ISBN: 9780521860369.

[58] N. Cabibbo, *Unitary Symmetry and Leptonic Decays*, Phys. Rev. Lett. **10** (1963) 531, [,648(1963)].

[59] D. J. Gross and F. Wilczek, *Ultraviolet Behavior of Non-Abelian Gauge Theories*, Phys. Rev. Lett. **30** (1973) 1343.

[60] H. D. Politzer, *Reliable Perturbative Results for Strong Interactions?* Phys. Rev. Lett. **30** (1973) 1346, [,274(1973)].

[61] D. Boito et al., *An Updated determination of α_s from τ decays*, Phys. Rev. D **85** (2012) 093015, arXiv: 1203.3146 [hep-ph].

[62] F. Herzog, B. Ruijl, T. Ueda, J. A. M. Vermaseren, and A. Vogt, *The five-loop beta function of Yang-Mills theory with fermions*, JHEP **02** (2017) 090, arXiv: 1701.01404 [hep-ph].

[63] Super-Kamiokande Collaboration, *Evidence for Oscillation of Atmospheric Neutrinos*, Phys. Rev. Lett. **81** (1998) 1562, arXiv: hep-ex/9807003.

[64] SNO Collaboration, *Direct Evidence for Neutrino Flavor Transformation from Neutral-Current Interactions in the Sudbury Neutrino Observatory*, Phys. Rev. Lett. **89** (2002) 011301, arXiv: nucl-ex/0204008.

[65] M. H. Goroff and A. Sagnotti, *Quantum gravity at two loops*, Phys. Lett. B **160** (1985) 81.

[66] T. Gleisberg et al., *Event generation with SHERPA 1.1*, JHEP **02** (2009) 007, arXiv: 0811.4622 [hep-ph].

[67] V. N. Gribov and L. N. Lipatov, *Deep inelastic e p scattering in perturbation theory*, Sov. J. Nucl. Phys. **15** (1972) 438.

[68] Y. L. Dokshitzer, *Calculation of the Structure Functions for Deep Inelastic Scattering and e+ e- Annihilation by Perturbation Theory in Quantum Chromodynamics.*, Sov. Phys. JETP **46** (1977) 641.

[69] G. Altarelli and G. Parisi, *Asymptotic Freedom in Parton Language*, Nucl. Phys. **B126** (1977) 298.

[70] S. Moch, J. A. M. Vermaseren, and A. Vogt, *The three-loop splitting functions in QCD: the non-singlet case*, Nucl. Phys. B **688** (2004) 101, arXiv: hep-ph/0403192.

[71] A. Vogt, S. Moch, and J. A. M. Vermaseren, *The three-loop splitting functions in QCD: the singlet case*, Nucl. Phys. B **691** (2004) 129, arXiv: hep-ph/0404111.

[72] R. K. Ellis et al., *Perturbation theory and the parton model in QCD*, Nucl. Phys. B **152** (1979) 285.

[73] J. C. Collins, D. E. Soper, and G. F. Sterman, *All-order factorization for Drell-Yan cross sections*, Phys. Lett. B **134** (1983) 263, URL: https://cds.cern.ch/record/148438.

[74] J. C. Collins, D. E. Soper, and G. F. Sterman, *Factorization for short distance hadron-hadron Scattering*, Nucl. Phys. B **261** (1985) 104.

[75] NNPDF Collaboration, *Parton distributions for the LHC Run II*, JHEP **04** (2015) 040, arXiv: 1410.8849 [hep-ph].

[76] S. Dulat et al., *New parton distribution functions from a global analysis of quantum chromodynamics*, Phys. Rev. D **93** (2016) 033006, arXiv: 1506.07443 [hep-ph].

[77] NNPDF Collaboration, *Parton distributions from high-precision collider data*, (2017), arXiv: 1706.00428 [hep-ph].

[78] T.-J. Hou et al., *CT14 Intrinsic Charm Parton Distribution Functions from CTEQ-TEA Global Analysis*, (2017), arXiv: 1707.00657 [hep-ph].

[79] A. C. Benvenuti et al., *A high statistics measurement of the deuteron structure functions $F_2(x, Q^2)$ and R from deep inelastic muon scattering at high Q^2*, Phys. Lett. B **237** (1990) 592.

[80] M. Goncharov et al., *Precise measurement of dimuon production cross-sections in muon neutrino Fe and muon anti-neutrino Fe deep inelastic scattering at the Tevatron*, Phys. Rev. D **64** (2001) 112006, arXiv: hep-ex/0102049.

[81] F. D. Aaron et al., *Combined measurement and QCD analysis of the inclusive $e^{\pm}p$ scattering cross sections at HERA*, JHEP **01** (2010) 109, arXiv: 0911.0884 [hep-ex].

[82] J. Rojo et al., *The PDF4LHC report on PDFs and LHC data: results from Run I and preparation for Run II*, J. Phys. G **42** (2015) 103103, arXiv: 1507.00556 [hep-ph].

[83] F. Maltoni, G. Ridolfi, and M. Ubiali, *b-initiated processes at the LHC: a reappraisal*, JHEP **07** (2012) 022, Erratum: JHEP **04** (2013) 095, arXiv: 1203.6393 [hep-ph].

[84] A. Sherstnev and R. S. Thorne, *Parton distributions for LO generators*, Eur. Phys. J. C **55** (2008) 553, arXiv: 0711.2473 [hep-ph].

[85] T. Kinoshita, *Mass Singularities of Feynman Amplitudes*, J. Math. Phys. **3** (1962) 650.

[86] T. D. Lee and M. Nauenberg, *Degenerate Systems and Mass Singularities*, Phys. Rev. **133** (1964) B1549, [,25(1964)].

[87] F. Bloch and A. Nordsieck, *Note on the Radiation Field of the Electron*, Phys. Rev. **52** (1937) 54.

[88] S. Höche, F. Krauss, and S. Prestel, *Implementing NLO DGLAP evolution in Parton Showers*, JHEP **10** (2017) 093, arXiv: 1705.00982 [hep-ph].

[89] V. V. Sudakov, *Vertex Parts at Very High Energies in Quantum Electrodynamics*, Sov. Phys. JETP **3** (1956) 65.

[90] J. M. Cornwall and G. Tiktopoulos, *Infrared behavior of non-Abelian gauge theories*, Phys. Rev. D **13** (1976) 3370.

[91] T. Sjöstrand, S. Mrenna, and P. Z. Skands, *PYTHIA 6.4 Physics and Manual*, JHEP **05** (2006) 026, arXiv: hep-ph/0603175.

[92] T. Sjöstrand, *A model for initial state parton showers*, Phys. Lett. B **157** (1985) 321.

[93] E. Norrbin and T. Sjöstrand, *QCD radiation off heavy particles*, Nucl. Phys. B **603** (2001) 297, arXiv: hep-ph/0010012.

[94] S. Catani, S. Dittmaier, M. H. Seymour, and Z. Trocsanyi, *The dipole formalism for next-to-leading order QCD calculations with massive partons*, Nucl. Phys. B **627** (2002) 189, arXiv: hep-ph/0201036.

[95] S. Catani and M. H. Seymour, *A general algorithm for calculating jet cross-sections in NLO QCD*, Nucl. Phys. B **485** (1997) 291, Erratum: Nucl. Phys. B **510** (1998) 503, arXiv: hep-ph/9605323.

[96] K. G. Wilson, *Confinement of quarks*, Phys. Rev. D **10** (1974) 2445.

[97] R. D. Field and R. P. Feynman, *A parametrization of the properties of quark jets*, Nucl. Phys. B **136** (1978) 1.

[98] C. D. Buchanan and S. B. Chun, *Simple predictive model for flavor production in hadronization*, Phys. Rev. Lett. **59** (1987) 1997.

[99] B. R. Webber, *A QCD model for jet fragmentation including soft gluon interference*, Nucl. Phys. B **238** (1984) 492.

[100] B. Andersson, G. Gustafson, G. Ingelman, and T. Sjöstrand, *Parton fragmentation and string dynamics*, Phys. Rept. **97** (1983) 31.

[101] D. Amati and G. Veneziano, *Preconfinement as a property of perturbative QCD*, Phys. Lett. B **83** (1979) 87.

[102] B. Webber, *Parton shower Monte Carlo event generators*, Scholarpedia **6** (2011) 10662.

[103] G. S. Bali and K. Schilling, *Static quark-antiquark potential: Scaling behavior and finite size effects in SU(3) lattice gauge theory*, Phys. Rev. D **46** (1992) 2636.

[104] E. Gotsman, E. Levin, and U. Maor, *Description of LHC data in a soft interaction model*, Phys. Lett. B **716** (2012) 425, arXiv: 1208.0898 [hep-ph].

[105] T. Sjöstrand and M. van Zijl, *A multiple-interaction model for the event structure in hadron collisions*, Phys. Rev. D **36** (1987) 2019.

[106] M. Bahr, J. M. Butterworth, and M. H. Seymour, *The underlying event and the total cross section from Tevatron to the LHC*, JHEP **01** (2009) 065, arXiv: 0806.2949 [hep-ph].

[107] T. Martin, P. Skands, and S. Farrington, *Probing collective effects in hadronisation with the extremes of the underlying event*, Eur. Phys. J. C **76** (2016) 299, arXiv: 1603.05298 [hep-ph].

[108] R. Corke and T. Sjöstrand, *Multiparton interactions and rescattering*, JHEP **01** (2010) 035, arXiv: 0911.1909 [hep-ph].

[109] T. Sjöstrand and P. Z. Skands, *Multiple interactions and the structure of beam remnants*, JHEP **03** (2004) 053, arXiv: hep-ph/0402078.

[110] T. Sjöstrand, S. Mrenna, and P. Z. Skands, *A brief introduction to PYTHIA 8.1*, Comput. Phys. Commun. **178** (2008) 852, arXiv: 0710.3820 [hep-ph].

[111] T. Sjöstrand and P. Z. Skands, *Transverse-momentum-ordered showers and interleaved multiple interactions*, Eur. Phys. J. C **39** (2005) 129, arXiv: hep-ph/0408302.

[112] J.-C. Winter, F. Krauss, and G. Soff, *A modified cluster-hadronization model*, Eur. Phys. J. C **36** (2004) 381, arXiv: hep-ph/0311085.

[113] S. Höche, F. Krauss, S. Schumann, and F. Siegert, *QCD matrix elements and truncated showers*, JHEP **05** (2009) 053, arXiv: 0903.1219 [hep-ph].

[114] S. Hoeche, F. Krauss, M. Schonherr, and F. Siegert, *QCD matrix elements + parton showers. The NLO case*, JHEP **04** (2013) 027, arXiv: 1207.5030 [hep-ph].

[115] J. Alwall et al., *The automated computation of tree-level and next-to-leading order differential cross sections, and their matching to parton shower simulations*, JHEP **07** (2014) 079, arXiv: 1405.0301 [hep-ph].

[116] S. Frixione and B. R. Webber, *Matching NLO QCD computations and parton shower simulations*, JHEP **06** (2002) 029, arXiv: hep-ph/0204244.

[117] S. Frixione, P. Nason, and C. Oleari, *Matching NLO QCD computations with parton shower simulations: the POWHEG method*, JHEP **11** (2007) 070, arXiv: 0709.2092 [hep-ph].

[118] R. Frederix and S. Frixione, *Merging meets matching in MC@NLO*, JHEP **12** (2012) 061, arXiv: 1209.6215 [hep-ph].

[119] S. Catani, M. Fontannaz, J. P. Guillet, and E. Pilon, *Cross section of isolated prompt photons in hadron-hadron collisions*, JHEP **05** (2002) 028, arXiv: hep-ph/0204023.

[120] T. Binoth, J. P. Guillet, E. Pilon, and M. Werlen, *A full next-to-leading order study of direct photon pair production in hadronic collisions*, Eur. Phys. J. C **16** (2000) 311, arXiv: hep-ph/9911340.

[121] ATLAS Collaboration, *Measurements of integrated and differential cross sections for isolated photon pair production in pp collisions at $\sqrt{s} = 8$ TeV with the ATLAS detector*, Phys. Rev. D **95** (2017) 112005, arXiv: 1704.03839 [hep-ex].

[122] J. P. Guillet, (2016), Private communication.

[123] L. Bourhis, M. Fontannaz, and J. P. Guillet, *Quarks and gluon fragmentation functions into photons*, Eur. Phys. J. C **2** (1998) 529, arXiv: hep-ph/9704447.

[124] D. d'Enterria and J. Rojo, *Quantitative constraints on the gluon distribution function in the proton from collider isolated-photon data*, Nucl. Phys. B **860** (2012) 311, arXiv: 1202.1762 [hep-ph].

[125] S. Frixione, *Isolated photons in perturbative QCD*, Phys. Lett. B **429** (1998) 369, arXiv: hep-ph/9801442.

[126] F. Krauss, D. Napoletano, and S. Schumann, *Simulating b-associated production of Z and Higgs bosons with the* SHERPA *event generator*, Phys. Rev. D **95** (2017) 036012, arXiv: 1612.04640 [hep-ph].

[127] M. Cacciari, P. Nason, and C. Oleari, *A study of heavy flavoured meson fragmentation functions in e^+e^- annihilation*, JHEP **04** (2006) 006, arXiv: hep-ph/0510032.

[128] B. Bailey, E. L. Berger, and L. E. Gordon, *Production of a prompt photon in association with a charm quark at next-to-leading order in QCD*, Phys. Rev. D **54** (1996) 1896, arXiv: hep-ph/9602373.

[129] A. Banfi, G. P. Salam, and G. Zanderighi, *Infrared-safe definition of jet flavour*, Eur. Phys. J. C **47** (2006) 113, arXiv: hep-ph/0601139.

[130] S. Frixione and M. L. Mangano, *Heavy-quark jets in hadronic collisions*, Nucl. Phys. B **483** (1997) 321, arXiv: hep-ph/9605270.

[131] F. Arleo, M. Fontannaz, J.-P. Guillet, and C. L. Nguyen, *Probing fragmentation functions from same-side hadron-jet momentum correlations in p-p collisions*, JHEP **04** (2014) 147, arXiv: 1311.7356 [hep-ph].

[132] ATLAS Collaboration, *Summary of ATLAS Pythia 8 tunes*, ATL-PHYS-PUB-2012-003, URL: https://cds.cern.ch/record/1474107.

[133] J. Pumplin et al., *New generation of parton distributions with uncertainties from global QCD analysis*, JHEP **07** (2002) 012, arXiv: hep-ph/0201195.

[134] T. Carli, T. Gehrmann, and S. Hoeche, *Hadronic final states in deep-inelastic scattering with* SHERPA, Eur. Phys. J. C **67** (2010) 73, arXiv: 0912.3715 [hep-ph].

[135] H.-L. Lai et al., *New parton distributions for collider physics*, Phys. Rev. D **82** (2010) 074024, arXiv: 1007.2241 [hep-ph].

[136] F. Krauss and D. Napoletano, *Towards a fully massive five-flavour scheme*, (2017), arXiv: 1712.06832 [hep-ph].

[137] A. Czarnecki and W. J. Marciano, *Electroweak Radiative Corrections to $b \to s\gamma$*, Phys. Rev. Lett. **81** (1998) 277, arXiv: hep-ph/9804252.

[138] T. Sjöstrand et al., *An introduction to PYTHIA 8.2*, Comput. Phys. Commun. **191** (2015) 159, arXiv: 1410.3012 [hep-ph].

[139] ATLAS Collaboration, *ATLAS Run 1 Pythia8 tunes*, ATL-PHYS-PUB-2014-021, URL: https://cds.cern.ch/record/1966419.

[140] S. Catani, M. Ciafaloni, and F. Hautmann, *Gluon contributions to small x heavy flavour production*, Phys. Lett. B **242** (1990) 97.

[141] A. V. Lipatov, M. A. Malyshev, and N. P. Zotov, *Prompt photon and associated heavy quark production at hadron colliders with k_T-factorization*, JHEP **05** (2012) 104, arXiv: 1204.3828 [hep-ph].

[142] T. P. Stavreva and J. F. Owens, *Direct photon production in association with a heavy quark at hadron colliders*, Phys. Rev. D **79** (2009) 054017, arXiv: 0901.3791 [hep-ph].

[143] K. Aamodt et al., *The ALICE experiment at the CERN LHC*, JINST **3** (2008) S08002.

[144] ATLAS Collaboration, *Measurement of the W^+W^- production cross section in pp collisions at a centre-of-mass energy of $\sqrt{s} = 13$ TeV with the ATLAS experiment*, ATLAS-CONF-2016-090, URL: https://cds.cern.ch/record/2206811.

[145] ATLAS Collaboration, *Measurement of the total ZZ production cross section in proton-proton collisions at $\sqrt{s} = 8$ TeV in 20 fb^{-1} with the ATLAS detector*, ATLAS-CONF-2013-020, URL: https://cds.cern.ch/record/1525555.

[146] ATLAS Top Physics Group Summary Plots, https://atlas.web.cern.ch/Atlas/GROUPS/PHYSICS/CombinedSummaryPlots/TOP.

[147] ATLAS Collaboration, *Luminosity determination in pp collisions at $\sqrt{s} = 8$ TeV using the ATLAS detector at the LHC*, Eur. Phys. J. C **76** (2016) 653, arXiv: 1608.03953 [hep-ex].

[148] A. Andronic and J. P. Wessels, *Transition radiation detectors*, Nucl. Instrum. Meth. A **666** (2012) 130, arXiv: 1111.4188 [physics.ins-det].

[149] C. W. Fabjan and F. Gianotti, *Calorimetry for particle physics*, Rev. Mod. Phys. **75** (2003) 1243.

[150] ATLAS Collaboration, *Topological cell clustering in the ATLAS calorimeters and its performance in LHC Run 1*, Eur. Phys. J. C **77** (2017) 490, arXiv: 1603.02934 [hep-ex].

[151] V. Cindro et al., *The ATLAS Beam Conditions Monitor*, JINST **3** (2008) P02004.

[152] ATLAS Collaboration, *ATLAS Forward Detectors for Luminosity Measurement and Monitoring*, CERN-LHCC-2004-010, URL: https://cds.cern.ch/record/721908.

[153] S. van der Meer, *Calibration of the effective beam height in the ISR*, CERN-ISR-PO-68-31, URL: https://cds.cern.ch/record/296752.

[154] ATLAS Public Data Quality Tables, https://twiki.cern.ch/twiki/bin/view/AtlasPublic/RunStatsPublicResults2010.

[155] ATLAS Public Luminosity Plots, https://twiki.cern.ch/twiki/bin/view/AtlasPublic/LuminosityPublicResults.

[156] S. Agostinelli et al., *GEANT4 - a simulation toolkit*, Nucl. Instrum. Meth. A **506** (2003) 250.

[157] ATLAS Collaboration, *The ATLAS Simulation Infrastructure*, Eur. Phys. J. C **70** (2010) 823, arXiv: 1005.4568 [physics.ins-det].

[158] A. D. Martin, W. J. Stirling, R. S. Thorne, and G. Watt, *Parton distributions for the LHC*, Eur. Phys. J. C **63** (2009) 189, arXiv: 0901.0002 [hep-ph].

[159] T. Cornelissen et al., *The new ATLAS track reconstruction (NEWT)*, J. Phys. Conf. Ser. **119** (2008) 032014.

[160] R. Fruhwirth, *Application of Kalman filtering to track and vertex fitting*, Nucl. Instrum. Meth. A **262** (1987) 444.

[161] R. O. Duda and P. E. Hart, *Use of the Hough Transformation to Detect Lines and Curves in Pictures*, Commun. ACM **15** (1972) 11.

[162] ATLAS Collaboration, *Performance of the ATLAS Inner Detector Track and Vertex Reconstruction in the High Pile-Up LHC Environment*, ATLAS-CONF-2012-042, URL: https://cds.cern.ch/record/1435196.

[163] C. Grupen and B. Shwartz, *Particle Detectors*, Cambridge University Press, 2008, ISBN: 9780521840064.

[164] ATLAS Collaboration, *Reconstruction of primary vertices at the ATLAS experiment in Run 1 proton-proton collisions at the LHC*, Eur. Phys. J. C **77** (2017) 332, arXiv: 1611.10235 [physics.ins-det].

[165] R. Fruhwirth, W. Waltenberger, and P. Vanlaer, *Adaptive vertex fitting*, J. Phys. G **34** (2007) N343.

[166] ATLAS Collaboration, *Measurement of the photon identification efficiencies with the ATLAS detector using LHC Run-1 data*, Eur. Phys. J. C **76** (2016) 666, arXiv: 1606.01813 [hep-ex].

[167] ATLAS Collaboration, *Electron and photon reconstruction and performance in ATLAS using a dynamical, topological cell clustering-based approach*, ATL-PHYS-PUB-2017-022, URL: https://cds.cern.ch/record/2298955.

[168] ATLAS Collaboration, *Expected photon performance in the ATLAS experiment*, ATL-PHYS-PUB-2011-007, URL: https://cds.cern.ch/record/1345329.

[169] ATLAS Collaboration, *Electron and photon energy calibration with the ATLAS detector using LHC Run 1 data*, Eur. Phys. J. C **74** (2014) 3071, arXiv: 1407.5063 [hep-ex].

[170] M. Cacciari and G. P. Salam, *Pileup subtraction using jet areas*, Phys. Lett. B **659** (2008) 119, arXiv: 0707.1378 [hep-ph].

[171] S. Catani, Y. L. Dokshitzer, M. H. Seymour, and B. R. Webber, *Longitudinally-invariant $k_\perp$-clustering algorithms for hadron–hadron collisions*, Nucl. Phys. B **406** (1993) 187.

[172] S. D. Ellis and D. E. Soper, *Successive combination jet algorithm for hadron collisions*, Phys. Rev. D **48** (1993) 3160, arXiv: hep-ph/9305266.

[173] M. Cacciari, G. P. Salam, and G. Soyez, *The anti-k_t jet clustering algorithm*, JHEP **04** (2008) 063, arXiv: 0802.1189 [hep-ph].

[174] ATLAS Collaboration, *Jet energy measurement and its systematic uncertainty in proton-proton collisions at $\sqrt{s} = 7$ TeV with the ATLAS detector*, Eur. Phys. J. C **75** (2015) 17, arXiv: 1406.0076 [hep-ex].

[175] ATLAS Collaboration, *Monte Carlo Calibration and Combination of In-situ Measurements of Jet Energy Scale, Jet Energy Resolution and Jet Mass in*

ATLAS, ATLAS-CONF-2015-037, URL: https://cds.cern.ch/record/2044941.

[176] ATLAS Collaboration, *Jet global sequential corrections with the ATLAS detector in proton-proton collisions at* $\sqrt{s} = 8$ *TeV*, ATLAS-CONF-2015-002, URL: https://cds.cern.ch/record/2001682.

[177] ATLAS Collaboration, *Data-driven determination of the energy scale and resolution of jets reconstructed in the ATLAS calorimeters using dijet and multijet events at* $\sqrt{s} = 8$ *TeV*, ATLAS-CONF-2015-017, URL: https://cds.cern.ch/record/2008678.

[178] ATLAS Collaboration, *Determination of the jet energy scale and resolution at ATLAS using* Z/γ*–jet events in data at* $\sqrt{s} = 8$ *TeV*, ATLAS-CONF-2015-057, URL: https://cds.cern.ch/record/2059846.

[179] ATLAS Collaboration, *Performance of pile-up mitigation techniques for jets in pp collisions at* $\sqrt{s} = 8$ *TeV using the ATLAS detector*, Eur. Phys. J. C **76** (2016) 581, arXiv: 1510.03823 [hep-ex].

[180] ATLAS Collaboration, *Performance of b-jet identification in the ATLAS experiment*, JINST **11** (2016) P04008, arXiv: 1512.01094 [hep-ex].

[181] ATLAS Collaboration, *Calibration of b-tagging using dileptonic top pair events in a combinatorial likelihood approach with the ATLAS experiment*, ATLAS-CONF-2014-004, URL: https://cds.cern.ch/record/1664335.

[182] ATLAS Collaboration, *Calibration of the performance of b-tagging for c and light-flavour jets in the 2012 ATLAS data*, ATLAS-CONF-2014-046, URL: https://cds.cern.ch/record/1741020.

[183] D. J. Lange, *The EvtGen particle decay simulation package*, Nucl. Instrum. Meth. A **462** (2001) 152.

[184] ATLAS Collaboration, *Performance of the ATLAS Electron and Photon Trigger in p-p Collisions at* $\sqrt{s} = 7$ *TeV in 2011*, ATLAS-CONF-2012-048, URL: https://cds.cern.ch/record/1450089.

[185] C. J. Clopper and E. S. Pearson, *The use of confidence or fiducial limits illustrated in the case of the binomial*, Biometrika **26** (1934) 404.

[186] E. L. Berger and J.-w. Qiu, *Calculations of prompt-photon production in QCD*, Phys. Rev. D **44** (1991) 2002.

[187] ATLAS Collaboration, *Measurements of fiducial cross-sections for* $t\bar{t}$ *production with one or two additional b-jets in pp collisions at* $\sqrt{s} = 8$ *TeV using the ATLAS detector*, Eur. Phys. J. C **76** (2016) 11, arXiv: 1508.06868 [hep-ex].

[188] ATLAS Collaboration, *Measurement of differential cross sections of isolated-photon plus heavy-flavour jet production in pp collisions at* $\sqrt{s} = 8$ *TeV using the ATLAS detector*, Phys. Lett. B **776** (2018) 295, arXiv: 1710.09560 [hep-ex].

[189] G. Cowan, *A survey of unfolding methods for particle physics*, Conf. Proc. C0203181 (2002) 248, URL: https://www.ippp.dur.ac.uk/Workshops/02/statistics/proceedings/cowan.pdf.

[190] G. D'Agostini, *A multidimensional unfolding method based on Bayes' theorem*, Nucl. Instrum. Meth. A **362** (1995) 487.

[191] G. Bohm and G. Zech, *Introduction to Statistics and Data Analysis for Physicists – Third Revised Edition*, Verlag Deutsches Elektronen-Synchrotron, 2017, ISBN: 978-3-945931-13-4, DOI: 10.3204/PUBDB-2017-08987.

[192] R. D. Ball et al., *Precision determination of electroweak parameters and the strange content of the proton from neutrino deep-inelastic scattering*, Nucl. Phys. B **823** (2009) 195, arXiv: 0906.1958 [hep-ph].

[193] J. Pumplin et al., *Uncertainties of predictions from parton distribution functions. II. The Hessian method*, Phys. Rev. D **65** (2001) 014013, arXiv: hep-ph/0101032.

[194] The complete set of numerical values regarding the measurement is available at the Durham HEPData repository: https://hepdata.net/record/ins1632756.

[195] Software allowing to reproduce the particle-level selection that defines the fiducial region of the measured cross section is available at the Rivet analysis repository: https://rivet.hepforge.org/analyses/ATLAS_2017_I1632756.

[196] ATLAS Collaboration, *Search for the standard model Higgs boson produced in association with top quarks and decaying into a $b\bar{b}$ pair in pp collisions at $\sqrt{s} = 13$ TeV with the ATLAS detector*, Phys. Rev. D **97** (2018) 072016, arXiv: 1712.08895 [hep-ex].

[197] D0 Collaboration, *Measurement of the differential $\gamma + c$-jet cross section and the ratio of differential $\gamma + c$ and $\gamma + b$ cross sections in $p\bar{p}$ collisions at $\sqrt{s} = 1.96$ TeV*, Phys. Lett. B **719** (2013) 354, arXiv: 1210.5033 [hep-ex].

[198] S. J. Brodsky, V. A. Bednyakov, G. I. Lykasov, J. Smiesko, and S. Tokar, *The physics of heavy quark distributions in hadrons: Collider tests*, Prog. Part. Nucl. Phys. **93** (2017) 108, arXiv: 1612.01351 [hep-ph].

[199] G. P. Salam and G. Soyez, *A practical seedless infrared-safe cone jet algorithm*, JHEP **05** (2007) 086, arXiv: 0704.0292 [hep-ph].

[200] G. P. Salam, *Towards jetography*, Eur. Phys. J. C **67** (2010) 637, arXiv: 0906.1833 [hep-ph].

[201] M. Wobisch and T. Wengler, *Hadronization Corrections to Jet Cross Sections in Deep-Inelastic Scattering*, Conf. Proc. C980427 (1998) 270, arXiv: hep-ph/9907280.